Regulation of VAP(P58S) neuroaggregation in a *Drosophila* model of Amyotrophic Lateral Sclerosis

A Thesis

Submitted in partial fulfillment of the requirements

of the degree of

Doctor of Philosophy

By

Kriti Chaplot

20133253

Indian Institute of Science Education and Research Pune

2019

CERTIFICATE

Certified that the work incorporated in the thesis entitled "*Regulation of VAP(P58S) neuroaggregation in a Drosophila model of Amyotrophic Lateral Sclerosis*", submitted by Kriti Chaplot was carried out by the candidate, under my supervision. The work presented here or any part of it has not been included in any other thesis submitted previously for the award of any degree or diploma from any other University or institution.

Dr. Girish Ratnaparkhi

DECLARATION

I declare that this written submission represents my ideas in my own words, and where others' ideas have been included, I have adequately cited and referenced the original sources. I also declare that I have adhered to all principles of academic honesty and integrity and have not misrepresented or fabricated or falsified any idea/data/fact/source in my submission. I understand that violation of the above will be cause for disciplinary action by the Institute and can also evoke penal action from the sources which have thus not been properly cited or from whom proper permission has not been taken when needed.

Kriti Chaplot
20133253

Acknowledgements

I would like to dedicate my PhD thesis to my supervisor, Dr. Girish Ratnaparkhi, for giving me the opportunity to pursue my graduate studies in his laboratory. I am immensely thankful to him for being an indulgent teacher and a patient listener. I am grateful to Dr. Anuradha Ratnaparkhi and Dr. Senthilkumar Deivasigamani for adding me to the lab as a project assistant way back in 2012. Senthil has been instrumental in mentoring me in my early years of PhD and still continues to be a supportive friend to this day. I would like to thank Dr. Anuradha Ratnaparkhi, Dr. Richa Rikhy, and Dr. Girish Deshpande for providing me valuable scientific inputs for my project. My research advisory committee members, Dr. Thomas Pucadyil and Dr. Vasudevan Seshadri are thanked for their comments and advice throughout the course of my PhD. I am grateful to my collaborators, Dr. Siddhesh Kamat and Balaji Ramalingam, for contributing to my research and teaching me about lipidomics and image analysis, respectively. I am thankful to Dr. L. S. Shashidhara for shaping the biology department at IISER Pune.

I would like to acknowledge my lab mates, Prajna Nayak, Amarendranath Soory, Shweta Tendulkar, Sushmitha Hegde, Aparna Thulasidharan, Kundan Kumar and Neel Wagh for being absolutely “MARVEL”ous. I have really enjoyed our conversations about science and otherwise, be it during lab meetings or coffee breaks, movies and dinners. I thank everyone for contributing to a lively lab atmosphere. I thank my supervisor, Girish, for giving me all the independence to drive my project, and the philosophical analogy-filled speeches (with tea) whenever I failed. My seniors from the lab, Bhagyashree Kaduskar, Vallari Shukla, Senthil, and Mithila Handu are thanked for their immense support and advice. The VAP group of Senthil, Lokesh Pimpale, Shweta, Aparna and Lovleen Garg require a special mention in helping me shape my research. I thank Srija Bhagvatula and Lokesh for being my partners in crime during my initial years at IISER.

I would like to thank the academic office staff, especially, Tushar Kurulkar and Priyadarshini Tamhane for their help with the funding applications for my visit to the Gordon Research Conference (GRC) in Castelldefels, Spain, 2018. I am thankful to the DMM travel grant, GRC, DBT as well as Infosys Foundation for funding my visit to Spain. The microscopy facility, fly facility as well as the biology office are thanked for their help throughout my PhD, notably, Vijay Vittal, Bhargavi Naik, Snehal Patil, Yashwant Pawar, Mrinalini Virkar, Shabnam Patil, Kalpesh Thakare, Piyush Gadekar, among others. I am grateful to the cleaning staff and security

staff for maintaining a safe environment at IISER. I would like to thank all the canteen workers who have provided me with the perfect cup of coffee or tea at Sai, G1, LHC, MDP, CCD and shivsagar!

My PhD would not have been possible without the constant love and care from my family and friends through all the ups and downs over the last few years. My parents, my brother Nipun, my sister-in-law Divya, and the source of all joys, my baby niece, Aashna, are thanked for always lifting my spirits on a bad day. My childhood friends Goda and Jyotsna have always been a source of comfort and support all through my PhD. I appreciate Raunaq Deo for being my family far from home, Prajna for the relaxing long walks and conversations, Devika Andhare for being a classy housemate, Kunalika Jain for being an inspiring tea-mate, and Lokesh for being an avid icecream/food-co-hunter. I cherish my college friends, Dhruti, Dhano, Abhijit and Raju for our (mostly) annual get-togethers, and especially, thank Dhruti for hosting me in Bangalore at the time of the submission of this thesis.

Table of Contents

List of Figures

Chapter I: Protein misfolding and aggregation in Neurodegenerative disease

Chapter II: SOD1 activity threshold and TOR signaling modulate VAP(P58S) aggregation via ROS-induced proteasomal degradation in a Drosophila model of Amyotrophic Lateral Sclerosis

Chapter III :Peptidyl-Prolyl Isomerases modify protein aggregation in a Drosophila model of VAP-B/ALS8 associated Amyotrophic Lateral Sclerosis

Appendix 4: Understanding the role of VAP in lipid metabolism in a *Drosophila* model of ALS8

Appendix 5: Reagents

List of Tables

Synopsis

Regulation of VAP(P58S) neuroaggregation in a *Drosophila* model of Amyotrophic Lateral Sclerosis

Kriti Chaplot

20133253

Amyotrophic lateral sclerosis, also known as Lou Gehrig's disease is a progressive neurodegenerative disorder that culminates in the death of motor neurons of the brain stem and spinal cord. The term: "A-myo-trophic" (In Greek, *A*: not, *myo*: muscle, *trophic*: nourishment) refers to lack of nourishment to the muscle. Death of motor neurons leads to disruption of signaling to the voluntary muscles which causes the atrophy. The term "lateral" refers to the lateral region of the spinal cord whose motor neurons are affected. "Sclerosis" refers to the scarring caused due to the degeneration of the motor neuron. A case of typical ALS disorder shows clinical symptoms by an average age of 55 year, resulting in rapid prognosis and death in 3-5 years of onset. A common reason for death is respiratory failure owning to the loss of control over the thoracic and diaphragm muscles. Both sporadic as well as familial cases have been identified in ALS with more than 50 potential genetic loci known to be involved in the disease. ALS is incurable with riluzole and edaravone being the only FDA-approved drugs that slow down the progression of the disease.

For my thesis, I have worked on a prominent cellular aspect of the disease which is protein aggregation. Protein aggregates in neurodegenerative disease are responsible for the formation of plaques or legions in the brain that can lead to loss of neuronal function and subsequent death. Various proteins have been characterized in ALS have been shown to form cellular inclusions in patient samples such as TDP-43, C9ORF72 and SOD1. Understanding the regulation of protein aggregates in the cell is important to gain insight into the development of the disease. One such locus is Vesicle Associated Membrane Protein (VAMP) - Associated protein-B (VAPB or VAP) that is known to cause ALS8. VAP plays several important roles in the cell regarding vesicular trafficking, lipid transport and maintaining membrane contact sites between organelles. A missense mutation in VAP, P56S, leads to misfolding and aggregation of the protein. I explore the

conformational and functional regulation to understand what triggers VAP to misfold, leading to subsequent aggregation, and which mechanisms aid in clearance of misfolded proteins in the cell reducing VAP aggregation. These studies are performed in a *Drosophila* model of ALS8 by overexpressing the *Drosophila* ortholog of the mutant protein, VAP(P58S), in the brain of the fly.

In Chapter I, I review literature known about the role of aggregation in neurodegenerative diseases. In each neurodegenerative disease, a set of specific proteins have been characterized to form aggregates such as lewy bodies, skein-like inclusions, neurofibrillary tangles as well as granular structures. Ageing or presence of mutations promote misfolding of the proteins, formation of toxic soluble and oligomeric species giving rise to larger aggregates, together causing a havoc for cellular homeostasis. With a focus on ALS loci, I explore the various cellular processes that become disrupted in the course of the disease, prominently, RNA processing and proteostasis, and their relationship with the aggregating species. A major regulator for proteostasis in the cell is the mTOR pathway, which affects protein synthesis as well as degradation based on nutrient availability, attaining a prominent seat in disease mechanisms.

In Chapter II, I introduce a cell-based RNA interference screen performed in the lab to identify modifiers of VAP(P58S) aggregation. We chose to target genes known to be involved in ALS, VAP function and proteostasis. We analyzed the images screen using a MATLAB code using the parameters, average cell intensity and total cell intensity, arriving at a list of 150 targets and 85 targets, respectively, with an overlap of 57 genes. Prominently, we identified other ALS loci such as SOD1 and TDP-43 as modulators of VAP(P58S) aggregation. Using the *Drosophila* model of ALS8, it was found that SOD1 knockdown could reduce the aggregation levels of overexpressed VAP(P58S) in the ventral nerve cord of third instar larval brains. This reduction was found to be a result of accumulated reactive oxygen species in the brain cells. The ROS appeared to be triggering the proteasomal degradation machinery for the clearance of VAP(P58S) protein/aggregates. mTOR pathway that regulates the two degradative pathways, proteasome and autophagy, was also found to modulate VAP(P58S) aggregation. Although, autophagy was not found to be directly involved in the degradation of VAP(P58S) aggregation, mTOR downregulation was found to induce ROS thereby triggering proteasomal degradation. This work integrates the functional relationship between three proteins, VAP, SOD1 and mTOR as regulators of ROS.

In Chapter III, I discuss the role of proline conformation for proper VAP folding. X-Proline peptide bond present in the *cis* conformation at the 58th position in *Drosophila* VAP protein, provides the N-terminal MSP domain an immunoglobulin-like fold. Replacement of proline at residues involved in *cis* peptide bonds causes a gain of *trans* conformation that leads the protein to misfold and form aggregates. VAP folding and aggregation is significantly depended on the conformational specificity provided by proline. We also found that inhibition of Peptidyl Prolyl Isomerases (PPIases) can induce VAP aggregation and modulate VAP(P58S) aggregation. PPIases that can aid in proper VAP folding can be identified and characterized in the *Drosophila* brain using the neuroaggregation assay.

In Chapter IV, I summarize the work in my thesis, while highlighting the cellular role of VAP known in literature. I further discuss the three *Drosophila* models for VAP/ALS8 that I have used in my research to study VAP function, folding and aggregation, providing future directions for the project.

Publications

1. *SOD1 activity threshold and TOR signalling modulate VAP(P58S) aggregation via ROS-induced proteasomal degradation in a Drosophila model of Amyotrophic Lateral Sclerosis.* Kriti Chaplot, Lokesh Pimpale, Balaji Ramalingam, Senthilkumar Deivasigamani, Siddhesh S. Kamat, Girish S. Ratnaparkhi. *Disease Models and Mechanisms.* Dis Model Mech. 2019 Jan 11. pii: dmm.033803. doi: 10.1242/dmm.033803.
2. *Understanding motor neuron disease in flies.* Kriti Chaplot, Anuradha Ratnaparkhi, Girish S. Ratnaparkhi. in 'Insights into human neurodegeneration: Lessons learnt from *Drosophila*'. Book Chapter. Springer-Nature. Submitted (2018).
3. *Peptidyl-Prolyl Isomerases modify VAPB/ALS8 aggregation in a Drosophila model of Amyotrophic Lateral Sclerosis.* Kriti Chaplot, Girish S. Ratnaparkhi. Manuscript in preparation (2019).
4. *The genetic basis of human Amyotrophic Lateral Sclerosis.* Senthilkumar D., Kriti Chaplot, Anuradha Ratnaparkhi, Girish S. Ratnaparkhi. Review in preparation (2019).
5. *Emerging view of aggregation in ALS pathogenesis.* Kriti Chaplot, Girish S. Ratnaparkhi. Review in preparation (2019).

Chapter I

Protein misfolding and aggregation in Neurodegenerative disease

Summary

Neuronal aggregation is a hallmark of neurodegenerative diseases. Neurodegeneration leads to the death of neurons, believed to be a consequence of malfunction of core cellular processes such as proteostasis, RNA metabolism and synaptic function. The breakdown of cellular regulatory networks is accompanied with a progressive deterioration of protein function and stability. In this chapter, we address the factors that regulate the formation, maintenance and degradation of misfolded proteins and aggregates in the cell. With a focus on amyotrophic lateral sclerosis, we explore the examples of different proteins that are involved in aggregation and its modulation in the disease.

Introduction

Motor Neuron Disorder

Amyotrophic lateral sclerosis, also known as Lou Gehrig's disease, is a late onset human neurodegenerative disease that results in loss of motor function and subsequent death. It was first identified as a neurological condition in 1874 by Jean-Martin Charcot. The disease involves the degeneration of motor neurons of the "lateral" regions of spinal cord and the brain stem resulting in scarring or "sclerosis" of the brain tissue. This causes a disruption of signaling at the neuromuscular junction that results in the lack of nourishment and subsequent atrophy of voluntary muscles (Fig. 1). Recent studies have also suggested the role of non-neuronal neighbours of motor neurons, particularly glial cells in a complex pathological interplay in the progression of the disease (Philips and Robberecht 2011). Symptoms of a typical case of ALS clinically manifest post an average age of 55 years. The patients start to develop muscular weakness, fasciculation, spasticity and ultimately, paralysis. Due to the loss of control over the thoracic and diaphragm muscles, death commonly occurs within 5-6 years of onset by respiratory failure. Examples of atypical forms of ALS include, among others, juvenile ALS which is early-onset, ALS with fronto-temporal dementia, and ALS with spinal muscular atrophy (Andersen and Al-Chalabi 2011).

The progression of the disease may be largely influenced by the genetic make-up of the patient and to a certain extent by environmental factors. The disease can be sporadic as well as familial. About 90% of the cases are sporadic where the patient may develop ALS phenotypes without a prior genetic history in the family. About 10% of the cases are familial in which an inheritable genetic mutation may be responsible for the patient's susceptibility for the disease. 29 genetic ALS loci have been identified till date in large cohorts of families across the world through pedigree analysis, genome-wide association studies (GWAS) and sequencing studies (Abel et al. 2012). These different genetic loci show variable prevalence and penetrance across populations. They are also pleiotropic in nature such that a single mutation may manifest its effects in the form of ALS and/or with an associated neurological disease for instance, fronto-temporal dementia (FTD) in ALS10 and spinal muscular atrophy (SMA) in ALS8 (Andersen and Al-Chalabi 2011).

At the cellular level, several hallmarks of ALS are known which point toward the breakdown of homeostasis pathways within the cell (Cluskey et al. 2001), invoking endoplasmic reticulum (ER) stress, unfolded protein response, proteasomal machinery, RNA pathology, oxidative stress, mitochondrial dysfunction and autophagy (Fig. 1). Structural abnormalities of neurofilaments, cytoskeleton, ER and neuromuscular junction (NMJ) (Pennetta et al. 2002) have also been reported. A prime feature shown in ALS patient tissue samples is the presence of cellular inclusions. These inclusions have been shown to contain misfolded proteins, forming neuronal aggregates (Blokhuis et al. 2013). Whether these aggregates are a cause or effect of the cellular disturbances observed in ALS is under debate. Along with cell-autonomous defects, disruption of signaling pathways across the tripartite synapse of motor neurons, muscle and glia have also been reported, incurring glutamate excitotoxicity (Boillée et al. 2006). Riluzole and edaravone are the only drugs known to slow down the progression of the disease. Riluzole acts by blocking voltage-gated sodium channels so as to reduce glutamate signaling, whereas edaravone acts by reducing oxidative stress (Rothstein 2017; Dharmadasa and Kiernan 2018). A combination of effects at the cell autonomous and cell non-autonomous level might concur in selective susceptibility of motor neurons in this disease.

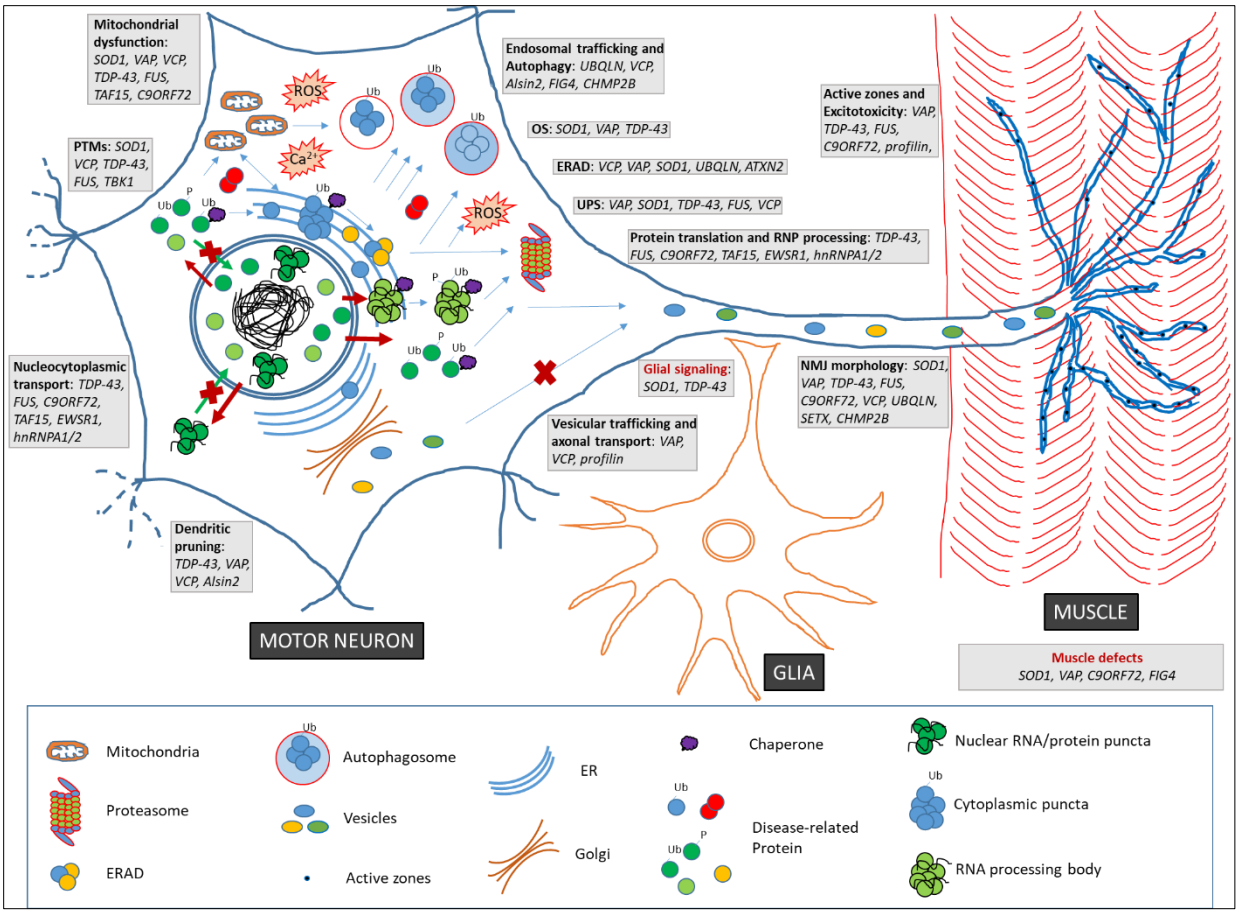

Figure 1: Schematic representation of known functions of genes that have been identified as causative loci for motor neuron disease.

Disease-causing mutations in ALS loci presumably cause a loss-of-function, or in some cases, a toxic gain-of-function. A class of these loci are RNA-binding proteins, DPRs, TDP-43, FUS, hnRNPA1/2, EWSR1 and TAF15. Defects associated with these loci include, nuclear toxicity, impaired nucleocytoplasmic transport, altered RNA binding and trafficking, disrupted protein translation, and toxic RNA-protein complex formation. Expression of some of these proteins such as TDP-43 and FUS also appears to be autoregulated. Another arm severely affected at the cellular level in ALS is proteostasis. This includes ER stress, unfolded protein response (URP), oxidative stress (OS), chaperone activity, ER associated degradation (ERAD), proteasomal degradation and autophagy. Loci actively involved in these mechanisms are SOD1, VAP, VCP and UBQLN. Mutant proteins in ALS can act as monomers with toxic gain-of-function and/or form toxic RNP complexes and protein aggregates. Monomeric, oligomeric or aggregated forms of can be subjected to post-translational modifications like phosphorylation and ubiquitination. Oligomers and aggregates can also be solubilized through chaperone activity. PTMs and solubilzation can prime these proteins for degradation through proteasome or autophagy. Certain loci such as SOD1, VAP, VCP, TDP-43, FUS, TAF15, and C9ORF72 can affect the mitochondria triggering mitochondrial fragmentation, energy imbalance, oxidative stress, autophagy and calcium signaling defects. Transport machineries such as vesicular trafficking, endosomal recycling and axonal trafficking can be disrupted due to microtubule disorganization along the axon and at the synapse, for instance in case of VAP, UBQLN, VCP, Alsin2, FIG4, CHMP2B and profilin. This can lead to NMJ morphology and function defects in

bouton shape and size, active zones and glutamate release. This is directly related to perturbation of signaling across the NMJ such as JNK, BMP and mTOR among others. NMJ morphology is a feature most commonly affected in almost every model of ALS studied in *Drosophila*. In a few cases like TDP-43, VAP, VCP and Alsin2, a similar disruption is also observed at dendritic nerve endings that synapse with interneurons. Though most of the functions are neuronal, a few genes contribute to the disease because of their function/malfunction in muscle and glia. Sarcomeric disorganization, myotubule disruption, nuclear envelop defects are some of the effects accompanied with muscle-expression of ALS loci such as SOD1, VAP, C9ORF72 and FIG4. Glial expression of loci such as SOD1 and TDP-43 directly affects oxidative stress, axonal wrapping and glutamate excitotoxicity.

Aggregation: a prime feature in neurodegeneration

Autopsied brain tissue samples of patients with neurodegenerative diseases are characterized with prominent lesions and plaques. Staining with congo red, thioflavin T and other dyes detect cellular inclusions in the brain, that are identified as “Lewy bodies”, “Bunina bodies”, or “Skein-like bodies”. Over the last few decades, certain key genetic loci identified as disease-causing agents have been characterized with the use of patient samples as well as model systems for specific neurodegenerative diseases. For example, α-synuclein in Parkinson’s disease (PD), amyloid β and tau in Alzheimer’s disease (AD), huntingtin in Huntington’s disease (HD). SOD1, TDP-43, C9ORF72 and many others in ALS, have been documented to form these inclusions (Table 1). These are mostly found as filamentous or granular, ubiquitinated aggregates consisting of misfolded proteins, and in some cases, RNA as well, often colocalizing with autophagic markers.

Table 1: Disease-causing proteins that aggregate in neurodegeneration

Neurodegenerative disorder	**Aggregating protein**
Alzheimer’s disease	Amyloid β, Tau
Parkinson’s disease	α-synuclein
Amyotrophic Lateral Sclerosis	SOD1, C9ORF72 dipeptide repeats, TDP-43
Huntington’s disease	Huntingtin
Prion disease	Prp
Frontotemporal dementia	TDP-43, FUS, Tau, C9ORF72 dipeptide repeats

Amyloid β: An aggregate prototype

Highly insoluble and stable filamentous aggregates are identified in a large number of neurodegenerative diseases as β-amyloid-like structures that essentially represent dimers of cross β-strands stacked into a fibril, such as in the case of α-synuclein, huntingtin, TDP-43 and DPRs of C9ORF72 (Prusiner et al. 1983; Scherzinger et al. 1997; Muchowski et al. 2000; Chen et al. 2010a; Edbauer and Haass 2016). In Alzheimer's disease, cleavage of amyloid precursor protein (APP) with specific proteases called β and γ-secretases gives rise to N-terminal products such as Aβ40 and Aβ42. These cleaved products give rise to the soluble oligomers, and insoluble protofilaments and β-amyloid fibrils. The soluble Aβ monomers and oligomers may be in equilibrium with one another and gradually elongate to form insoluble fibrillary aggregates. Structurally, Aβ42 appears to have a higher propensity for aggregation than Aβ40, owing to an additional β-hairpin structure providing more stability. The oligomeric and prefibrillar species are known to be more toxic in nature as compared to insoluble aggregates. Formation of insoluble aggregates of Aβ may serve a neuroprotective role by intervening toxic downstream signaling cascades initiated by soluble Aβ (Fig. 2). Soluble Aβ peptides can act as ligands to a range of receptor molecules, triggering stress-related downstream signaling pathways such as JNK and ERK, and promoting inflammatory responses and death cascades. Aβ signaling also causes tau hyper-phosphorylation and neurofibrillary tangles in the axons that affect synaptic function. Collectively, the amyloid β fibrils and the tau neurofibrillary tangles represent the plaques. Through carrier or receptor-mediated transport across the blood-brain barrier, Aβ monomers and oligomers can accumulate in the bloodstream, a function that determines the extent of the disease. The accumulation of these Aβ species in the brain, the extracellular matrix and in the bloodstream are countered with the action of a range of proteases capable of degrading soluble and in some cases, fibrillar Aβ aggregates. Synthetic proteases and inhibitors of transport receptors serve as therapeutic agents for treatment of AD (Chen et al. 2017).

The inheritance of aggregating tendencies

In familial cases, where the patient history is well documented, various mutations have been tracked in disease-causing genes. Genetic mutations tend to increase the propensity for aggregation. Mutant proteins can misfold, nucleate to form toxic oligomers, sequester interactor molecules, and subsequently aggregate. Misfolding of the protein could be triggered by the

missense mutations that change the property imparted by the amino acid at that position such as a substitution of hydrophilic to hydrophobic moieties or vice versa, or due to a change in the charge of the side chain. Some of the examples of such point mutations include SOD1, TDP-43, etc (Johnson et al. 2009; Prudencio et al. 2009). Repeat expansion of bases is another kind of mutation that typically produces long peptide chains that stably aggregate, prominently seen in the case of huntingtin protein and dipeptide repeats of C9ORF72 (Hoffner et al. 2007; Lee et al. 2016). These mutations bring about a tendency for the proteins to self-assemble into a stable non-native structure. Prion-like domains provide a template of alternately folded structure that in turn nudge other protein molecules to acquire the same fold. This event of nucleation gives rise to small oligomers that are often found to gain toxic functions and altered interactions that can trigger stress (Fig. 2). For instance, SOD1 mutant has been shown to interact with Derlin-1, disrupting the ER-associated degradation (ERAD) pathway (Nishitoh et al. 2008). TDP-43 and other RNA binding proteins involved in stress granule formation can bind mRNA targets and affect their processing (Gal et al. 2011; Bentmann et al. 2012). Prominently, nucleocytoplasmic transport seems to be affected in cases of C9ORF72 and TDP-43- mediated ALS, owing to disruption of nuclear pore complexes (Freibaum et al. 2015; Zhang et al. 2015; Chou et al. 2018). The presence of misfolded proteins in a number of cases, is known to disturb the proteostasis in the cell invoking the unfolded protein response and degradative mechanism, such that more than 90% of all ALS cases are known to show TDP-43 pathology (Neumann et al. 2006; Scotter et al. 2014; Webster et al. 2017; Hughes and Mallucci 2018). Membrane-associated aggregates such as VAPB mutant aggregates, can affect morphology of different organelles such as ER, nucleus and mitochondria triggering stress (Teuling et al. 2007; Kim et al. 2010; De Vos et al. 2012). Presence of aggregates can alter ROS, calcium signaling, metabolism and subsequently, promote cell death (Han et al. 2012; Stoica et al. 2014; Jaiswal et al. 2015; Paillusson et al. 2017).

The dynamicity of an aggregate

In vivo, based on localization and composition, aggregates can be classified as aggresomes that are more dynamic in nature, or they can be found as insoluble protein deposits (IPOD) that are much more resilient to degradation. Fluorescent recovery after photobleaching (FRAP) studies on cyclosporine A treatment- induced aggregates of PrP prion protein uncovered two distinct pools, one that recovered after bleaching, the other that did not (Ben-Gedalya et al. 2011a). The

pool of aggregates that could recover were characterized as dynamic and found adjacent to the nucleus; they were termed as juxtanuclear quality control compartment (JUNQ). Dynamic aggregates are often ubiquitinated and associated with chaperones as well as autophagic markers representing the aggresomes. The other pool of aggregates composed of non-ubiquitinated misfolded insoluble protein deposits (IPOD). The difference in nature of these aggregates is the protective cellular response that is involved in either correcting or degrading misfolded proteins in dynamic aggresomes, or is involved in the quarantine of misfolded insoluble proteins (Ben-Gedalya et al. 2011a). Dissimilar disease-causing proteins can seed and nucleate independently of one another forming distinct aggregating compartments with different dynamicity and compositions (Farrawell et al. 2015). ALS spinal cord patient samples show misfolded SOD1 inclusions in cells displaying TDP-43 and FUS pathologies in familial as well as sporadic cases (Pokrishevsky et al. 2012). In presence of VAPB mutant aggregates, wildtype TDP-43 proteinopathy has also been observed that compartmentalizes as a distinct structure in the cytoplasm (Tudor et al. 2010). Protein aggregates can be dual in nature such as in case of TDP-43 and FUS that form aggregates that are found as both JUNQ and IPOD-like, as opposed to SOD1 aggregates that seems to mainly form JUNQ compartments (Farrawell et al. 2015).

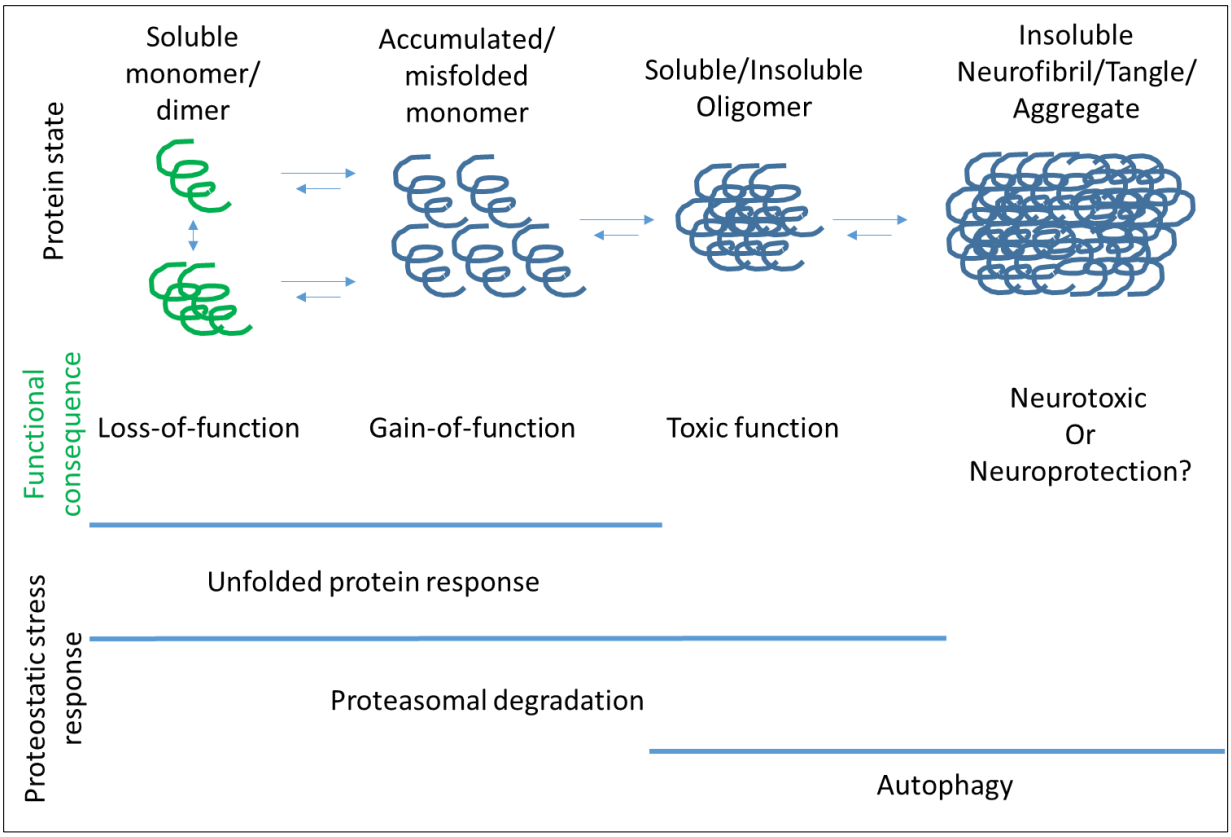

Figure 2: A schematic representation of a regulation of aggregating proteins in neurodegeneration. Under normal conditions, proteins are translated and folded into their correct conformations in soluble or membrane-bound state as monomers, dimers or as part of protein complexes. These forms are transient, and dependent on their function and regulation. With age, proteins tend to be misfolded and mislocalized, giving rise to gain-of-function such as altered protein interactions. In this state, they can be refolded with the help of chaperones in an unfolded protein response (UPR); or they can be ubiquitinated and degraded via the proteasomal machinery (UPS). This state is more highly observed in disease conditions that deal with mutant destabilized proteins. If these cellular responses of UPR and UPS fail to prevent the accumulation of misfolded proteins, toxic oligomeric species can form that can essentially sequester functional interacting proteins leading to loss-of-function. Toxic oligomeric species can be tackled by the cell through degradative mechanisms such as UPS and autophagy. These oligomers can act as nucleators of microaggregates and macroaggregates in the cell. These aggregates can acquire neuroprotective roles of insoluble protein deposits that sequester more toxic soluble monomers and oligomers; or they can serve as "aggresomes" that are associated with chaperones and ubiquitin ligases; or they can be dispensed by the cell via "aggrephagy" which is essentially, autophagic degradation of aggregates. Each of these species have been documented in neurodegeneration to breach the cell boundary and propagate to other cells in a prion-like manner.

The phase separating aggregate

A class of proteins more prone to aggregation contain intrinsically disordered domains. They are essentially low complexity domains (LCDs), rich in glycine, tyrosine, asparagine and glutamine, which are responsible for protein-protein interaction. Best examples of these found in ALS are the RNA-binding proteins (RBPs) such as Tar DNA-binding protein-43 (TDP-43), Fused in Sarcoma (FUS), heterogeneous ribonucleoproteins (hnRNPs) and ataxin1 (Neumann et al. 2006, 2010; Vance et al. 2009; Elden et al. 2010; van Blitterswijk et al. 2012; Appocher et al. 2017). These protein commonly contain RNA recognition motifs (RRMs), LCDs, Nuclear localization sequence (NLS), nuclear export sequence (NES), and glycine rich regions. Under normal conditions, these proteins, through RRMs that aid them to bind RNA, and LCDs that promote protein assembly, form ribonucleoprotein (RNP) complexes such as P-bodies, stress granules and others, involved in RNA processing, localization and translation. These complexes essentially act as membraneless organelles that can reversibly phase separate based on cellular cues. In the disease condition or in the presence of mutations, this property is altered leading to loss of RNA binding and toxic prion-like granule formation (Patel et al. 2015). The LCDs are prion-like domains that can attain alternately-folded stable structures that self-assemble to form stacks or fibrils. This self-assembly is also seen in the dipeptide repeats (DPRs) of C9ORF72 expansion, which appear to phase separate with RBPs, disrupting membraneless organelles in the cytoplasm (Lee et al. 2016). Ubiquilin 2 appears to contain intrinsically disordered regions that have been recently found to display liquid-liquid phase separating-like properties, albeit without containing an RNA-binding domain (Castaneda and Dao 2017; Dao et al. 2018). *In vitro* studies have shown that Ubiquilin 2 appears to negatively regulate stress granule formation by solubilizing FUS droplets, thereby targeting FUS for degradation (Alexander et al. 2018). These granules prove to be more difficult to dissolve or dissociate, and are unable to recover upon photobleaching in FRAP experiments. Thus, these RNP complexes or aggregates are formed as a result of liquid-liquid phase separation that are immiscible in the surrounding cellular environment (Guenther et al. 2018; Matsumoto et al. 2018).

A number of RBPs are predominantly found in the nucleus and shuttle back and forth from the cytoplasm for RNA transport. In conditions of cellular stress, these proteins such as TDP-43 and FUS, form stress granules that sequester mRNA to prevent translation. In the disease

condition, due to altered protein-protein interactions and post-translational modification, these proteins become mislocalized to the cytoplasm forming aggregated structures. Missense mutations associated with the disease in genes, like TDP-43 and FUS, seem to span across different domains, altering RNA binding and RNA processing. A common phenomenon associated with this is the disruption of nucleocytoplasmic transport (Freibaum et al. 2015; Zhang et al. 2015; Chou et al. 2018). An avalanche of studies on the phase separating properties of RNA-binding proteins, both *in vivo* and *in vitro* now look at the role of RNA and other factors on the formation of membraneless organelles. RNA concentration appears to have a direct effect on the phase separating property of wildtype RBPs. It has been found that up till a critical concentration, RNA favors phase separation and detectable aggregation of RBPs, in the cytoplasm. In the nucleus, at RNA levels higher than this threshold, detectable RBP aggregates fail to appear. *In vitro*, the phase separated aggregate can take the form of a gel or even a solid. *In vivo*, these structures can be identified based on their decreasing dynamicity based on FRAP-based techniques. The functional consequences of these different states in the disease is largely unknown (Maharana et al. 2018).

Factors that modulate aggregation

An aggregate is thermodynamically a low energy stable structure arising as a result of an alternative protein fold. However, aggregation is as much dependent on the structure of the protein as it is on its environment. *In vitro*, aggregates are largely described based on their properties of detergent solubility, proteinase K susceptibility and hydrophobicity. Different species of mutant proteins can be distinguished as monomers, oligomers or higher molecular weight assemblies based on their solubility in weaker to stronger detergents. The assay, coupled with mass spectrometry studies, is also useful in correlating aggregating tendency of these proteins with proteolytic cleavage and different post translational modifications, such as phosphorylation, ubiquitination, SUMOylation and others. For instance, TDP-43 undergoes proteolytic cleavage forming a C-terminal truncated product, TDP-25, which has been found to be more toxic and less soluble than the full length protein. TDP-25 is localized in the cytoplasm and form toxic oligomers. TDP-25, consisting of the glycine-rich region and a truncated RRM2, leads to the formation of ubiquitinated and phosphorylated insoluble aggregates giving rise to TDP-43 pathology (Zhang et al. 2009; Brady et al. 2011; Wang et al. 2013). The sites of phosphorylation in FUS appears to be present throughout the length of the protein such as RGG domain, prion-like domain as well as

RNA binding domain, altering RNA binding and phase separating properties. While some reports suggest hyperphosphorylated TDP-43 and FUS to be more prone to aggregation, others suggest otherwise . Acetylation of TDP-43 also appears to increase hyperphosphorylation due to reduced RNA binding in response to reactive oxygen species (ROS). Acetylation and phosphorylation-specific antibodies have been useful in detecting TDP-43 inclusions in patient spinal cord samples (Cohen et al. 2015). Different TDP-43 aggregating species isolated from brain tissue samples of different FTD subtypes show different aggregating tendencies and toxicity when provided to cell culture models (Laferrière et al. 2018). Valosin containing protein (VCP) has been shown to be mutated in ALS and Inclusion Body Myopathy with Paget's disease and FTD (IBMFTD) (Kovach et al. 2001) These mutations appear to cause of a loss of SUMOlyation of VCP lead to a loss of function phenotype. VCP is involved in cellular stress responses in the cell, which become disrupted in the disease condition (Wang et al. 2016).

The process of aggregation could be affected by a number of cellular components such as reactive oxygen species, metal ions, and lipids. For instance, in presence of oxidative stress, oxidative damage of macromolecules such as proteins, phospholipids and DNA can take place initiating cell death mechanisms. Lipids appear to be associated with aggregation and can modulate aggregation propensity. It has been shown that unsaturated fatty acids accelerate aggregation of proteins involved in neurodegenerative diseases such as SOD1 in ALS (Kim et al. 2005), amyloid β in Alzheimer's disease (Wilson and Binder 1997), and α-synuclein in Parkinson's disease (Sharon et al. 2001, 2003). Similarly, in case of tauopathies, the rate of tau polymerization is facilitated by PUFAs, and further enhanced by oxidized PUFA. However, it is inhibited in presence of over-oxidized fatty acids (Gamblin et al. 2000). Oxidized proteins tend to be misfolded and aggregated, triggering the unfolded protein response that then ubiquitinates and directs them for proteasomal degradation. In response to ROS, TDP-43 aggregation appears to be enhanced and can be reduced with the inhibition of MAP kinase pathways (Meyerowitz et al. 2011). SOD1 is an antioxidant enzyme that is responsible for containing the ROS levels in the cell by converting superoxide species to free oxygen and peroxide. SOD1 is the oldest known genetic locus for ALS and till date more than 150 different mutations have been reported in both familial as well as sporadic cases of the disease (Rosen et al. 1993; Taylor et al. 2016). Being an ROS-scavenging protein, it has been debated whether ALS1 manifests as a result of enzymatic loss-of-function and subsequent accumulation of ROS. SOD1-immunoreactive puncta are observed in SOD1-ALS

patients. Most of the SOD1 mutations tested in model systems render the protein to form cellular oligomeric inclusions. The nature of these aggregates is shown to be variable; some mutations have been shown to form thioflavin-reactive insoluble amyloids, while others have been shown to form soluble inclusions (Sheng et al. 2012). Different mutations have been shown to render the protein to form aggregates with different propensities (Prudencio et al. 2009). The study shows that mutations that lower the net charge on SOD1 protein or increase the hydrophobicity of the molecule have an increased propensity for aggregation in comparison with wild type (Sheng et al. 2012). The study has also correlated increased aggregation propensity to faster progression of disease and death post-diagnosis (Prudencio et al. 2009). Most of the mutations appear to functionally impair the protein. Most, but a few, SOD1 mutants lose their ability to bind to Cu and/ Zn ions responsible for its catalytic activity and stability, respectively. This could be a possible reason for increased ROS levels in SOD1 patients. However, SOD1- knockdown mice have been shown to not develop ALS. Disease mutants such as SOD1-G93A and SOD1-A4V that do not lose their catalytic activity have also been identified, indicating that increased ROS levels may not be crucial read-out for disease phenotype, and that these mutations might be gain-of-function (Prudencio et al. 2009).

Misfolded and aggregated species are capable of being transported from cell to cell. This can occur actively via exosomes as in the case of SOD1 aggregates (Grad et al. 2014b, a). It can also occur due to neuronal cell death, where aggregating species are exposed and can be taken up by the neighboring cells. These species thus propagate in a prion-like manner nucleating more aggregates. TDP-43 aggregation has been found to propagate in cocultures of neurons and glial cells. The aggregates also appear to be released from dying TDP-43 expressing cells and acquired by neighbouring untransfected cells. TDP-43 proteinopathy could develop in glial cells as well (Ishii et al. 2017). The glial cells such as microglia, astrocytes and oligodendrocytes play an important role in eliciting an immune response. Glial activation has been observed as both non-cell-autonomous, in case of astrocytes from SOD1 and sporadic patients, as well as cell-autonomous, in case of iPSC-derived astrocytes from TDP-43 patients, highlighting a difference in ALS manifestation between the two loci (Haidet-Phillips et al. 2011; Serio et al. 2013). Glial cells under disease conditions also develop “reactive astrogliosis” that activates TGF-β1 signaling promoting protein aggregation and neuronal cell death via autophagy (Phatnani et al. 2013; Tripathi et al. 2017).

Cellular forces against aggregation

Presence of aggregates in the cell can lead to breakdown of protein homeostasis, also known as proteostasis affecting the balance of protein turnover. This involves the cycles of protein synthesis and degradation. Process such as the UPR, the UPS and autophagy play a major role in combating proteostatic failure in the cell. Each of these processes have been shown to be affected in ALS. Indeed, mutations have been identified in several ALS loci, Alsin (Als2), valosin containing protein (VCP), VAMP associated protein B (VAPB), ubiquilin 2, C9ORF72 that are involved in proteostasis (Fig. 3). Nascent soluble protein chains, upon translation, are folded with the help of chaperones and sorted to their respective destinations in the cell. Membrane proteins are simultaneously translated, folded and integrated into the ER membrane with the help of an entourage of chaperones and translocase machinery that regulate the correct orientation of the proteins in the membrane. The ER plays an important role in managing the protein sorting, first to the golgi bodies for processing, from where they are packaged into endosomes for their transport to their site of function. Each of these processes are governed by protein quality control check points. Over time, proteins become unstable and lose their integrity leading to misfolding. The quality control then responds with triggering the unfolded protein response (Fig. 3).

In the case of neurodegenerative disease, in presence of misfolded and aggregated proteins, based on different cellular markers, the ER stress and UPR have been found to be upregulated in patient brain samples. The UPR activates three downstream pathways that affect transcription and translation of target genes. A key modulator, inositol requiring enzyme 1 (IRE 1), activated with its oligomerization and auto-phosphorylation, splices the mRNA of X-box binding protein 1 (*xbp 1*). Translated protein product of the spliced *xbp 1* translocates to the nucleus and acts as a transcription factor for chaperones and members of the ER associated degradation (ERAD) pathway. Another key modulator is activating transcription factor 6 (ATF-6) that again participates in evoking transcription of specific genes. VAPA and VAPB appear to bind ATF6 through the FFAT motif, thereby inhibiting its activity. The mutant VAPB appears to bind more strongly to ATF6 proving to be a more potent inhibitor, thus, suppressing the UPR in ALS (Gkogkas et al. 2008). The third key modulator is protein kinase R-like ER kinase (PERK) which is activated upon phosphorylation (pPERK) and involved in regulating both translation via translation initiation factor 2 α (eIF2α) and transcription via activating transcription factor 4 (ATF4). PERK inhibits

eIF2α by its phosphorylation thereby temporarily halting further translation. ATF4 is responsible for expression of autophagy and apoptosis related genes. Different effectors of UPR have been observed in spinal cord samples of ALS patients, both sporadic and familial, such as pPERK, ATF4, XBP-1, p- eIF2α using immunostaining or immunoblotting techniques, signifying which arm of the UPR plays a prominent role in the disease (Atkin et al. 2008).

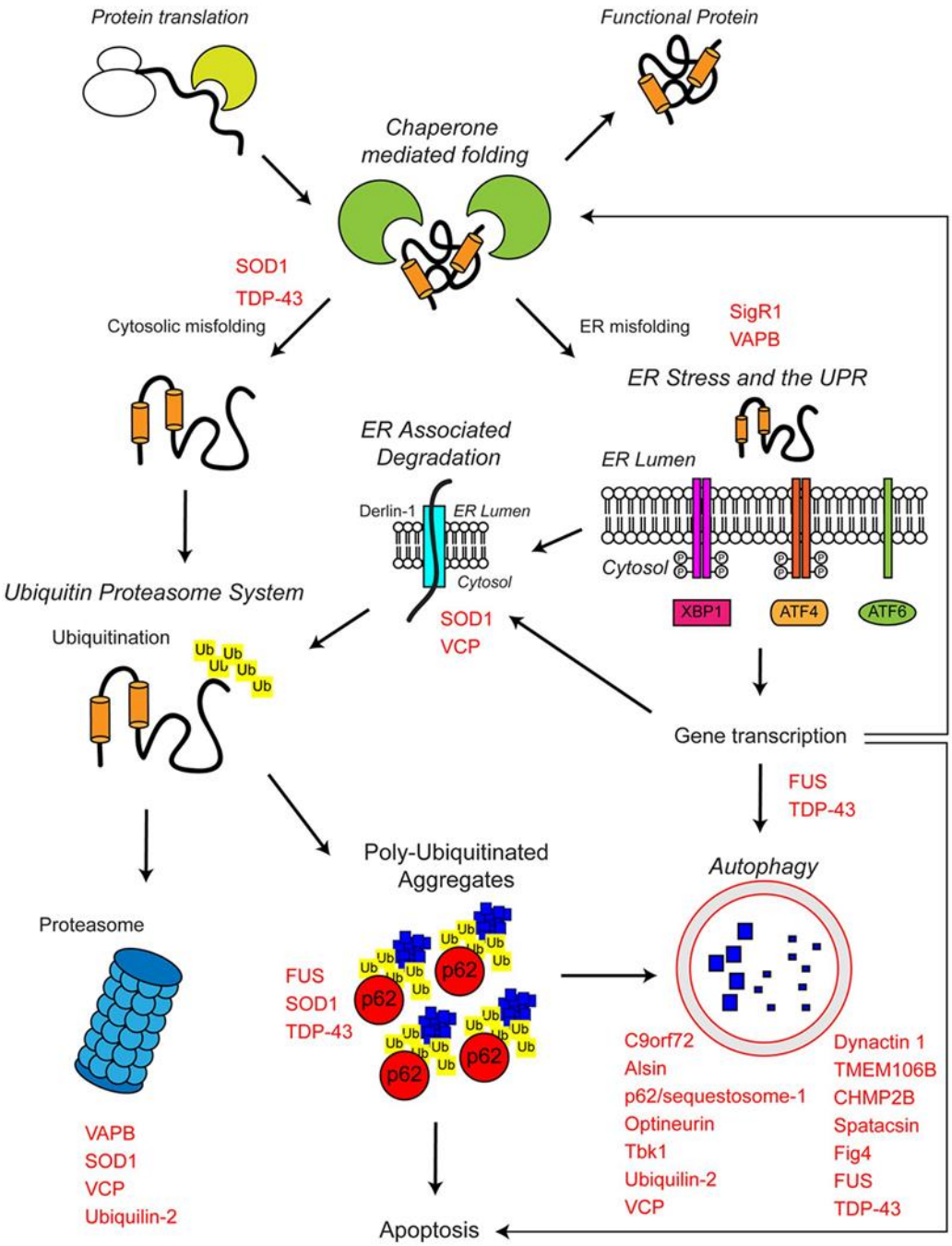

Figure 3: The proteostasis network and ALS.
Reproduced from (Webster et al. 2017). Protein folding takes place simultaneously with protein translation with the help of chaperones. The proteins are targeted to either the cytoplasm or to the ER lumen or membrane. Chronic accumulation of misfolded proteins in the ER in the disease condition, form oligomers and microaggregates, evoking the UPR. The UPR mediates proteostasis by upregulating chaperones, ERAD pathway and by inducing autophagy. The ERAD pathway aids in solubilizing misfolded proteins and targeting them to the UPS via polyubiquitination. Misfolded proteins in the cytosol are targeted to the UPS as well. If the UPR and the UPS fail to downregulate the toxic misfolded proteins, aggregation ensues. These aggregates are then cleared by autophagy. In case of failure of the proteostatic pathways and subsequent spread of aggregation, neuronal death follows. Various ALS loci are involved in the processes involved in proteostasis, such as VAPB, VCP, Ubiquilin, p62, C9ORF72, among others. Aggregation of various mutant ALS proteins serve as substrates of these pathways such as SOD1, TDP-43, FUS, VAPB, p62 and others. This indicates the central role proteostasis plays in the manifestation of the disease.

Pharmacological inhibition of pPERK and eIF2α could ameliorate neurodegenerative effects in mice models of prion disease and FTD, even at earlier stages of the disease since UPR is affected early on in the disease. In flies, UPR inhibition in PD and ALS models could reverse pink-1 and parkin-induced cell death as well as TDP-43 pathology, respectively (Kim et al. 2014; Celardo et al. 2016). These studies indicate that targeting UPR in therapy for neurodegenerative diseases shows promise. However, pPERK pharmacological inhibition is not devoid of side effects. PERK knockout has been shown to cause pancreatic toxicity in a mouse prion disease model (Harding et al. 2001), an effect that can be overcome by inhibiting its substrate, eIF2α. The effect is not consistent throughout the disease progression. Studies in SOD1 and TDP-43 mice models have shown that drug-induced prolonged phosphorylation of eIF2α, upregulating its downstream effects, could mediate protective effects (Vaccaro et al. 2013; Wang et al. 2014). URP perturbation may be more beneficial at earlier stages than later, such that it can act to sustain the build-up of misfolded proteins in the disease. In another study, inhibiting IRE1 to prevent XBP1 splicing in SOD1 mice model was found to be protective as it could lead to an upregulation of autophagic clearance of SOD1 aggregates in the cell (Hetz et al. 2009). With an overexpression of IRE1 in a cell culture model, mutant huntingtin aggregates were increased as a result of downregulation of autophagy (Lee et al. 2011). Specific inhibition of any effector of the UPR could generate feedback responses onto the other effectors. The nature of aggregating species in the progression of the disease may also respond in different ways to UPR suppression.

ER stress and the UPR engage the ERAD pathway as well. When the bulk of misfolded proteins cannot be restored to its correct conformational state with the help of chaperones, their

propensity for aggregation increases. This elicits degradative mechanisms in the cell. Misfolded and aggregated proteins from the ER are cleared away through the ERAD pathway. ERAD is essentially the retrotranslocation machinery that solubilizes, ubiquitinates and translocates ER membrane and luminal proteins to the proteasome situated in the cytoplasm for degradation. For this, the ERAD complex employs a host of proteins, such as chaperones for unfolding the proteins, ubiquitin-binding proteins for ubiquitin recruitment, E3 ubiquitin ligases for ubiquitin conjugation and ATPases for translocation. Members of the ERAD complex, Ubiquilin 2, a ubiquitin-binding protein, and Valosin containing protein (VCP), an ATPase have been found to be mutated in ALS (Deng et al. 2011; Koppers et al. 2012). It has been found to be associated with inclusions formed in ALS, AD, PD and HD (Mah et al. 2000; Doi et al. 2004; Stieren et al. 2011; Rutherford et al. 2013; Mori et al. 2013). VCP loss-of-function mutations have also been identified in IBMPFD that lead to a disruption of the ERAD complex (Kovach et al. 2001). In presence of mutant VCP, wildtype TDP-43 has been shown to accumulate and form inclusion bodies in the cytoplasm as a result of failure of degradative mechanisms (Gitcho et al. 2009). Ubiquilin 2, via its ubiquitin-association domain, targets ubiquitinated proteins for degradation through the proteasome by binding to it via its ubiquitin-like domain (Ko et al. 2004). VAPB, through its interaction with a cofactor of VCP, Fas-associated factor1 (FAF1), associates with the ERAD complex (Baron et al. 2014). Thus, VAPB appear to gain access to ubiquitinated proteins in the cell, modulating their degradation (Baron et al. 2014). Due to the presence of VAPB mutant aggregates, the ER quality control compartment is blocked which causes the ERAD pathway to be compromised (Kuijpers et al. 2013; Abel et al. 2013; Moustaqim-barrette et al. 2014) (Fig. 3).

Accumulation of ubiquitinated proteins and aggregating species in neurodegenerative diseases indicates a breakdown of degradative mechanisms in the cell. Proteins can be degraded largely through two pathways, the UPS and autophagy. The 26S proteasome consists of structural protein that oligomerize to form its framework of the 20S subunit which is capped with two 19S subunits. It consists of a number of chaperones, proteases and ATPases that unfold, cleave, and provide energy for the degradation of the protein. In neurodegeneration, with ER stress and downregulation of ERAD pathway, the presence of aggregates could also affect the UPS. For instance, in sporadic cases of ALS, the chymotrypsin-like, caspase and trypsin-like protease activity of the proteasome has been found to be lowered, along with a reduction of proteasomal subunits in motor neurons of patient spinal cord samples (Agar et al. 2012). Mutations in VCP and

ubiquilin 2 have been found to cause failure of target delivery to the proteasome for degradation (Chang and Monteiro 2015; Barthelme et al. 2015). Mutants of proteins such as SOD1 and VAPB appear to directly interact with and sequester proteasomal subunits, thereby inhibiting the UPS (Urushitani et al. 2002; Kabashi et al. 2004; Cheroni et al. 2008; Moumen et al. 2011). This further enhances the accumulation of misfolded protein in the ER as well as the cytoplasm (Fig. 3).

A bulk of macroaggregates represent insoluble protein deposits in the cell which can no longer be managed by the chaperone system or the proteasomal machinery. These aggresomes formed with an increasingly impaired proteasomal machinery, are ultimately degraded by autophagy, a process known as "aggrephagy" (Olzmann et al. 2008). Autophagy is the cell's response to lack of nutrients, through which it can break down complex macromolecules to generate simple monomeric biomolecules (Suraweera et al. 2012). It is also a process through which the cell clear defective organelles. Autophagy is impaired in certain cases of neurodegeneration with a resultant accumulation of ubiquitin-positive aggregates (Menzies et al. 2015). Autophagy initiates with the formation of the isolation membrane or phagophore derived from the ER, to form a double membrane structure called the autophagosome, which is then decorated with LC3-II/Atg8 (Nakatogawa et al. 2012). This structure encapsulates the substrates for degradation. p62 is one such substrate that associates with LC3-II and acts as an autophagic receptor for recruiting substrates for degradation. Like ubiquilin 2, p62 is also a ubiquitin-binding protein and plays a role in both degradative pathways (Liu et al. 2016). p62 is also a known locus in ALS and was found to be mutated in several sporadic as well as familial cases (Fecto et al. 2011). C9ORF72 patient samples show p62 - positive inclusions indicating autophagy failure (Mahoney et al. 2012). While C9ORF72 expansion leads to RNA toxicity and DPR pathology, C9ORF72 loss-of-function mice have also been found to show p62 accumulation in the brain (Webster et al. 2016). The protein coded by C9ORF72 was identified as an effector of Rab1a which appears to be involved in this initiation process associated with the Unc-51 Like Autophagy Activating Kinase 1/ FAK Family Kinase-Interacting Protein Of 200 KDa (ULK1/FIP200) complex (Webster et al. 2016, 2018). Other ALS loci that are mutated in the disease such as VAPB, alsin, optineurin and TBK1 are also known to be involved in autophagy (Webster et al. 2017). VAPB downregulation in mice and cells has been shown to upregulate autophagy as seen by the accumulation of LC3-II levels (Larroquette et al. 2015; Gomez-Suaga et al. 2017). VAPB also appears to play a role in the formation of the initiation membrane by interacting with the

ULK1/FIP200 complex via the FFAT motif (Zhao et al. 2018). p62 or sequestosome-1 has been found to be accumulated in hungtintin and SOD1 aggregates formed in neurodegenerative diseases (Bjørkøy et al. 2005; Gal et al. 2007). While p62 accelerates autophagy of hungtintin aggregates via autophagy, in case of SOD1, it further promotes aggregation and toxicity (Bjørkøy et al. 2005; Gal et al. 2007; Mitsui et al. 2018).

Aggregates found in the disease are tackled by the cell through the pathways involved in proteostasis as described above. A major pathway in the cell that regulates proteostasis in the cell is the mechanistic Target of Rapamycin (mTOR) pathway via nutrient sensing. mTOR kinase mediates its effect through two complexes, mTORC1 and mTORC2 that are regulated by Tuberous sclerosis 1/2 (Tsc1/ Tsc2), downstream of the insulin pathway. The mTORC1 complex operates through three arms that are involved in protein translation via p70S6 kinase (p70S6K) and Eukaryotic initiation factor 4E binding protein (4E-BP), as well as autophagy via Autophagy related gene 1 (Atg1) or ULK1. Apart from these the mTORC1 complex has several targets in the cell that regulate transcription, UPR, ROS, and metabolism. mTORC1 regulates the degradative pathways autophagy and ubiquitin proteasomal machinery (Noda and Ohsumi 1998; Zhao et al. 2015). mTORC1 inhibition downregulates translation and activates degradative mechanisms. mTOR dissociates from Atg1, thereby allowing Atg1 complex to initiate autophagy. By regulating the ERK5 pathway, mTOR modulates the expression levels of proteasomal subunits and associated chaperones, thereby affecting the UPS (Rousseau and Bertolotti 2016).

How different aggregates are sorted for clearance through specific degradative mechanisms is not completely understood. Different aggregating species of disease-causing proteins serve as substrates for polyubiquitination by specific E3 ligases, and degradation via different pathways. SOD1 and TDP-43 aggregating species have been shown to be degraded via both autophagy and proteasomal degradation. On one hand, Dorfin, an E3 ubiquitin ligase and carboxyl terminus of Hsc70-interacting protein (CHIP), a co-chaperone have been found to be present in SOD1 mutant aggregates and seem to be responsible for targeting the aggregates to the proteasomal machinery via its S5a subunit (Niwa et al. 2002; Urushitani et al. 2004; Kabuta et al. 2006). On the other hand, parkin, an E3 ligase involved in Parkinson's disease, has been found to polyubiquitinate SOD1 aggregates at K63-lysine, targeting it for autophagic degradation, thereby reducing toxicity (Yung et al. 2016). Trehalose, an mTOR-independent autophagy enhancer, could downregulate

the levels of TDP-43 and TDP-25, as well as SOD1 mutant aggregation in cell models (Wang et al. 2010; Zhang et al. 2014). Pharmacological inhibition of both the UPS and autophagy in cell models appears to upregulate the protein levels of TDP-43 and the truncated TDP-25 (Wang et al. 2010). Soluble TDP-43 oligomers could be degraded via the UPS. With inhibition of the UPS alone, monomeric, oligomeric and microaggregates of TDP-43 accumulate to form macroaggregates, modelling ALS phenotypes. With autophagy inhibition alone, TDP-43 does not appear to aggregate (Tashiro et al. 2012). The insoluble aggregates formed in the disease with prolonged accumulation of TDP-43 could be degraded via autophagy (Urushitani et al. 2010; Scotter et al. 2014; Cascella et al. 2017).

Aggregates: friend or foe?

Neurodegenerative diseases are a progressively devastating set of conditions that severely damage the brain and the spinal cord. A breakdown in cellular homeostasis and intercellular signaling culminates in the death of neurons. Cellular proteinaceous inclusions are a common determinant in neurodegenerative diseases. For instance, proteins such as Amyloid β, α-synuclein, and TDP-43 form aggressive forms of inclusions characteristically found in specific neurodegenerative diseases. A debilitating protein homeostasis is a major contributor that accompanies misfolding and aggregation of proteins in the cell. In several cases these aggregating species can spread with cell-to-cell transport in the brain. It is unclear how these aggregates form and propagate, or whether they serve as a cause or a consequence of disease progression. The mutated forms of proteins often develop alternate conformations, altered protein interactions as well as toxic gain-of-function. Alternate protein conformations engage chaperone activity and posttranslational modifications, leading to altered protein interactions. With disease progression, and increasing stress in the system, misfolded proteins acquire toxic gain-of-function and undergo oligomerization. In an attempt to quarantine these toxic oligomers, aggresomes develop, serving as an assemblage for the degradation of the mutant proteins. The degradative machineries in the cell, the UPS and autophagy, deal with excess of protein aggregates in different ways. While the UPS appears to solubilize and cleave the proteins into amino acids, autophagy encases the aggregates for lysosomal degradation. While misfolded and oligomeric microaggregates seem to be more neurotoxic in nature, the formation of macroaggregates into the aggresome appear to

provide a neuroprotective function. A balance between these protein states will help determine the extent of disease manifestation, and thereby, therapeutic conditions.

References

Abel O, Powell JF, Andersen PM, et al (2013) The amyotrophic lateral sclerosis 8 protein, VAP, is required for ER protein quality control. Hum Mol Genet 3:24. doi: 10.1093/hmg/ddt594

Abel O, Powell JF, Andersen PM, Al-Chalabi A (2012) ALSoD: A user-friendly online bioinformatics tool for amyotrophic lateral sclerosis genetics. Hum Mutat 33:1345–51. doi: 10.1002/humu.22157

Agar JN, Strong MJ, Durham HD (2012) Impaired proteasome function in sporadic amyotrophic lateral sclerosis AU - Kabashi, Edor. Amyotroph Lateral Scler 13:367–371. doi: 10.3109/17482968.2012.686511

Alexander EJ, Ghanbari Niaki A, Zhang T, et al (2018) Ubiquilin 2 modulates ALS/FTD-linked FUS–RNA complex dynamics and stress granule formation. Proc Natl Acad Sci 115:201811997. doi: 10.1073/pnas.1811997115

Andersen PM, Al-Chalabi A (2011) Clinical genetics of amyotrophic lateral sclerosis: what do we really know? Nat Rev Neurol 7:603–15. doi: 10.1038/nrneurol.2011.150

Appocher C, Mohagheghi F, Cappelli S, et al (2017) Major hnRNP proteins act as general TDP-43 functional modifiers both in Drosophila and human neuronal cells. Nucleic Acids Res 45:8026–8045. doi: 10.1093/nar/gkx477

Atkin JD, Farg MA, Walker AK, et al (2008) Endoplasmic reticulum stress and induction of the unfolded protein response in human sporadic amyotrophic lateral sclerosis. Neurobiol Dis 30:400–407. doi: https://doi.org/10.1016/j.nbd.2008.02.009

Baron Y, Pedrioli PG, Tyagi K, et al (2014) VAPB/ALS8 interacts with FFAT-like proteins including the p97 cofactor FAF1 and the ASNA1 ATPase. BMC Biol 12:39. doi: 10.1186/1741-7007-12-39

Barthelme D, Jauregui R, Sauer RT (2015) An ALS disease mutation in Cdc48/p97 impairs 20S proteasome binding and proteolytic communication. Protein Sci 24:1521–1527. doi: 10.1002/pro.2740

Ben-Gedalya T, Lyakhovetsky R, Yedidia Y, et al (2011a) Cyclosporin-A-induced prion protein

aggresomes are dynamic quality-control cellular compartments. J Cell Sci 124:1891–902. doi: 10.1242/jcs.077693

Ben-Gedalya T, Lyakhovetsky R, Yedidia Y, et al (2011b) Cyclosporin-A-induced prion protein aggresomes are dynamic quality-control cellular compartments. J Cell Sci 124:1891–902. doi: 10.1242/jcs.077693

Bentmann E, Neumann M, Tahirovic S, et al (2012) Requirements for stress granule recruitment of fused in sarcoma (FUS) and TAR DNA-binding protein of 43 kDa (TDP-43). J Biol Chem 287:23079–23094

Bernasconi R, Soldà T, Galli C, et al (2010) Cyclosporine A-sensitive, cyclophilin B-dependent endoplasmic reticulum-associated degradation. PLoS One 5:1–7. doi: 10.1371/journal.pone.0013008

Bjørkøy G, Lamark T, Brech A, et al (2005) p62/SQSTM1 forms protein aggregates degraded by autophagy and has a protective effect on huntingtin-induced cell death. J Cell Biol 171:603–614. doi: 10.1083/jcb.200507002

Blair LJ, Baker JD, Sabbagh JJ, Dickey C a (2015) The emerging role of peptidyl-prolyl isomerase chaperones in tau oligomerization, amyloid processing, and Alzheimer's disease. J Neurochem 133:1–13. doi: 10.1111/jnc.13033

Blokhuis AM, Groen EJN, Koppers M, et al (2013) Protein aggregation in amyotrophic lateral sclerosis. Acta Neuropathol 125:777–94. doi: 10.1007/s00401-013-1125-6

Boillée S, Vande Velde C, Cleveland DW (2006) ALS: A Disease of Motor Neurons and Their Nonneuronal Neighbors. Neuron 52:39–59. doi: 10.1016/j.neuron.2006.09.018

Brady OA, Meng P, Zheng Y, et al (2011) Regulation of TDP-43 aggregation by phosphorylation andp62/SQSTM1. J Neurochem 116:248–259. doi: 10.1111/j.1471-4159.2010.07098.x

Cascella R, Fani G, Capitini C, et al (2017) Quantitative assessment of the degradation of aggregated TDP-43 mediated by the ubiquitin proteasome system and macroautophagy. FASEB J 31:5609–5624. doi: 10.1096/fj.201700292RR

Castaneda C, Dao T (2017) ALS and Ubiquilin-2: Effects of ALS Mutations on Ubiquilin-2 Structure and Function. FASEB J 31:914.11-914.11. doi: 10.1096/fasebj.31.1_supplement.914.11

Celardo I, Costa AC, Lehmann S, et al (2016) Mitofusin-mediated ER stress triggers neurodegeneration in pink1/parkin models of Parkinson's disease. Cell Death Dis 7:e2271–e2271. doi: 10.1038/cddis.2016.173

Chai A, Withers J, Koh YH, et al (2008) hVAPB, the causative gene of a heterogeneous group of motor neuron diseases in humans, is functionally interchangeable with its Drosophila homologue DVAP-33A at the neuromuscular junction. Hum Mol Genet 17:266–280. doi: 10.1093/hmg/ddm303

Chang L, Monteiro MJ (2015) Defective proteasome delivery of polyubiquitinated proteins by ubiquilin-2 proteins containing ALS mutations. PLoS One. doi: 10.1371/journal.pone.0130162

Chen AK-H, Lin RY-Y, Hsieh EZ-J, et al (2010a) Induction of Amyloid Fibrils by the C-Terminal Fragments of TDP-43 in Amyotrophic Lateral Sclerosis. J Am Chem Soc 132:1186–1187. doi: 10.1021/ja9066207

Chen GF, Xu TH, Yan Y, et al (2017) Amyloid beta: Structure, biology and structure-based therapeutic development. Acta Pharmacol Sin 38:1205–1235. doi: 10.1038/aps.2017.28

Chen H-J, Anagnostou G, Chai A, et al (2010b) Characterization of the Properties of a Novel Mutation in VAPB in Familial Amyotrophic Lateral Sclerosis. J Biol Chem 285:40266–40281. doi: 10.1074/jbc.M110.161398

Cheroni C, Marino M, Tortarolo M, et al (2008) Functional alterations of the ubiquitin-proteasome system in motor neurons of a mouse model of familial amyotrophic lateral sclerosis†. Hum Mol Genet 18:82–96. doi: 10.1093/hmg/ddn319

Chou C-C, Zhang Y, Umoh ME, et al (2018) TDP-43 pathology disrupts nuclear pore complexes and nucleocytoplasmic transport in ALS/FTD. Nat Neurosci 21:228–239. doi: 10.1038/s41593-017-0047-3

Cluskey S, Ramsden DB, Hospital E (2001) Mechanisms of neurodegeneration in amyotrophic

lateral sclerosis. 386–392

Cohen TJ, Hwang AW, Restrepo CR, et al (2015) An acetylation switch controls TDP-43 function and aggregation propensity. Nat Commun 6:1–13. doi: 10.1038/ncomms6845

Cutler RG, Kelly J, Storie K, et al (2004) Involvement of oxidative stress-induced abnormalities in ceramide and cholesterol metabolism in brain aging and Alzheimer's disease. Proc Natl Acad Sci 101:2070–2075. doi: 10.1073/pnas.0305799101

Dao TP, Kolaitis RM, Kim HJ, et al (2018) Ubiquitin Modulates Liquid-Liquid Phase Separation of UBQLN2 via Disruption of Multivalent Interactions. Mol Cell 965–978. doi: 10.1016/j.molcel.2018.02.004

De Vos KJ, Mórotz GM, Stoica R, et al (2012) VAPB interacts with the mitochondrial protein PTPIP51 to regulate calcium homeostasis. Hum Mol Genet 21:1299–311. doi: 10.1093/hmg/ddr559

Deivasigamani S, Verma HK, Ueda R, et al (2014) A genetic screen identifies Tor as an interactor of VAPB in a Drosophila model of amyotrophic lateral sclerosis. Biol Open 3:1127–38. doi: 10.1242/bio.201410066

Deng H-X, Chen W, Hong S-T, et al (2011) Mutations in UBQLN2 cause dominant X-linked juvenile and adult-onset ALS and ALS/dementia. Nature 477:211

Dey G, Gupta GD, Ramalingam B, et al (2014) Exploiting cell-to-cell variability to detect cellular perturbations. PLoS One 9:. doi: 10.1371/journal.pone.0090540

Dharmadasa T, Kiernan MC (2018) Riluzole, disease stage and survival in ALS. Lancet Neurol 17:385–386. doi: 10.1016/S1474-4422(18)30091-7

Doi H, Mitsui K, Kurosawa M, et al (2004) Identification of ubiquitin-interacting proteins in purified polyglutamine aggregates. FEBS Lett 571:171–176. doi: 10.1016/j.febslet.2004.06.077

Edbauer D, Haass C (2016) An amyloid-like cascade hypothesis for C9orf72 ALS/FTD. Curr Opin Neurobiol 36:99–106. doi: 10.1016/j.conb.2015.10.009

Elden AC, Kim HJ, Hart MP, et al (2010) Ataxin-2 intermediate-length polyglutamine

expansions are associated with increased risk for ALS. Nature 466:1069–1075. doi: 10.1038/nature09320

Farrawell NE, Lambert-Smith I a, Warraich ST, et al (2015) Distinct partitioning of ALS associated TDP-43, FUS and SOD1 mutants into cellular inclusions. Sci Rep 5:13416. doi: 10.1038/srep13416

Fecto F, Yan J, Vemula SP, et al (2011) SQSTM1 Mutations in Familial and Sporadic Amyotrophic Lateral Sclerosis. Arch Neurol 68:1440–1446. doi: 10.1001/archneurol.2011.250

Forrest S, Chai A, Sanhueza M, et al (2013) Increased levels of phosphoinositides cause neurodegeneration in a Drosophila model of amyotrophic lateral sclerosis. Hum Mol Genet 22:2689–2704. doi: 10.1093/hmg/ddt118

Freibaum BD, Lu Y, Lopez-Gonzalez R, et al (2015) GGGGCC repeat expansion in C9orf72 compromises nucleocytoplasmic transport. Nature 525:129–133. doi: 10.1038/nature14974

Gal J, Ström AL, Kilty R, et al (2007) P62 Accumulates and Enhances Aggregate Formation in Model Systems of Familial Amyotrophic Lateral Sclerosis. J Biol Chem 282:11068–11077. doi: 10.1074/jbc.M608787200

Gal J, Zhang J, Kwinter DM, et al (2011) Nuclear localization sequence of FUS and induction of stress granules by ALS mutants. Neurobiol Aging 32:2323.e27-2323.e40. doi: 10.1016/j.neurobiolaging.2010.06.010

Gamblin TC, King ME, Kuret J, et al (2000) Oxidative regulation of fatty acid-induced tau polymerization. Biochemistry 39:14203–14210. doi: 10.1021/bi001876l

Gerard M, Deleersnijder A, Demeulemeester J, et al (2011) Unraveling the role of peptidyl-prolyl isomerases in neurodegeneration. Mol Neurobiol 44:13–27. doi: 10.1007/s12035-011-8184-2

Gitcho M a, Strider J, Carter D, et al (2009) VCP mutations causing frontotemporal lobar degeneration disrupt localization of TDP-43 and induce cell death. J Biol Chem 284:12384–98. doi: 10.1074/jbc.M900992200

Gkogkas C, Middleton S, Kremer AM, et al (2008) VAPB interacts with and modulates the activity of ATF6. Hum Mol Genet 17:1517–1526. doi: 10.1093/hmg/ddn040

Golbik R, Yu C, Weyher-Stingl E, et al (2005) Peptidyl prolyl cis/trans-isomerases: comparative reactivities of cyclophilins, FK506-binding proteins, and parvulins with fluorinated oligopeptide and protein substrates. Biochemistry 44:16026–34. doi: 10.1021/bi051442w

Gomez-Suaga P, Paillusson S, Stoica R, et al (2017) The ER-Mitochondria Tethering Complex VAPB-PTPIP51 Regulates Autophagy. Curr Biol 27:371–385. doi: 10.1016/j.cub.2016.12.038

Grad LI, Pokrishevsky E, Silverman JM, Cashman NR (2014a) Exosome-dependent and independent mechanisms are involved in prion-like transmission of propagated Cu/Zn superoxide dismutase misfolding. Prion 8:331–335. doi: 10.4161/19336896.2014.983398

Grad LI, Yerbury JJ, Turner BJ, et al (2014b) Intercellular propagated misfolding of wild-type Cu/Zn superoxide dismutase occurs via exosome-dependent and -independent mechanisms. Proc Natl Acad Sci U S A 111:3620–5. doi: 10.1073/pnas.1312245111

Guenther EL, Cao Q, Trinh H, et al (2018) Atomic structures of TDP-43 LCD segments and insights into reversible or pathogenic aggregation. Nat Struct Mol Biol 25:463–471. doi: 10.1038/s41594-018-0064-2

Haidet-Phillips AM, Hester ME, Miranda CJ, et al (2011) Astrocytes from familial and sporadic ALS patients are toxic to motor neurons. Nat Biotechnol 29:824–828. doi: 10.1038/nbt.1957

Han SM, Tsuda H, Yang Y, et al (2012) Secreted VAPB/ALS8 Major Sperm Protein Domains Modulate Mitochondrial Localization and Morphology via Growth Cone Guidance Receptors. Dev Cell 22:348–362. doi: 10.1016/j.devcel.2011.12.009

Harding HP, Zeng H, Zhang Y, et al (2001) Diabetes Mellitus and Exocrine Pancreatic Dysfunction in Perk−/− Mice Reveals a Role for Translational Control in Secretory Cell Survival. Mol Cell 7:1153–1163. doi: 10.1016/S1097-2765(01)00264-7

Harding MW, Galat A, Uehling DE, Schreiber SL (1989) A receptor for the immunosuppressant

FK506 is a cis-trans peptidyl-prolyl isomerase. Nature 341:758–60. doi: 10.1038/341758a0

Hetz C, Thielen P, Matus S, et al (2009) XBP-1 deficiency in the nervous system protects against amyotrophic lateral sclerosis by increasing autophagy. Genes Dev 23:2294–2306

Hoffner G, Souès S, Djian P (2007) Aggregation of expanded huntingtin in the brains of patients with Huntington disease. Prion 1:26–31

Hsu T, McRackan D, Vincent TS, Gert de Couet H (2001) Drosophila Pin1 prolyl isomerase Dodo is a MAP kinase signal responder during oogenesis. Nat Cell Biol 3:538–43. doi: 10.1038/35078508

Hughes D, Mallucci GR (2018) The unfolded protein response in neurodegenerative disorders - therapeutic modulation of the PERK pathway. FEBS J 1–14. doi: 10.1093/isle/isv094

Ishii T, Kawakami E, Endo K, et al (2017) Formation and spreading of TDP-43 aggregates in cultured neuronal and glial cells demonstrated by time-lapse imaging. PLoS One 12:e0179375

Jaiswal M, Haelterman NA, Sandoval H, et al (2015) Impaired mitochondrial energy production causes light-induced photoreceptor degeneration independent of oxidative stress. PLoS Biol 13:. doi: 10.1371/journal.pbio.1002197

Johnson BS, Snead D, Lee JJ, et al (2009) TDP-43 is intrinsically aggregation-prone, and amyotrophic lateral sclerosis-linked mutations accelerate aggregation and increase toxicity. J Biol Chem 284:20329–20339. doi: 10.1074/jbc.M109.010264

Juhász G, Puskás LG, Komonyi O, et al (2007) Gene expression profiling identifies FKBP39 as an inhibitor of autophagy in larval Drosophila fat body. Cell Death Differ 14:1181–90. doi: 10.1038/sj.cdd.4402123

Kabashi E, Agar JN, Taylor DM, et al (2004) Focal dysfunction of the proteasome: a pathogenic factor in a mouse model of amyotrophic lateral sclerosis. J Neurochem 89:1325–1335. doi: 10.1111/j.1471-4159.2004.02453.x

Kabuta T, Suzuki Y, Wada K (2006) Degradation of amyotrophic lateral sclerosis-linked mutant Cu,Zn-superoxide dismutase proteins by macroautophagy and the proteasome. J Biol Chem

281:30524–30533. doi: 10.1074/jbc.M603337200

Kaiser SE, Brickner JH, Reilein AR, et al (2005) Structural basis of FFAT motif-mediated ER targeting. Structure 13:1035–45. doi: 10.1016/j.str.2005.04.010

Kanekura K, Nishimoto I, Aiso S, Matsuoka M (2006) Characterization of amyotrophic lateral sclerosis-linked P56S mutation of vesicle-associated membrane protein-associated protein B (VAPB/ALS8). J Biol Chem 281:30223–33. doi: 10.1074/jbc.M605049200

Kim H-J, Raphael AR, LaDow ES, et al (2014) Therapeutic modulation of eIF2α phosphorylation rescues TDP-43 toxicity in amyotrophic lateral sclerosis disease models. Nat Genet 46:152–160. doi: 10.1038/ng.2853

Kim S, Leal SS, Ben Halevy D, et al (2010) Structural requirements for VAP-B oligomerization and their implication in amyotrophic lateral sclerosis-associated VAP-B(P56S) neurotoxicity. J Biol Chem 285:13839–49. doi: 10.1074/jbc.M109.097345

Kim YJ, Nakatomi R, Akagi T, et al (2005) Unsaturated fatty acids induce cytotoxic aggregate formation of amyotrophic lateral sclerosis-linked superoxide dismutase 1 mutants. J Biol Chem 280:21515–21521. doi: 10.1074/jbc.M502230200

Ko HS, Uehara T, Tsuruma K, Nomura Y (2004) Ubiquilin interacts with ubiquitylated proteins and proteasome through its ubiquitin-associated and ubiquitin-like domains. FEBS Lett 566:110–114. doi: 10.1016/j.febslet.2004.04.031

Koppers M, van Blitterswijk MM, Vlam L, et al (2012) VCP mutations in familial and sporadic amyotrophic lateral sclerosis. Neurobiol Aging 33:837.e7-837.e13. doi: 10.1016/J.NEUROBIOLAGING.2011.10.006

Kovach MJ, Waggoner B, Leal SM, et al (2001) Clinical delineation and localization to chromosome 9p13.3-p12 of a unique dominant disorder in four families: hereditary inclusion body myopathy, Paget disease of bone, and frontotemporal dementia. Mol Genet Metab 74:458–475. doi: 10.1006/mgme.2001.3256

Kuijpers M, van Dis V, Haasdijk ED, et al (2013) Amyotrophic lateral sclerosis (ALS)-associated VAPB-P56S inclusions represent an ER quality control compartment. Acta Neuropathol Commun 1:24. doi: 10.1186/2051-5960-1-24

Laferrière F, Maniecka Z, Pérez-Berlanga M, et al (2018) TDP-43 extracted from frontotemporal lobar degeneration subject brains displays distinct aggregate assemblies and neurotoxic effects reflecting disease progression rates. Nat Neurosci 22:. doi: 10.1038/s41593-018-0294-y

Larroquette F, Seto L, Gaub PL, et al (2015) Vapb/Amyotrophic lateral sclerosis 8 knock-in mice display slowly progressive motor behavior defects accompanying ER stress and autophagic response. Hum Mol Genet 24:6515–6529. doi: 10.1093/hmg/ddv360

Lauranzano E, Pozzi S, Pasetto L, et al (2015) Peptidylprolyl isomerase A governs TARDBP function and assembly in heterogeneous nuclear ribonucleoprotein complexes. Brain 138:974–91. doi: 10.1093/brain/awv005

Lee H, Chang J-W, Noh J-Y, et al (2011) IRE1 plays an essential role in ER stress-mediated aggregation of mutant huntingtin via the inhibition of autophagy flux. Hum Mol Genet 21:101–114. doi: 10.1093/hmg/ddr445

Lee JP, Palfrey HC, Bindokas VP, et al (1999) The role of immunophilins in mutant superoxide dismutase-1linked familial amyotrophic lateral sclerosis. Proc Natl Acad Sci U S A 96:3251–6

Lee K, Zhang P, Kim H, et al (2016) C9orf72 dipeptide repeats impair the assembly, dynamics, and function of membrane-less organelles. Elsevier 167:774–788

Lev S, Halevy D Ben, Peretti D, Dahan N (2008) The VAP protein family: from cellular functions to motor neuron disease. Trends Cell Biol 18:282–290. doi: 10.1016/j.tcb.2008.03.006

Linkert M, Rueden CT, Allan C, et al (2010) Metadata matters: Access to image data in the real world. J Cell Biol 189:777–782. doi: 10.1083/jcb.201004104

Liu WJ, Ye L, Huang WF, et al (2016) P62 Links the Autophagy Pathway and the Ubiqutin-Proteasome System Upon Ubiquitinated Protein Degradation. Cell Mol Biol Lett 21:1–14. doi: 10.1186/s11658-016-0031-z

Lorenzen S, Peters B, Goede A, et al (2005) Conservation of cis prolyl bonds in proteins during evolution. Proteins 58:589–95. doi: 10.1002/prot.20342

Lu P-J, Zhou XZ, Liou Y-C, et al (2002) Critical role of WW domain phosphorylation in regulating phosphoserine binding activity and Pin1 function. J Biol Chem 277:2381–4. doi: 10.1074/jbc.C100228200

Mah AL, Perry G, Smith MA, Monteiro MJ (2000) Identification of ubiquilin, a novel presenilin interactor that increases presenilin protein accumulation. J Cell Biol 151:847–862

Maharana S, Wang J, Papadopoulos DK, et al (2018) RNA buffers the phase separation behavior of prion-like RNA binding proteins. Science (80-) 921:918–921

Mahoney CJ, Warrington EK, Warren JD, et al (2012) Frontotemporal dementia with the C9ORF72 hexanucleotide repeat expansion: clinical, neuroanatomical and neuropathological features. Brain 135:736–750. doi: 10.1093/brain/awr361

Massignan T, Casoni F, Basso M, et al (2007) Proteomic analysis of spinal cord of presymptomatic amyotrophic lateral sclerosis G93A SOD1 mouse. Biochem Biophys Res Commun 353:719–25. doi: 10.1016/j.bbrc.2006.12.075

Matsuda S, Koyasu S (2000) Mechanisms of action of cyclosporine. Immunopharmacology 47:119–125. doi: 10.1016/S0162-3109(00)00192-2

Matsumoto T, Matsukawa K, Watanabe N, et al (2018) Self-assembly of FUS through its low-complexity domain contributes to neurodegeneration. Hum Mol Genet 27:1353–1365. doi: 10.1093/hmg/ddy046

Menzies FM, Fleming A, Rubinsztein DC (2015) Compromised autophagy and neurodegenerative diseases. Nat Rev Neurosci 16:345

Meyerowitz J, Parker SJ, Vella LJ, et al (2011) C-Jun N-terminal kinase controls TDP-43 accumulation in stress granules induced by oxidative stress. Mol Neurodegener 6:57. doi: 10.1186/1750-1326-6-57

Mitsui S, Otomo A, Nozaki M, et al (2018) Systemic overexpression of SQSTM1/p62 accelerates disease onset in a SOD1(H46R)-expressing ALS mouse model. Mol Brain 11:30. doi: 10.1186/s13041-018-0373-8

Mori F, Tanji K, Toyoshima Y, et al (2013) Valosin-containing protein immunoreactivity in

tauopathies, synucleinopathies, polyglutamine diseases and intranuclear inclusion body disease. Neuropathology 33:637–644. doi: 10.1111/neup.12050

Moumen A, Virard I, Raoul C (2011) Accumulation of wildtype and ALS-linked mutated VAPB impairs activity of the proteasome. PLoS One 6:e26066. doi: 10.1371/journal.pone.0026066

Moustaqim-barrette A, Lin YQ, Pradhan S, et al (2014) The amyotrophic lateral sclerosis 8 protein, VAP, is required for ER protein quality control. Hum Mol Genet 23:1975–1989. doi: 10.1093/hmg/ddt594

Moustaqim-barrette A, Lin YQ, Pradhan S, et al (2013) The Amyotrophic Lateral Sclerosis 8 protein , VAP , is required for ER protein quality control Department of Neurology and Neurosurgery , Montreal Neurological Institute , McGill University , Montreal , Department of Molecular and Human Genetics Howard Hu. 1–47

Muchowski PJ, Schaffar G, Sittler A, et al (2000) Hsp70 and Hsp40 chaperones can inhibit self-assembly of polyglutamine proteins into amyloid-like fibrils. Proc Natl Acad Sci 97:7841 LP-7846. doi: 10.1073/pnas.140202897

Mukai H, Kuno T, Chang CD, et al (1993) FKBP12-FK506 complex inhibits phosphatase activity of two mammalian isoforms of calcineurin irrespective of their substrates or activation mechanisms. J Biochem 113:292–8

Murphy LA, Ramirez EA, Trinh VT, et al (2011) Endoplasmic reticulum stress or mutation of an EF-hand Ca(2+)-binding domain directs the FKBP65 rotamase to an ERAD-based proteolysis. Cell Stress Chaperones 16:607–19. doi: 10.1007/s12192-011-0270-x

Nakatogawa H, Ohbayashi S, Sakoh-Nakatogawa M, et al (2012) The autophagy-related protein kinase Atg1 interacts with the ubiquitin-like protein Atg8 via the Atg8 family interacting motif to facilitate autophagosome formation. J Biol Chem 287:28503–28507. doi: 10.1074/jbc.C112.387514

Nardo G, Pozzi S, Pignataro M, et al (2011) Amyotrophic lateral sclerosis multiprotein biomarkers in peripheral blood mononuclear cells. PLoS One 6:e25545. doi: 10.1371/journal.pone.0025545

Neumann M, Roeber S, Kretzschmar HA, et al (2010) Abundant FUS-immunoreactive pathology

in neuronal intermediate filament inclusion disease. 118:605–616. doi: 10.1007/s00401-009-0581-5.Abundant

Neumann M, Sampathu DM, Kwong LK, et al (2006) Ubiquitinated TDP-43 in Frontotemporal Lobar Degeneration and Amyotrophic Lateral Sclerosis. Science (80-) 314:130 LP-133

Nishimura Y, Hayashi M, Inada H, Tanaka T (1999) Molecular cloning and characterization of mammalian homologues of vesicle-associated membrane protein-associated (VAMP-associated) proteins. Biochem Biophys Res Commun 254:21–6. doi: 10.1006/bbrc.1998.9876

Nishitoh H, Kadowaki H, Nagai A, et al (2008) ALS-linked mutant SOD1 induces ER stress- and ASK1-dependent motor neuron death by targeting Derlin-1. Genes Dev 22:1451–1464. doi: 10.1101/gad.1640108

Niwa JI, Ishigaki S, Hishikawa N, et al (2002) Dorfin ubiquitylates mutant SOD1 and prevents mutant SOD1-mediated neurotoxicity. J Biol Chem 277:36793–36798. doi: 10.1074/jbc.M206559200

Noda T, Ohsumi Y (1998) Tor, a phosphatidylinositol kinase homologue, controls autophagy in yeast. J Biol Chem 273:3963–3966. doi: 10.1074/jbc.273.7.3963

Olzmann JA, Li L, Chin LS (2008) Aggresome formation and neurodegenerative diseases: therapeutic implications. Curr Med Chem 15:47–60

Paillusson S, Gomez-Suaga P, Stoica R, et al (2017) α-Synuclein binds to the ER–mitochondria tethering protein VAPB to disrupt Ca2+ homeostasis and mitochondrial ATP production. Acta Neuropathol 134:129–149. doi: 10.1007/s00401-017-1704-z

Patel A, Lee HO, Jawerth L, et al (2015) A Liquid-to-Solid Phase Transition of the ALS Protein FUS Accelerated by Disease Mutation. Cell 162:1066–1077. doi: 10.1016/j.cell.2015.07.047

Pemberton TJ, Kay JE (2005) Identification and comparative analysis of the peptidyl-prolyl cis/trans isomerase repertoires of H. sapiens, D. melanogaster, C. elegans, S. cerevisiae and Sz. pombe. Comp Funct Genomics 6:277–300. doi: 10.1002/cfg.482

Pennetta G, Hiesinger PR, Fabian-Fine R, et al (2002) Drosophila VAP-33A directs bouton formation at neuromuscular junctions in a dosage-dependent manner. Neuron 35:291–306

Peretti D, Dahan N, Shimoni E, et al (2008) Coordinated Lipid Transfer between the Endoplasmic Reticulum and the Golgi Complex Requires the VAP Proteins and Is Essential for Golgi-mediated Transport. 19:3871–3884. doi: 10.1091/mbc.E08

Phatnani HP, Guarnieri P, Friedman BA, et al (2013) Intricate interplay between astrocytes and motor neurons in ALS. Proc Natl Acad Sci 110:E756 LP-E765. doi: 10.1073/pnas.1222361110

Philips T, Robberecht W (2011) Neuroinflammation in amyotrophic lateral sclerosis: role of glial activation in motor neuron disease. Lancet Neurol 10:253–63. doi: 10.1016/S1474-4422(11)70015-1

Pimpale L (2015) A high throughput RNAi screen to identify modifiers of ALS8 aggregation using automated computational image analysis. Master's thesis, IISER Pune

Pokrishevsky E, Grad LI, Yousefi M, et al (2012) Aberrant localization of FUS and TDP43 is associated with misfolding of SOD1 in amyotrophic lateral sclerosis. PLoS One 7:e35050. doi: 10.1371/journal.pone.0035050

Prudencio M, Hart PJ, Borchelt DR, Andersen PM (2009) Variation in aggregation propensities among ALS-associated variants of SOD1: correlation to human disease. Hum Mol Genet 18:3217–26. doi: 10.1093/hmg/ddp260

Prusiner SB, McKinley MP, Bowman KA, et al (1983) Scrapie prions aggregate to form amyloid-like birefringent rods. Cell 35:349–358. doi: https://doi.org/10.1016/0092-8674(83)90168-X

Ratnaparkhi A, Lawless GM, Schweizer FE, et al (2008) A Drosophila model of ALS: Human ALS-associated mutation in VAP33A suggests a dominant negative mechanism. PLoS One 3:e2334. doi: 10.1371/journal.pone.0002334

Rosen DR, Siddique T, Patterson D, et al (1993) Mutations in Cu/Zn superoxide dismutase gene are associated with familial amyotrophic lateral sclerosis. Nature 362:59

Rothstein JD (2017) Edaravone: A new drug approved for ALS. Cell 171:725. doi: https://doi.org/10.1016/j.cell.2017.10.011

Rousseau A, Bertolotti A (2016) An evolutionarily conserved pathway controls proteasome homeostasis. Nature 536:184–189. doi: 10.1038/nature18943

Rutherford NJ, Lewis J, Clippinger AK, et al (2013) Unbiased screen reveals ubiquilin-1 and -2 highly associated with huntingtin inclusions. Brain Res 1524:62–73. doi: 10.1016/j.brainres.2013.06.006

Sanhueza M, Zechini L, Gillespie T, Pennetta G (2014) Gain-of-function mutations in the ALS8 causative gene VAPB have detrimental effects on neurons and muscles. Biol Open 3:59–71. doi: 10.1242/bio.20137070

Scherzinger E, Lurz R, Turmaine M, et al (1997) Huntingtin-Encoded Polyglutamine Expansions Form Amyloid-like Protein Aggregates In Vitro and In Vivo. Cell 90:549–558. doi: https://doi.org/10.1016/S0092-8674(00)80514-0

Schiene-Fischer C (2014) Multidomain peptidyl prolyl cis/trans Isomerases. Biochim Biophys Acta. doi: 10.1016/j.bbagen.2014.11.012

Scotter EL, Vance C, Nishimura AL, et al (2014) Differential roles of the ubiquitin proteasome system and autophagy in the clearance of soluble and aggregated TDP-43 species. J Cell Sci 127:1263–1278. doi: 10.1242/jcs.140087

Serio A, Bilican B, Barmada SJ, et al (2013) Astrocyte pathology and the absence of non-cell autonomy in an induced pluripotent stem cell model of TDP-43 proteinopathy. Proc Natl Acad Sci 110:4697 LP-4702. doi: 10.1073/pnas.1300398110

Sharon R, Bar-joseph I, Frosch MP, et al (2003) The Formation of Highly Soluble Oligomers of ␣ -Synuclein Is Regulated by Fatty Acids and Enhanced in Parkinson ' s Disease Brigham and Women ' s Hospital. Neuron 37:583–595. doi: 10.1016/S0896-6273(03)00024-2

Sharon R, Goldberg MS, Bar-Josef I, et al (2001) Alpha-Synuclein occurs in lipid-rich high molecular weight complexes, binds fatty acids, and shows homology to the fatty acid-binding proteins. Proc Natl Acad Sci U S A 98:9110–9115. doi: 10.1073/pnas.171300598

Sheng Y, Chattopadhyay M, Whitelegge J, Valentine JS (2012) SOD1 Aggregation and ALS : Role of Metallation States and Disulfide. 2560–2572

Shi J, Lua S, Tong JS, Song J (2010) Elimination of the native structure and solubility of the hVAPB MSP domain by the Pro56Ser mutation that causes amyotrophic lateral sclerosis. Biochemistry 49:3887–97. doi: 10.1021/bi902057a

Stieren ES, El Ayadi A, Xiao Y, et al (2011) Ubiquilin-1 is a molecular chaperone for the amyloid precursor protein. J Biol Chem 286:35689–35698. doi: 10.1074/jbc.M111.243147

Stoica R, De Vos KJ, Paillusson S, et al (2014) ER-mitochondria associations are regulated by the VAPB-PTPIP51 interaction and are disrupted by ALS/FTD-associated TDP-43. Nat Commun 5:3996. doi: 10.1038/ncomms4996

Sun Y, Dong Y, Wang J, et al (2017) A novel mutation of VAPB in one Chinese familial amyotrophic lateral sclerosis pedigree and its clinical characteristics. J Neurol 264:2387–2393. doi: https://doi.org/10.1007/s00415-017-8628-3

Suraweera A, Münch C, Hanssum A, Bertolotti A (2012) Failure of amino acid homeostasis causes cell death following proteasome inhibition. Mol Cell 48:242–253. doi: 10.1016/j.molcel.2012.08.003

Tashiro Y, Urushitani M, Inoue H, et al (2012) Motor neuron-specific disruption of proteasomes, but not autophagy, replicates amyotrophic lateral sclerosis. J Biol Chem 287:42984–42994. doi: 10.1074/jbc.M112.417600

Taylor JP, Brown RH, Cleveland DW (2016) Decoding ALS: From genes to mechanism. Nature 539:197–206. doi: 10.1038/nature20413

Teuling E, Ahmed S, Haasdijk E, et al (2007) Motor neuron disease-associated mutant vesicle-associated membrane protein-associated protein (VAP) B recruits wild-type VAPs into endoplasmic reticulum-derived tubular aggregates. J Neurosci 27:9801–15. doi: 10.1523/JNEUROSCI.2661-07.2007

Tripathi P, Rodriguez-Muela N, Klim JR, et al (2017) Reactive Astrocytes Promote ALS-like Degeneration and Intracellular Protein Aggregation in Human Motor Neurons by Disrupting Autophagy through TGF-β1. Stem Cell Reports 9:667–680. doi:

10.1016/j.stemcr.2017.06.008

Tsuda H, Han SM, Yang Y, et al (2008) The Amyotrophic Lateral Sclerosis 8 Protein VAPB Is Cleaved, Secreted, and Acts as a Ligand for Eph Receptors. Cell 133:963–977. doi: 10.1016/j.cell.2008.04.039

Tudor EL, Galtrey CM, Perkinton MS, et al (2010) Amyotrophic lateral sclerosis mutant vesicle-associated membrane protein-associated protein-B transgenic mice develop TAR-DNA-binding protein-43 pathology. Neuroscience 167:774–85. doi: 10.1016/j.neuroscience.2010.02.035

Urushitani M, Kurisu J, Tateno M, et al (2004) CHIP promotes proteasomal degradation of familial ALS-linked mutant SOD1 by ubiquitinating Hsp/Hsc70. J Neurochem 90:231–244. doi: 10.1111/j.1471-4159.2004.02486.x

Urushitani M, Kurisu J, Tsukita K, Takahashi R (2002) Proteasomal inhibition by misfolded mutant superoxide dismutase 1 induces selective motor neuron death in familial amyotrophic lateral sclerosis. J Neurochem 83:1030–1042. doi: 10.1046/j.1471-4159.2002.01211.x

Urushitani M, Sato T, Bamba H, et al (2010) Synergistic effect between proteasome and autophagosome in the clearance of polyubiquitinated TDP-43. J Neurosci Res 88:784–797. doi: 10.1002/jnr.22243

Vaccaro A, Patten SA, Aggad D, et al (2013) Pharmacological reduction of ER stress protects against TDP-43 neuronal toxicity in vivo. Neurobiol Dis 55:64–75. doi: https://doi.org/10.1016/j.nbd.2013.03.015

van Blitterswijk M, van Es M a, Koppers M, et al (2012) VAPB and C9orf72 mutations in 1 familial amyotrophic lateral sclerosis patient. Neurobiol Aging 33:2950.e1-4. doi: 10.1016/j.neurobiolaging.2012.07.004

Vance C, Boris R, Hortobágyi T, et al (2009) Mutations in FUS, an RNA Processing Protein, Cause Familial Amyotrophic Lateral Sclerosis Type 6. 323:1208–1211

Wang L, Popko B, Tixier E, Roos RP (2014) Guanabenz, which enhances the unfolded protein response, ameliorates mutant SOD1-induced amyotrophic lateral sclerosis. Neurobiol Dis

71:317–324. doi: https://doi.org/10.1016/j.nbd.2014.08.010

Wang T, Xu W, Qin M, et al (2016) Pathogenic mutations in the valosin-containing protein/p97(VCP) N-domain inhibit the SUMOylation of VCP and lead to impaired stress response. J Biol Chem 291:14373–14384. doi: 10.1074/jbc.M116.729343

Wang X, Fan H, Ying Z, et al (2010) Degradation of TDP-43 and its pathogenic form by autophagy and the ubiquitin-proteasome system. Neurosci Lett 469:112–116. doi: https://doi.org/10.1016/j.neulet.2009.11.055

Wang YT, Kuo PH, Chiang CH, et al (2013) The truncated C-terminal RNA recognition motif of TDP-43 protein plays a key role in forming proteinaceous aggregates. J Biol Chem 288:9049–9057. doi: 10.1074/jbc.M112.438564

Webster CP, Smith EF, Bauer CS, et al (2016) The C9orf72 protein interacts with Rab1a and the ULK1 complex to regulate initiation of autophagy. EMBO J 35:1656 LP-1676. doi: 10.15252/embj.201694401

Webster CP, Smith EF, Grierson AJ, De Vos KJ (2018) C9orf72 plays a central role in Rab GTPase-dependent regulation of autophagy. Small GTPases 9:399–408. doi: 10.1080/21541248.2016.1240495

Webster CP, Smith EF, Shaw PJ, De Vos KJ (2017) Protein Homeostasis in Amyotrophic Lateral Sclerosis: Therapeutic Opportunities? Front Mol Neurosci 10:1–22. doi: 10.3389/fnmol.2017.00123

Wilson DM, Binder LI (1997) Free fatty acids stimulate the polymerization of tau and amyloid beta peptides. In vitro evidence for a common effector of pathogenesis in Alzheimer's disease. Am J Pathol 150:2181–2195. doi: 10.1073/pnas.85.12.4506

Yadav S, Thakur R, Georgiev P, et al (2018) RDGBα localization and function at membrane contact sites is regulated by FFAT–VAP interactions. J Cell Sci 131:jcs207985. doi: 10.1242/jcs.207985

Yung C, Sha D, Li L, Chin L-S (2016) Parkin Protects Against Misfolded SOD1 Toxicity by Promoting Its Aggresome Formation and Autophagic Clearance. Mol Neurobiol 53:6270–6287. doi: 10.1007/s12035-015-9537-z

Zhang K, Donnelly CJ, Haeusler AR, et al (2015) The C9orf72 repeat expansion disrupts nucleocytoplasmic transport. Nature 525:56–61. doi: 10.1038/nature14973

Zhang X, Chen S, Song L, et al (2014) MTOR-independent, autophagic enhancer trehalose prolongs motor neuron survival and ameliorates the autophagic flux defect in a mouse model of amyotrophic lateral sclerosis. Autophagy 10:588–602. doi: 10.4161/auto.27710

Zhang Y-J, Xu Y-F, Cook C, et al (2009) Aberrant cleavage of TDP-43 enhances aggregation and cellular toxicity. Proc Natl Acad Sci 106:7607 LP-7612. doi: 10.1073/pnas.0900688106

Zhao J, Zhai B, Gygi SP, Goldberg AL (2015) mTOR inhibition activates overall protein degradation by the ubiquitin proteasome system as well as by autophagy. Proc Natl Acad Sci 112:15790–15797. doi: 10.1073/pnas.1521919112

Zhao YG, Liu N, Miao G, et al (2018) The ER Contact Proteins VAPA/B Interact with Multiple Autophagy Proteins to Modulate Autophagosome Biogenesis. Curr Biol 1–12. doi: 10.1016/j.cub.2018.03.002

Chapter II

SOD1 activity threshold and TOR signaling modulate VAP(P58S) aggregation via ROS-induced proteasomal degradation in a *Drosophila* model of Amyotrophic Lateral Sclerosis

Summary

Familial Amyotrophic Lateral Sclerosis (F-ALS) is an incurable, late onset motor neuron disease, linked strongly to various causative genetic loci. *ALS8* codes for a missense mutation, P56S, in VAMP-associated Protein B (VAPB) that causes the protein to misfold and form cellular aggregates. Uncovering genes and mechanisms that affect aggregation dynamics would greatly help increase our understanding of the disease and lead to potential therapeutics.

We developed a quantitative high-throughput, *Drosophila* S2R+ cell-based kinetic assay coupled with fluorescent microscopy to score for genes involved in the modulation of aggregates of fly ortholog, VAP(P58S), fused with GFP. A targeted RNAi screen against 900 genes identified 150 hits that modify aggregation, including the ALS loci *SOD1*, *TDP43* and also genes belonging to the TOR pathway. Further, a system to measure the extent of VAP(P58S) aggregation in the *Drosophila* larval brain was developed in order to validate the hits from the cell based screen. In the larval brain, we find that reduction of SOD1 level or decreased TOR signalling reduces aggregation, presumably by increasing levels of cellular reactive oxygen species (ROS). The mechanism of aggregate clearance is, primarily, proteasomal degradation which appears to be triggered by an increase in ROS.

We have thus uncovered an interesting interplay between SOD1, ROS and TOR signalling that regulates the dynamics of VAP aggregation. Mechanistic processes underlying such cellular regulatory networks will lead us to a better understanding of initiation and progression of ALS.

Abbreviations: VAP, VAMP-associated Protein B; SOD1, Superoxide dismutase 1; mTOR or TOR, mechanistic Target of Rapamycin; ALS, Amyotrophic Lateral Sclerosis; ROS, Reactive Oxygen Species, PS, phosphatidylserine, PE, phosphatidylethanolamine; PUFA, polyunsaturated fatty acids; Atg1, Autophagy-related 1; UPS, Ubiquitin Proteasomal System; ERAD, Endoplasmic Reticulum Associated Degradation.

Introduction

Amyotrophic lateral sclerosis (ALS) is a progressive, fatal neurodegenerative disease characterized by loss of motor neurons resulting in muscular atrophy, gradual paralysis and ultimately death of the patient within 2-5 years post diagnosis (Cleveland and Rothstein 2001; Tarasiuk et al. 2012). Most often, the disease occurs sporadically (S-ALS). However, in ~10% of the cases, the disease occurs due to inheritance of altered gene(s) (F-ALS). *ALS1/SOD1* coding for superoxide dismutase 1, was the first causative locus to be discovered (Rosen et al. 1993; Deng et al. 1993), with more than 170 SOD1 mutations attributed to the diseased state. Since then, about 50 potential genetic loci (Taylor et al. 2016) have been identified in ALS through Genome-wide association (GWAS), linkage and sequencing studies. Recent studies have emphasized on the oligogenic basis for ALS (van Blitterswijk et al. 2012a; Deivasigamani et al. 2014), suggesting that ALS loci may be a part of a gene regulatory network (GRN) that breaks down late in the life of a diseased individual. At the cellular level, several hallmarks of ALS include breakdown of cellular homeostasis (Cluskey et al. 2001), endoplasmic reticulum (ER) stress, unfolded protein response, aggregation, oxidative stress, mitochondrial dysfunction and autophagy. While several studies have demonstrated the wide-range of consequences of the genetic alterations on cellular function, no clear unifying mechanism has emerged that might explain the pathogenesis of the disease (Walker and Atkin 2011; Andersen and Al-Chalabi 2011; Turner et al. 2013; Mulligan and Chakrabartty 2013; Taylor et al. 2016).

In 2004, Mayana Zatz's group (Nishimura et al. 2004) discovered a novel causative genetic locus, VAMP-associated protein B (VAPB), termed as ALS8, in a large Brazilian family whose members succumbed to ALS and/or Spinal muscular atrophy (SMA). The point mutation of P56S was identified in the N-terminal, Major Sperm Domain (MSP) of VAPB (Nishimura et al. 2004) (Fig. 1B). VAPB is an integral membrane protein present in the ER membrane, ER-Golgi intermediate compartment, mitochondrial-associated membrane and the plasma membrane, implicated in important functions in the cell such as vesicular trafficking, ER structure maintenance, lipid biosynthesis, microtubule organization, mitochondrial mobility and calcium homeostasis (Lev et al. 2008; Murphy and Levine 2016). Recent studies have highlighted its critical role in membrane contact sites (De Vos et al. 2012; Alpy et al. 2013; Metz et al. 2017; Yadav et al. 2018; Zhao et al. 2018) (Fig. 1A). The *Drosophila* ortholog of VAPB is

VAP33A/CG5014 (Called VAP hereafter) and has been used to develop models for ALS (Chai et al. 2008; Ratnaparkhi et al. 2008a; Moustaqim-barrette et al. 2014; Deivasigamani et al. 2014; Sanhueza et al. 2015). We have previously identified a *Drosophila* VAP gene regulatory network comprising of 406 genes, including a novel interaction with the mTOR pathway (Deivasigamani et al. 2014). The ALS8 mutation can also alter VAP's physical interaction with other proteins, including FFAT motif containing proteins (Loewen et al. 2003; Murphy and Levine 2016), impairing cellular functions (De Vos et al. 2012; Moustaqim-barrette et al. 2014; Huttlin et al. 2015). Ubiquitinated cellular aggregates (Ratnaparkhi et al. 2008a; Papiani et al. 2012) are seen on VAP mutant expression, and are capable of sequestering the wildtype VAP protein in a dominant negative manner (Teuling et al. 2007; Ratnaparkhi et al. 2008a) (Fig. 1C, 1D). In *Drosophila*, neuronal overexpression of VAP(P58S), and subsequent formation of aggregates, in the background of endogenous VAP appear to lead to only mild neurodegenerative phenotypes, such as flight defects, as compared to the more severe phenotypes associated with wild type VAP neuronal overexpression (Ratnaparkhi et al. 2008a; Tsuda et al. 2008). Previously, we have used the UAS-GAL4 system to study the interaction between VAP and mTOR signalling using the NMJ phenotype associated with neuronally overexpressed VAP(P58S) (Deivasigamani et al. 2014). The functional consequence of neuronal VAP(P58S) aggregation in this system is not fully understood and its contribution to disease remains elusive.

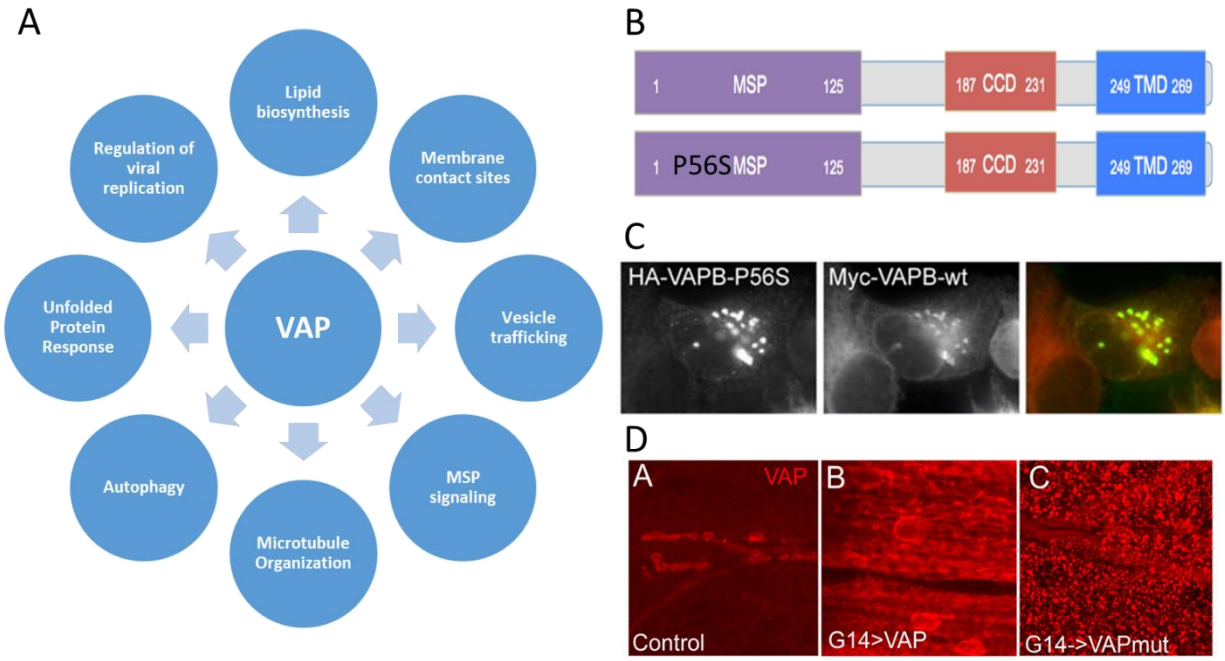

Figure 1: VAP structure, function and aggregation
A. VAP performs diverse range of functions in the cell.
B. VAP contains three domains, namely, the N-terminal Major Sperm Protein domain (MSP), the central Coiled Coil Domain (CCD), and the C-terminal Transmembrane Domain (TMD).
C. Overexpression of HA-VAPB-P56S and Myc-VAPB-wt in HeLa cells and immunostaining with α-HA and α-myc antibody. Colocalisation demonstrates recruitment of wtVAP into VAP-P56S aggregates. (Teuling et al. 2007)
D. Overexpression of wildtype VAP or VAP mutant in *Drosophila* third instar larval muscles. Wildtype VAP localizes to internal membranes whereas VAP mutant forms puncta. (Ratnaparkhi et al. 2008a).

In this study, we identify 150 genetic modifiers of VAP(P58S) aggregation by conducting a directed S2R+ cell based RNAi screen, targeting 900 unique genes belonging to different categories that are associated either with ALS or VAP function or proteostasis. We used the previously described (*C155-GAL4;UAS-VAP(P58S)*) system (Ratnaparkhi et al. 2008a; Deivasigamani et al. 2014) to validate one such modifier, SOD1, *in vivo,* in the third instar larval brain of *Drosophila* by measuring changes in aggregation of VAP(P58S) in response to modulation of *SOD1* levels. Our data indicates that clearance of VAP(P58S) aggregates via the proteasomal machinery is enhanced by inducing reactive oxygen species (ROS) due to loss of SOD1 function. We also find a similar clearance of aggregates, attributed to proteasomal degradation, with mTOR downregulation accompanied by elevated ROS. We find that wild type VAP, but not mutant VAP, elevates ROS. Accumulated ROS results in inhibition of endogenous *VAP* transcription, a phenomenon that may directly affect both familial as well as sporadic ALS pathogenesis.

Results

A Drosophila S2R+ cell culture model to study VAP(P58S) aggregation

C-terminal and N-terminal fusions of VAP and VAP(P58S) with GFP were used to transfect cells and generate stable S2R+ lines, as described in Materials & Methods (Fig. 2A). VAP:GFP showed a non-nuclear, reticular localization in the cell with <10% of the transfected (GFP-positive) cells showing high intensity puncta (Fig. 2B, 2F). In contrast, >80% of the GFP-positive VAP(P58S):GFP, cells showed distinct high intensity puncta with little or no background staining within the cell (Fig. 2C, 2F). Super resolution imaging confirmed that VAP appeared to be reticular, while VAP(P58S) was found in inclusion bodies (Fig. 2E). In contrast, GFP, when expressed showed a uniform cytoplasmic signal (Fig. 2D). Both N-terminal GFP fusions, GFP:VAP and GFP:VAP(P58S) showed puncta formation at levels comparable to VAP(P58S):GFP, and hence were not used further in the study (Fig. 2F) (Pimpale, 2015). All further experiments (see next section) were carried out with stable lines expressing VAP:GFP or VAP(P58S):GFP, which showed expected/relevant localization and levels of aggregation.

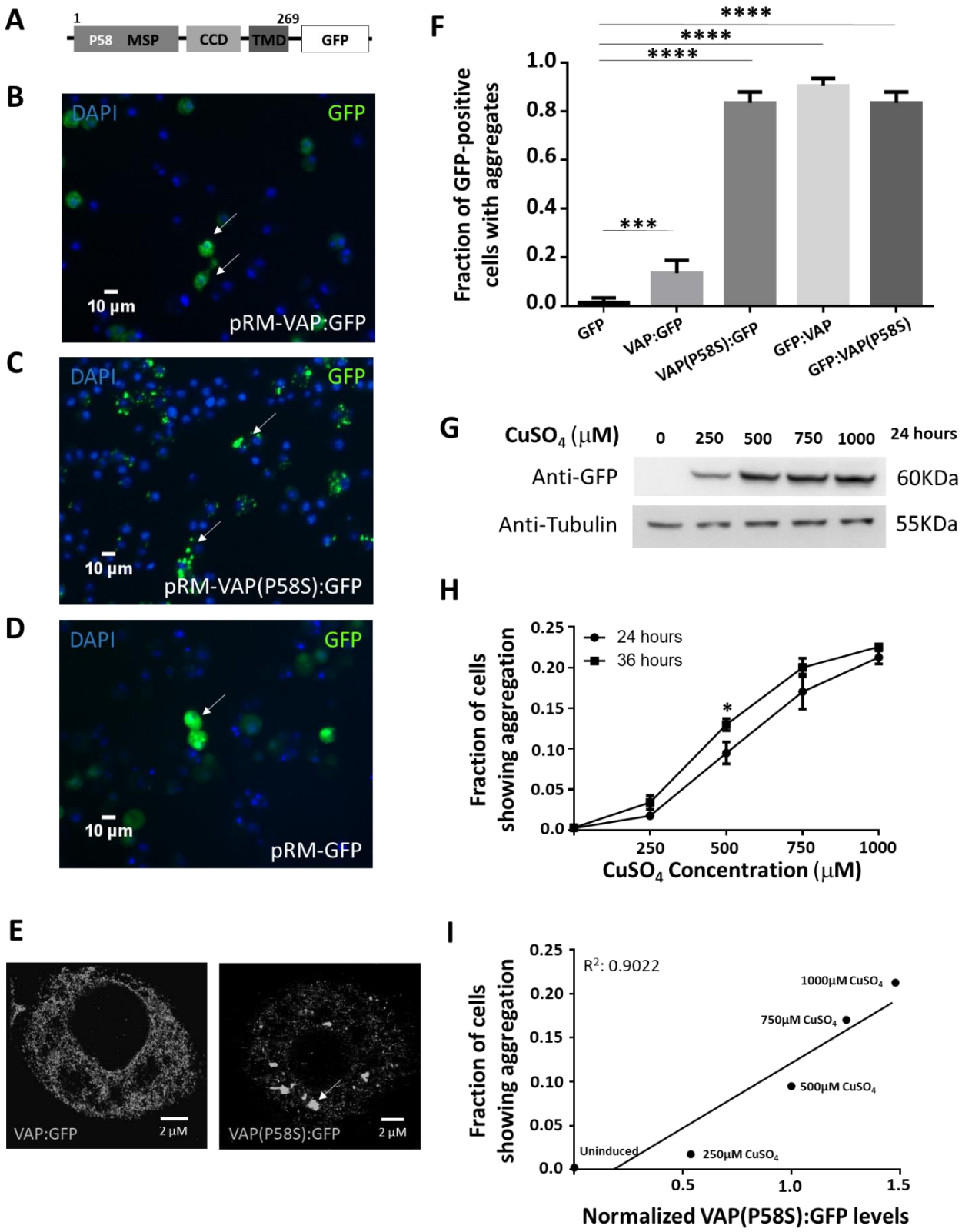
A
1
269
P58
MSP
CCD
TMD
GFP
B
DAPI
GFP
10 µm
pRM-VAP:GFP
C
DAPI
GFP
10 µm
pRM-VAP(P58S):GFP
D
DAPI
GFP
10 µm
pRM-GFP
E
VAP:GFP
2 µM
VAP(P58S):GFP
2 µM
F
Fraction of GFP-positive cells with aggregates
1.0
0.8
0.6
0.4
0.2
0.0
***
****
****
****
GFP
VAP:GFP
VAP(P58S):GFP
GFP:VAP
GFP:VAP(P58S)
G
CuSO4 (µM)
0
250
500
750
1000
24 hours
Anti-GFP
60KDa
Anti-Tubulin
55KDa
H
Fraction of cells showing aggregation
24 hours
36 hours
*
0.25
0.20
0.15
0.10
0.05
0.0
250
500
750
1000
CuSO4 Concentration (µM)
I
Fraction of cells showing aggregation
R2: 0.9022
1000µM CuSO4
750µM CuSO4
500µM CuSO4
250µM CuSO4
Uninduced
0.25
0.20
0.15
0.10
0.05
0.0
0.5
1.0
1.5
Normalized VAP(P58S):GFP levels

Figure 2: A *Drosophila* cell culture model to study VAP(P58S) aggregation

A: Schematics of VAP:GFP or VAP(P58S):GFP constructs, with VAP or VAP(P58S), C-terminally tagged with GFP, when expressed in S2R+ cells, allow efficient visualization of VAP protein in the cell by epifluorescence.

B, C, D: Stable cell lines: expressing *VAP(P58S):GFP*, under an inducible metallothionein promoter, results in aggregation (C), unlike wild-type VAP:GFP (B). GFP is visualized by epifluorescence and chromatin by DAPI, post-fixation. GFP shows a homogenous cytoplasmic expression in S2R+ cells. Arrows point towards cells expressing GFP fluorescence.

E: A super resolution image, using Ground State Depletion microscopy, showing GFP inclusions formed in cells expressing VAP(P58S):GFP (Arrow) but not in VAP:GFP.

F: Fraction of GFP-positive cells showing aggregates plotted for S2R+ cells transiently transfected with C-terminal or N-terminal tagged GFP constructs of VAP or VAP(P58S) as also only GFP construct at 24 hours post 500µM $CuSO_4$ induction. Unlike C-terminal tagged VAP, N-terminal tagged VAP forms, mutant and wild type, both aggregate. GFP, when expressed alone does not aggregate or form puncta. N=4, ~200 GFP-positive cells counted. ANOVA (P-value: ****<0.0001) Fisher's LSD multiple comparison test (P-values, ***<0.001, ****<0.0001).

G: VAP(P58S):GFP protein levels in cells increase with increasing $CuSO_4$ concentration at 24 hours post induction.

H: Increase in fraction of S2R+ cells showing GFP positive inclusions increases with $CuSO_4$ concentration. At 500 mM $CuSO_4$, inclusions significantly increase between 24 hours and 36 hours. N=3, ~ 1000 total cells counted. Student's t-test (P-value: *<0.05)

I: A linear correlation between fraction of cells showing aggregation (F), measured using microscopy plotted against relative VAP(P58S):GFP protein levels (G), as quantified by western blotting (N=3), at 24 hours post induction. Two-tailed test (P-value: 0.0134).

An S2R+ cell based reverse genetics screen is developed to identify modifiers of VAP(P58S) aggregation

In an attempt to identify genetic modifiers of VAP(P58S) aggregation kinetics, we conducted a focused S2R+ cell based RNAi screen, targeting 900 unique genes belonging to nine different categories or families associated with ALS or VAP function (Fig. 3A). We generated stable S2R+ cell lines expressing VAP(P58S):GFP under a Cu^{2+} induced promoter. The inducible cell culture system allowed us to increase the VAP(P58S):GFP protein levels in the cell with increasing copper sulphate ($CuSO_4$) concentrations (250µM, 500µM, 750µM and 1000µM) at 24 hours post induction (Fig. 2G). Using fluorescence microscopy, we found a linear relationship between the copper sulphate ($CuSO_4$) concentrations and also the fraction of cells showing VAP(P58S):GFP aggregates that also increased with time (24 and 36 hours) post induction (Fig. 2H). The concentration dependent increase in relative levels of VAP(P58S):GFP correlated with an increase in fraction of cells showing aggregates (Fig. 2I), indicating the propensity of the

mutant protein to aggregate. Early time points (12-16 hours) gave very few cells with aggregates; while non-linearity, high confluency, and cell death became a concern at time points beyond 48 hours and concentrations greater than 750 µM. The aggregation kinetics curve was used to define the extent of aggregation in the cell culture system and select optimum parameters to conduct the RNAi screen. Keeping a modest confluency and well-separated cells for ease of imaging, the screen was performed at a fixed concentration of 500 µM $CuSO_4$ at 24 and 36 hours post induction.

We chose 900 genes (Table 1, Appendix 1), based on their availability in the Open Biosystems Library (See Materials & Methods) to screen for modifiers that could change aggregation levels of VAP(P58S):GFP. A Gene Ontology (GO) chart (Fig. 3A) represents the biological process associated with these 900 genes, as defined by FlyBase. The genes were selected and categorized on the following basis (Table 2, Appendix 1). First, known *Drosophila* Orthologs of ALS loci (20 genes) and ALS related genes (36 genes) as tabulated in the online ALS database (ALSOD) were chosen. The next category included 273 genes from a VAP *Drosophila* GRN comprising of 406 genes (Deivasigamani et al. 2014). As *mTOR* was identified as a major interactor of *VAP* in our previous study (Deivasigamani et al. 2014), we chose 22 genes of the extended mTOR pathway. To explore the functional aspects of VAP(P58S), we also screened genes involved in lipid biosynthesis (92 genes) and FFAT motif interactors of VAP (34 genes). In order to investigate the role of proteostasis in aggregation, we screened genes involved in unfolded protein response (123 genes), ubiquitin–proteasomal pathway (212 genes), and autophagy (88 genes).

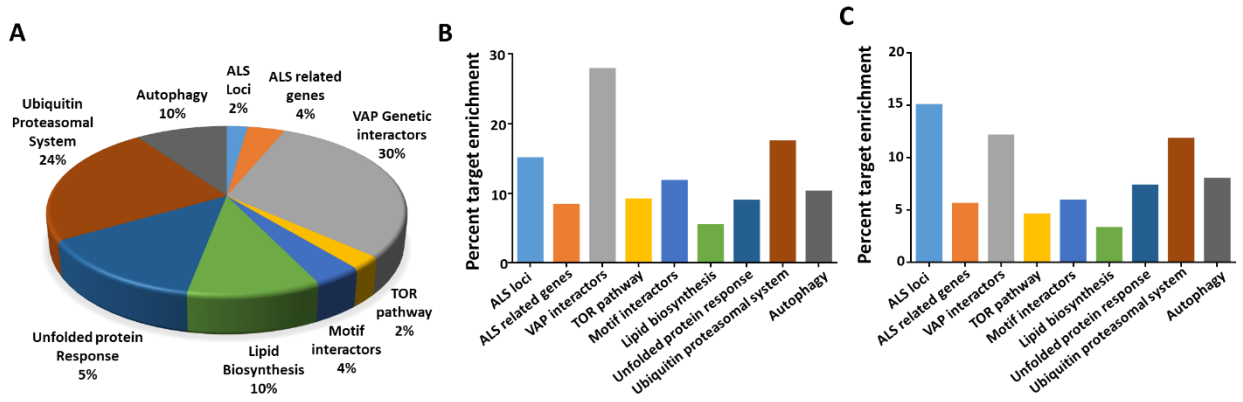

Figure 3: A targeted dsRNA screen in S2R+ cells to discover modifiers of VAP(P58S):GFP aggregation.

A: dsRNA for 900 genes (Table 1, Appendix 1) were chosen for knockdown. GO representation indicates the categories of genes chosen and percentage (%) for each category. Genes were categorized as described in text.

B: The end result of the screen is a list of 150 genes identified, based on average cell intensity, which have been found to modify aggregation of VAP(P58S):GFP. Graph indicates the percent of genes identified as targets within each gene category. Genes are listed in *Table 1*.

C: A list of 85 genes identified based on total cell intensity as a parameter. Based on the analysis of the S2R+ screen, these genes modify aggregation of VAP(P58S):GFP. Graph indicates the percent of genes identified as targets within each gene category. Genes are listed in *Table 2*. (See Appendix 1).

The images collected at the end of the screen (Appendix 1) were analysed by an automated MATLAB analysis (Fig. 2, Appendix 1). Based on average cell intensity, 150 targets (Table 1), and based on total cell intensity, 85 targets (Table 2) that modulated VAP(P58S):GFP aggregation kinetics were identified; 57 genes were found to be overlapping for both parameters, increasing confidence in our analysis (Table3, Appendix 1). Percent genes identified as modulators from each category are plotted in Fig 3B and 3C, as percent target enrichment. ALS loci, notably *SOD1* and *TBPH*, were found as interesting modulators perturbing VAP(P58S):GFP aggregation. Targets belonging to the VAP genetic network, as defined by (Deivasigamani et al. 2014), were also enriched. As identified earlier (Deivasigamani et al. 2014), components of the mTOR pathway also appeared to be key regulators of VAP(P58S):GFP aggregation. Less than 10% of genes screened belonging to families associated with lipid biosynthesis and motif interactors, were identified as targets. Interestingly, genes related to ubiquitin proteasomal system such as ubiquitin ligases and proteasome components were enriched, as were the autophagy related genes, *ATG7* and *ATG3*. From the unfolded protein response category, along with chaperones such as heat shock proteins, *HSP60C*, *HSP23* and *HSP83*, we also identified a few peptidyl prolyl isomerases as targets. Overall, in our primary targeted screen, we found various genetic interactors of wildtype VAP as modulators of VAP(P58S) aggregation as well. Importantly, the uncovering of two ALS loci, *SOD1* and *TDP-43*, mTOR pathway genes such as *Rheb* and *S6K*, and genes enriched in ubiquitin proteasomal system as modulators of VAP(P58S) aggregation dynamics, lead us to develop an *in vivo* model to validate these genes and to understand mechanisms underlying these interactions in the animal.

Table 1. List of 150 modifiers of VAP(P58S) aggregation, based on average cell intensity, along with their human orthologs.

Category	Genes	Name	Symbol	Human orthologs
ALS loci	CG5977	spastin	spas	SPAST FIGNL1 FIGN
	CG11793	Superoxide dismutase 1	Sod1	SOD1 SOD3
	CG10327	TAR DNA-binding protein-43 homolog	TBPH	TARDBP
ALS related genes	CG6963	gilgamesh	gish	CSNK1G3 CSNK1G2 CSNK1G1
	CG18803	Presenilin	Psn	PSEN2 PSEN1
	CG11940	pico	pico	RAPH1 APBB1IP GRB10 GRB7 GRB14
VAP interactors	CG9984	TH1	TH1	NELFCD
	CG9874	TATA binding protein	Tbp	TBP TBPL2
	CG9750	reptin	rept	RUVBL2
	CG9603	Cytochrome c oxidase subunit 7A	COX7A	COX7A1 COX7A2 COX7A2L COX7A2P2
	CG9543	Coat Protein (coatomer) epsilon	epsilon COP	COPE
	CG9495	Sex comb on midleg	Scm	SCMH1 SCML2 SCML4
	CG9485	-	CG9485	AGL
	CG9244	Aconitase	Acon	ACO2
	CG9200	Ada2a-containing complex component 1	Atac1	ZZZ3
	CG9172	NADH dehydrogenase (ubiquinone) 20 kDa subunit	ND-20	NDUFS7 TSG101 UEVLD
	CG8376	apterous	ap	LHX2 LHX9
	CG8095	scab	scb	POLR2C
	CG7885	RNA polymerase II 33kD subunit	RpII33	PHKA2 PHKA1
	CG7766	-	CG7766	MCM2
	CG7538	Minichromosome maintenance 2	Mcm2	HDAC1 HDAC2 HDAC3
	CG7471	Histone deacetylase 1	HDAC1	UBE2M UBE2F
	CG7217	Peroxiredoxin 5	Prx5	HSD17B10
	CG6987	Splicing factor 2	SF2	FEM1C FEM1A FEM1B
	CG6904	Glycogen synthase	GlyS	GYS1 GYS2
	CG6647	porin	porin	VDAC2 VDAC3 VDAC1
	CG6474	enhancer of yellow 1	e(y)1	TAF9 TAF9B
	CG6342	Iron regulatory protein 1B	Irp-1B	ACO1 IREB2

	CG6337	-	CG6337	CTSL CTSZ CTSS CTSC CTSK CTSH CTSB CTSV
	CG6292	Cyclin T	CycT	CCNT1 CCNT2 CCNK CCNQ
	CG6048	-	CG6048	HABP2 KLK14 KLK10 AZU1 CFD PRSS55
	CG5953	-	CG5953	
	CG5931	lethal (3) 72Ab	l(3)72Ab	SNRNP200 ASCC3
	CG5847	zye	zye	SPRR3 KRTAP16-1
	CG5585	Retinoblastoma binding protein 5	Rbbp5	RBBP5
	CG5179	Cyclin-dependent kinase 9	Cdk9	CDK9 CDK13 CDK12
	CG5109	Polycomblike	Pcl	PHF19 MTF2 PHF1
	CG4913	ENL/AF9-related	ear	MLLT1 MLLT3
	CG4912	eukaryotic translation elongation factor 1 delta	eEF1delta	EEF1D EEF1B2
	CG4817	Structure specific recognition protein	Ssrp	SSRP1
	CG4646	-	CG4646	C1orf123
	CG4528	sans fille	snf	SNRPA SNRPB2
	CG4453	Nucleoporin 153kD	Nup153	NUP153
	CG4347	UGP	UGP	UGP2
	CG4206	Minichromosome maintenance 3	Mcm3	MCM3
	CG4169	Ubiquinol-cytochrome c reductase core protein 2	UQCR-C2	UQCRC2
	CG4079	TBP-associated factor 11	Taf11	TAF11 LOC391742
	CG4012	genghis khan	gek	CDC42BPA CDC42BPB CDC42BPG DMPK ROCK1 ROCK2
	CG3949	hoi-polloi	hoip	SNU13
	CG3688	RNA guanine-7 methyltransferase	Rnmt	RNMT
	CG3605	Splicing factor 3b subunit 2	Sf3b2	SF3B2
	CG3582	U2 small nuclear riboprotein auxiliary factor 38	U2af38	U2AF1L5 U2AF1L4 U2AF1 ZRSR2
	CG3476	Mitochondrial Magnesium Exporter 1	MME1	SLC25A20 SLC25A29 SLC25A45 SLC25A48 SLC25A47
	CG3460	Nonsense-mediated mRNA 3	Nmd3	NMD3
	CG3299	Vinculin	Vinc	VCL
	CG32703	Extracellularly regulated kinase 7	Erk7	MAPK15 MAPK11 MAPK13 MAPK7 MAPK1 MAPK14 MAPK12 MAPK3
	CG3192	NADH dehydrogenase (ubiquinone) ASHI subunit	ND-ASHI	NDUFB8

	CG3181	Thymidylate synthase	Ts	TYMS
	CG3127	Phosphoglycerate kinase	Pgk	PGK1 PGK2
	CG3069	TBP-associated factor 10b	Taf10b	TAF10
	CG30043	-	CG30043	ERMP1
	CG2964	-	CG2964	PKM PKLR
	CG17985	-	CG17985	LYSMD3 LYSMD4
	CG17982	-	CG17982	
	CG17689	Spt20	Spt20	SUPT20H SUPT20HL2 SUPT20HL1
	CG17028	-	CG17028	IMPA1 IMPA2 IMPA2 IMPA1
	CG17026	-	CG17026	
	CG1625	dilatory	dila	CEP131
	CG15434	NADH dehydrogenase (ubiquinone) B8 subunit	ND-B8	NDUFA2
	CG14941	extra sexcombs	esc	EED
	CG14935	Maltase B2	Mal-B2	SLC3A1 SLC3A2
	CG14837	-	CG14837	
	CG14813	Coat Protein (coatomer) delta	deltaCOP	ARCN1
	CG14606	-	CG14606	SLC2A8 SLC2A6
	CG13994	-	CG13994	PPP1R11
	CG12372	spt4	spt4	SUPT4H1
	CG12233	lethal (1) G0156	l(1)G0156	IDH3A
	CG12079	NADH dehydrogenase (ubiquinone) 30 kDa subunit	ND-30	NDUFS3
	CG11994	Adenosine deaminase	Ada	ADAL ADA
	CG11811	-	CG11811	GUK1 LRGUK
	CG10743	Liprin-beta	Liprin-beta	PPFIBP2 PPFIBP1
	CG10124	eukaryotic translation initiation factor 4E4	eIF4E4	EIF4E, EIF4E1B
mTOR pathway	CG1081	Ras homolog enriched in brain	Rheb	RHEB RHEBL1
	CG10539	Ribosomal protein S6 kinase	S6k	RPS6KB1 RPS6KB2 RPS6KA2 RPS6KA1 RPS6KA3 SGK2 RPS6KA4 RPS6KA5 RPS6KA6 AKT1 AKT3 AKT2 SGK1 SGK3
	CG6198	CHORD	CHORD	CHORDC1 ITGB1BP2

Motif Interactors	CG5285	-	CG5285	SMUG1
	CG4699	non-specific lethal 1	nsl1	KANSL1 KANSL1L
	CG31423	Ionotropic receptor 94c	Ir94c	
Lipid Biosynthesis	CG7113	scully	scu	CBL CBLB CBLC
	CG5231	Lipoic acid synthase	Las	LIAS
	CG32380	SMSr	SMSr	SAMD8 SGMS2 SGMS1
	CG13969	brain washing	bwa	ACER2 ACER1 ACER3
	CG11198	Acetyl-CoA carboxylase	ACC	ACACA ACACB
Unfolded Protein Response	CG7235	Heat shock protein 60C	Hsp60C	PRDX5
	CG6155	Roe1	Roe1	GRPEL1 GRPEL2
	CG5330	Nucleosome assembly protein 1	Nap1	NAP1L1 NAP1L4 NAP1L3 NAP1L2 NAP1L5
	CG4463	Heat shock protein 23	Hsp23	HSPB2 CRYAB HSPB1 HSPB6 CRYAA CRYAA2 HSPB8 HSPB3 HSPB9 HSPB7
	CG30350	-	CG30350	PPIF RANBP2 LOC105371242 PPIAL4E PPIAL4G NPHS1 PPIAL4C PPIAL4D PPIA PPIAL4A
	CG3024	Torsin	Torsin	TOR1A TOR1B TOR2A TOR3A TOR4A
	CG2852	-	CG2852	PPIB PPIC PPIF PPIAL4C PPIA LOC105371242 PPID PPIG NKTR PPIAL4F PPIH PPIAL4A
	CG1966	ATP-dependent chromatin assembly factor large subunit	Acf	BAZ1A
	CG1937	septin interacting protein 3	sip3	SYVN1 RNF139 AMFR
	CG14715	-	CG14715	FKBP2 FKBP11 FKBP9 FKBP7 FKBP14 FKBP10
	CG1242	Heat shock protein 83	Hsp83	HSP90AA1 HSP90AB1 HSP90B1 HSP90AA4P
Ubiquitin Proteasomal System	CG9242	burgundy	bur	GMPS
	CG9198	shattered	shtd	ANAPC1
	CG8392	Proteasome beta1 subunit	Prosbeta1	PSMB6 PSMB9
	CG8337	Enhancer of split malpha, Bearded family member	E(spl)malpha-BFM	ITGA4 ITGA9 ITGAL ITGAE ITGAM ITGA2 ITGAD ITGA11 ITGAX ITGA10 ITGA1
	CG7375	Ubiquitin conjugating enzyme E2M	UbcE2M	HSPD1
	CG7037	Cbl proto-oncogene	Cbl	SRSF1 SRSF9 SRSF6 SRSF5 SRSF4
	CG6966	-	CG6966	
	CG5271	Ribosomal protein S27A	RpS27A	RPS27A
	CG5266	Proteasome alpha2 subunit	Prosalpha2	PSMA2
	CG5186	scruin like at the midline	slim	KLHDC10

	CG4943	SMAD specific E3 ubiquitin protein ligase	Smurf	SMURF2 SMURF1 ITCH NEDD4L NEDD4 WWP2 WWP1
	CG4319	reaper	rpr	TSC1, RIN1
	CG4274	fizzy	fzy	CDC20 CDC20B FZR1
	CG4166	non-stop	not	USP22 USP27X USP51 USP3
	CG3455	Regulatory particle triple-A ATPase 4	Rpt4	PSMC6
	CG32486	-	CG32486	CYHR1
	CG3234	timeless	tim	TIMELESS
	CG3018	lesswright	lwr	UBE2I
	CG2960	Ribosomal protein L40	RpL40	UBA52
	CG2048	discs overgrown	dco	CSNK1D LOC400927-CSNK1E CSNK1E CSNK1A1 CSNK1A1L
	CG2038	COP9 signalosome subunit 7	CSN7	COPS7B COPS7A
	CG2028	Casein kinase Ialpha	CkIalpha	CSNK1A1 CSNK1A1L CSNK1D LOC400927-CSNK1E CSNK1E
	CG1877	Cullin 1	Cul1	CUL1
	CG18341	Proteasome beta2 subunit-related 1	Prosbeta2R1	PSMB7 PSMB10
	CG18319	bendless	ben	UBE2N UBE2NL UBE2T
	CG17437	will die slowly	wds	WDR5 WDR5B
	CG1736	Proteasome alpha3 subunit, Testis-specific	Prosalpha3T	PSMA4
	CG1591	REG	REG	PSME3 PSME1 PSME2
	CG15645	cervantes	cerv	NSMCE2
	CG15237	-	CG15237	ANAPC15
	CG13732	quijote	qjt	NSMCE2
	CG12423	kelch like family member 10	klhl10	KLHL10
	CG12265	Deterin	Det	BIRC5 BIRC7 BIRC3 XIAP BIRC2 BIRC8 BIRC6 NAIP
	CG11579	armadillo	arm	CTNNB1 JUP
	CG10938	Proteasome alpha5 subunit	Prosalpha5	PSMA5
	CG10370	Regulatory particle triple-A ATPase 5	Rpt5	PSMC3
	CG10108	phyllopod	phyl	MAG
Autophagy	CG6770	-	CG6770	NUPR1 NUPR2
	CG6116	UV-resistance associated gene	Uvrag	UVRAG
	CG5602	DNA ligase 1	DNAlig1	LIG1
	CG5489	Autophagy-related 7	Atg7	ATG7
	CG2621	shaggy	sgg	GSK3B GSK3A
	CG16944	stress-sensitive B	sesB	SLC25A4 SLC25A5 SLC25A6 SLC25A31

	CG1560	myospheroid	mys	ITGB1 ITGB2 ITGB7 ITGB3 ITGB5 ITGB6 ITGB4 ITGB8 ITGBL1
	CG10798	Myc	Myc	MYC MYCN MYCL
	CG10360	refractory to sigma P	ref(2)P	SQSTM1

Table 2: List of 85 modifiers of VAP(P58S) aggregation, based on total cell intensity, along with their human orthologs

Category	Gene	Name	Symbol	Human Ortholog
ALS loci	CG7919	farinelli	fan	VAPB VAPA MOSPD3
	CG11793	Superoxide dismutase 1	Sod1	SOD1 SOD3
	CG10327	TAR DNA-binding protein-43 homolog	TBPH	TARDBP
ALS related genes	CG8160	-	CG8160	UBQLN4 UBQLN2 UBQLN1
	CG11940	pico	pico	RAPH1 APBB1IP GRB10 GRB7 GRB14
VAP interactors	CG9750	reptin	rept	RUVBL2
	CG9200	Ada2a-containing complex component 1	Atac1	ZZZ3
	CG9172	NADH dehydrogenase (ubiquinone) 20 kDa subunit	ND-20	NDUFS7 TSG101 UEVLD
	CG8095	scab	scb	ITGA4 ITGA9 ITGAL ITGAE ITGAM ITGA2 ITGA2 ITGA11 ITGAX ITGA10 ITGA1
	CG7766	-	CG7766	PHKA2 PHKA1
	CG7538	Minichromosome maintenance 2	Mcm2	MCM2
	CG7217	Peroxiredoxin 5	Prx5	PRDX5
	CG6674	-	CG6674	TSSC4
	CG6543	-	CG6543	ECHS1
	CG6292	Cyclin T	CycT	CCNT1 CCNT2 CCNK CCNQ
	CG6048	-	CG6048	HABP2 KLK14 KLK10 AZU1 CFD PRSS55
	CG5828	-	CG5828	PANK4 PANK2 PANK3 PANK1
	CG5198	hole-in-one	holn1	CD2BP2
	CG5179	Cyclin-dependent kinase 9	Cdk9	CDK9 CDK13 CDK12
	CG4924	icln	icln	CLNS1A
	CG4817	Structure specific recognition protein	Ssrp	SSRP1
	CG4646	-	CG4646	C1orf123
	CG4528	sans fille	snf	SNRPA SNRPB2
	CG4347	UGP	UGP	UGP2
	CG4206	Minichromosome maintenance 3	Mcm3	MCM3
	CG4088	Origin recognition complex subunit 3	Orc3	ORC3

	CG3688	RNA guanine-7 methyltransferase	Rnmt	RNMT
	CG3605	Splicing factor 3b subunit 2	Sf3b2	SF3B2
	CG3299	Vinculin	Vinc	VCL
	CG32703	Extracellularly regulated kinase 7	Erk7	MAPK15 MAPK11 MAPK13 MAPK7 MAPK1 MAPK14 MAPK12 MAPK3
	CG3192	NADH dehydrogenase (ubiquinone) ASHI subunit	ND-ASHI	NDUFB8
	CG2964	-	CG2964	PKM PKLR
	CG17689	Spt20	Spt20	SUPT20H SUPT20HL2 SUPT20HL1
	CG14935	Maltase B2	Mal-B2	SLC3A1 SLC3A2
	CG14837	-	CG14837	
	CG14813	Coat Protein (coatomer) delta	deltaCOP	ARCN1
	CG12746	-	CG12746	PLPP5 PLPP4 PLPP1 PLPP3
	CG10743	Liprin-beta	Liprin-beta	PPFIBP2 PPFIBP1
mTOR pathway	CG3493	Golgin-245	Golgin245	GOLGA4 GOLGB1
Motif Interactors	CG6198	CHORD	CHORD	CHORDC1 ITGB1BP2
	CG4699	non-specific lethal 1	nsl1	KANSL1 KANSL1L
Lipid Biosynthesis	CG9160	NADH dehydrogenase (ubiquinone) acyl carrier protein	ND-ACP	NDUFAB1
	CG7923	Fad2	Fad2	SCD SCD5
	CG4200	small wing	sl	PLCG1 PLCG2
Unfolded Protein Response	CG6155	Roe1	Roe1	GRPEL1 GRPEL2
	CG5330	Nucleosome assembly protein 1	Nap1	NAP1L1 NAP1L4 NAP1L3 NAP1L2 NAP1L5
	CG4463	Heat shock protein 23	Hsp23	HSPB2 CRYAB HSPB1 HSPB6 CRYAA CRYAA2 HSPB8 HSPB3 HSPB9 HSPB7
	CG3895	polyhomeotic distal	ph-d	PHC2 PHC3 PHC1
	CG2947	Hsc/Hsp70-interacting protein related	HIP-R	ST13
	CG1489	Regulatory particle triple-A ATPase 6	Rpt6	PSMC5
	CG12919	eiger	egr	EDA TNFSF13 TNFSF12-TNFSF13 TNFSF13B
	CG1242	Heat shock protein 83	Hsp83	PLPP5 PLPP4 PLPP1 PLPP3
	CG11858	-	CG11858	PIN4
Ubiquitin Proteasomal System	CG9324	Pomp	Pomp	POMP
	CG9242	burgundy	bur	GMPS
	CG8979	Proteasome inhibitor 31 kDa	PI31	PSMF1
	CG7037	Cbl proto-oncogene	Cbl	CBL CBLB CBLC
	CG5186	scruin like at the midline	slim	KLHDC10

	CG4943	SMAD specific E3 ubiquitin protein ligase	Smurf	SMURF2 SMURF1 ITCH NEDD4L NEDD4 WWP2 WWP1
	CG4443	Ubiquitin conjugating enzyme 7	Ubc7	UBE2G2
	CG4166	non-stop	not	USP22 USP27X USP51 USP3
	CG3455	Regulatory particle triple-A ATPase 4	Rpt4	PSMC6
	CG3416	Regulatory particle non-ATPase 8	Rpn8	PSMD7
	CG32486	-	CG32486	CYHR1
	CG3234	timeless	tim	TIMELESS
	CG3018	lesswright	lwr	UBE2I
	CG2960	Ribosomal protein L40	RpL40	UBA52
	CG2038	COP9 signalosome subunit 7	CSN7	COPS7B COPS7A
	CG1945	fat facets	faf	USP9X USP9Y USP24
	CG18341	Proteasome beta2 subunit-related 1	Prosbeta2R1	PSMB7 PSMB10
	CG17437	will die slowly	wds	WDR5 WDR5B
	CG1736	Proteasome alpha3 subunit, Testis-specific	Prosalpha3T	PSMA4
	CG1512	Cullin 2	Cul2	CUL2
	CG1403	Septin 1	1-Sep	2-Sep 4-Sep 6-Sep 11-Sep 8-Sep 10-Sep 12-Sep 1-Sep 5-Sep 7-Sep 14-Sep 9-Sep 3-Sep
	CG12265	Deterin	Det	BIRC5 BIRC7 BIRC3 XIAP BIRC2 BIRC8 BIRC6 NAIP
	CG11552	Regulatory particle non-ATPase 12-related	Rpn12R	PSMD8
	CG10938	Proteasome alpha5 subunit	Prosalpha5	PSMA5
	CG10108	phyllopod	phyl	MAG
Autophagy	CG8068	Suppressor of variegation 2-10	Su(var)2-10	PIAS1 PIAS3 PIAS2 PIAS4 ZMIZ1 ZMIZ2
	CG6877	Autophagy-related 3	Atg3	ATG3
	CG6116	UV-resistance associated gene	Uvrag	UVRAG
	CG5602	DNA ligase 1	DNAlig1	LIG1
	CG5489	Autophagy-related 7	Atg7	ATG7
	CG16944	stress-sensitive B	sesB	SLC25A4 SLC25A5 SLC25A6 SLC25A31
	CG10360	refractory to sigma P	ref(2)P	SQSTM1

A model system for measuring VAP(P58S) aggregation in the Drosophila larval brain.

In order to validate targets from the screen *in vivo*, we used the *UAS-GAL4* system to specifically overexpress wild-type *VAP* or *VAP(P58S)* in the brain using a pan-neuronal driver, *C155 (elav)* (Deivasigamani et al., 2014; Ratnaparkhi et al., 2008). Based on anti-VAP immunostaining, unlike wild-type VAP (Fig. 4A), mutant VAP(P58S) formed distinct cellular puncta and could be used as a model to study aggregation in the animal (Fig. 4B). These aggregates have been shown to be ubiquitinated and dominant-negative when expressed in muscle (Ratnaparkhi et al, 2008).

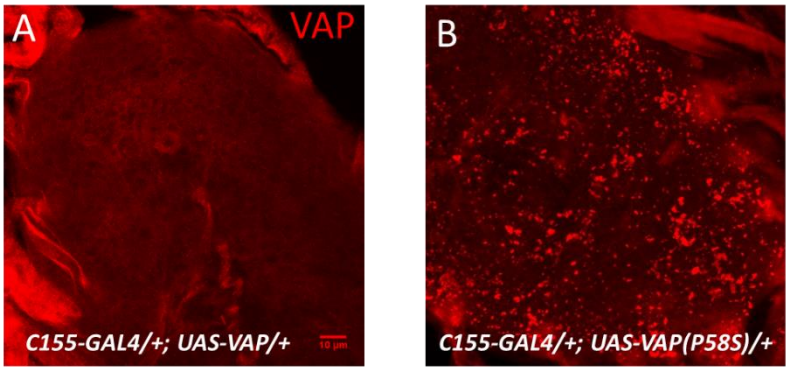

Figure 4: Visualization of VAP in wandering third instar larval brain.
A: Overexpression of VAP in the ventral nerve cord of the third instar larval brain, driven by pan-neuronal *C155-GAL4*, immunostained with rabbit anti-CCD (VAP) antibody, shows membrane localization.
B: Overexpression of VAP(P58S) in the ventral nerve cord of the third instar larval brain, driven by pan-neuronal *C155-GAL4*, immunostained with rabbit anti-CCD (VAP) antibody, shows punctate localization.

To develop a methodology for quantitation of aggregates in the brain (described in Materials & Methods), we used temperature as a means to increase GAL4 activity, which would increase VAP(P58S) dosage and possibly, aggregation. An increase in mean VAP(P58S) aggregation density was observed from 18 ºC to 25 ºC, but not significantly between 25 ºC and 28 ºC (Fig. 5A-C, 5G). Neuronal knockdown of VAP, using RNAi, in *CI55-GAL4/+; UAS-VAP(P58S)/+* flies, at each temperature (Fig. 5D-F), led to a significant decrease in corresponding aggregation density of the ventral nerve cord (Fig. 5G). The above experiments suggest that at 25 ºC, we could quantify changes in VAP(P58S) aggregation density in the brain of the larvae, and here onwards, we use this system to further validate modifiers of aggregation identified from the cell-based screen.

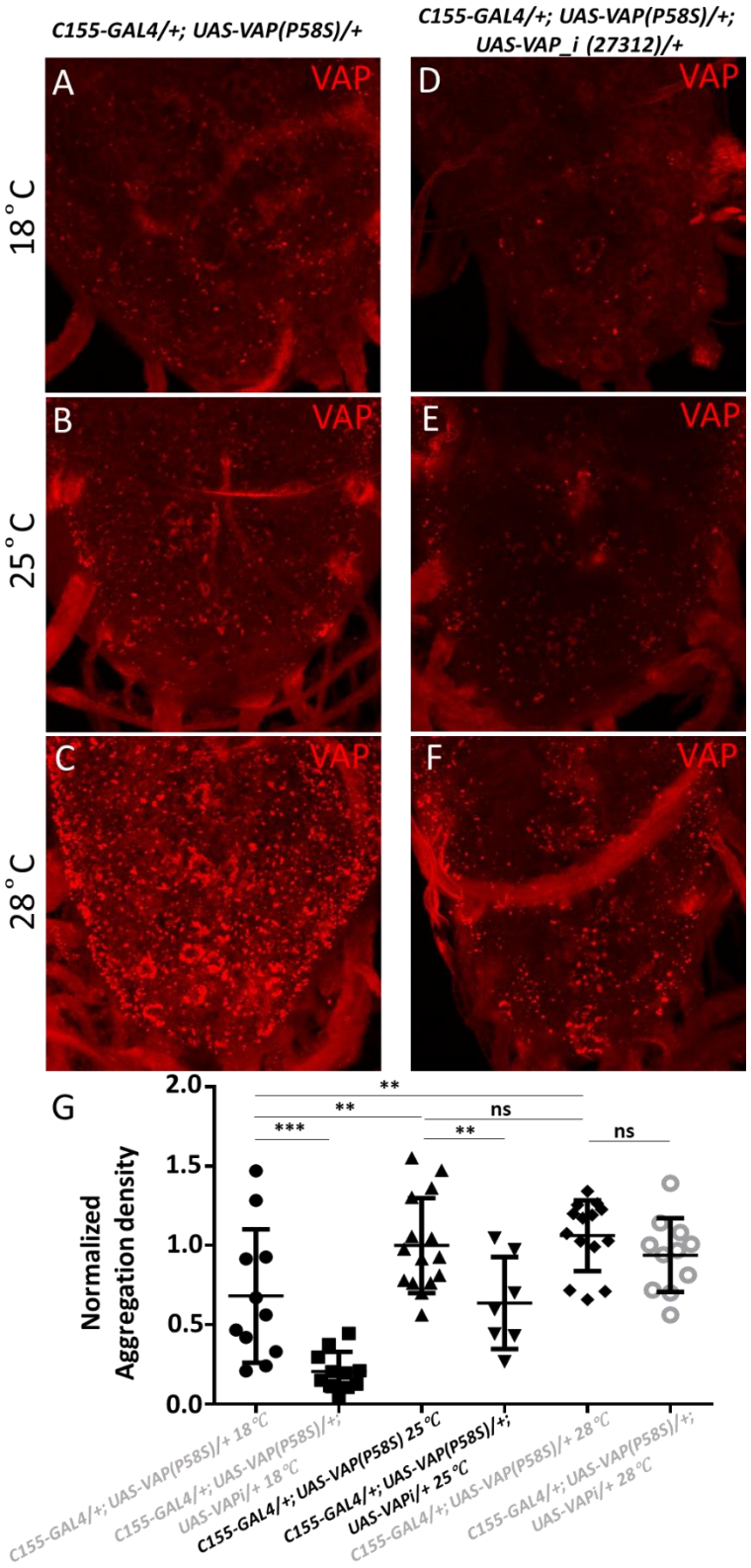
C155-GAL4/+; UAS-VAP(P58S)/+
C155-GAL4/+; UAS-VAP(P58S)/+; UAS-VAP_i (27312)/+
18°C
25°C
28°C
A
B
C
D
E
F
VAP
G
Normalized Aggregation density
2.0
1.5
1.0
0.5
0.0
***
**
**
ns
**
ns
C155-GAL4/+; UAS-VAP(P58S)/+ 18°C
C155-GAL4/+; UAS-VAP(P58S)/+; UAS-VAPi/+ 18°C
C155-GAL4/+; UAS-VAP(P58S) 25°C
C155-GAL4/+; UAS-VAP(P58S)/+; UAS-VAPi/+ 25°C
C155-GAL4/+; UAS-VAP(P58S)/+ 28°C
C155-GAL4/+; UAS-VAP(P58S)/+; UAS-VAPi/+ 28°C

Figure 5: A system for measuring VAP(P58S) aggregation in the larval brain.
A-C: Overexpression of VAP(P58S) is visualized as inclusions in the third instar larval brains. Temperature dependent increase in aggregation density is seen in the ventral nerve cord in *C155-GAL4/+; UAS-VAP(P58S)/+* larvae.
D-F: Knockdown of *VAP* in *C155-GAL4/+; UAS-VAP(P58S)/+* larvae leads to a corresponding decrease in aggregation density at each temperature.
G: Plot showing significant increase in VAP(P58S) aggregation density with increase in temperature, and a significant decrease in aggregation density in the ventral nerve cord in *C155-GAL4/+; UAS-VAP(P58S); UAS-VAP_i (27312)/+* as compared to *C155-GAL4/+; UAS-VAP(P58S)/+* control in a temperature dependent manner.
All images were taken at the same magnification. ANOVA (P-value: ****<0.0001) Fisher's LSD multiple comparison test (P values, **<0.01, ***<0.001). The '*_i*' appended to the gene name indicates the RNAi line with the number in brackets denoting a unique BDSC number.

Drosophila SOD1 is a modifier of VAP(P58S) aggregation

SOD1, first known ALS locus (Rosen et al. 1993), has been implicated in both sporadic as well as familial cases and was our first choice for validation of the S2R+ based screen, in the animal. We previously identified *SOD1* as a genetic interactor of *VAP* in a fly-based reverse genetics screen (Deivasigamani et al. 2014). Here, we individually knocked down *SOD1* using three independent RNAi lines in the *CI55-GAL4/+; UAS-VAP(P58S)/+* background and observed a significant decrease in aggregation density in the ventral nerve cord (Fig. 6A, 6B, 6E). This three-fold decrease in VAP aggregates was comparable to the reduction seen with VAP knockdown (Fig 6B). Likewise, we overexpressed *SOD1* in the *CI55-GAL4/+; UAS-VAP(P58S)/+* background. Here, however, we did not find a significant change in aggregation density (Fig. 6C, 6D, 6F). Taken together, these results suggest a need for a threshold level of *SOD1* to maintain VAP(P58S) inclusions.

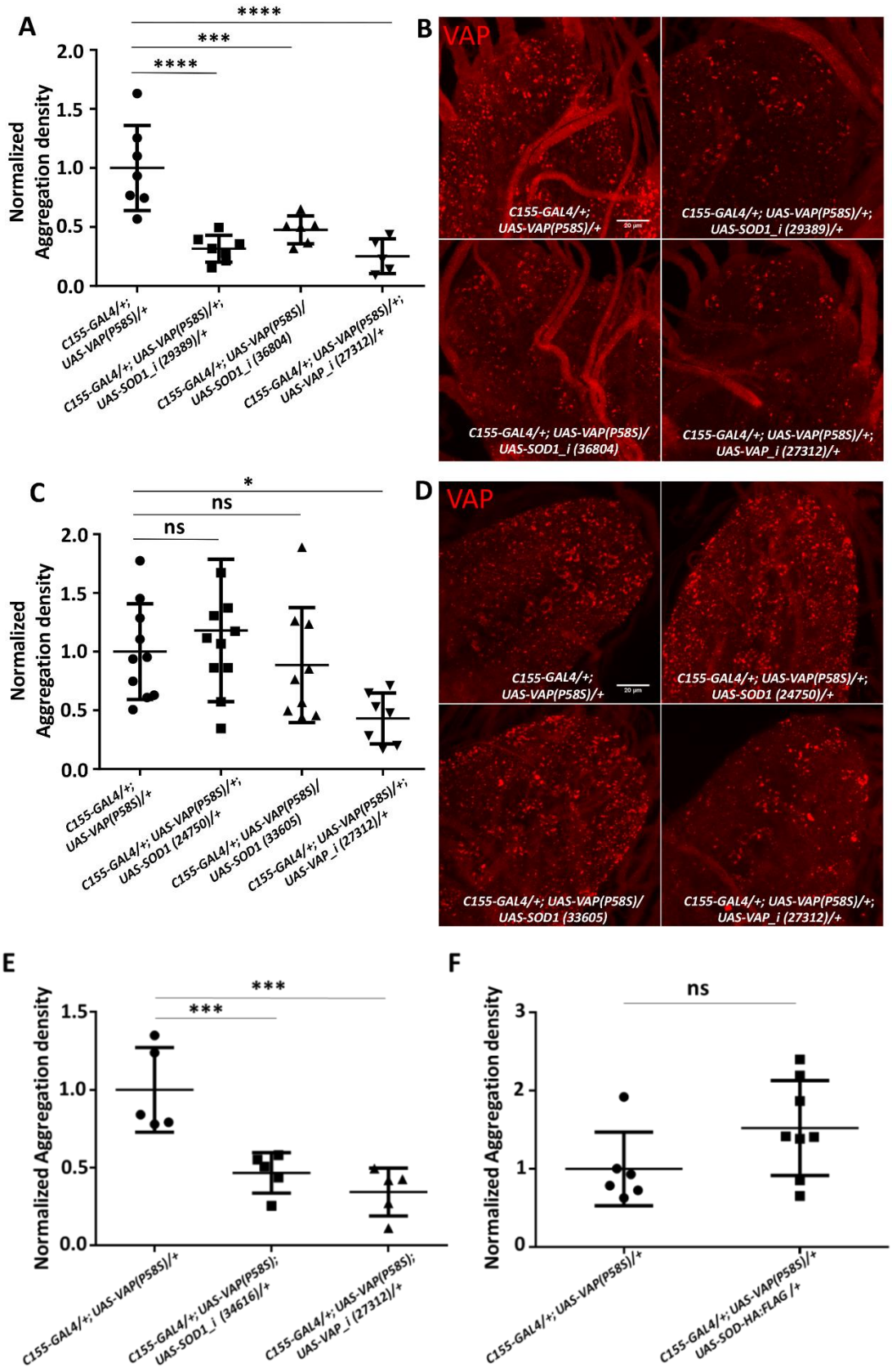
A
****
***
****
Normalized Aggregation density
2.0
1.5
1.0
0.5
0.0
C155-GAL4/+; UAS-VAP(P58S)/+
C155-GAL4/+; UAS-VAP(P58S)/+; UAS-SOD1_i (29389)/+
C155-GAL4/+; UAS-VAP(P58S)/ UAS-SOD1_i (36804)
C155-GAL4/+; UAS-VAP(P58S)/+; UAS-VAP_i (27312)/+
B
VAP
C155-GAL4/+; UAS-VAP(P58S)/+
C155-GAL4/+; UAS-VAP(P58S)/+; UAS-SOD1_i (29389)/+
C155-GAL4/+; UAS-VAP(P58S)/ UAS-SOD1_i (36804)
C155-GAL4/+; UAS-VAP(P58S)/+; UAS-VAP_i (27312)/+
C
*
ns
ns
Normalized Aggregation density
2.0
1.5
1.0
0.5
0.0
C155-GAL4/+; UAS-VAP(P58S)/+
C155-GAL4/+; UAS-VAP(P58S)/+; UAS-SOD1 (24750)/+
C155-GAL4/+; UAS-VAP(P58S)/ UAS-SOD1 (33605)
C155-GAL4/+; UAS-VAP(P58S)/+; UAS-VAP_i (27312)/+
D
VAP
C155-GAL4/+; UAS-VAP(P58S)/+
C155-GAL4/+; UAS-VAP(P58S)/+; UAS-SOD1 (24750)/+
C155-GAL4/+; UAS-VAP(P58S)/ UAS-SOD1 (33605)
C155-GAL4/+; UAS-VAP(P58S)/+; UAS-VAP_i (27312)/+
E
***
***
Normalized Aggregation density
1.5
1.0
0.5
0.0
C155-GAL4/+; UAS-VAP(P58S)/+
C155-GAL4/+; UAS-VAP(P58S); UAS-SOD1_i (34616)/+
C155-GAL4/+; UAS-VAP(P58S); UAS-VAP_i (27312)/+
F
ns
Normalized Aggregation density
3
2
1
0
C155-GAL4/+; UAS-VAP(P58S)/+
C155-GAL4/+; UAS-VAP(P58S)/+ UAS-SOD-HA:FLAG /+

Figure 6: *SOD1* knockdown reduces VAP(P58S) aggregation in larval brains
A, E: *SOD1* knockdown in the nervous system decreases aggregation density in the ventral nerve cord. VAP knockdown also reduces aggregation due to reduction in VAP and VAP(P58S) protein expression. The '*_i*' appended to the gene name indicates an RNAi line. ANOVA (P value: ****< 0.0001).
B: Representative images of the ventral nerve cord showing aggregation of VAP(P58S) with *SOD1* knockdown (29389 and 36804) and with *VAP* knockdown (27312).
C, F: *SOD1* overexpression does not affect aggregation density in the ventral nerve cord. ANOVA (P value: *, 0.0208).
D: Representative images of the ventral nerve cord showing aggregation of VAP(P58S) with *SOD1* overexpression (24750 and 33605) and with *VAP* knockdown (27312).
Numbers in brackets indicate BDSC stock numbers.
All images were taken at the same magnification. Fisher's LSD multiple comparison (P-values, *<0.05, ***<0.001, ****<0.0001, ns, not significant).

Oxidative stress reduces VAP(P58S) aggregation

Enzymatically, SOD1 metabolizes superoxide species to hydrogen peroxide, thereby preventing oxidative stress. A loss of function of SOD1 would, in principle, increase ROS. We tested whether a chemical mimic, paraquat, which increases cellular ROS (Castello et al. 2007; Drechsel and Patel 2009; Cocheme et al. 2011), could phenocopy the effect of *SOD1* knockdown. Larvae with the genotype *CI55-GAL4/+; UAS-VAP(P58S)/+* were hatched, fed and grown on non-lethal concentration of 5 mM paraquat at 25 ºC. We found a decrease in aggregation density in the third instar larval brain, reminiscent of the *SOD1* knockdown phenotype (Fig. 7A, 7B). We also checked the effect of other ROS scavenging genes such as *SOD2* and *catalase* on VAP(P58S) aggregation. Knockdown of both these genes resulted in a drastic reduction in aggregation density in the ventral nerve cord of *CI55-GAL4/+; UAS-VAP(P58S)/+* larval brains (Fig 7C). As seen with SOD1, overexpression of SOD2 did not change aggregation density; however, catalase overexpression resulted in a fractional increase in aggregation density (Fig 7C). These results strongly suggest a ROS dependent maintenance and/or stability of VAP(P58S) aggregates (Fig. 7D).

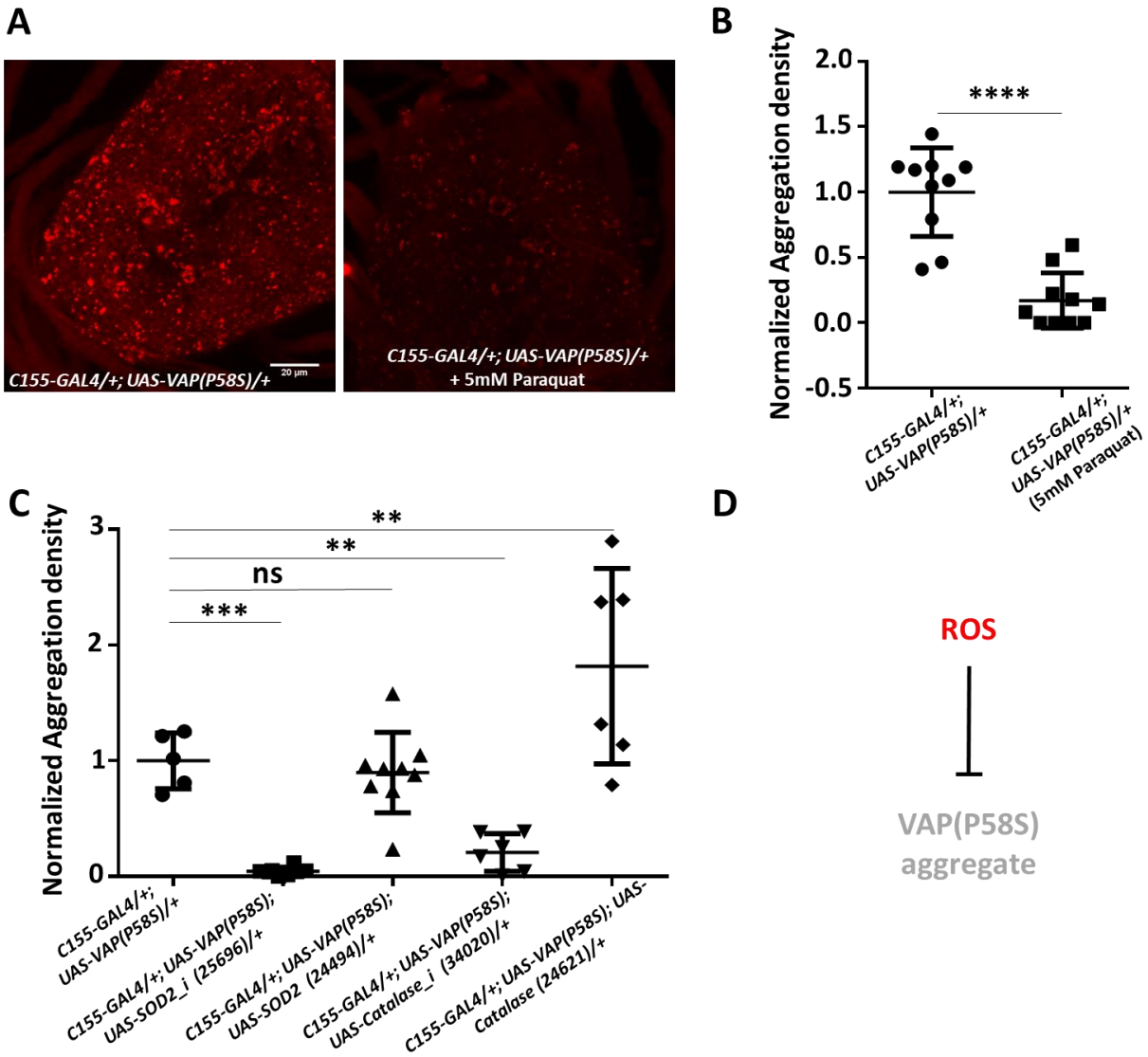

Figure 7: Increase in ROS leads to decrease in VAP(P58S) aggregation levels.

A: Representative images of ventral nerve cord showing a decrease in aggregation density in *C155-GAL4/+; UAS-VAP(P58S)/+* with 5 mM paraquat feeding. All images are taken at the same magnification.

B: Paraquat feeding decreases aggregation density in the ventral nerve cord of third instar larval brains in *C155-GAL4/+; UAS-VAP(P58S)/+* flies. Student's t-test (P-value: ****<0.0001).

C: *SOD2* or *Catalase* knockdown reduces aggregation density. Overexpression of *SOD2* does not change aggregation density, however overexpression of *Catalase* increases aggregation density. The '*_i*' appended to the gene name indicates an RNAi line. ANOVA (P-value: ****<0.0001) Fisher's LSD multiple comparison test (P-values, **<0.01, ***<0.001, ns, not significant).

D: Model depicting the effect of ROS on overexpression of mutant VAP.

To confirm whether feeding of paraquat and loss of SOD1 function led to an increase in ROS levels in the larval brain, we measured the levels of oxidized proteins and lipids, using the oxyblot kit and quantitative mass spectrometry based lipidomics, respectively. Using the oxyblot assay, we found that feeding *C155-GAL4/+* larvae with increasing concentrations of paraquat (0 mM, 0.05 mM, 0.5 mM, 5 mM) was sufficient to increase ROS in the brain, observed as an increase in intensity of oxidized proteins as compared to unfed larvae (Fig. 8A). As expected, neuronal knockdown of *SOD1* in presence of VAP(P58S) aggregates, led to a corresponding increase in intensity of oxidized proteins, demonstrating oxidative stress (Fig. 8B). We found that VAP(P58S) aggregation alone did not significantly change oxidized protein levels as compared to the *C155-GAL4/+* control (Fig. 8B). Unexpectedly, we found that overexpression of *VAP* in neurons led to a distinct increase in oxidation of proteins, indicating a role for VAP in regulation of ROS (Fig. 8B).

To further bolster our findings, we measured levels of oxidized phospholipids in larval brains (Tyurina et al. 2000; Kamat et al. 2015; Kory et al. 2017; Pathak et al. 2018). On feeding *C155-GAL4/+* larvae with 5 mM paraquat, we enriched and detected 9 oxidized polyunsaturated fatty acids (PUFAs), belonging to phosphatidylserine (PS) and phosphatidylethanolamine (PE) (Fig. 8C, Appendix 6) families of phospholipids, which were significantly elevated in larval brains, compared to the unfed control. PUFA containing oxidatively damaged phospholipids showed a mass addition of +16 (denoted as ox-, likely an epoxide across the double bond) or +18 (denoted as hy-, likely the addition of water across the double bond) to the parent phospholipid, as a consequence of addition of different ROS. Of note, the parent or precursor phospholipids did not change in concentration, and the concentrations of the oxidized phospholipids were less than 1% of the parent or precursor phospholipids. We found a similar elevation in concentrations of oxidized phospholipids in *C155-GAL4/+; UAS-VAP(P58S)/+; UAS-SOD1_i/+*, but not in *CI55-GAL4/+; UAS-VAP(P58S)/+* which was equivalent to *C155-GAL4/+* control (Fig. 8C, Appendix 6). This elevation in oxidized phospholipids was found to be inversely correlated with corresponding fold change in aggregation density (Fig. 8D). Interestingly, as suggested by the oxyblot data, we found that overexpression of *VAP* had a curious effect of increasing oxidation of lipids, indicating that wild type VAP has a cryptic yet important role in regulating ROS levels. Taken together, these results indicate that ROS initiates processes that aid clearance of VAP(P58S) aggregates, and is in turn regulated by VAP wildtype levels in the cell (Fig. 8E).

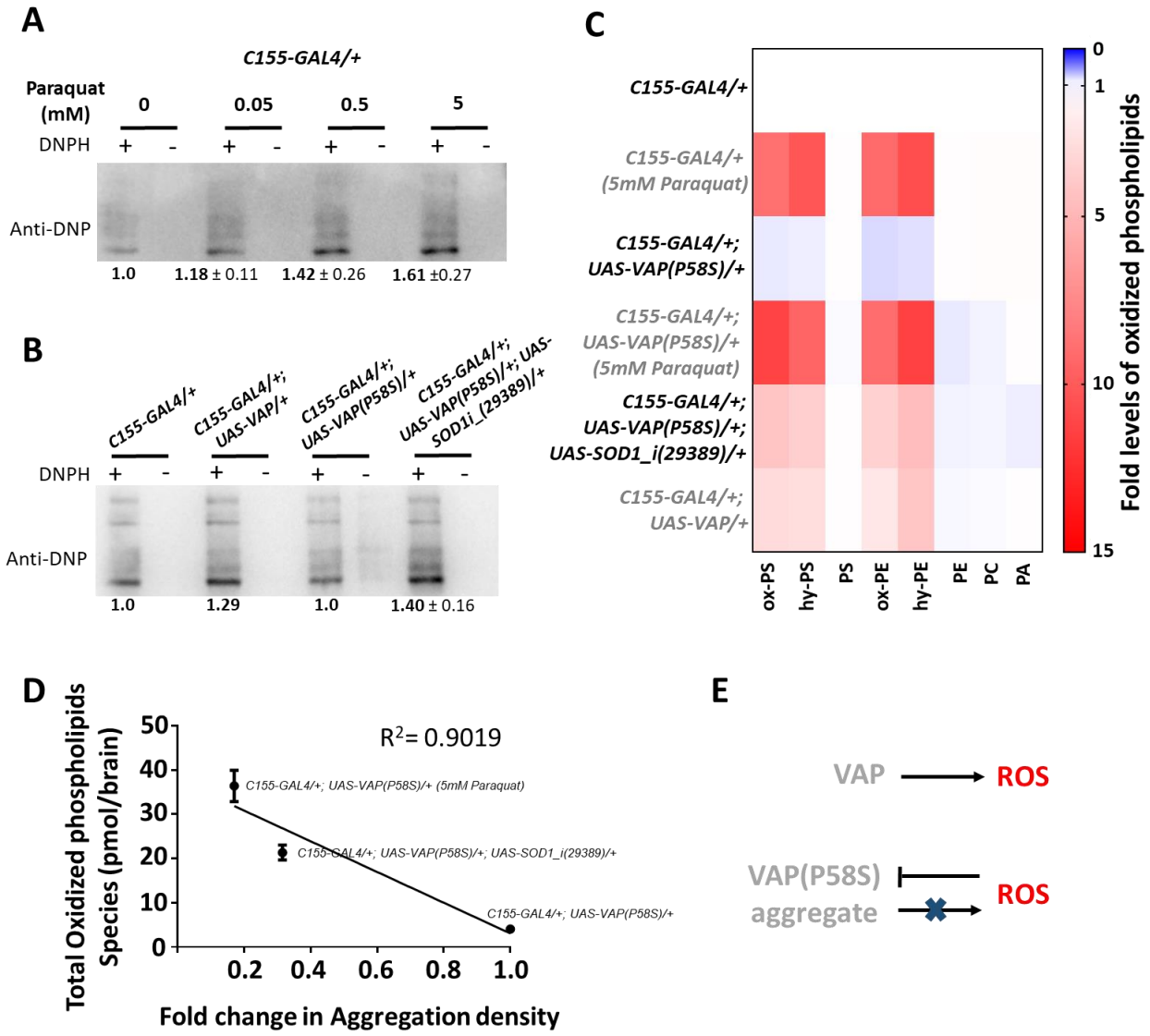

Figure 8: ROS levels are modulated by SOD1 and VAP

A-B: Higher levels of protein oxidation is seen using Oxyblot, in response to (**A**) Paraquat feeding, (**B**) *VAP* overexpression or *SOD1* knockdown in third instar larval brains (n=10), whereas no change was observed in presence of VAP(P58S) aggregates (**B**), as compared to control, *C155-GAL4/+*. Values below the gel indicate fold intensity of the strongest band, when compared to controls. Oxyblot showing lowered levels of oxidized proteins in larval brains (n=14) upon VAP knockdown as compared to *C155-GAL4* control, indicating a role for VAP in modulating ROS levels.

C: Heat map depicting change in levels of oxidized phospholipids normalized to *C155-GAL4/+*, quantified using MS in response to ROS generated in third instar larval brains (N=4) for the listed genotypes. SOD knockdown as well as VAP overexpression appears to increase cellular ROS levels. Statistical tests are described in Appendix 6.

D: Inverse correlation between total oxidized phospholipids and fold change in aggregation density.

E: Model depicting the effect of overexpression of wildtype and mutant VAP on ROS.

ROS activates proteasomal machinery

We further investigated protein degradative mechanisms that may be activated in response to ROS leading to the clearance of VAP(P58S) aggregates. In order to test whether the proteasomal machinery was responsible for reduction in aggregation, we hatched, fed, and grew larvae on food containing a proteasomal inhibitor, 5µM MG132. Larval brains were dissected at the wandering third instar stage and analysed for aggregation density. As expected, unfed *C155-GAL4/+; UAS-VAP(P58S)/+; UAS-SOD1_i/+*, showed reduced aggregation density (Fig. 9C), as compared to unfed control (Fig. 9A, 9E). Upon MG132 feeding, *C155-GAL4/+; UAS-VAP(P58S)/+; UAS-SOD1_i/+*, showed a complete recovery/retention of VAP(P58S) aggregation (Fig. 9D, 9E). Fed *C155-GAL4/+; UAS-VAP(P58S)/+; UAS-SOD1_i/+* also showed an enhanced aggregation density as compared to fed *CI55-GAL4/+; UAS-VAP(P58S)/+* (Fig. 9B, 9E). Aggregates in presence of ROS (with SOD1 knockdown) and proteasomal inhibition (with MG132) appeared to be predominantly smaller, scattered and mislocalized around the nuclear membrane/ER as compared to the respective controls (Fig. 9D'). The localization of the aggregates suggest that may be residing in the Juxtanuclear Quality Control compartment (JUNQ)-like compartment (Ogrodnik et al. 2014). These results indicate that the proteasomal machinery is facilitated in presence of ROS for active degradation of VAP(P58S) aggregates (Fig 9F). However, fed *CI55-GAL4/+; UAS-VAP(P58S)/+* larvae (Fig. 9A) did not show accumulation of aggregation as compared to unfed control (Fig. 9B, 9E), indicating other mechanisms may be at play to maintain the aggregation density.

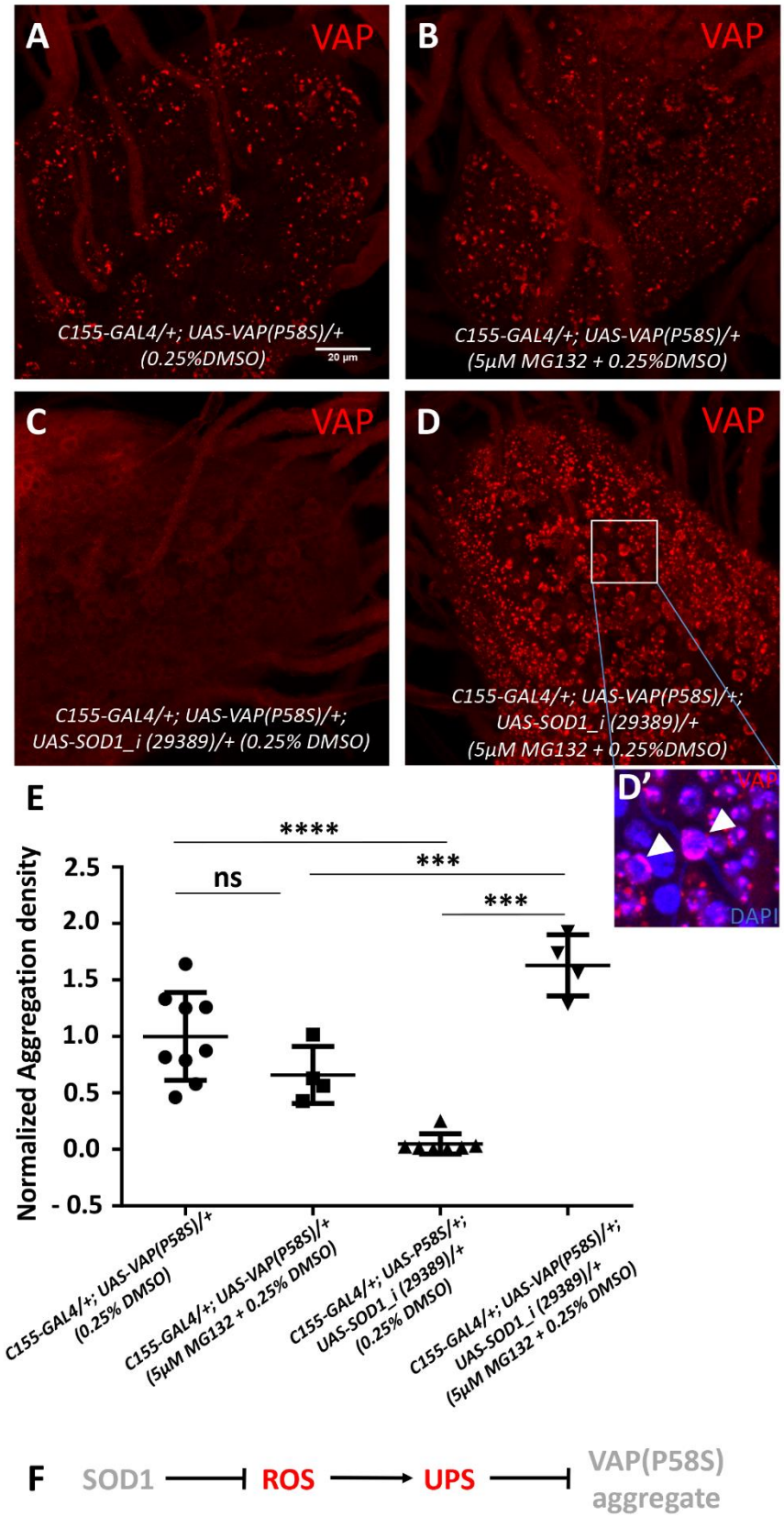
A
VAP
C155-GAL4/+; UAS-VAP(P58S)/+
(0.25%DMSO)
20 µm
B
VAP
C155-GAL4/+; UAS-VAP(P58S)/+
(5µM MG132 + 0.25%DMSO)
C
VAP
C155-GAL4/+; UAS-VAP(P58S)/+;
UAS-SOD1_i (29389)/+ (0.25% DMSO)
D
VAP
C155-GAL4/+; UAS-VAP(P58S)/+;
UAS-SOD1_i (29389)/+
(5µM MG132 + 0.25%DMSO)
D'
VAP
DAPI
E
Normalized Aggregation density
2.5
2.0
1.5
1.0
0.5
0.0
- 0.5
****
***
***
ns
C155-GAL4/+; UAS-VAP(P58S)/+
(0.25% DMSO)
C155-GAL4/+; UAS-VAP(P58S)/+
(5µM MG132 + 0.25% DMSO)
C155-GAL4/+; UAS-P58S/+;
UAS-SOD1_i (29389)/+
(0.25% DMSO)
C155-GAL4/+; UAS-VAP(P58S)/+;
UAS-SOD1_i (29389)/+
(5µM MG132 + 0.25% DMSO)
F
SOD1
ROS
UPS
VAP(P58S)
aggregate

Figure 9: ROS activates proteasomal machinery

A,B: MG132 feeding of *C155-GAL4/+; UAS-VAP(P58S)/+*, to inhibit proteasomal machinery, does not accumulate VAP aggregates as compared to unfed control.

C,D,D': MG132 feeding of *C155-GAL4/+; UAS-VAP(P58S)/+; UAS-SOD1_i (29389)/+*, leads to a dramatic accumulation of VAP aggregates. The aggregates, in presence of ROS and MG132, seem to be localized around the nuclear membrane (arrowheads) as depicted in inset (**D'**).

E: Plot showing significant decrease in aggregation density in the ventral nerve cord in *C155-GAL4/+; UAS-VAP(P58S); UAS-SOD1_i (29389)/+* as compared to *C155-GAL4/+; UAS-VAP(P58S)/+* control. This decrease is rescued by feeding 5µM MG132 and is significantly higher than the *C155-GAL4/+; UAS-VAP(P58S)/+* control, both unfed and fed with MG132.

All images were taken at the same magnification. ANOVA (P-value: ****<0.0001) Fisher's LSD multiple comparison test (P-values, ***<0.001, ****<0.0001, ns, not significant)

F: Model depicting the role of SOD1-regulated ROS in activating proteasomal degradation of VAP(P58S) protein/aggregates.

mTOR downregulation, but not autophagy, lowers VAP(P58S) aggregation

We examined whether aggregates could be cleared via autophagy in the third instar larval brain. mTOR downregulation is known to activate autophagy (Noda and Ohsumi, 1998) and this could be achieved chemically, by feeding rapamycin (Heitman et al. 1991), and genetically, by *Tor* knockdown. Upon feeding *CI55-GAL4/+; UAS-VAP(P58S)/+* larvae with 200nM rapamycin as described before (Deivasigamani et al. 2014), we observed a drastic clearance of aggregates in the ventral nerve cord as compared to unfed controls (Fig. 10A, 10B, 10C). When *Tor* transcripts were reduced using RNAi in *CI55-GAL4/+; UAS-VAP(P58S)/+*, a similar decrease in aggregation density was found (Fig. 10D, 10E, 10F). To verify the effect of mTOR downregulation on aggregates, we induced autophagy by overexpressing Atg1 in *CI55-GAL4/+; UAS-VAP(P58S)/+* larval brains as described before (Shen and Ganetzky 2009; Deivasigamani et al. 2014). Validation of the UAS-Atg1 line is described in Materials and Methods. With overexpression of Atg1, however, we did not observe a change in aggregation density (Fig. 10G, 10H, 10I) suggesting that mTOR signalling may perturb downstream effectors other than Atg1 which may affect VAP(P58S) aggregation dynamics (Fig. 10J). The data also raise the possibility of an autophagy independent pathway.

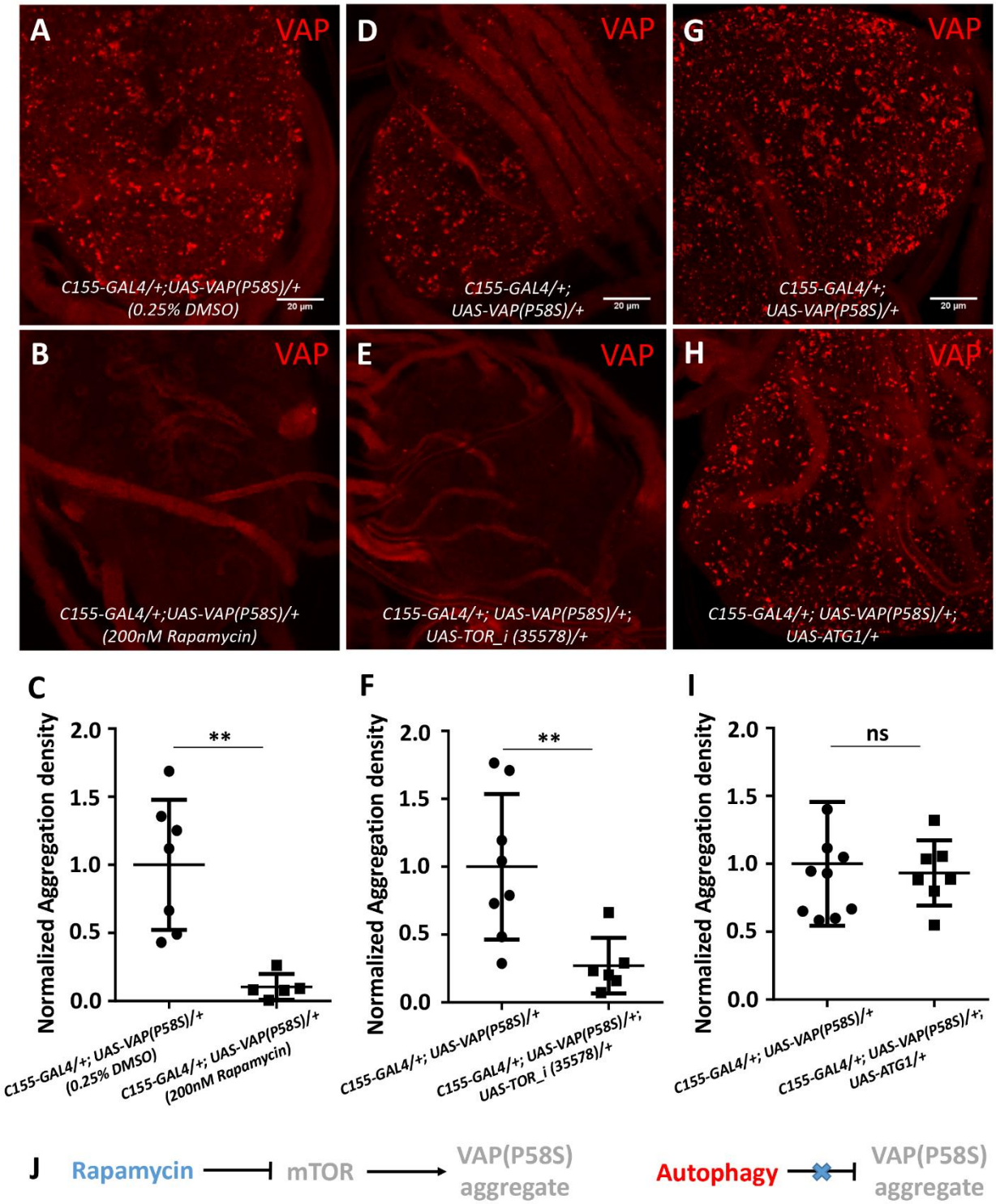

Figure 10: mTOR downregulation, but not autophagy, reduces VAP(P58S) aggregation.
A-C: Rapamycin feeding decreases aggregation density in the ventral nerve cord of third instar larval brains in *C155-GAL4/+; UAS-VAP(P58S)/+* flies.
D-F: Neuronal *TOR* knockdown decreases aggregation density in the ventral nerve cord. The '*_i*' appended to the gene name indicates an RNAi line.

G-I: Neuronal overexpression of Atg1 did not affect the aggregation density in the ventral nerve cord. All images were taken at the same magnification. Students's t-test (P-value, **<0.01, ns, not significant)
J: Model depicting mTOR-regulated clearance of aggregates, independent of autophagy.

mTOR inhibition promotes proteasomal clearance of VAP(P58S) aggregation via ROS

We first decided to check whether clearance of aggregates with mTOR inhibition correlated with increase in ROS, as in the case of *SOD1* knockdown. We found that levels of several species of oxidized phospholipids were indeed higher with *Tor* knockdown with or without neuronal overexpression of VAP(P58S) in third instar larval brains to levels similar to *SOD1* knockdown (Fig. 11A). mTOR pathway downregulation has recently been shown to activate not only autophagy but also ubiquitin proteasomal machinery (Zhao et al. 2015) via Mpk1/ERK5 pathway in yeast and humans (Rousseau and Bertolotti 2016). We tested whether ROS upregulation with *Tor* knockdown could be inducing proteasomal clearance of VAP(P58S) aggregation by feeding *CI55-GAL4/+; UAS-VAP(P58S)/+; UAS-TOR_i/+* with 5µM MG132 (Fig 11B, 11C-E). Although there was a significant decrease in aggregation density with *Tor* knockdown (Fig. 11D), we found only a slight recovery of aggregation in MG132-fed animals (Fig. 11E) as compared to unfed *CI55-GAL4/+; UAS-VAP(P58S)/+* control larvae (Fig. 11C). This recovery appeared to be far less dramatic than that seen in the case of *SOD1* knockdown. Taken together, these results indicate that in context of ROS, proteasomal degradation could be the major pathway responsible for clearance of VAP(P58S) aggregation (Fig. 11F), although other downstream effectors of mTOR signalling, including autophagy, cannot be conclusively ruled out as additional mechanisms.

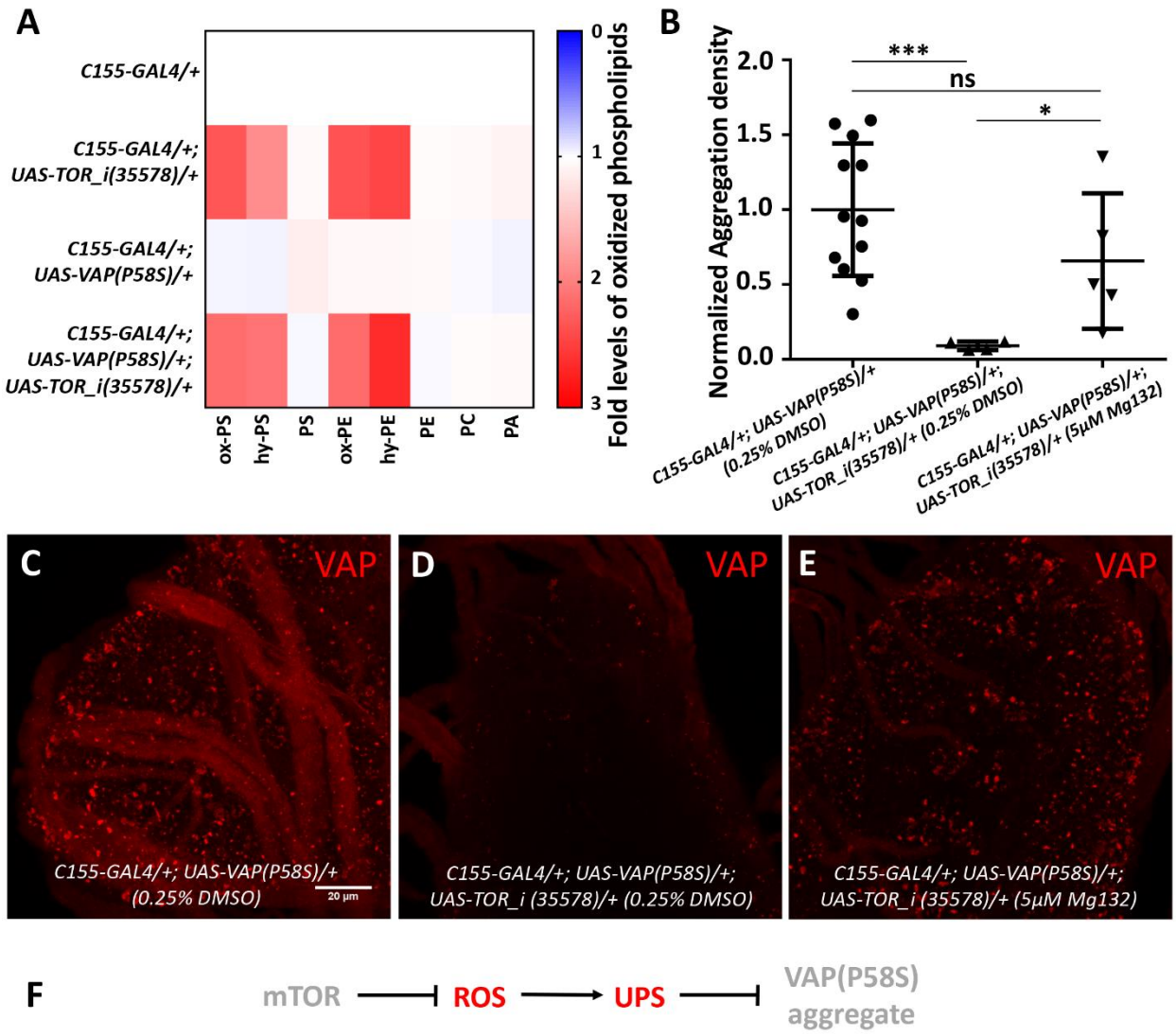

Figure 11: mTOR inhibition induces ROS and promotes proteasomal degradation of VAP(P58S) protein/aggregates.

A: Heat map depicting change in levels of oxidized phospholipids with *TOR* knockdown normalized to *C155-GAL4/+*, quantified using MS in response to ROS generated in third instar larval brains (N=3-4) for the listed genotypes. Statistical tests are described in Appendix 6.

B: Plot showing significant decrease in aggregation density in the ventral nerve cord in *C155-GAL4/+; UAS-VAP(P58S); UAS-TOR_i (35578)/+* as compared to *C155-GAL4/+; UAS-VAP(P58S)/+* control. This decrease is partially rescued by feeding 5µM MG132. ANOVA (P-value: **, 0.0042) Fisher's LSD multiple comparison test (P-values, *<0.05, ***<0.001).

C,D,E: Representative images of third instar larval brains showing the partial recovery of aggregates upon 5µM MG132 feeding in *C155-GAL4/+; UAS-VAP(P58S)/+; UAS-TOR_i (35578)/+* larvae. All images were taken at the same magnification.

F: Model depicting the role of mTOR-regulated ROS in activating proteasomal degradation of VAP(P58S) protein/aggregates.

mTOR pathway is known to be regulated by ROS. Sestrin, an antioxidant protein, is a negative regulator of mTOR pathway. Forkhead Box O (FOXO) is a transcription factor responsible for the expression of sestrin in oxidative stress conditions (Demontis and Perrimon 2010; Lee et al. 2010; Hay 2011). We investigated whether these regulators, sestrin and FOXO, that respond to the levels of ROS in the cell, could modulate VAP(P58S) aggregation in the larval brain. We knockdown *sestrin* using two RNAi lines. We found that with one line, the aggregation density increased to more than twice the control level (Fig. 12A, 12B, 12E). However, with the other line, the aggregation density did not show a significant change (Fig. 12C, 12E). The extent of *sestrin* knockdown with each line needs to be tested using quantitative PCR in order to validate its effect on VAP(P58S) aggregation. The aggregation density remained unchanged upon FOXO:GFP overexpression as well (Fig. 12D, 12E). These results suggest that levels of sestrin, but not its expression, could potentially affect VAP(P58S) aggregation (Fig. 12F).

We also explored the possible relationship between *VAP* and ROS at a transcriptional level. Larvae of the control, *CI55-GAL4/+* genotype were hatched and fed on 5mM paraquat, and the brains were dissected at the wandering third instar larval stage. The levels of endogenous *VAP* and *SOD1* mRNA, in response to ROS, were measured using qPCR in control larval brains. We found that endogenous *VAP* mRNA levels were lowered in the presence of high levels of ROS (Fig. 12G), while *SOD1* mRNA levels remained unchanged (Fig. 12H). This result may indicate the presence of a negative feedback loop wherein VAP overexpression leads to accumulation of ROS (Fig. 12C), which in turn downregulates endogenous *VAP* transcription (Fig. 12I). This phenomenon merits detailed investigation in future studies.

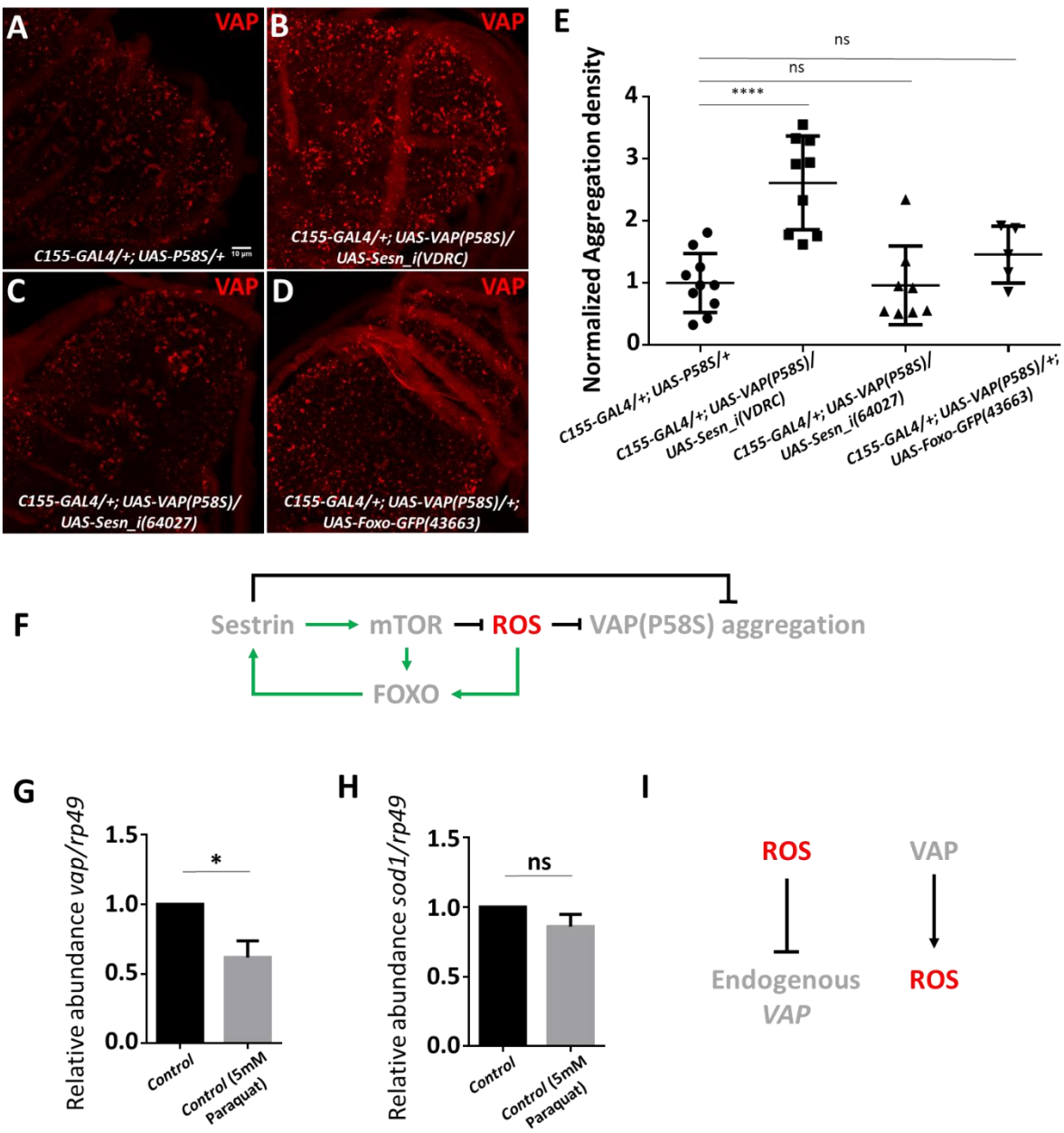

Figure 12: ROS levels modulate VAP

A-D: Representative images of third instar larval brains showing an increase in aggregation density with knockdown of *Sestrin* (VDRC), but not with knockdown of *Sesn* (64027) or with overexpression of *FOXO:GFP* (43663). All images were taken at the same magnification.

E: Plot showing a significant increase in VAP(P58S) aggregation density in the ventral nerve cord in *C155-GAL4/+; UAS-VAP(P58S)/UAS-Sesn_i (VDRC)/+* as compared to *C155-GAL4/+; UAS-VAP(P58S)/+* control. However, *C155-GAL4/+; UAS-VAP(P58S)/UAS-Sesn_i (64027)/+* and *C155-GAL4/+; UAS-VAP(P58S); UAS-FOXO:GFP (43663)/+* do not show a significant change. ANOVA (P-value: ****<0.0001) Fisher's LSD multiple comparison test (P-value, ****<0.0001).

F: Model depicting the possible effect of sestrin on VAP(P58S) aggregation via ROS. Sestrin is known to negatively regulate mTOR via JNK/FOXO (Demontis and Perrimon 2010; Lee et al. 2010).
G: Relative mRNA levels *VAP*, in the *C155-GAL4* control larval brain, are lowered upon feeding animals 5mM paraquat, suggesting that high levels of ROS may negatively regulate *VAP* transcripts. Student's t test (P-value *<0.05).
H: Relative mRNA levels of *sod1*, in the *C155-GAL4* control larval brain, do not change upon feeding 5mM paraquat.
I: Model depicting the differential relationship of ROS with VAP.

Discussion

A targeted RNAi screen uncovers SOD1, TDP43 and TOR signalling elements as targets to understand dynamics of VAP(P58S) aggregation

Drosophila S2R+ cell based whole genome RNAi screens serve as powerful tools due of the relative ease with which transcript knockdown can be achieved (Echeverri and Perrimon 2006). Similar systems have been used for identifying modifiers of aggregation of Huntingtin protein (Zhang et al. 2010). Our screen was aimed at enriching genes that are known players in ALS, VAP interactors and proteostasis. First and foremost, we found ALS loci, *SOD1* and *TDP-43* as modifiers of VAP(P58S) aggregation, which we had previously identified as VAP genetic interactors (Deivasigamani et al. 2014). In this study, we have explored the interaction between *SOD1* and *VAP*, while *TDP-43* also serves as an exciting candidate for further investigation. TDP-43 has been shown to perturb membrane-associated mitochondrial (Turner et al. 2008) sites that are maintained by VAPB-PTPIP51 interactions in mammalian cell culture (Stoica et al. 2014). Additionally, TDP-43 proteinopathy has been identified in motor neurons of mice models of VAP(P58S) aggregation (Tudor et al. 2010). TDP-43 driven neurodegeneration has also been shown to be modulated by oxidative stress related MAP kinase pathways in a *Drosophila* screen (Zhan et al. 2015) and associated with Nrf2 dependent antioxidant pathway (Moujalled et al. 2017). In addition to SOD1, we have also identified other ROS related genes such as peroxiredoxin V, NADH dehydrogenase, cytochrome c oxidase, that localise to the mitochondria, perturbation of which will lead to oxidative stress, potentially affecting aggregation kinetics of VAP(P58S).

Secondly, we enriched a subset of targets involved in protein degradation, UPS and autophagy, an *in vivo* validation of which would shed light on the how these aggregates are compartmentalized and managed in the neurons. Thirdly, this screen highlighted specific chaperones that could be involved in the misfolding and formation of VAP(P58S) aggregates providing insight into the initiation of the disease condition. Most importantly, through our

previous study (Deivasigamani et al. 2014), and our cell-based screen followed by subsequent experimentation, we have established mTOR signalling as a strong modulator of VAP(P58S) aggregation. mTOR signalling responds and integrates signals from nutrients, growth factors, energy, and stress, regulates cellular proteostasis, thus contributing to age-related neurodegenerative diseases (Perluigi et al. 2015), making it an attractive target for further investigation in ALS pathogenesis. Indeed, rapamycin, a TORC1 inhibitor inducing autophagy, known to be effective in ALS models of TDP-43 in flies and mice, as well as sequestosome 1 (SQSTM1) in zebrafish, is now being used for phase-II clinical trials for ALS (Mandrioli et al. 2018). Lastly, through our screen, targeting processes involved in neurodegeneration, we have identified interactions that point towards a role for VAP as a contributor to a common gene regulatory network (GRN), in agreement with several examples in literature (Tudor et al. 2010; van Blitterswijk et al. 2012b; Prause et al. 2013; Deivasigamani et al. 2014; Stoica et al. 2014, 2016; Paillusson et al. 2017). When we compared our list of targets with the results from another fly-based screen for VAP(P58S)-induced eye degeneration (Sanhueza et al. 2015), we only found one overlap, *Atg7*, a gene coding for a E1-like ubiquitin activating enzyme with a role in autophagy (Mizushima and Komatsu 2011). This lack of significant overlap could possibly be because of differences in sets of genes screened, cell types, and phenotypes visualized.

An ROS dependant physiological mechanism that triggers proteasomal clearance of VAP(P58S) aggregation

In our study, we have used a dosage-dependent pan-neuronal GAL4 expression of VAP(P58S) in order to study changes in aggregation in the third instar larval brain. We found two targets, SOD1 and mTOR (Deivasigamani et al. 2014), downregulation of which, led to a decrease in VAP(P58S) aggregation accompanied by oxidative stress. We identified a role of ROS in upregulating the proteasomal machinery and, thereby facilitating the degradation of misfolded VAP(P58S) protein/aggregates (Integrated Model; Fig. 13A). However, in absence of ROS, we did not find any change in aggregation density upon pharmacological proteasomal inhibition. This is consistent with the cell culture studies that point towards the downregulation of Ubiquitin-proteasome system (UPS) with VAP(P58S) aggregation as a dominant negative effect on wild type VAP function (Kanekura et al. 2006; Gkogkas et al. 2008; Papiani et al. 2012; Genevini et al. 2014). Overexpression of VAP(P58S) or loss of VAP in *Drosophila* has been shown to enhance

ER stress in the adult brains and may be a result of suspended proteasomal degradation (Tsuda et al. 2008; Moustaqim-barrette et al. 2014). In mice, VAP(P56S) aggregates have been shown to represent an ER-Quality Control (ERQC) compartment that develops as a result of a debilitated ER-Associated Degradative (ERAD) pathway (Kuijpers et al. 2013). Indeed, VAP has been shown to interact with UPR sensor AFT6 in mice and the ERAD complex thereby regulating proteostasis and lipid homeostasis in HeLa cell lines (Gkogkas et al. 2008; Ernst et al. 2016). Studies in mammalian cell lines suggest that VAP(P56S) is ubiquitinated, aggregates on the ER membrane and is cleared by the AAA+ valsolin containing protein (VCP)/p97, which interacts with Fas associated factor 1(FAF1) and may use the FFAT motif in FAF1 as an adapter to interact with VAP (Papiani et al. 2012; Baron et al. 2014). In *Drosophila*, VAP has been shown to be essential for ER homeostasis by maintaining lipid transport, whereas the mutant VAP flies show accumulation of ubiquitinated and membrane proteins in neuronal cells (Moustaqim-barrette et al. 2014). Hence, although ER stress is build up with VAP(P58S) aggregation, it does not lead to subsequent oxidative stress, as shown in our results. This suggests that ROS enhances the proteasomal degradation of VAP(P58S) through an ER stress-independent mechanism. Although neuronal VAP(P58S) aggregates appeared to be non-toxic to flies *per se*, our study highlights the effects of ROS on the dynamics of VAP(P58S) from misfolded protein to aggregate formation and subsequent clearance.

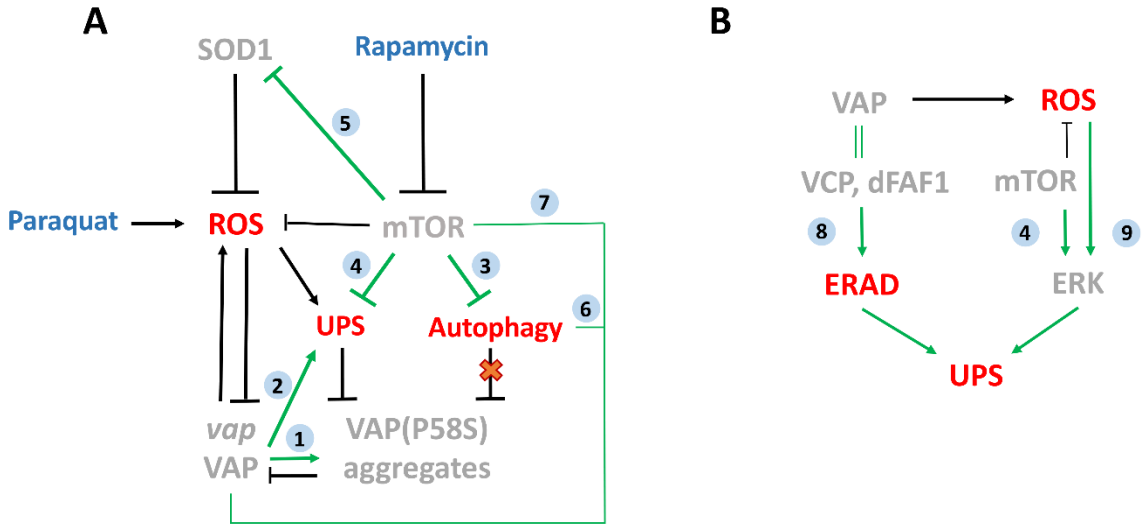

Figure 13: An integrated model for ROS mediated clearance of VAP(P58S) aggregates via UPS.
A: Model depicting novel relationships of SOD1(ALS1) and mTOR- induced ROS with VAP and VAP(P58S) aggregates. Clearance of VAP(P58S) protein/aggregates appears to be primarily via the Ubiquitin-Proteosomal system (UPS), triggered by ROS, which is in turn regulated by cellular pathways

such as mTOR pathway, SOD1 and VAP activity. Autophagy does not appear to be a major contributor for aggregate clearance, under the conditions of our experiment.
B: A hypothetical model proposing the possible link between VAP, ROS and UPS. VAP could regulate the UPS via the ERAD pathway due to its interaction with VCP via dFAF1/Caspar. ROS could be the connecting link between mTOR pathway and ERK pathway that together regulate the components of the proteasomal machinery. The link between VAP and ROS that we have demonstrated could modulate proteasomal activity in the cell.
Gray text indicates Genes (*italics*) and proteins (Capitals); Red text indicates cellular mechanisms; Blue text indicates drugs; Arrows: Black: Experimental evidence, this study; Green: Relationship described in literature; Numbers inside blue circles indicate research papers: **1.** Ratnaparkhi *et al.*, 2008; **2**. Kanekura *et al.*, 2006; Kuijpers *et al.*, 2013; **3.** Noda and Ohsumi, 1998; Perluigi *et al.*, 2015; **4.** Zhao *et al.*, 2015; Rousseau and Bertolotti, 2016; **5.** Sun *et al.*, 2012; Tsang *et al.*, 2018; **6.** Gomez-Suaga *et al.*, 2017; Zhao *et al.*, 2018; Wu *et* al., 2018 **7.** Deivaisigamini *et al.*, 2014; **8.** Baron *et al.*, 2014; Papiani *et al.*, 2012; **9.** Cavanaugh *et al.*, 2006; Su *et al.*, 2014.

TOR signaling regulates VAP(P58S) dynamics by a UPS dependent and Atg1 independent mechanisms.

We previously identified mTOR pathway as a strong regulator of both VAP and VAP(P58S) phenotypes at the neuromuscular junction (Deivasigamani et al. 2014). Here, we have shown that inhibition of mTOR pathway also reduces VAP(P58S) aggregation levels in third instar larval brains in presence of ROS. mTOR pathway downregulation is known to activate autophagy (Noda and Ohsumi 1998), a process that has been shown to reduce mutant huntingtin fragments (Ravikumar et al. 2004) and amyloid-β levels (Spilman et al. 2010) in mice models. Role of VAP in autophagy is unclear. With *VAP* knockdown in mammalian cell culture, autophagy is upregulated due to the loss of calcium homeostasis that arises with the disruption of ER-mitochondrial contact sites (Gomez-Suaga et al. 2017b, a). This upregulation appears to be beclin-1-dependent, which has a role in autophagosome formation (Wu et al. 2018). However, VAP is also suggested to have a role in autophagosomal biogenesis through direct interaction with ULK1/FIP200 complex (Zhao et al. 2018). Previously, we have observed that neuronal overexpression of VAP or Atg1 reduces bouton size at the NMJ, an effect that is exacerbated in combination (Deivasigamani et al. 2014). On the other hand, Atg1 overexpression rescues the large bouton size associated with VAP(P58S) overexpression in the third instar larval brains (Deivasigamani et al. 2014). In this study, however, we do not observe any clearance of VAP(P58S) aggregates with overexpression of Atg1 alone (Fig. 13A).

mTOR and SOD1 have been shown to be genetic interactors in *Drosophila* with mTOR inhibition enhancing the lifespan defect incurred with SOD1 knockdown (Sun et al. 2012). Recently, mTOR has been directly shown to regulate SOD1 activity by its phosphorylation based on nutrient availability in yeast and mammalian cells (Tsang et al. 2018). Although this phosphorylation site does not appear to be conserved in *Drosophila*, this study demonstrates the role of mTOR pathway in regulating ROS via SOD1. In response to increased ROS, with high TOR activity, sestrin, an antioxidant, has been shown to accumulate and negatively regulate the mTOR pathway in the wing disc. This increase in sestrin levels is attributed to the activation of JNK/FOXO pathway in response to oxidative stress (Demontis and Perrimon 2010; Lee et al. 2010). However, we found ROS to be upregulated with mTOR inhibition in third instar larval brains, suggesting a possible accumulation of sestrin. Indeed, when sestrin was knocked down in the *CI55-GAL4/+; UAS-VAP(P58S)/+* larval brains, we found a significant increase in aggregation density with one of the two lines tested (Fig. 12F). However, activating dFOXO did not phenocopy the effect of mTOR inhibition on VAP(P58S) aggregates. Recently, mTOR inhibition, specifically, mTORC1 has also been shown to activate proteasomal degradation independent of its other targets, such as, 4EBP, S6K and Ulk (Cavanaugh et al. 2006; Zhao et al. 2015). An evolutionarily conserved regulation of components of proteasomal assembly by mTORC1 via Mpk1/ERK5 has been reported in yeast as well as mammalian cell culture (Rousseau and Bertolotti 2016). ERK5 signalling has been implicated in neuroprotective roles in response to mild levels of oxidative stress (Cavanaugh et al. 2006; Su et al. 2014). These studies suggest that ROS regulation by mTOR inhibition via SOD1 and ERK5, serves as a plausible mechanism for the proteasomal degradation of VAP(P58S) protein/aggregation, and by extension, the rescue of VAP(P58S) NMJ phenotype (Deivasigamani et al. 2014) (Fig. 13B).

Increase in ROS by VAP, but not VAP(P58S) expression

SOD1-associated elevation in ROS levels and oxidative stress is suggested as a plausible factor of motor neuron death in ALS (Barber et al. 2006; Saccon et al. 2013). Teuling *et al.*, 2007 (Teuling et al. 2007) have shown that VAPB protein levels decrease in an age-dependent manner in a mouse model of SOD1-G93A, providing the first evidence of a link between *ALS1* and *VAP/ALS8.* We now find that overexpressed VAP, unlike VAP(P58S), promotes the accumulation of ROS in the system. This is consistent with a study that shows lowered ROS in a *vpr* (VAP

ortholog) mutant of *C. elegans* in response to increased mitochondrial connectivity and altered function (Han et al. 2013). VAP neuronal overexpression in *Drosophila* has also been shown to increase bouton number (Pennetta et al. 2002) similar to SOD1 mutant phenotype at the NMJ (Milton et al. 2011), and is correlated with increased ROS in both scenarios. VAP may be important in regulating pathways that respond to changes in ROS levels, such as mTOR and ERK pathways that can regulate UPS (Rousseau and Bertolotti 2016). VAP also modulates ERAD (and UPS), via its interaction with VCP and FAF1 (Papiani et al. 2012; Baron et al. 2014). We hypothesize that the interaction between VAP and ROS could lead to crosstalk between these pathways regulating global proteostasis (Hypothetical model, Fig. 13B).

ROS may regulate VAP levels by regulating VAP transcription

In our study, we have found that in presence of ROS, *VAP* transcription is downregulated in wild type flies. We had previously shown that *SOD1* knockdown rescues VAP macrochaetae phenotype (Deivasigamani et al. 2014), which may be a consequence of excessive ROS accumulation, and subsequent downregulation of VAP levels and function. Two independent studies (Qiu et al. 2013; Kim et al. 2016), that overexpressed VAPB in *ALS1* (SOD1-G93A) mice as an attempt at rescuing ALS defects, found contradictory observations, owing mainly to differences in expression levels of the protein. *VAPB* mRNA levels are known to be lowered in spinal cords of patients with sporadic ALS (Anagnostou et al. 2010), as well as in IPSC- derived motor neurons from ALS8 patients (Mitne-Neto et al. 2007). Based on our results and taking into consideration earlier observations (Teuling et al. 2007; Anagnostou et al. 2010; Deivasigamani et al. 2014), we submit that a possible ALS disease scenario may include increased ROS resulting in downregulation of VAP, at the transcript level (Model, Fig. 13A). It remains to be tested whether ROS-activated pathways such as MAP kinase pathways or mTOR pathway, could directly control VAP expression. This VAP/ROS regulation that we have uncovered may have significant implications in ALS pathogenesis for both sporadic and familial ALS.

In Summary, we find that the dynamics of VAP(P58S) neural aggregates, a species intimately linked to disease in the human context, is sensitive to levels of ROS. Change in physiological levels of ROS appear to dictate the equilibrium between the aggregated and non-aggregated forms. The cellular levels of ROS are themselves dictated by well characterized

regulatory mechanisms that include ROS generators and scavengers. As shown in this study, TOR signalling and VAP/VAP(P58S) expression levels would contribute to the extent of aggregation, and may act as regulatory feedback loops to regulate physiological ROS levels. SOD1, VAP/ALS8, TOR and ROS appear to be part of physiological regulatory circuit that maintains levels of VAP(P58S) aggregates.

Materials & Methods

Generation of constructs and dsRNA: The cDNA sequence of VAP and VAP(P58S) mutant were cloned into *pRM-GFP* plasmid (Bhaskar et al. 2000) to generate both N and C-terminal GFP fusions, using the *EcoR1* restriction site. The pRM-GFP vector has GFP cloned into pRM-HA3 vector at the *BamHI* site. dsRNA for the secondary screen was generated using MEGAscript® T7 Kit (AM1333) by ThermoFisher Scientific. Template for dsRNA was generated by using cDNA as template, prepared from flies. Primers for the dsRNA and site-directed mutagenesis (Chapter-III) were ordered from Sigma-Aldrich.

Handling of Schneider cells: *Drosophila* S2R+ cells, a kind gift from Dr. Satyajit Mayor, NCBS, Bangalore, were maintained in Schneider cell Media (#21720-024; GIBCO) with 10% Heat inactivated Fetal Bovine Serum (FBS, #10270; GIBCO). Batches of cells were frozen in 10% DMSO (D2650; Sigma) and stored in liquid nitrogen as per the DRSC protocol (http://www.flyrnai.org/DRSC-PRC.html). After reviving, cells were used for 25-30 passages before discarding. Cells were incubated at 23° C, and passaged every 4 days at a ratio of 1:5.

Cell culture and generation of S2R+ stable lines: Stable S2R+ cell lines were generated by co-transfecting with pRM-HA3 constructs of VAP:GFP, VAP(P58S):GFP or GFP along with pCo-Hygro in 20:1 ratio, using Effectene (QIAGEN) and/or Mirus TransIT 2020 (MIR 5400), and selected under 250 µg/ml of hygromycin (Sigma) for 10-15 passages. Stable as well as transiently transfected cell lines were induced to express the gene of interest under a metallothionein promoter using increasing concentrations 250µM, 500µM, 750µM and 1000µM of copper sulphate and analysed at 12, 24, 36 and 48 hours post induction. Transient transfections assays were performed using Mirus TransIT-2020 (MIR 5400) transfection reagent. Protocol for dsRNA knockdown assay was modified from (Rogers and Rogers 2008). Briefly, the cells were treated with dsRNA for 48 hours, induced with 500µM $CuSO_4$ for 24 hours, and then processed further for imaging or western blotting (Appendix 1, 2). Fixation with 4% paraformaldehyde, DAPI staining and imaging

was done using EVOS FL Auto Cell Imaging system. Super-resolution images of fixed VAP:GFP and VAP(P58S):GFP cells were acquired using Leica SR GSD 3D system.

Western blotting: Cells were centrifuged at 604Xg for 5 minutes in Eppendorf 5414R centrifuge. The pellet was resuspended in 20 µl of supernatant and boiled with 1X SDS Dye at 95°C. Samples were centrifuged again at 12045Xg for 10 minutes. Whole cell lysates were separated by 12% SDS-PAGE and transferred onto 0.45 µm PVDF membrane (Millipore). Membranes were blocked for 1 hour in 5% skimmed milk in 1X TBS containing 0.1% Tween-20 at room temperature and probed with 1:10,000 diluted mouse anti-Tubulin (T6074; Sigma-Aldrich) and 1:5,000 diluted mouse anti-GFP (Roche life science), overnight at 4 °C (12 hours). Anti-rabbit and anti-mouse secondary antibodies conjugated to horseradish peroxide (Pierce) were used at a dilution of 1:10,000 for 1 hour at room temperature. Blots were developed with Immobilon Chemiluminescent Substrate (LuminataClassico Western HRP substrate from Millipore) using a LAS4000 Fuji imaging System.

S2R+ cell culture imaging and analysis: Cell culture images were taken using 20x air objective DAPI (405nm) and GFP (488nm) channels to image nuclei and GFP-tagged protein/aggregates in each field, respectively, using EVOS F L Auto Cell Imaging system. DAPI and GFP channel images were processed using ImageJ 1.48V. Macro scripts were recorded to quantify total number of cells and number of cells showing aggregates. Total number of cells were quantified by converting DAPI channel image to 8-bit, subtracting the measured mean intensity to remove background, converting greyscale to Binary, using watershed function for segmentation, and analyzing particles of size 10-500 and circularity 1. Number of cells showing aggregates were quantified by converting the GFP channel image to 8-bit. Rolling ball background subtraction with 0.3 radius was used to integrate aggregates belonging to the same cell, based on proximity, as one object; the image was converted to Binary, and objects of size 10-500 were counted using "analyze particles" tool.

GO analysis: The list of genes and Gene Ontology (GO) information was obtained based on Flybase (http://flybase.org) (Marygold et al., 2013) entries. Genes were categorized manually in the broad categories of ALS genes, VAP interactome (Deivasigamani et al. 2014) and proteostasis. List of ALS loci and ALS related genes were obtained from http://alsod.iop.kcl.ac.uk/ (Wroe et al., 2008). The *Drosophila melanogaster* homologs of these ALS genes were identified using Ensembl biomart tool (http://asia.ensembl.org/biomart/martview) and Flybase batch download

tool. Human orthologs of the target genes listed in Table 1 and 2 were identified using Flybase batch download tool.

Fly husbandry and brain aggregation assay: *Drosophila melanogaster* lines were maintained on standard corn meal agar medium. *UAS-GAL4* system (Brand and Perrimon 1993) was used for overexpression of transgenes. *UAS-VAP* wildtype, *UAS-VAP(P58S)* and *C155-GAL4* lines used for fly experiments have been described earlier (Ratnaparkhi et al. 2008b; Deivasigamani et al. 2014). Canton S flies were used as wildtype control. *UAS-VAP_i* (27312), *UAS-SOD1_i* (34616, 29389, 36804), *UAS-TOR_i* (35578) and *UAS-Sesn_i* (64027) where the suffix 'I' indicates an RNAi line, and *UAS-SOD1* (24750, 33605) and *UAS-FOXO:GFP* (43633) were obtained from Bloomington *Drosophila* Stock Centre (BDSC). Clones for *UAS-SOD1-HA:FLAG* and *UAS-PPIase-HA:FLAG* (Chapter III) in pUASt vector were obtained for expression in *Drosophila* from DGRC and injected in the NCBS-CCAMP transgenic facility. *MS1096-GAL4* was used to express and validate the transgenic PPIases lines by immunostaining the wing imaginal disks with anti-HA (Alexa Fluor 594 conjugated) antibody (A-21288, ThermoFisher Scientific) and imaging using fluorescent microscopy (Chapter III). Flies for knockdown of Sestrin (v38481) and PPIases (v104316, CG13892; v108775, CG11777; v4991, CG5482; v108489, CG11858- Chapter III) were obtained from Vienna *Drosophila* Research Center (VDRC) *UAS-Atg1* line was kindly provided by Dr. Chen, Academia Sinica. The line was validated in the wing and thorax using *ptc-GAL4* as described (Chen et al. 2008). Briefly, expression of the Atg1 in the *ptc* domain results in missing anterior cross veins (acv) and loss of thoracic bristles. Additionally, expression of Atg1 using *actin-GAL4* also caused early lethality. Atg1 overexpression in the larval brain using BDSC (51654) has been shown to increase LysoTracker staining in the larval brain hemisphere indicating an activation of autophagy (Shen and Ganetzky 2009). The readout of autophagy in our experiments is thus indirect and not based on specific cellular markers. All fly lines are listed in Appendix 5. For all genetic crosses, experiments were set at 18°C, 25°C or 28°C, as indicated. Brains were dissected from third instar larvae and processed for immunostaining assay. 4% paraformaldehyde containing 0.1% Triton-X was used for fixation followed by washes with 1X PBS. Blocking treatment and washes were performed with 0.3% Triton-X with 2% BSA. Brains were stained with 1:500 diluted anti-VAP antibody (Yadav et al. 2018) and 1:1000 anti-rabbit secondary (Invitrogen) was used. Z-stacks of five-ten brains for each sample were imaged under 63X oil objective of Ziess LSM 710 Confocal Microscope. 16-bit images of 1024X1024 pixels

were taken at 90µm pinhole size. The number of aggregates were quantified per cubic micron of the ventral nerve cord, defined as "aggregation density" using the Huygen professional software. The high intensity puncta were considered as aggregates. A single arbitrary threshold was set for controls as well as for test samples that achieved removing low intensity background signal emitted by the tissue, along with separation of high intensity puncta that were adjacent to one another. An object filter was used to remove objects of size greater than 1000 pixels and garbage size smaller than 10 pixels was excluded. Three 3D region of interests of fixed size were drawn along the tip of the ventral nerve cord and the number of aggregates were counted from each of these ROIs and averaged for each animal. The volume (in cubic micron) of ROI depicting the thickness of the brain tissue was measured as the range of the z-stack of the image. The aggregation density obtained for each brain has been normalised to the mean of the control group, *C155-GAL4; UAS-VAP(P58S)* (+ 0.25% DMSO, in case of DMSO-soluble drug experiments) and plotted as "normalized aggregation density" in each graph. Student t-test and one-way ANOVA with Fisher's LSD multiple comparison test were used to measure statistical significance using GraphPad Prism 7.

Drug treatment: For Chapter III, drug treatment assays were standardized in house for PPIase inhibiting drugs, 10µm cyclosporine A (C3662, Sigma-Aldrich), 1µm FK506 (F4679, Sigma-Aldrich) and 5µm parvulin inhibitor (B7688, Sigma-Aldrich). The drugs were dissolved and diluted in DMSO. Cells were exposed to a final concentration of 0.2% DMSO. Fixation, DAPI staining and imaging was done using EVOS FL Auto Cell Imaging system. For flies, 10-12 virgins were mated with CS males, for each genotype and animals were allowed to mate for 24 hours and transferred to standard cornmeal fly media containing 5mM paraquat (36541, Sigma-Aldrich), 5µM MG132 (M8699, Sigma-Aldrich), 200nM rapamycin (PHZ1235, Invitrogen) or DMSO (0.25%).

Oxyblot assay: Third instar larval brains were lysed in RIPA containing 50 mM DTT and centrifuged at 10000 rcf. The lysate containing 10µg of protein was incubated with 2,4-dinitrophenylhydrazine (DNPH) to derivatize the carbonyl groups of oxidized proteins with 2,4-dinitrophenylhydrazone (DNP-hydrazone) as described by the Oxyblot Protein Oxidation Detection Kit (S7150) from EMD Milipore. The derivatized protein lysate was separated on a 12% SDS-PAGE and transferred onto 0.45 µm PVDF membrane (Millipore). Oxidized protein levels

in the lysate were detected by probing with anti-DNP antibody on western blot as per the Oxyblot Protein Oxidation Detection Kit manual.

Lipid extraction and targeted LC-MS lipidomics: All MS quantitation phospholipid standards were purchased from Avanti Polar Lipids Inc., USA. The brain samples were washed with PBS (x 3 times), and transferred into a glass vial using 1 mL PBS. 3 mL of 2:1 (vol/vol) $CHCl_3$: MeOH with the internal standard mix (1 nmol 17:1 FFA, 100 pmol each of 17:0-20:4 PS, 17:0-20:4 PC, 17:0-20:4 PE, and 17:0-20:4 PA) was added, and the mixture was vigorously vortexed. The two phases were separated by centrifugation at 2800 x g for 5 minutes. The organic phase (bottom) was removed, 50 µL of formic acid was added to acidify the aqueous homogenate (to enhance extraction of phospholipids), and $CHCl_3$ was added to make up 4 mL volume. The mixture was vortexed, and separated using centrifugation described above. Both the organic extracts were pooled, and dried under a stream of N_2. The lipidome was re-solubilized in 200 µL of 2:1 (vol/vol) $CHCl_3$: MeOH, and 20 µL was used for the targeted LC-MS analysis All the phospholipid species analyzed in this study were quantified using the multiple reaction monitoring high resolution (MRM-HR) scanning method on a Sciex X500R QTOF LC-MS with an Exion-LC series quaternary pump. All data was acquired and analysed using the SciexOS software as described before (Pathak et al. 2018). The LC separation was achieved using a Gemini 5U C-18 column (Phenomenex, 5 µm, 50 x 4.6 mm) coupled to a Gemini guard column (Phenomenex, 4 x 3 mm, Phenomenex security cartridge). The LC solvents were: For positive mode: buffer A: 95:5 (vol/vol) H_2O: MeOH + 0.1% formic acid + 10 mM ammonium formate; and buffer B: 60:35:5 (vol/vol) iPrOH: MeOH: H_2O + 0.1% formic acid + 10 mM ammonium formate, For Negative mode: buffer A: 95:5 (vol/vol) H_2O: MeOH + 0.1% ammonium hydroxide; and buffer B: 60:35:5 (vol/vol) iPrOH: MeOH: H_2O + 0.1% ammonium hydroxide. All the MS based lipid estimations was performed using an electrospray ion source, using the following MS parameters: ion source = turbo spray, collision gas = medium, curtain gas = 20 L/min, ion spray voltage = 4500 V, temperature = 400 ^{o}C. A typical LC-run consisted of 55 minutes, with the following solvent run sequence post injection: 0.3 ml/min 0% buffer B for 5 minutes, 0.5 ml/min 0% buffer B for 5 minutes, 0.5 ml/min linear gradient of buffer B from 0 – 100% over 25 minutes, 0.5 ml/min of 100% buffer B for 10 minutes, and re-equilibration with 0.5 ml/min of 0% buffer B for 10 minutes. A detailed list of all the species targeted in this MRM study, describing the precursor parent ion mass and adduct, the product ion targeted can be found in Appendix 6. All the endogenous lipid

species were quantified by measuring the area under the curve in comparison to the respective internal standard, and then normalizing to the number of larval brains. All oxidized phospholipids detected were normalized to the corresponding non-oxidized phospholipid internal standard. All the data is represented as mean ± s. e. m. of at least 4 biological replicates per genotype.

mRNA isolation, cDNA preparation and qRT PCR: About 1 µg of mRNA was isolated from 12-18 third instar larval brains using Direct-zol™ RNA MicroPrep Kit (R2062) from Zymo Research. The cDNA reaction was carried out using High Capacity cDNA Reverse Transcriptase Kit (4368814) by Applied Biosystems. The qPCR reaction was carried out using KAPA SYBR FAST (KK4602) by Sigma using Replex Mastercycler by Eppendorf. A two-step protocol with denaturation at 95℃ for 15 seconds and annealing/amplification at 60℃ for 30 seconds was performed, with a prior denaturation at 95℃ for 2 minutes. Standard melt curve analysis was performed. The experiment was carried out in three biological replicates with technical triplicates. VAP forward primer: CCAGCGAGGATAAGTTTAAGCC; reverse primer: CGAGCTCCGGAAACGTGTGA. SOD1 forward primer: TGAAGGTCTCCGGTGAGGTGT; reverse primer: AGCGCCATGCTCCTTGCCATA.

Regulatory oversight: All experimental protocols were considered and approved by the IISER Institutional Biosafety Committee (IBSC). The IBSC is overseen by the Review Committee on Genetic Manipulation (RCGM), Department of Biotechnology, Government of India.

Data Availability: All raw images related to the S2R+ screen as well as the larval brain data are available with the authors on request. The raw images of the S2R+ screen are also uploaded in the EBI Biostudies database (https://www.ebi.ac.uk/biostudies) with the study number S-BSST211.

Contributions

The S2R+ screen was carried out as a paid service at the NCBS:C-CAMP high throughput screening facility. Lokesh Pimpale, a BS-MS student in the laboratory travelled to NCBS-TIFR to set up and oversee the screen in Bangalore. A version of the screen with a different methodology for analysis has been described in Lokesh's thesis (Pimpale, 2015). The analysis of the screen was carried out by by Dr. Balaji Ramalingam (Oxford Nanoimaging Ltd.) using custom MATLAB programs that he developed. The Mass Spectrometry experiments that relate

to the quantitative measurement of oxidized lipids were suggested by and carried out under the supervision of Dr. Siddhesh Kamat.

Acknowledgements

At NCBS, we thank MS Shahab Uddin, Lokavya Kurup and Vandana for technical assistance during the execution of the screen; Kausik Chakraborty, IGIB for advice on the analysis of the screen. We thank Bloomington *Drosophila* Stock Center (BDSC), Indiana, supported by NIH grant P40OD018537, for fly stocks; *Drosophila* Genome Research Centre (DGRC), Indiana supported by NIH grant 2P40OD010949 for vectors and clones; TRiP collection at Harvard Medical School (NIH/NIGMS R01-GM084947) for providing transgenic RNAi fly stocks. We thank IISER Microscopy/Confocal Facility and Dr. Nagaraj Balasubramaniam for access to the EVOS system. Shubham Singh and Shabnam Patil are thanked for technical assistance with the mass spectrometry experiments.

References

Alpy F, Rousseau A, Schwab Y, et al (2013) STARD3 or STARD3NL and VAP form a novel molecular tether between late endosomes and the ER. J Cell Sci 126:5500 LP-5512. doi: 10.1242/jcs.139295

Anagnostou G, Akbar MT, Paul P, et al (2010) Vesicle associated membrane protein B (VAPB) is decreased in ALS spinal cord. Neurobiol Aging 31:969–85. doi: 10.1016/j.neurobiolaging.2008.07.005

Andersen PM, Al-Chalabi A (2011) Clinical genetics of amyotrophic lateral sclerosis: what do we really know? Nat Rev Neurol 7:603–15. doi: 10.1038/nrneurol.2011.150

Barber SC, Mead RJ, Shaw PJ (2006) Oxidative stress in ALS: a mechanism of neurodegeneration and a therapeutic target. Biochim Biophys Acta 1762:1051–1067. doi: 10.1016/j.bbadis.2006.03.008

Baron Y, Pedrioli PG, Tyagi K, et al (2014) VAPB/ALS8 interacts with FFAT-like proteins including the p97 cofactor FAF1 and the ASNA1 ATPase. BMC Biol 12:39. doi: 10.1186/1741-7007-12-39

Bhaskar V, Valentine SA, Courey AJ (2000) A functional interaction between dorsal and components of the Smt3 conjugation machinery. J Biol Chem 275:4033–4040

Brand AH, Perrimon N (1993) Targeted Gene-Expression as a Means of Altering Cell Fates and Generating Dominant Phenotypes. Development 118:401–415

Castello PR, Drechsel DA, Patel M (2007) Mitochondria are a major source of paraquat-induced reactive oxygen species production in the brain. J Biol Chem 282:14186–14193. doi: 10.1074/jbc.M700827200

Cavanaugh JE, Jaumotte JD, Lakoski JM, Zigmond MJ (2006) Neuroprotective role of ERK1/2 and ERK5 in a dopaminergic cell line under basal conditions and in response to oxidative stress. J Neurosci Res 84:1367–1375. doi: 10.1002/jnr.21024

Chai A, Withers J, Koh YH, et al (2008) hVAPB, the causative gene of a heterogeneous group of motor neuron diseases in humans, is functionally interchangeable with its Drosophila homologue DVAP-33A at the neuromuscular junction. Hum Mol Genet 17:266–280. doi:

10.1093/hmg/ddm303

Chen G-C, Lee JY, Tang H-W, et al (2008) Genetic interactions between *Drosophila melanogaster* Atg1 and paxillin reveal a role for paxillin in autophagosome formation. Autophagy 4:37–45. doi: 10.4161/auto.5141

Cleveland DW, Rothstein JD (2001) From charcot to lou gehrig: deciphering selective motor neuron death in als. Nat Rev Neurosci 2:806

Cluskey S, Ramsden DB, Hospital E (2001) Mechanisms of neurodegeneration in amyotrophic lateral sclerosis. 386–392

Cocheme HM, Quin C, McQuaker SJ, et al (2011) Measurement of H2O2 within living Drosophila during aging using a ratiometric mass spectrometry probe targeted to the mitochondrial matrix. Cell Metab 13:340–350. doi: 10.1016/j.cmet.2011.02.003

De Vos KJ, Mórotz GM, Stoica R, et al (2012) VAPB interacts with the mitochondrial protein PTPIP51 to regulate calcium homeostasis. Hum Mol Genet 21:1299–311. doi: 10.1093/hmg/ddr559

Deivasigamani S, Verma HK, Ueda R, et al (2014) A genetic screen identifies Tor as an interactor of VAPB in a Drosophila model of amyotrophic lateral sclerosis. Biol Open 3:1127–38. doi: 10.1242/bio.201410066

Demontis F, Perrimon N (2010) FOXO/4E-BP signaling in Drosophila muscles regulates organism-wide proteostasis during aging. Cell 143:813–825. doi: 10.1016/j.cell.2010.10.007

Deng HX, Hentati A, Tainer JA, et al (1993) Amyotrophic lateral sclerosis and structural defects in Cu,Zn superoxide dismutase. Science (80-) 261:1047 LP-1051. doi: 10.1126/science.8351519

Drechsel DA, Patel M (2009) Differential contribution of the mitochondrial respiratory chain complexes to reactive oxygen species production by redox cycling agents implicated in parkinsonism. Toxicol Sci 112:427–434. doi: 10.1093/toxsci/kfp223

Echeverri CJ, Perrimon N (2006) High-throughput RNAi screening in cultured cells: a user's

guide. Nat Rev Genet 7:373–384. doi: 10.1038/nrg1836

Ernst WL, Shome K, Wu CC, et al (2016) VAMP-associated Proteins (VAP) as Receptors That Couple Cystic Fibrosis Transmembrane Conductance Regulator (CFTR) Proteostasis with Lipid Homeostasis. J Biol Chem 291:5206–5220. doi: 10.1074/jbc.M115.692749

Genevini P, Papiani G, Ruggiano A, et al (2014) Amyotrophic lateral sclerosis-linked mutant VAPB inclusions do not interfere with protein degradation pathways or intracellular transport in a cultured cell model. PLoS One 9:. doi: 10.1371/journal.pone.0113416

Gkogkas C, Middleton S, Kremer AM, et al (2008) VAPB interacts with and modulates the activity of ATF6. Hum Mol Genet 17:1517–1526. doi: 10.1093/hmg/ddn040

Gomez-Suaga P, Paillusson S, Miller CCJ (2017a) ER-mitochondria signaling regulates autophagy. Autophagy 13:1250–1251. doi: 10.1080/15548627.2017.1317913

Gomez-Suaga P, Paillusson S, Stoica R, et al (2017b) The ER-Mitochondria Tethering Complex VAPB-PTPIP51 Regulates Autophagy. Curr Biol 27:371–385. doi: 10.1016/j.cub.2016.12.038

Han SM, El Oussini H, Scekic-Zahirovic J, et al (2013) VAPB/ALS8 MSP ligands regulate striated muscle energy metabolism critical for adult survival in caenorhabditis elegans. PLoS Genet 9:e1003738. doi: 10.1371/journal.pgen.1003738

Hay N (2011) Interplay between FOXO, TOR, and Akt. Biochim Biophys Acta - Mol Cell Res 1813:1965–1970. doi: 10.1016/j.bbamcr.2011.03.013

Heitman J, Movva NR, Hall MN (1991) Targets for cell cycle arrest by the immunosuppressant rapamycin in yeast. Science (80-) 253:905–909

Huttlin EL, Ting L, Bruckner RJ, et al (2015) The BioPlex Network: A Systematic Exploration of the Human Interactome. Cell 162:425–440. doi: https://doi.org/10.1016/j.cell.2015.06.043

Kamat SS, Camara K, Parsons WH, et al (2015) Immunomodulatory lysophosphatidylserines are regulated by ABHD16A and ABHD12 interplay. Nat Chem Biol 11:164–171. doi: 10.1038/nchembio.1721

Kanekura K, Nishimoto I, Aiso S, Matsuoka M (2006) Characterization of amyotrophic lateral sclerosis-linked P56S mutation of vesicle-associated membrane protein-associated protein B (VAPB/ALS8). J Biol Chem 281:30223–33. doi: 10.1074/jbc.M605049200

Kim JY, Jang A, Reddy R, et al (2016) Neuronal overexpression of human VAPB slows motor impairment and neuromuscular denervation in a mouse model of ALS. Hum Mol Genet 25:4661–4673. doi: 10.1093/hmg/ddw294

Kory N, Grond S, Kamat SS, et al (2017) Mice lacking lipid droplet-associated hydrolase, a gene linked to human prostate cancer, have normal cholesterol ester metabolism. J Lipid Res 58:226–235. doi: 10.1194/jlr.M072538

Kuijpers M, van Dis V, Haasdijk ED, et al (2013) Amyotrophic lateral sclerosis (ALS)-associated VAPB-P56S inclusions represent an ER quality control compartment. Acta Neuropathol Commun 1:24. doi: 10.1186/2051-5960-1-24

Lee JH, Budanov A V, Park EJ, et al (2010) Sestrin as a feedback inhibitor of TOR that prevents age-related pathologies. Science (80-) 327:1223–1228. doi: 10.1126/science.1182228

Lev S, Halevy D Ben, Peretti D, Dahan N (2008) The VAP protein family: from cellular functions to motor neuron disease. Trends Cell Biol 18:282–290. doi: 10.1016/j.tcb.2008.03.006

Loewen CJ, Roy A, Levine TP (2003) A conserved ER targeting motif in three families of lipid binding proteins and in Opi1p binds VAP. EMBO J 22:2025–2035. doi: 10.1093/emboj/cdg201

Mandrioli J, D'Amico R, Zucchi E, et al (2018) Rapamycin treatment for amyotrophic lateral sclerosis. Medicine (Baltimore) 97:e11119. doi: 10.1097/MD.0000000000011119

Metz J, Castro IG, Schrader M (2017) Peroxisome Motility Measurement and Quantification Assay. Bio Protoc 7:. doi: 10.21769/BioProtoc.2536

Milton VJ, Jarrett HE, Gowers K, et al (2011) Oxidative stress induces overgrowth of the Drosophila neuromuscular junction. Proc Natl Acad Sci 108:17521–17526. doi: 10.1073/pnas.1014511108

Mitne-Neto M, Ramos CR, Pimenta DC, et al (2007) A mutation in human VAP-B--MSP domain, present in ALS patients, affects the interaction with other cellular proteins. Protein Expr Purif 55:139–146. doi: S1046-5928(07)00096-4 [pii]10.1016/j.pep.2007.04.007

Mizushima N, Komatsu M (2011) Autophagy: renovation of cells and tissues. Cell 147:728–741. doi: 10.1016/j.cell.2011.10.026

Moujalled D, Grubman A, Acevedo K, et al (2017) TDP-43 mutations causing amyotrophic lateral sclerosis are associated with altered expression of RNA-binding protein hnRNP K and affect the Nrf2 antioxidant pathway. Hum Mol Genet 26:1732–1746. doi: 10.1093/hmg/ddx093

Moustaqim-barrette A, Lin YQ, Pradhan S, et al (2014) The amyotrophic lateral sclerosis 8 protein, VAP, is required for ER protein quality control. Hum Mol Genet 23:1975–1989. doi: 10.1093/hmg/ddt594

Mulligan VK, Chakrabartty A (2013) Protein misfolding in the late-onset neurodegenerative diseases: Common themes and the unique case of amyotrophic lateral sclerosis. Proteins Struct Funct Bioinforma 81:1285–1303. doi: 10.1002/prot.24285

Murphy SE, Levine TP (2016) VAP, a Versatile Access Point for the Endoplasmic Reticulum: Review and analysis of FFAT-like motifs in the VAPome. Biochim Biophys Acta - Mol Cell Biol Lipids 1861:952–961. doi: 10.1016/j.bbalip.2016.02.009

Nishimura AL, Mitne-neto M, Silva HCA, et al (2004) A Mutation in the Vesicle-Trafficking Protein VAPB Causes Late-Onset Spinal Muscular Atrophy and Amyotrophic Lateral Sclerosis. 2:822–831

Noda T, Ohsumi Y (1998) Tor, a phosphatidylinositol kinase homologue, controls autophagy in yeast. J Biol Chem 273:3963–3966. doi: 10.1074/jbc.273.7.3963

Ogrodnik M, Salmonowicz H, Brown R, et al (2014) Dynamic JUNQ inclusion bodies are asymmetrically inherited in mammalian cell lines through the asymmetric partitioning of vimentin. Proc Natl Acad Sci U S A 111:8049–8054. doi: 10.1073/pnas.1324035111

Paillusson S, Gomez-Suaga P, Stoica R, et al (2017) α-Synuclein binds to the ER–mitochondria tethering protein VAPB to disrupt Ca2+ homeostasis and mitochondrial ATP production.

Acta Neuropathol 134:129–149. doi: 10.1007/s00401-017-1704-z

Papiani G, Ruggiano A, Fossati M, et al (2012) Restructured endoplasmic reticulum generated by mutant amyotrophic lateral sclerosis-linked VAPB is cleared by the proteasome. J Cell Sci 125:3601–3611. doi: 10.1242/jcs.102137

Pathak D, Mehendale N, Singh S, et al (2018) Lipidomics Suggests a New Role for Ceramide Synthase in Phagocytosis. ACS Chem Biol 13:2280–2287. doi: 10.1021/acschembio.8b00438

Pennetta G, Hiesinger PR, Fabian-Fine R, et al (2002) Drosophila VAP-33A directs bouton formation at neuromuscular junctions in a dosage-dependent manner. Neuron 35:291–306

Perluigi M, Di Domenico F, Butterfield DA (2015) mTOR signaling in aging and neurodegeneration: At the crossroad between metabolism dysfunction and impairment of autophagy. Neurobiol Dis 84:39–49. doi: 10.1016/j.nbd.2015.03.014

Pimpale L (2015) A high throughput RNAi screen to identify modifiers of ALS8 aggregation using automated computational image analysis. Master's thesis, IISER Pune

Prause J, Goswami A, Katona I, et al (2013) Altered localization, abnormal modification and loss of function of Sigma receptor-1 in amyotrophic lateral sclerosis. Hum Mol Genet 22:1581–1600. doi: 10.1093/hmg/ddt008

Qiu L, Qiao T, Beers M, et al (2013) Widespread aggregation of mutant VAPB associated with ALS does not cause motor neuron degeneration or modulate mutant SOD1 aggregation and toxicity in mice. Mol Neurodegener 8:1. doi: 10.1186/1750-1326-8-1

Ratnaparkhi A, Lawless GM, Schweizer FE, et al (2008a) A Drosophila model of ALS: Human ALS-associated mutation in VAP33A suggests a dominant negative mechanism. PLoS One 3:e2334. doi: 10.1371/journal.pone.0002334

Ratnaparkhi A, Lawless GM, Schweizer FE, et al (2008b) A Drosophila Model of ALS: Human ALS-Associated Mutation in VAP33A Suggests a Dominant Negative Mechanism. PLoS One 3:e2334. doi: 10.1371/journal.pone.0002334

Ravikumar B, Vacher C, Berger Z, et al (2004) Inhibition of mTOR induces autophagy and

reduces toxicity of polyglutamine expansions in fly and mouse models of Huntington disease. Nat Genet 36:585–595. doi: 10.1038/ng1362

Rogers SL, Rogers GC (2008) Culture of Drosophila S2 cells and their use for RNAi-mediated loss-of-function studies and immunofluorescence microscopy. Nat Protoc 3:606–611. doi: 10.1038/nprot.2008.18

Rosen DR, Siddique T, Patterson D, et al (1993) Mutations in Cu/Zn superoxide dismutase gene are associated with familial amyotrophic lateral sclerosis. Nature 362:59

Rousseau A, Bertolotti A (2016) An evolutionarily conserved pathway controls proteasome homeostasis. Nature 536:184–189. doi: 10.1038/nature18943

Saccon RA, Bunton-Stasyshyn RKA, Fisher EMC, Fratta P (2013) Is SOD1 loss of function involved in amyotrophic lateral sclerosis? Brain 136:2342–2358. doi: 10.1093/brain/awt097

Sanhueza M, Chai A, Smith C, et al (2015) Network Analyses Reveal Novel Aspects of ALS Pathogenesis. PLoS Genet 11:1–32. doi: 10.1371/journal.pgen.1005107

Shen W, Ganetzky B (2009) Autophagy promotes synapse development in. 187:71–79. doi: 10.1083/jcb.200907109

Spilman P, Podlutskaya N, Hart MJ, et al (2010) Inhibition of mTOR by rapamycin abolishes cognitive deficits and reduces amyloid-β levels in a mouse model of alzheimer's disease. PLoS One 5:1–8. doi: 10.1371/journal.pone.0009979

Stoica R, De Vos KJ, Paillusson S, et al (2014) ER-mitochondria associations are regulated by the VAPB-PTPIP51 interaction and are disrupted by ALS/FTD-associated TDP-43. Nat Commun 5:3996. doi: 10.1038/ncomms4996

Stoica R, Paillusson S, Gomez-Suaga P, et al (2016) ALS/FTD-associated FUS activates GSK-3β to disrupt the VAPB–PTPIP51 interaction and ER–mitochondria associations. EMBO Rep 17:1326–1342. doi: 10.15252/embr.201541726

Su C, Sun F, Cunningham RL, et al (2014) ERK5/KLF4 signaling as a common mediator of the neuroprotective effects of both nerve growth factor and hydrogen peroxide preconditioning. Age 36:9685. doi: 10.1007/s11357-014-9685-5

Sun X, Komatsu T, Lim J, et al (2012) Nutrient-dependent requirement for SOD1 in lifespan extension by protein restriction in Drosophila melanogaster. Aging Cell 11:783–793. doi: 10.1111/j.1474-9726.2012.00842.x

Tarasiuk J, Kułakowska A, Drozdowski W, et al (2012) CSF markers in amyotrophic lateral sclerosis. J Neural Transm 119:747–757. doi: 10.1007/s00702-012-0806-y

Taylor JP, Brown RH, Cleveland DW (2016) Decoding ALS: From genes to mechanism. Nature 539:197–206. doi: 10.1038/nature20413

Teuling E, Ahmed S, Haasdijk E, et al (2007) Motor neuron disease-associated mutant vesicle-associated membrane protein-associated protein (VAP) B recruits wild-type VAPs into endoplasmic reticulum-derived tubular aggregates. J Neurosci 27:9801–15. doi: 10.1523/JNEUROSCI.2661-07.2007

Tsang CK, Chen M, Cheng X, et al (2018) SOD1 Phosphorylation by mTORC1 Couples Nutrient Sensing and Redox Regulation. Mol Cell 70:502–515 e8. doi: 10.1016/j.molcel.2018.03.029

Tsuda H, Han SM, Yang Y, et al (2008) The Amyotrophic Lateral Sclerosis 8 Protein VAPB Is Cleaved, Secreted, and Acts as a Ligand for Eph Receptors. Cell 133:963–977. doi: 10.1016/j.cell.2008.04.039

Tudor EL, Galtrey CM, Perkinton MS, et al (2010) Amyotrophic lateral sclerosis mutant vesicle-associated membrane protein-associated protein-B transgenic mice develop TAR-DNA-binding protein-43 pathology. Neuroscience 167:774–85. doi: 10.1016/j.neuroscience.2010.02.035

Turner BJ, Baumer D, Parkinson NJ, et al (2008) TDP-43 expression in mouse models of amyotrophic lateral sclerosis and spinal muscular atrophy. BMC Neurosci 9:104. doi: 10.1186/1471-2202-9-104

Turner MR, Hardiman O, Benatar M, et al (2013) Controversies and priorities in amyotrophic lateral sclerosis. Lancet Neurol 12:310–322. doi: https://doi.org/10.1016/S1474-4422(13)70036-X

Tyurina YY, Shvedova AA, Kawai K, et al (2000) Phospholipid signaling in apoptosis:

peroxidation and externalization of phosphatidylserine. Toxicology 148:93–101. doi: 10.1016/S0300-483X(00)00199-2

van Blitterswijk M, van Es M a, Hennekam E a M, et al (2012a) Evidence for an oligogenic basis of amyotrophic lateral sclerosis. Hum Mol Genet 21:3776–84. doi: 10.1093/hmg/dds199

van Blitterswijk M, van Es M a, Koppers M, et al (2012b) VAPB and C9orf72 mutations in 1 familial amyotrophic lateral sclerosis patient. Neurobiol Aging 33:2950.e1-4. doi: 10.1016/j.neurobiolaging.2012.07.004

Walker AK, Atkin JD (2011) Stress signaling from the endoplasmic reticulum: A central player in the pathogenesis of amyotrophic lateral sclerosis. IUBMB Life 63:754–63. doi: 10.1002/iub.520

Wu D, Hao Z, Ren H, Wang G (2018) Loss of VAPB Regulates Autophagy in a Beclin 1-Dependent Manner. Neurosci Bull. doi: 10.1007/s12264-018-0276-9

Yadav S, Thakur R, Georgiev P, et al (2018) RDGBα localization and function at membrane contact sites is regulated by FFAT–VAP interactions. J Cell Sci 131:jcs207985. doi: 10.1242/jcs.207985

Zhan L, Xie Q, Tibbetts RS (2015) Opposing roles of p38 andJNKin a Drosophila model of TDP-43 proteinopathy reveal oxidative stress and innate immunity as pathogenic components of neurodegeneration. Hum Mol Genet 24:757–772. doi: 10.1093/hmg/ddu493

Zhang S, Binari R, Zhou R, Perrimon N (2010) A genomewide RNA interference screen for modifiers of aggregates formation by mutant huntingtin in drosophila. Genetics 184:1165–1179. doi: 10.1534/genetics.109.112516

Zhao J, Zhai B, Gygi SP, Goldberg AL (2015) mTOR inhibition activates overall protein degradation by the ubiquitin proteasome system as well as by autophagy. Proc Natl Acad Sci 112:15790–15797. doi: 10.1073/pnas.1521919112

Zhao YG, Liu N, Miao G, et al (2018) The ER Contact Proteins VAPA/B Interact with Multiple Autophagy Proteins to Modulate Autophagosome Biogenesis. Curr Biol 1–12. doi: 10.1016/j.cub.2018.03.002

Chapter III

Peptidyl-Prolyl Isomerases modify protein aggregation in a *Drosophila* model of VAP-B/ALS8 associated Amyotrophic Lateral Sclerosis

Summary

Amyotrophic lateral sclerosis (ALS), also called "Lou Gehrig's disease" is a progressive, lethal neurodegenerative disease characterized by loss of motor neurons leading to gradual paralysis and death of the patient within 2-5 years post diagnosis. The disease can occur sporadically; or in 5-10% of the patients, the disease occurs due to inheritance of a mutation. A missense mutation (P56S) in the VAMP Associated Protein gene [VAPB/ALS8], a highly conserved gene is one such familial locus. *Drosophila* models of ALS8 have been generated that show that VAP(P58S) aggregates and recruits wildtype protein to these aggregates, eliciting a dominant negative effect.

The proline residue at the 56th position is present in the *cis*-conformation in human VAPB. This leads to the possibility that any change of a *cis* peptide bond to a *trans* peptide bond may be a central feature in ALS8 (P56S) aggregation. Aggregation of VAPB in neurons has been proposed to be either a cause or a consequence of mechanistic changes in the cell that lead to neuronal cell death. We are exploring the necessity for having a *cis*- conformation at the X-proline bond for the proper folding of VAP. Further, we attempt to identify the Peptidyl prolyl isomerase(s) in the cell that are responsible for aiding VAP fold to its correct conformation and that are may modify aggregation kinetics of the protein. Our study should provide insights into the mechanism and progression of the ALS8 in humans by identifying specific Peptidyl prolyl isomerase(s) which may also be potential drug targets.

Abbreviations: VAP: VAMP-associated protein B, PPIase: peptidyl-prolyl *cis-trans* isomerase, CsA: cyclosporine A, PiB: Parvulin inhibitor, FKBP: FK506-binding protein.

Introduction

VAPB in an integral membrane protein present on ER membrane, ER golgi intermediate compartment, mitochondrial-associated membrane and the plasma membrane. It has several important functions in the cell such as vesicular trafficking, ER structure maintenance, lipid biosynthesis, microtubule organization, mitochondrial mobility and calcium homeostasis (Lev et al. 2008) (Fig. 1B, Chapter II). The VAPB protein consists of three domains (Fig. 1A, Chapter II), the N-terminal Major Sperm Domain (MSP), the middle coiled coil domain (CCD) and the C-terminal transmembrane domain (TMD)(Nishimura et al. 1999). VAPB integrates into the membrane through the TMD, while forming homodimers or heterodimers with VAPA through interaction with the CCD. The MSP domain can interact with protein containing FFAT motifs that are involved in lipid biosynthesis and ceramide transport (Kaiser et al. 2005). The MSP domain can also be cleaved, secreted and act as a ligand for ephrin and Robo/Lar like receptors at the NMJ (Tsuda et al. 2008). The missense mutation, P56S, in VAPB disrupts several of these key functions displaying a loss-of-function phenotype. Furthermore, the mutation causes VAPB to misfold and form cellular aggregates in the disease (Fig. 1C, Chapter II).

These aggregates have been found to be ER localized and ubiquitinated, and have been shown to sequester the wild type protein, thereby acting in a dominant-negative manner (Teuling et al. 2007; Ratnaparkhi et al. 2008) (Fig. 1C, 1D, Chapter II). The mutation in the MSP domain causes the exposure and interaction of hydrophobic residues in the CCD and the TMD, resulting in the aggregation of the protein (Kim et al. 2010). Presence of aggregates has been linked to inhibition of unfolded protein response in the cell (Kanekura et al. 2006). In the fly model system, overexpressed mutant VAPB in the muscle, shows punctate localization while overexpressed wild type protein does not shows membrane localization (Ratnaparkhi et al. 2008).

The missense mutation in ALS8 is a substitution of a proline for a serine in the MSP domain. Loss of proline can severely affect the proper folding of protein. Proline is unique in its structure. It is the only amino acid wherein the side-chain is covalently bound to the main chain at the nitrogen atom forming a pentameric ring structure. Due to this arrangement, the hydrogen atom is unavailable for bond formation, which is required for stabilizing α-helices or β-sheets. Hence, proline is often found at turns and is responsible for bends or kinks in the peptide chain. Secondly, the pentameric side chain confers rigidity to the bond angles in the phi-psi plane such that it

becomes restricted to an angle of 60˚, limiting the number of conformations possible (Fig. 1A). Finally, in the folded state of the protein amino acids usually form thermodynamically stable peptide bonds only in *trans* conformation. However, proline can occur in both states, *cis* and *trans*. 5% of peptide bonds containing proline can be stably found in *cis* conformation (Lorenzen et al. 2005). The interconversion between *trans* and *cis* conformation of the proline containing peptide bond is a slow rate-limiting step in protein folding (Fig. 1B). In biological systems, a family of enzymes known as prolyl peptidyl *cis-trans* isomerases (PPIases) are responsible for its catalysis during protein folding and unfolding, as well as at exposed proline residues of folded proteins.

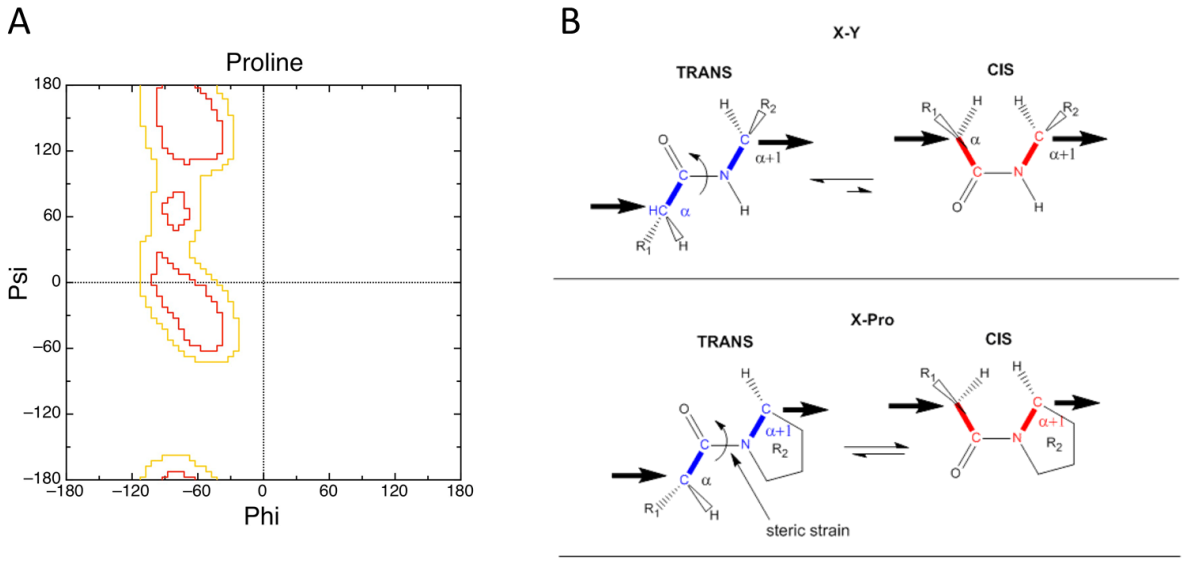

Figure 1: X-proline peptides exist in two extreme conformers
A. Ramachandran plot of peptide bond X-Pro depicting the restricted conformations possible in the psi-phi plane.
B. *Cis* and *trans* conformations of peptide bonds. The isomerization between *cis* and *trans* conformations for X-Pro bond is catalyzed by peptidyl prolyl isomerases.

Three different classes of prolyl isomerases are known and are classified based on their susceptibility to immunosuppressive drugs. Cyclosporine A (CsA) and FK506 (Harding et al. 1989) are fungal derived drugs that inhibit the PPIase activity of cyclophilins and FK506-binding proteins (FKBPs), respectively, by binding at their active sites. Parvulins are another class of PPIases that are not inhibited by immunosuppressive drugs and do not play a role in immunity. Drug complexes of CsA-cyclophilin A (Matsuda and Koyasu 2000) and FK506-FKBP12 were identified as inhibitors of the kinase, calcineurin, preventing the translocation of transcription factor, NFAT, thus suppressing immune reaction (Mukai et al. 1993). Although essentially similar

in enzymatic function, about 30 PPIases from all three classes are known to be conserved between humans and *Drosophila*. The simplest PPIases are small proteins that are mainly cytoplasmic or ER associated and composed entirely of the catalytic domain such as the cyclophilin domain or the FK506-binding domain or the rotamase in parvulin. The more complex PPIases consist of additional domains such as EF-hand domain, TPR domain, RRM domain, WD40 domain, E3 ligase domain or moca domain (Schiene-Fischer 2014). The presence of such domains confers variable properties to the protein such as differential localization, regulation and substrate specificity. PPIases have been found to be cytoplasmic, ER associated, nuclear as well as mitochondrial based on signal sequences and specific domain architecture (Pemberton and Kay 2005). These domains can aid by specifically binding to potential targets and bringing them in proximity of the active site for isomerization. Pin1, a well characterized parvulin, is known to recognize and act only upon targets phosphorylated at the WW motif present close to the target proline in the sequence (Lu et al. 2002). EF-hand of FKBP65 has been reported to act as a sensor for calcium release from ER stores and get rapidly degraded in response to ER stress (Murphy et al. 2011). PPIases are known to be involved in several signal transduction pathways. For instance, Pin1 is has been found to be a cell cycle regulator acting through the MAP kinase pathway during *Drosophila* oogenesis (Hsu et al. 2001). FKBP39 has been shown to act as an inhibitor of autophagy by downregulating the PI3K pathway and through modulation by Foxo transcription activity in the *Drosophila* larval fat body cells (Juhász et al. 2007). Cyclophilin B has been reported to be involved in ER-associated degradation of protein containing proline-containing peptide bonds in *cis* conformation (Bernasconi et al. 2010). Thus, various PPIases play a significant role in folding, regulating and degrading proteins within the cell.

PPIases have been previously implicated in neurodegenerative diseases. A study in PC12 cells showed that treatment with PPIase inhibiting drugs, cyclosporine A and FK506, enhanced cell death incurred by overexpression of mutant SOD1 in ALS1 (Lee et al. 1999). Cyclophilin A has been shown to be enriched in spinal cords of presymptomatic SOD1 mutant mice models (Massignan et al. 2007) as well as in peripheral blood mononuclear cells in ALS cases (Nardo et al. 2011). Disease condition has also been shown to be worsened in SOD1 mutants in cyclophilin A isomerase mutant consistent with the earlier study. The recent study conducted on HEK293 cells, mice models and human patient spinal cord samples has highlighted the important role of cyclophilin A in regulating the function of TARDBP in hnRNP formation. TARDBP pathology is

one of the most commonly found phenotype in sporadic and in ALS10 cases and has been shown to be enhanced with loss of cyclophilin A isomerase activity (Lauranzano et al. 2015). Tau pathology, a commonly found feature in Alzheimer's disease and other neurodegenerative diseases leads to formation of neurofibrillary tangles and toxic oligomers. Tau is an intrinsically disordered protein containing proline-rich domains interspersed with serine/threonine that provide sites for phosphorylation and interaction with other proteins. The formation of these structures has been shown to be regulated by Pin1, and members of FKBP family, FKBP52, FKBP51 and FKBP12, in a phosphorylation dependent manner (Blair et al. 2015). FKBP12 was initially found as an impurity in in-bacto purified α-synuclein aggregates associated with Parkinson's disease (Golbik et al. 2005)(Gerard et al. 2011). α-synuclein consists of five consecutive prolines in the C-terminal region. Further studies showed that inhibition or knock-down of FKBP12 or FKBP52 decreased α-synuclein aggregation in cell culture, whereas overexpression of these PPIases accelerated aggregate formation. Drug inhibition using FK506 reduced aggregate formation of α-synuclein in adult mouse brain (Gerard et al. 2011). A proline mutation in PrP protein aggregates and is implicated prion diseases. Cyclosporine A treatment on wild type PrP has also been shown to form dynamic cellular aggregates. A subpopulation of these aggregates, however, undergoes much slower degradation acting more similarly to mutant aggregates (Ben-Gedalya et al. 2011b).

Of the seven conserved prolines present in the MSP domain of human VAP, the prolines at 12th, 21st and 56th position are found to form peptide bonds in *cis* conformation. Missense mutation at any of these positions would switch the conformation of the X-Pro bond to *trans*. A point mutation at the 56th position from proline to serine in VAP leading to misfolding and aggregation of the protein may be incurred due to a loss of *cis* conformation. This may imply an important contribution of *cis* conformation at the 56th position for the correct folding and functionality of VAP. It is hypothesized that aggregation of VAP-P56S may be a direct consequence of loss of conformation at the 56th position in ALS8. We show that loss of conformational properties of proline at this position in VAP significantly affects folding and thereby its function, giving rise to disease phenotypes. Specific cellular peptidyl-prolyl isomerases may be responsible for aiding proper folding of VAP and rescuing subsequent detrimental effects.

Results

P56 in MSP domain of VAP forms a peptide bond in a cis conformation

The structure of MSP domain of human VAPB has been solved through X-ray crystallography and NMR (Shi et al. 2010). It consists of seven anti-parallel β-sheets that form a typical immunoglobulin fold stabilised by two S-loops. The proline at the 56th position is found to be present on one of the two S-loops. Structural studies have shown that the peptide bond formed between this proline and its previous amino acid in the chain is in the *cis* conformation. With a mutation replacing proline by serine, the protein is known to aggregate. At pH 3, the mutant, P56S, structure of the immunoglobulin fold has been shown to break down, forming non-resident α-helices (Shi et al. 2010) (Fig. 2A). The P56 proline is one of the seven conserved prolines in the MSP domain across species (Fig. 2B). Among the other six, 12th and 21st positions are found to be in the *cis* conformation whereas prolines at the 49th, 77th, 96th, and 111th position are found to be in the *trans* conformation. Structural studies have shown that P12 also resides in one of the S-loops and the mutation, P12S, similarly disrupts the folding of the MSP domain (Shi et al. 2010).

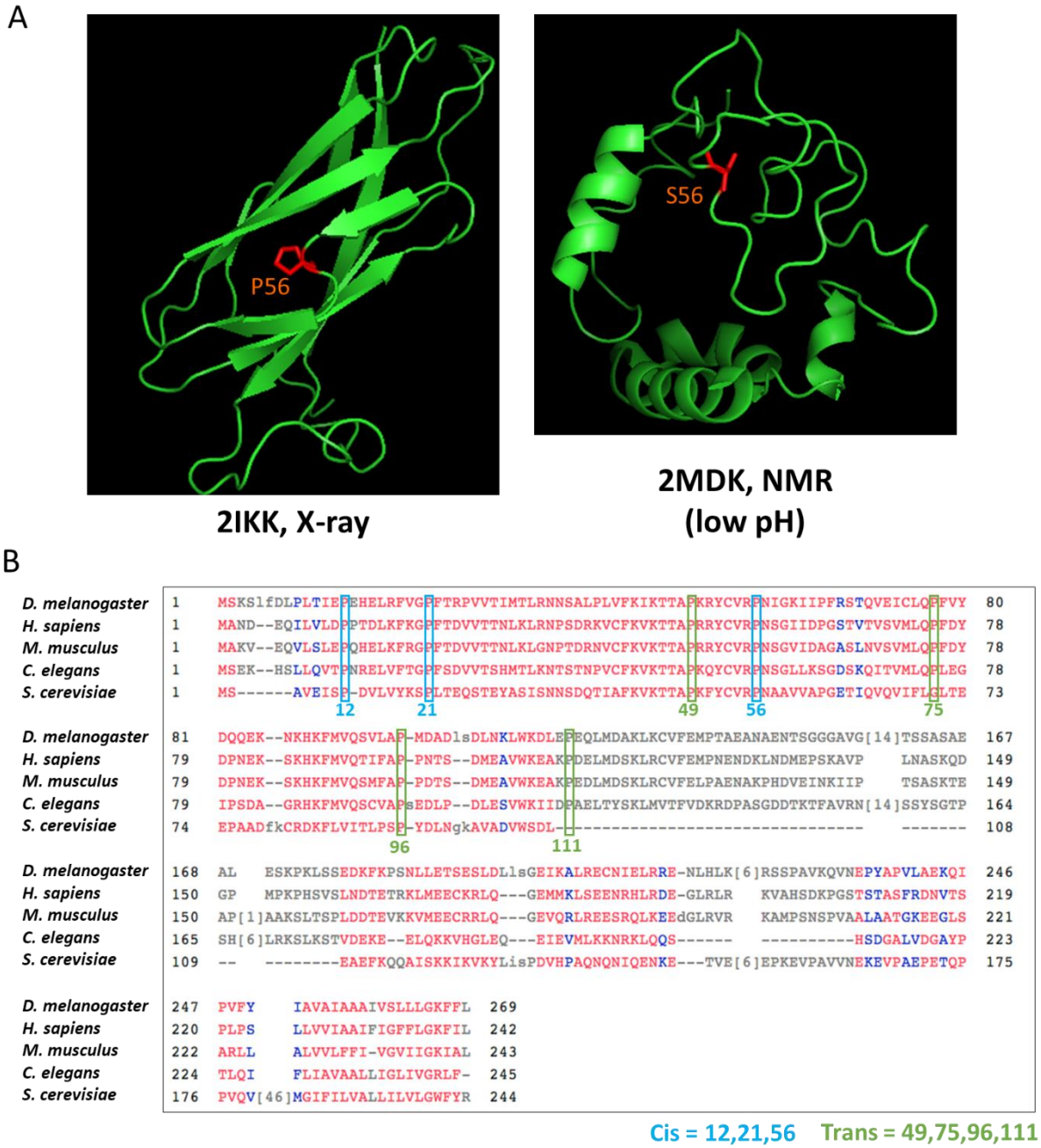

Figure 2: Conformations of Proline in VAP

A. Structures of MSP domain of VAP and VAP-P56S. VAP forms an immunoglobulin fold whereas VAP-P56S is unstructured (Data adapted from RCSB Protein Data bank).

B. Sequence homology of VAP across five species highlighting seven conserved prolines in the MSP domain. Modelling studies show that prolines at position (marked in blue) 12, 21 and 56 form bonds in *cis* conformation and at positions (marked in green) 49, 75, 96 and 111 form bonds in *trans* conformation.

VAP aggregation is a result of loss of conformational specificity provided by Proline

If VAP aggregation is a result of conformational specificity provided by the X-Pro *cis* conformation, one would predict that any mutation that converts a *cis* peptide bond to a *trans* peptide bond would lead to aggregation of the protein. To test this, we used the *Drosophila* S2R+ cell culture system to express wildtype VAP:GFP, that marked the membranes (Fig. 3A) or mutant VAP(P58S):GFP that formed cellular inclusions (Fig. 3B, Materials and Methods, Chapter II). We created site-directed mutations in *VAP:GFP* cloned into *pRM-HA3* vector, targeting both, the 58th proline as well as other conserved proline residues in the MSP domain. First, through site-directed mutagenesis, proline at the 58th position was replaced by six amino acids other than serine. A variety of amino acids with different charge, polarity, and size of the R groups were chosen. When transiently transfected and expressed in S2R+ cells, the mutants of VAP:GFP formed cellular aggregates at levels similar to VAP(P58S):GFP (Fig. 3C). This phenotype is observed irrespective of the properties imparted by the substitute amino acids. This indicated that any amino acid replacing proline at the 58th position caused a loss of *cis* conformation and a gain of *trans* conformation at that position, leading to misfolding and subsequent aggregation (Materials and Methods, Chapter II).

Next, *pRM-VAP:GFP* constructs were mutated to replace conserved prolines in the MSP domain in bonds in *cis* conformation at position 14 or 23, or in bonds in *trans* conformation at proline 49, 77, 98 or 115, with serine. These constructs were transiently transfected in S2R+ cells and induced with $CuSO_4$. At 24 hrs post induction of protein, 70% and 81% of the GFP-positive cells expressing mutations, P14S and P23S, respectively, showed aggregation comparable to P58S mutation where 73% GFP-positive cells showed aggregation (Fig. 3D). In contrast, only 13%, 18%, 10% and 9% of the GFP-positive cells expressing mutations, P49S, P77S, P98S and P115S, respectively, showed aggregation, similar to VAP(wt) overexpression that showed aggregation in 11% of the GFP-positive cells (Fig. 3D, Materials and Methods, Chapter II).

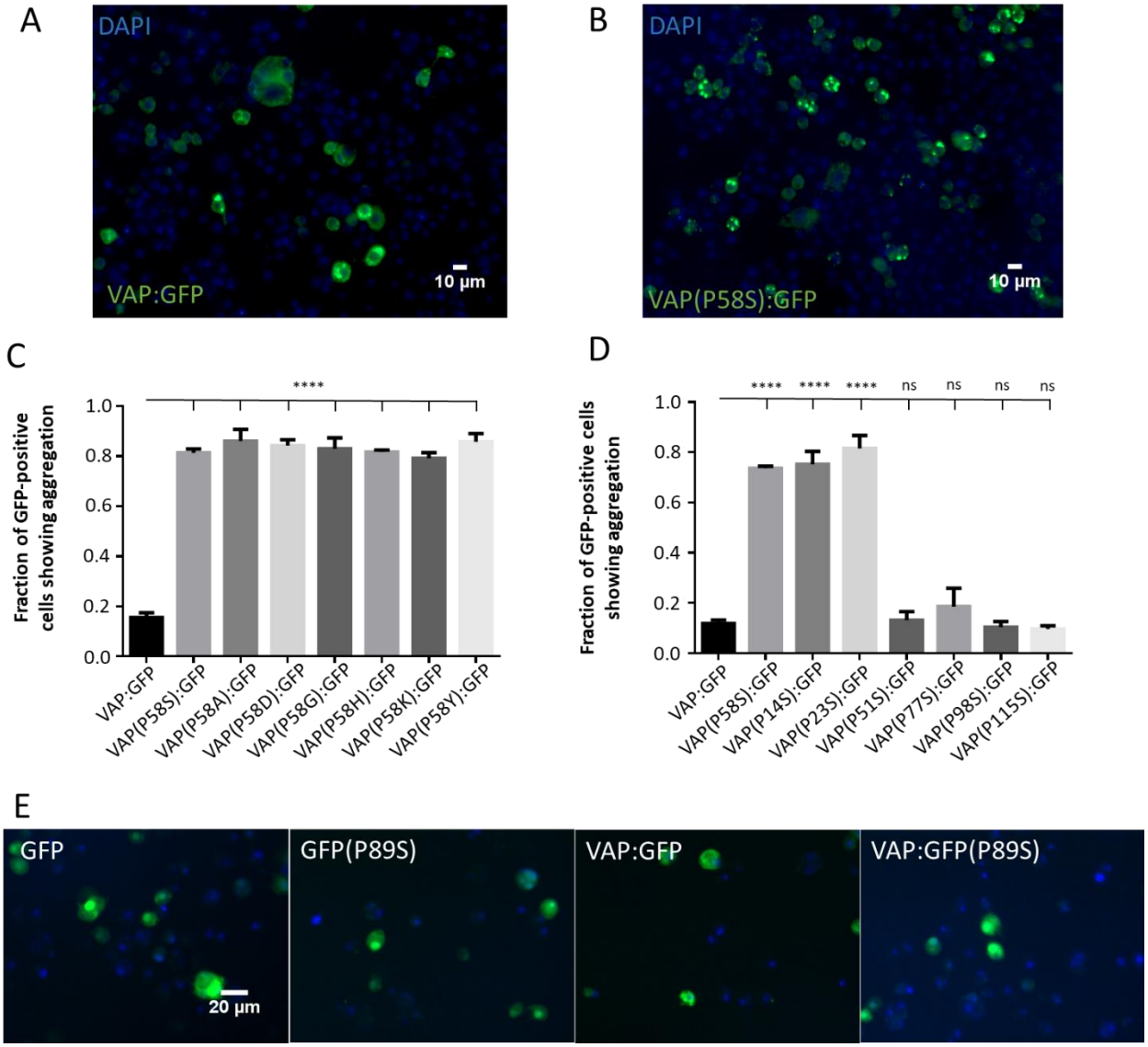

Figure 3: Proline conformation is crucial for VAP folding

A,B: *Drosophila* S2R+ cell line transfected with constructs of VAP:GFP (**A**) or VAP(P58S):GFP (**B**) under an inducible metallothionin promotor. VAP:GFP is membrane-bound whereas VAP(P58S):GFP forms intracellular aggregates.

C: S2R+ cells are transiently transfected with VAP:GFP or VAP(P58):GFP missense mutant constructs. The mutation at the 58th position causes the protein to form aggregates. N=3, ~ 750 total cells counted, ANOVA ****<0.0001; Fisher's LSD ****<0.0001, ns: not significant.

D: S2R+ cells are transiently transfected with VAP:GFP mutant constructs. The substitution of proline at *cis* conformation causes aggregation whereas substitution of proline at *trans* conformation shows normal localization. N=3, ~ 600 total cells counted, ANOVA ****<0.0001; Fisher's LSD ****<0.0001, ns: not significant.

E: Transient transfections of *GFP, GFP(P89S), VAP:GFP* and *VAP:GFP(P89S)* constructs in S2R+ cells. GFP protein mutated by replacing proline is *cis* conformation with serine can fluoresce and localize like wildtype GFP.
All images are taken at the same magnification.

The data suggests that mutations P14S and P23S induced the conformation of the peptide bond to change from *cis* to *trans*, similar to P58S, whereas the other mutations did not induce any conformational change behave more like the VAP:GFP. The data shows that loss of *cis* conformation at any of the conserved proline residues disrupts VAP structure to a greater extent than for *trans*. This data emphasised the importance of conformational state of proline in VAP folding.

To assess whether a control protein, such as GFP, shows an aggregation phenotype alike VAP:GFP, a similar mutation was made replacing the only *cis*-bonded proline to serine in *pRM-GFP* or in *pRM-VAP:GFP* constructs. When these constructs were transfected and expressed in S2R+ cells, it was observed that neither of the mutant products lost fluorescence or localization nor formed aggregates on conversion of *cis* to *trans* conformation of the peptide bond at the 89th position (Fig. 3E). This indicated that a *cis* to *trans* mutation leading to aggregation is not a general feature of overexpressed proteins in S2R+ cells and that the *cis* conformation in VAP is particularly critical not only at the 58th position, but also at the 14th or 23th position.

Role of peptidyl prolyl isomerases in VAP folding

Since, conformational change in proline bonds in *cis* conformation severely disrupt structure of VAP and cause aggregation, we decided to explore the possibility of involvement of peptidyl prolyl isomerase (PPIase) in VAP folding. We expect that if PPIases are involved, drugs that inhibit their activity may modify aggregation kinetics of either VAP(P58S) or wild type VAP or both. As a first step in establishing the role for PPIases, we incubated cells expressing VAP:GFP and VAP(P58S):GFP with drugs that inhibit their activity.

Stable cell line expressing VAP:GFP (Fig. 4A) was subjected to 10 µM cyclosporine A (Fig. 4C), 1 µM FK506 (Fig. 4D) or 5 µM parvulin inhibitor (PiB) (Fig. 4E) in 0.2% DMSO with 0.2% DMSO only as control (Fig. 4B), for 12 hours prior to induction of protein (Materials and Methods, Chapter II). After 24 hours post induction, intracellular inclusions were observed as high intensity puncta in presence of Cyclosporine A and FK506 treatment in around 14% of GFP-

positive cells, and with PiB treatment in around 10% as compared to 6% of GFP-positive cells treated with DMSO only (Fig. 4F). The data showed that the PPIases may indeed be largely involved in VAP folding.

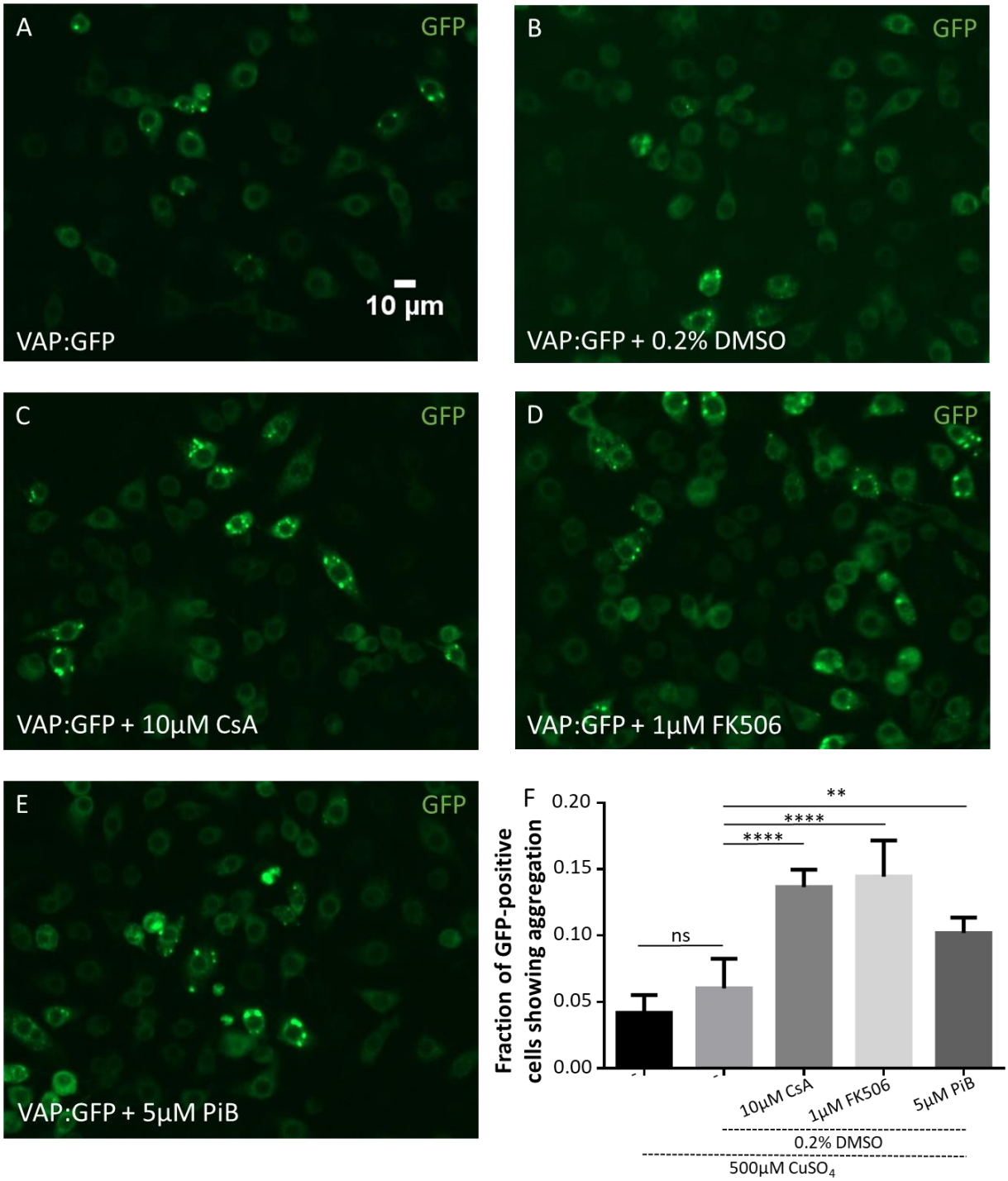

Figure 4: Chemical inhibition of PPIases induces VAP aggregation
A-E: Representative images of VAP:GFP aggregation upon treatment with PPIase inhibiting drugs for 12 hours, prior to induction with 500µM $CuSO_4$ for 24 hours, in a stable S2R+ cell line. All images are taken at the same magnification.
F: Fraction of GFP-positive cells showing aggregation, 24 hours post induction (500µM $CuSO_4$), increase with prior PPIase drug inhibition for 12 hours. N=3, ~ 1000 total cells counted, ANOVA ***≤0.001; Fisher's LSD test ****≤0.0001, **≤0.01, ns= not significant

To further assess the involvement of PPIase in VAP folding, we decided to study whether they modify VAP(P58S):GFP aggregation kinetics. The stable cell line overexpressing VAP(P58S):GFP was treated with PPIase inhibiting drugs for 4 hours before induction (Fig. 5A-E, Materials and Methods, Chapter II). We found that Cyclosporine A treatment significantly lowered the fraction of total number of cells showing aggregation as compared to the DMSO only control. However, we did not observe a drastic change in aggregation levels with FK506 and PiB (Fig. 5F). We also quantified the relative protein levels of VAP(P58S):GFP using western blotting with each of these treatments. Cyclosporine A as well as FK506 treatment appeared to show a significant decrease in VAP(P58S):GFP levels in the cell as compared to the DMSO only control (Fig. 5G. 5H).

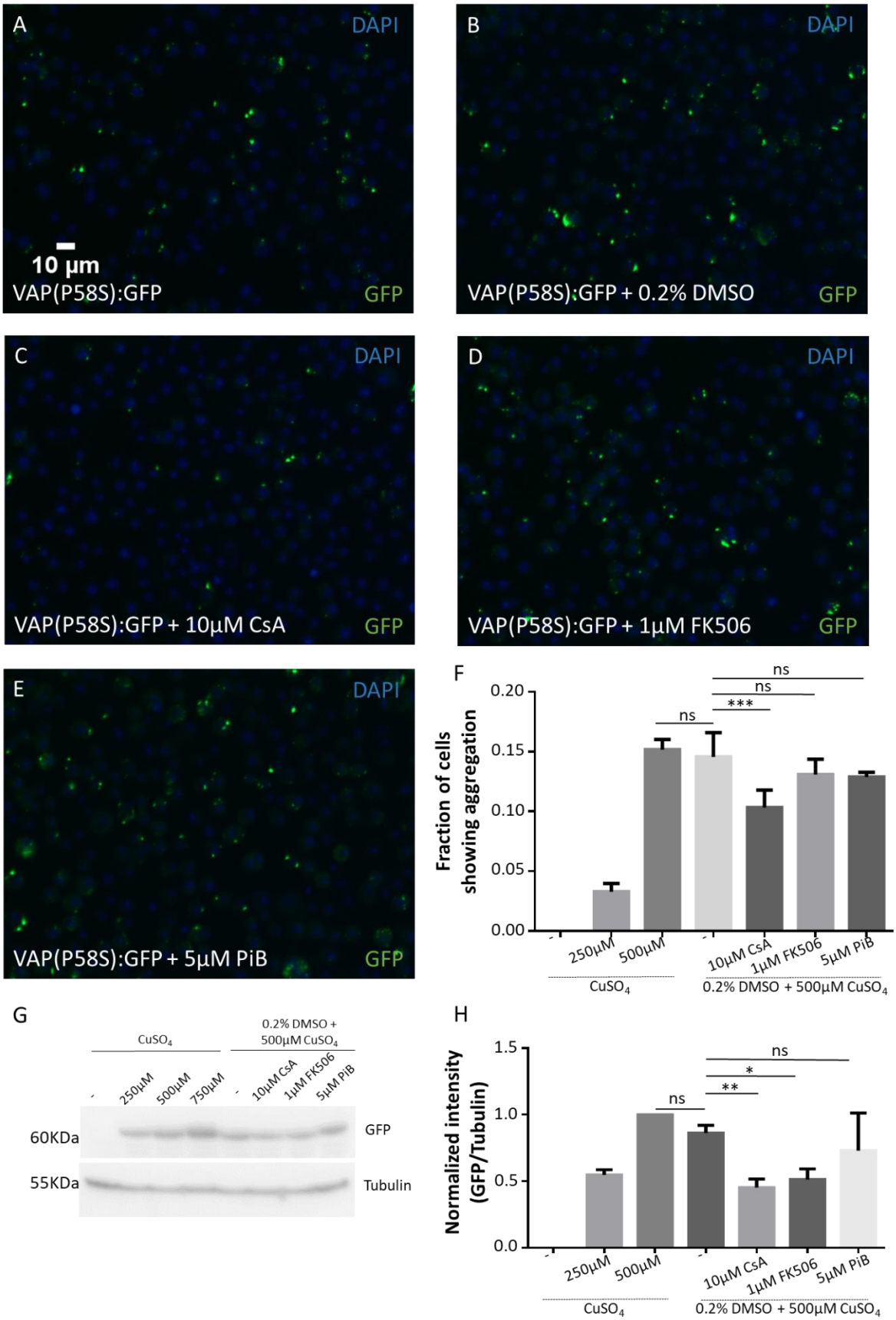
A
DAPI
10 µm
VAP(P58S):GFP
GFP
B
DAPI
VAP(P58S):GFP + 0.2% DMSO
GFP
C
DAPI
VAP(P58S):GFP + 10µM CsA
GFP
D
DAPI
VAP(P58S):GFP + 1µM FK506
GFP
E
DAPI
VAP(P58S):GFP + 5µM PiB
GFP
F
Fraction of cells showing aggregation
0.20
0.15
0.10
0.05
0.00
ns
ns
***
ns
-
250µM
500µM
-
10µM CsA
1µM FK506
5µM PiB
CuSO4
0.2% DMSO + 500µM CuSO4
G
CuSO4
0.2% DMSO + 500µM CuSO4
-
250µM
500µM
750µM
-
10µM CsA
1µM FK506
5µM PiB
60KDa
GFP
55KDa
Tubulin
H
Normalized intensity (GFP/Tubulin)
1.5
1.0
0.5
0.0
ns
*
**
ns
-
250µM
500µM
-
10µM CsA
1µM FK506
5µM PiB
CuSO4
0.2% DMSO + 500µM CuSO4

Figure 5: Chemical inhibition of Cyclophilins, but not FKBPs and Parvulins, lowers VAP(P58S):GFP aggregation and protein levels

A-E: Representative images of VAP(P58S):GFP aggregation upon treatment with PPIase inhibiting drugs for 4 hours, prior to induction with 500µM $CuSO_4$ for 24 hours, in a stable S2R+ cell line. All images are taken at the same magnification.

F: Fraction of cells showing VAP(P58S):GFP aggregation observed 24 hours post induction (500µM $CuSO_4$), is lowered when treated with Cyclosporine A, but not FK506 or PiB, for 4 hours prior to induction. N=3, ~1000 total cells counted. ANOVA ***≤0.001; Fisher's LSD test ***≤0.001, ns= not significant.

G-H: Protein level of VAP(P58S):GFP quantified 24 hours post induction (500µM $CuSO_4$), is lowered when treated with Cyclosporine A, but not FK506 or PiB, for 4 hours prior to induction. N=2, ANOVA ****≤0.001; Fisher's LSD test **≤0.01, *≤0.05, ns= not significant.

Genetic screens to identify PPIases involved in VAP folding

Drosophila genome codes for 34 known PPIases. To explore the possible role of specific individual PPIase in VAP folding, we decided to conduct an RNAi screen targeting various PPIases in cells and shortlisting targets capable of inducing VAP:GFP inclusions or modulating VAP(P58S):GFP aggregates as observed in drug treatment (See future directions).

In stable lines expressing VAP(P58S):GFP, 28 individual PPIases; 19 cyclophilins, 9 FKBPs and 3 parvulins were knocked down using dsRNA. The screen was a part of "a high throughput screen to identify modifiers of ALS8 aggregation using automated computational image analysis"; (Appendix 1) carried out by Lokesh Pimpale as part of his M.S thesis (Pimpale 2015). As described in Appendix 1, based on average and total cell intensity, we identified 4 PPIases; 2 cyclophilins, 1 FKBP and 1 parvulin, that could modulate VAP(P58S):GFP aggregation in S2R+ cells (Table 1). In order to understand the effect of these PPIases on VAP aggregation, these targets will be further validated and characterized in the *Drosophila* models of ALS8, as described in the next section.

Table 1: List of target PPIases shortlisted from the High-throughput RNAi screen on stable S2R+ cell line expressing VAP(P58S)GFP

PPIase	Category
CG14715	FKBP
CG11858	Parvulin
CG30350	Cyclophillin
CG2852	Cyclophillin

Drosophila model of ALS8: Overexpression of VAP(P58S) using the UAS-GAL4 system

A system for VAP(P58S) protein aggregation was developed in *Drosophila melanogaster* (Fig. 5, Chapter II). Wild type VAP or mutant VAP(P58S) was overexpressed in the third instar *Drosophila* larval brain using the UAS-GAL4 system driven by a pan-neuronal promotor, *elav* (Ratnaparkhi et al. 2008). The larval brains were probed with an anti-VAP antibody developed in our laboratory (Deivasigamani et al. 2014) to visualize expressed protein. While wild type VAP marked the cellular membranes and cell boundary when visualized by immunostaining in the ventral nerve cord of the larval brain, mutant VAP(P58S) formed distinct cellular puncta. Using this system, we could measure changes in aggregation density (Materials and Methods, Chapter II). We tested the effect of various PPIases using EP lines or RNAi lines available with BDSC for enhancement or suppression of aggregation levels in larval brains. Table 2 details the fly lines tested in the background of wildtype or mutant overexpression in the brain (See also Appendix 5).

Table 2: Fly lines for different PPIases tested in *C155-GAL4; UAS-VAP* and *C155-GAL4; UAS-VAP(P58S)* third instar *Drosophila* larval brain aggregation system (*experiments performed)

Class	Gene	Localization	Genotype	VAP	P58S
Cyp	CG5808	Nuclear	w[*]; p{w[+mC]=UAS-CG5808-FLAG-HA}attP2		*
	CG8336	Cytoplasmic	w[1118]; Mi{ET1}Or67b[MB04909] CG8336[MB04909]	*	*
			w[*]; p{w[+mC]=UAS-CG8336-FLAG-HA}attP2		*
	CG1866 (moca-cyp)	Nuclear	y[1] w[67c23]; P{w[+mC] y[+mDint2]=EPgy2}Moca-cyp[EY06157]	*	*
	CG9916 (cyclophillin 1)	Cytoplasmic	y[1] sc[*] v[1]; P{y[+t7.7] v[+t1.8]=TRiP.HMS00902}attP2	*	*
	CG13892	Cytoplasmic	P{KK107406}VIE-260B	*	*

	CG11777	Cytoplasmic	P{KK108775}VIE-260B	*	
	CG7768	Cytoplasmic	w[*]; p{w[+mC]=UAS-CG7768-FLAG-HA}attP2		*
	CG3511	Cytoplasmic	w[*]; p{w[+mC]=UAS-CG3511-FLAG-HA}attP2		*
FKBP	CG4535 (FKbp59)	Cytoplasmic	y[1] w[67c23]; P{w[+mC] y[+mDint2]=EPgy2}FKBP59[EY03538]	*	*
	CG14715	ER	w[1118]; P{w[+mC]=EP}CG14715[G6908]	*	*
	CG6226 (FK506 BP-1, FKBP39)	Nuclear	y[1] sc[*] v[1]; P{y[+t7.7] v[+t1.8]=TRiP.HMS00339}attP2	*	
	CG5482	Cytoplasmic	w[1118]; P{GD2071}v4991	*	*
Parvulin	CG11858	Cytoplasmic	P{KK108489}VIE-260B	*	

Of the 10 listed EP or RNAi lines, we did not observe any induction of wildtype VAP aggregation, unlike the results from cell culture experiments. In the background of VAP(P58S) overexpression (Fig. 6A), we found lowered aggregation density with five of the genes tested (Fig. 6C) using EP lines or RNAi lines- Cyclophilins: CG8336, Cyp1 and CG13892, and FK506: CG14715 (Fig. 6B) and CG5482.

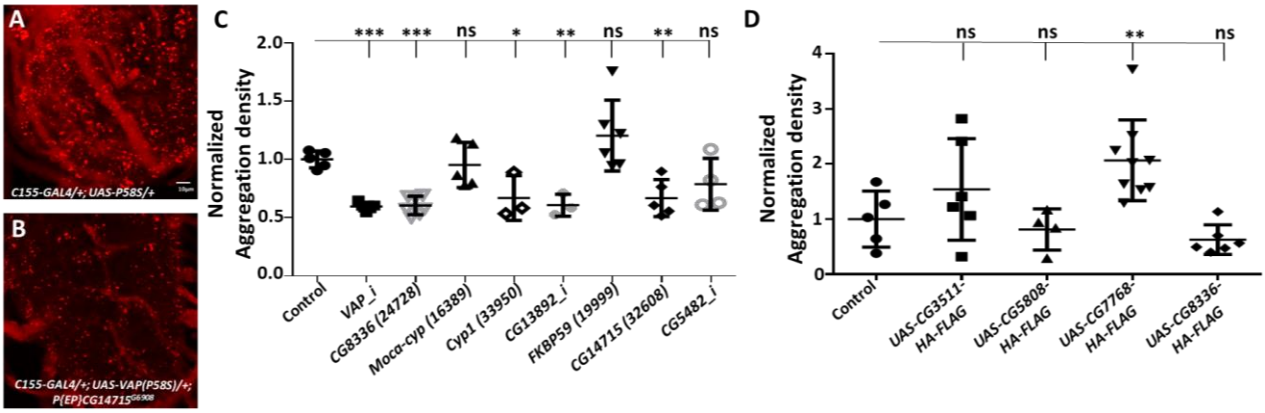

Figure 6: PPIases modulate VAP(P58S) aggregation in wandering third instar larval brains

A, B: Representative images of the ventral nerve cord of third instar larval brain showing a decrease in aggregation density of VAP(P58S) in presence of a P-element insertion in CG14715. All images are taken at the same magnification.

C: Out of the seven PPIases screened, knockdown or loss-of-function mutation of 3 cyclophilins and 2 FKBPs shows a reduction in aggregation density of VAP(P58S) aggregation in the ventral nerve cord of larval brains. ANOVA ****≤0.001; Fisher's LSD test ***≤0.001, **≤0.01, ns= not significant.

D: Overexpression of CG7768 significantly increases aggregation levels in the ventral nerve cord of larval brains. ANOVA **≤0.01; Fisher's LSD test **≤0.01, ns= not significant.

The same brain aggregation system was used to test the effect of overexpression of PPIases on VAP folding. As a beginning, eight transgenic fly lines were generated (Fig. 7A) with *UAS-Flag-HA-tagged PPIases* constructs, cloned in *pUASt*. The constructs were procured from DGRC and injected in the NCBS-CCamP transgenic facility (Materials and Methods, Chapter II). Expression was observed only in 4 of these lines using a *MS1096*-GAL4 that expresses in the dorsal wing pouch of *Drosophila* third instar larval wing imaginal dics (Fig. 7B). These four transgenic lines were used to overexpress PPIases in third instar larval brains in the VAP(P58S) background. Overexpressing CG7768 could significantly increase aggregation levels in the ventral nerve cord (Fig. 6D).

A

Gene	Expression
CG3511	+++
CG5808	++
CG7768	++
CG8336	++
CG32236	-
CG9847	-
CG2852	-
CG14715	-

B

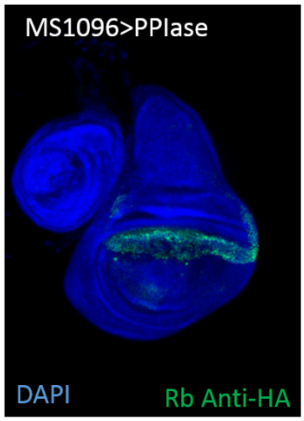

Figure 7: Expression of Flag-HA-tagged PPIases fly lines obtained from DGRC
A: 4 fly lines out of eight showed high expression levels when overexpressed in the third instar larval wing imaginal discs using the UAS-GAL4 system.
B: Representative image of third instar larval wing imaginal disc overexpressing Flag-HA-tagged PPIase in the dorsal wing pouch under a MS1096 promoter and visualized using anti-HA antibody by immunostaining, and DAPI to mark the nuclei.

Drosophila model of ALS8: Genomic expression of VAP(P58S)

A model for ALS8 was generated by Hiroshi Tsuda's lab and is described in Appendix 3 (Moustaqim-barrette et al. 2014). Expression of the mutant VAP protein under its own promoter is sufficient to rescue the lethality associated with VAP precise null mutation (Moustaqim-barrette et al. 2014). In our lab, we generated balanced lines rescuing the hypomorphic allele of VAP, Δ166 (Pennetta et al. 2002), with genomic constructs of VAP wildtype as well as VAP(P58S) (Appendix 5). Unlike VAP wildtype, flies rescued with VAP(P58S) show motor defects as early as day 10

and shortened lifespan of less than 30 days post eclosion. Thus, this system, expressing the protein at levels equivalent to endogenous VAP, more closely resembles ALS phenotypes. A reverse genetic screen to identify interactors that could enhance or suppress the lifespan of these flies would help identity therapeutic targets. We used this system to find PPIases that could affect lifespan using the fly lines listed in table 2 (Fig. 8A-H). Our preliminary results indicate CG5808 and CG8663 as modulators of lifespan (Fig. 8B, 8H). These results will be further confirmed with use of RNAi and overexpression lines. An investigation including other markers of ALS such as motor defects, protein aggregation and cell death will provide further insight.

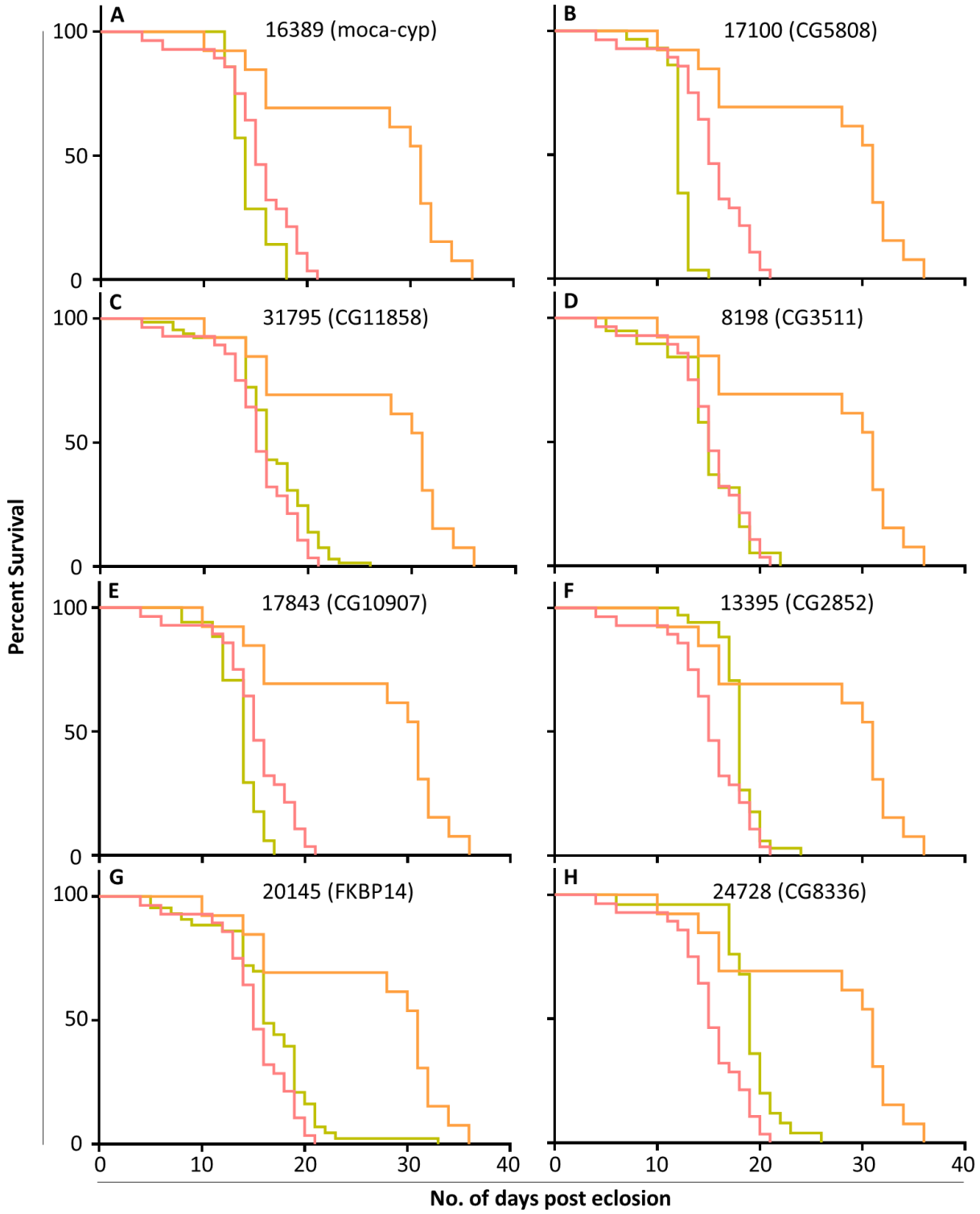

Figure 8: Effect of PPIases on lifespan of genomic VAP(P58S) rescue line

A-H: Kaplan- Meier survival analysis curves showing the percentage survival of males from each test genotype (green) compared with negative control, *Δ166/Y; vap>VAP(P58S)/+* (pink), and positive control, *Δ166/Y; vap>VAP(P58S)/vap>VAP* (orange). (P value ****≤0.0001). In this preliminary experiment,

approximately 10-50 male flies were counted for each genotype. The positive control (orange) could rescue the lifespan increasing the median survival to 31 days (n=13). EP line (17100) used for CG5808 could marginally worsen the lifespan of the flies with a decrease in median survival from 15 days (n=28) to 12 days (n=29) **(E)**. EP line (24728) used for CG8336 could marginally rescue the lifespan of the flies with an increase in median survival from 15 days (n=28) to 19 days (n=25) **(H)**. Number in parenthesis indicates the BDSC stock number.

Discussion

In this study, we have demonstrated that VAP folding and aggregation is significantly dependent on the conformational specificity provided the prolines bound in *cis* isomer form. Replacing proline to various other amino acids at the 58th position of the *Drosophila* ortholog of the protein led to aggregate formation implying that it is the loss of proline rather than the gain of serine at that position which is involved in VAP structure maintenance. This data is consistent with a previously published study in mouse motoneuronal NSC34 cell line which has shown that mutating proline to other residues such as positively charged lysine, negatively charged aspartic acid and non-polar alanine or removing it altogether reduced the solubility of VAP protein (Kanekura et al. 2006). Recently, a Chinese Han family was found to harbour a P56H mutation in VAP, showing clinical ALS features similar to that seen in patients with VAP(P56S) (Sun et al. 2017). It is possible that the functional and aggregating behaviour of both these mutant proteins are similar in nature causing similar manifestation of the disease.

The structure of human MSP domain containing the mutation, P12S, was found to be similar to the mutant, P56S. The prolines in the 12th and the 56th position were found to be in the S-loops of the immunoglobulin fold that are responsible for its stability. In the *Drosophila* VAP protein, conversion of conformation from *cis* to *trans* by replacing proline with serine at other conserved positions, 14th and 23rd, also caused aggregation of the *Drosophila* VAP protein, unlike the positions, 51st, 77th, 98th and 115th, where mutation did not cause a change in conformation. These results clearly highlight the importance of *cis* conformation for VAP folding and aggregation. However, the composition and dynamics of these aggregating mutants, P58X, P14S and P23S, may be different from one another in the cell, depending on the properties of the amino acid used to replace the proline as well as the effect of the position of proline in the sequence. Additionally, the non-aggregating mutant proteins could differ from the wildtype in terms of localization, protein interaction as well as function. It would be interesting to explore whether these mutants are implied in disease conditions using *Drosophila* brain and NMJ as model systems.

Further, the mutation, P89S responsible for a *cis* to *trans* conversion in soluble GFP or in the membrane-bound GFP (tagged to VAP) did not cause change in function or localization of the protein. In human VAP(P56S) mutant protein, the mutation is known to cause the disruption of the MSP fold, followed by the unravelling of the hydrophobic regions of the coiled coil domain and the transmembrane domain (Kim et al. 2010). Mutation, P56S, in human VAP-A, when expressed in HeLa cells, also leads to aggregation. Our results show that not only the conformation of proline but also its presence in the immunoglobulin-like fold of the MSP domain of VAP may be crucial in determining the fate of its structural organization.

Treatment of PPIases inhibiting drug on stable cell line expressing VAP:GFP lead to aggregate formation. The induced VAP:GFP cellular inclusions observed with loss of cis conformation through drug treatment or individual knockdowns of PPIases may be characteristically dissimilar from the VAP(P58S):GFP aggregates. These may differ from one another in composition, dynamicity, protein turnover and ease of clearance, and localization. VAP mutant aggregates have been previously shown to be non-dynamic in mammalian cell culture based on FRAP assays (Teuling et al. 2007). Treatment of Cyclosporine A has been shown to effectively induce prion protein, PrP, aggregation in cell culture; a part of the population of these aggregates appear to be immobile, non-ubiquitinated and protease K resistant, while some aggregates appear to be more dynamic and permeable to its environment, are ubiquitinated and degraded via the proteasomal machinery (Ben-Gedalya et al. 2011a).

Inhibition of PPIases using drugs on the stable line expressing VAP(P58S):GFP showed a decrease in aggregation levels as well as protein levels. It is known that wild type VAP can interact with misfolded VAP(P58S) and be sequestered into the aggregates (Teuling et al. 2007; Ratnaparkhi et al. 2008). Thus, PPIases may affect VAP(P58S) in at least two ways, one by modulating isomerization of prolines other than residue 58 and other by affecting VAP folding and regulating its recruitment into VAP(P58S) aggregates. Reduction in aggregation with inhibition of PPIases might be a result of loss of interaction with PPIase(s) that destabilizes aggregation and promotes its clearance. This effect could also be achieved as a result of global consequences that may affect protein expression or may be involved in initiating degradative mechanisms. It is also possible that the effect shown by the immunophilins, cyclosporine A and

FK506, may be through a secondary mechanism inhibiting calcineurin and inducing an immune response (Mukai et al. 1993).

In order to identify which PPIase(s) may be responsible for VAP folding and affect its aggregation, we performed a series of genetic screens in cell culture as well as fly models. RNAi screen scoring for perturbation of aggregation kinetics of mutant VAP(P58S) identified 4 modifiers. An RNAi screen knocking down individual PPIases on stable cell line expressing VAP:GFP and identifying targets that can induce VAP aggregation is in progress. Fly models developed to study the process of aggregation in the brain serve as a better system to mimic the cellular conditions in ALS8. Based on the availability of reagents, through the *UAS-GAL4* model system, we have identified 5 modifiers in our ongoing screen. CG14715, an FKBP identified in the cell culture screen, was also tested in flies and found to be modulate aggregation. The cyclophilin, CG8336, was identified as modifier using an EP line (BDSC 24728) but did not show a change in aggregation density when overexpressed. The lifespan assay used to determine the effect on longevity of the genomic rescue fly model, identified CG8336 (BDSC 24728) as an enhancer of phenotype. On the basis of the site of insertion, the EP line (BDSC 24728) appears to be disrupting the gene, CG8336 along with a neighboring gene, Odorant receptor 67B (Or67b), that could have contributed to the phenotype. Another cyclophilin, CG5808, did not show a change in aggregation levels in the *UAS-GAL4* model. However, the EP line, CG5808 (BDSC 17100), could further reduce the lifespan of the genomic rescue line.

It is possible that different model systems may influence aggregation kinetics differentially. Since ALS is a late-onset disease, it is also likely that the process of aggregation modulation is age-dependent. It may imply that the phenotype may not be strongly observable in larval stages, and may develop in adult fly stages. Exploring different stages of the fly as well as monitoring parameters such as aggregation levels, motor function and lifespan will help assess the progression of the disease. Drug assays and genetic screens will shed light on identifying specific PPIase(s) involved in chaperoning VAP structure. Further understanding the mechanism of interaction of PPIase(s) with VAP aggregation may help identify potential therapeutic application in ALS.

Caveats and alternative strategies

Side-directed mutations made in VAP:GFP lead to aggregation phenotype due to loss of *cis*-conformation at positions 14, 23 and 58. On the other hand, mutations that did not affect conformation at positions 51, 77, 98 and 115, did not lead to aggregation. Immunofluorescence assays, inhibition of proteasomal machinery or autophagy or protein translation, and microscopy techniques such as fluorescent recovery after photobleaching (FRAP) or fluorescence loss in photobleaching (FLIP) may shed some light on the properties of aggregating species of VAP. It would also be interesting to find whether double mutants for VAP:GFP would affect the phenotype significantly as compared to single mutations. Since, MSP domain of VAP contains three evolutionarily conserved prolines bonded in *cis* conformation, it is possible that each of these sites may be regulated by different PPIases. Screening for PPIase(s) involved in correct VAP folding will provide genetically interacting targets. These may influence VAP folding either by physical interaction or by acting on intermediate players such as chaperones or interacting proteins that may stabilize VAP structure. Alternatively, PPIases identified as interactors of VAP may not influence mutant VAP aggregation and, thus may not be relevant in disease. Likewise, PPIases identified as interactors of VAP and influencing mutant VAP aggregation in RNAi screen may not rescue the phenotype in overexpression studies. Phenotypes seen through drug treatment and individual knockdowns may be explained by different mechanisms. Drugs will cause a global inhibition of PPIase in the cell leading to which may be unaccounted for due to the limitation of the read-out (GFP-fluorescence from aggregation). Drugs such as cyclosporine A and FK506 may also invoke immune reaction and the effect observed may be a result of that instead of an effect of loss of PPIase activity. It would be interesting to dissect out such alternate mechanisms as they may be implicated in the disease condition.

Future directions

An RNAi screen to knockdown individual PPIases in stable cell line expressing VAP:GFP will be performed and targets that can induce VAP:GFP aggregation will be identified. Target PPIases identified from RNAi screens will be validated by quantitating protein levels of VAP:GFP and VAP(P58S):GFP through western blotting. Target PPIases will be overexpressed in VAP:GFP and VAP(P58S) expressing stable cell lines to score for effect on aggregation. FMO clones tagged with HA and Flag of the short-listed targets obtained from DGRC and checked for expression in

S2R+ cells by western blotting, will be transfected and expressed in the stable line expressing VAP(P58S):GFP to look for percentage cells showing aggregation and relative protein levels

PPIases will be knocked down or overexpressed in third instar *Drosophila* larval brain system or in adult *Drosophila* brain, using the procured fly lines, to look for effect on aggregation of VAP and VAP(P58S). The effect of PPIases will also be determined in the genomic rescue lines of VAP(P58S) using motor, lifespan and aggregation assays.

Acknowledgments

Lokesh Pimpale is thanked for performing the RNAi screen in S2R+ stable cell lines to identify modifiers of VAP(P58S):GFP aggregation in the high-throughput screening facility at C-CAMP, NCBS (Appendix 1). He is also thanked for the performing preliminary experiments for PPIase inhibitors in cell culture.

References

Ben-Gedalya T, Lyakhovetsky R, Yedidia Y, et al (2011a) Cyclosporin-A-induced prion protein aggresomes are dynamic quality-control cellular compartments. J Cell Sci 124:1891–902. doi: 10.1242/jcs.077693

Ben-Gedalya T, Lyakhovetsky R, Yedidia Y, et al (2011b) Cyclosporin-A-induced prion protein aggresomes are dynamic quality-control cellular compartments. J Cell Sci 124:1891–902. doi: 10.1242/jcs.077693

Bernasconi R, Soldà T, Galli C, et al (2010) Cyclosporine A-sensitive, cyclophilin B-dependent endoplasmic reticulum-associated degradation. PLoS One 5:1–7. doi: 10.1371/journal.pone.0013008

Blair LJ, Baker JD, Sabbagh JJ, Dickey C a (2015) The emerging role of peptidyl-prolyl isomerase chaperones in tau oligomerization, amyloid processing, and Alzheimer's disease. J Neurochem 133:1–13. doi: 10.1111/jnc.13033

Deivasigamani S, Verma HK, Ueda R, et al (2014) A genetic screen identifies Tor as an interactor of VAPB in a Drosophila model of amyotrophic lateral sclerosis. Biol Open 3:1127–38. doi: 10.1242/bio.201410066

Gerard M, Deleersnijder A, Demeulemeester J, et al (2011) Unraveling the role of peptidyl-prolyl isomerases in neurodegeneration. Mol Neurobiol 44:13–27. doi: 10.1007/s12035-011-8184-2

Golbik R, Yu C, Weyher-Stingl E, et al (2005) Peptidyl prolyl cis/trans-isomerases: comparative reactivities of cyclophilins, FK506-binding proteins, and parvulins with fluorinated oligopeptide and protein substrates. Biochemistry 44:16026–34. doi: 10.1021/bi051442w

Harding MW, Galat A, Uehling DE, Schreiber SL (1989) A receptor for the immunosuppressant FK506 is a cis-trans peptidyl-prolyl isomerase. Nature 341:758–60. doi: 10.1038/341758a0

Hsu T, McRackan D, Vincent TS, Gert de Couet H (2001) Drosophila Pin1 prolyl isomerase Dodo is a MAP kinase signal responder during oogenesis. Nat Cell Biol 3:538–43. doi: 10.1038/35078508

Juhász G, Puskás LG, Komonyi O, et al (2007) Gene expression profiling identifies FKBP39 as an inhibitor of autophagy in larval Drosophila fat body. Cell Death Differ 14:1181–90. doi:

10.1038/sj.cdd.4402123

Kaiser SE, Brickner JH, Reilein AR, et al (2005) Structural basis of FFAT motif-mediated ER targeting. Structure 13:1035–45. doi: 10.1016/j.str.2005.04.010

Kanekura K, Nishimoto I, Aiso S, Matsuoka M (2006) Characterization of amyotrophic lateral sclerosis-linked P56S mutation of vesicle-associated membrane protein-associated protein B (VAPB/ALS8). J Biol Chem 281:30223–33. doi: 10.1074/jbc.M605049200

Kim S, Leal SS, Ben Halevy D, et al (2010) Structural requirements for VAP-B oligomerization and their implication in amyotrophic lateral sclerosis-associated VAP-B(P56S) neurotoxicity. J Biol Chem 285:13839–49. doi: 10.1074/jbc.M109.097345

Lauranzano E, Pozzi S, Pasetto L, et al (2015) Peptidylprolyl isomerase A governs TARDBP function and assembly in heterogeneous nuclear ribonucleoprotein complexes. Brain 138:974–91. doi: 10.1093/brain/awv005

Lee JP, Palfrey HC, Bindokas VP, et al (1999) The role of immunophilins in mutant superoxide dismutase-1linked familial amyotrophic lateral sclerosis. Proc Natl Acad Sci U S A 96:3251–6

Lev S, Halevy D Ben, Peretti D, Dahan N (2008) The VAP protein family: from cellular functions to motor neuron disease. Trends Cell Biol 18:282–290. doi: 10.1016/j.tcb.2008.03.006

Lorenzen S, Peters B, Goede A, et al (2005) Conservation of cis prolyl bonds in proteins during evolution. Proteins 58:589–95. doi: 10.1002/prot.20342

Lu P-J, Zhou XZ, Liou Y-C, et al (2002) Critical role of WW domain phosphorylation in regulating phosphoserine binding activity and Pin1 function. J Biol Chem 277:2381–4. doi: 10.1074/jbc.C100228200

Massignan T, Casoni F, Basso M, et al (2007) Proteomic analysis of spinal cord of presymptomatic amyotrophic lateral sclerosis G93A SOD1 mouse. Biochem Biophys Res Commun 353:719–25. doi: 10.1016/j.bbrc.2006.12.075

Matsuda S, Koyasu S (2000) Mechanisms of action of cyclosporine. Immunopharmacology 47:119–125. doi: 10.1016/S0162-3109(00)00192-2

Moustaqim-barrette A, Lin YQ, Pradhan S, et al (2014) The amyotrophic lateral sclerosis 8 protein, VAP, is required for ER protein quality control. Hum Mol Genet 23:1975–1989. doi: 10.1093/hmg/ddt594

Mukai H, Kuno T, Chang CD, et al (1993) FKBP12-FK506 complex inhibits phosphatase activity of two mammalian isoforms of calcineurin irrespective of their substrates or activation mechanisms. J Biochem 113:292–8

Murphy LA, Ramirez EA, Trinh VT, et al (2011) Endoplasmic reticulum stress or mutation of an EF-hand Ca(2+)-binding domain directs the FKBP65 rotamase to an ERAD-based proteolysis. Cell Stress Chaperones 16:607–19. doi: 10.1007/s12192-011-0270-x

Nardo G, Pozzi S, Pignataro M, et al (2011) Amyotrophic lateral sclerosis multiprotein biomarkers in peripheral blood mononuclear cells. PLoS One 6:e25545. doi: 10.1371/journal.pone.0025545

Nishimura Y, Hayashi M, Inada H, Tanaka T (1999) Molecular cloning and characterization of mammalian homologues of vesicle-associated membrane protein-associated (VAMP-associated) proteins. Biochem Biophys Res Commun 254:21–6. doi: 10.1006/bbrc.1998.9876

Pemberton TJ, Kay JE (2005) Identification and comparative analysis of the peptidyl-prolyl cis/trans isomerase repertoires of H. sapiens, D. melanogaster, C. elegans, S. cerevisiae and Sz. pombe. Comp Funct Genomics 6:277–300. doi: 10.1002/cfg.482

Pennetta G, Hiesinger PR, Fabian-Fine R, et al (2002) Drosophila VAP-33A directs bouton formation at neuromuscular junctions in a dosage-dependent manner. Neuron 35:291–306

Pimpale L (2015) A high throughput RNAi screen to identify modifiers of ALS8 aggregation using automated computational image analysis. Master's thesis, IISER Pune

Ratnaparkhi A, Lawless GM, Schweizer FE, et al (2008) A Drosophila model of ALS: Human ALS-associated mutation in VAP33A suggests a dominant negative mechanism. PLoS One 3:e2334. doi: 10.1371/journal.pone.0002334

Schiene-Fischer C (2014) Multidomain peptidyl prolyl cis/trans Isomerases. Biochim Biophys Acta. doi: 10.1016/j.bbagen.2014.11.012

Shi J, Lua S, Tong JS, Song J (2010) Elimination of the native structure and solubility of the

hVAPB MSP domain by the Pro56Ser mutation that causes amyotrophic lateral sclerosis. Biochemistry 49:3887–97. doi: 10.1021/bi902057a

Sun Y, Dong Y, Wang J, et al (2017) A novel mutation of VAPB in one Chinese familial amyotrophic lateral sclerosis pedigree and its clinical characteristics. J Neurol 264:2387–2393. doi: https://doi.org/10.1007/s00415-017-8628-3

Teuling E, Ahmed S, Haasdijk E, et al (2007) Motor neuron disease-associated mutant vesicle-associated membrane protein-associated protein (VAP) B recruits wild-type VAPs into endoplasmic reticulum-derived tubular aggregates. J Neurosci 27:9801–15. doi: 10.1523/JNEUROSCI.2661-07.2007

Tsuda H, Han SM, Yang Y, et al (2008) The Amyotrophic Lateral Sclerosis 8 Protein VAPB Is Cleaved, Secreted, and Acts as a Ligand for Eph Receptors. Cell 133:963–977. doi: 10.1016/j.cell.2008.04.039

Chapter IV

Conclusions, Current Status & Future Directions

In this Chapter, I list out the conclusions of my research along with the current status of the field. I also spell out future directions for the laboratory, based on my findings. For my thesis, I have worked on a *Drosophila* model of the incurable late-onset progressive neurodegenerative disease amyotrophic lateral sclerosis (ALS). I have addressed the manifestation of aggregation of one of the familial ALS loci, *VAPB* (aka *VAP*). VAP has notable cell-autonomous as well as cell non-autonomous roles in the brain. A C-tail anchored ER membrane protein, VAP serves by tethering membranes between the ER and other organelles, thus playing a role in membrane trafficking, lipid transport, as well as calcium signaling. These roles of VAP also have implications in protein homeostasis such as unfolded protein response, ubiquitin proteasomal degradation as well as autophagy. These effects are mediated via the interaction of the N-terminal Major Sperm Protein (MSP) domain of VAP with protein containing the FFAT motif. The protein essentially acts as a dimer with VAPA and VAPB interacting through the central coiled coil domain (CCD) (Fig. 1) (Murphy and Levine 2016; Kamemura and Chihara 2019). Through an unknown mechanism, VAP MSP domain is cleaved and can be secreted out in the synapse to serve as a ligand for Robo/Lar like receptors at the muscle, mediating changes in the muscle cytoskeleton and mitochondrial morphology (Tsuda et al. 2008; Han et al. 2012, 2013). A single point mutation in VAP, P56S, in the MSP domain, was first identified in a large Brazilian family in 2004 by Mayana Zats group, leading to ALS as well as spinal muscular atrophy (Nishimura et al. 2004). The mutation confers a conformational change causing the protein to misfold and aggregate (Mitne-Neto et al. 2007; Papiani et al. 2012).

Neurodegeneration can be largely described as a set of protein conformational diseases. Protein aggregates can be modulated by several factors in the cell, such as changes in binding partners, metal binding, local pH, oxidative states (Wang et al. 2008; Sheng et al. 2012; Blokhuis et al. 2013; Vasconcellos et al. 2016). Deaggregating mechanisms are addressed in the cell by the chaperone system and the unfolded protein response (Hughes and Mallucci 2018). Finally, the aggregates can be cleared through proteasomal as well as autophagic degradation (Webster et al. 2017). In our studies, we have addressed the conformational as well as functional regulation of VAP aggregation using a *Drosophila* model of ALS. A proline to serine mutation leading to a

change in cis-trans isomerization, causes a drastic change in conformation of the MSP domain such that it takes an unstructured form (Shi et al. 2010). This causes the protein domains to unravel, exposing the hydrophobic regions of the CCD and TMD. The hydrophobic interactions promote misfolding and aggregation of VAP mutant protein (Kim et al. 2010).

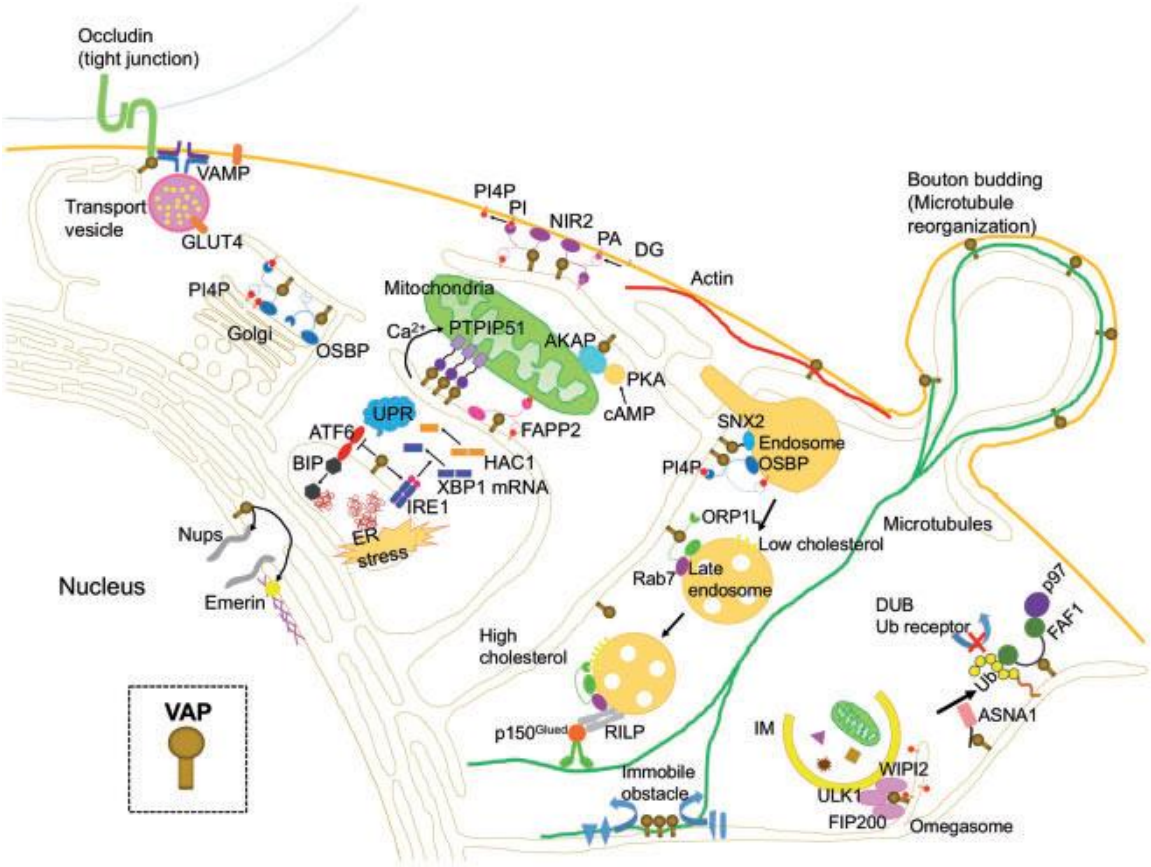

Figure 1: Functions of VAP in neuronal cells
VAP is a membrane protein that interacts via its N-terminal MSP domain with FFAT-containing proteins. VAP thus performs diverse roles in lipid biosynthesis and trafficking that have implications in ER stress, unfolded protein response, ER-associated degradation, mitochondrial function, vesicular transport, autophagosome formation, calcium signaling, endosomal trafficking as well as cytoskeleton reorganization. The physical interaction of VAP with proteins on other organelles helps in the formation of membrane contact sites that are crucial in inter-organelle communication and homeostasis. Reproduced from (Kamemura and Chihara 2019)

Models of ALS8 in cell culture, *Drosophila*, *C. elegans* as well as mouse show aggregate formation upon expression of VAP(P58S). These aggregates also appear to be capable of interacting with VAP wildtype, thus depleting the pool of functional VAP leading to loss-of-

function phenotypes. In our studies, as shown in Fig. 2, we have utilized an S2R+ cell culture model and two models of *Drosophila* third instar larval brains in order to study aggregation (Chapter 2, 3, Appendix 1-4). As described in Chapter 2 and 3 as well as Appendix 1 and 2, the cell culture model expresses VAP(P58S) protein under an inducible metallothionin promoter which can be used to modulate aggregate formation and aggregation kinetics. Characterization of the various VAP mutants that cause a change in proline conformation, as described in Chapter 3, will further help understand VAP folding and aggregating properties. Using this model, we conducted a screen for 900 genes associated with ALS, VAP and proteostasis, obtaining 150 targets. The cell culture model can also be used to perform chemical screens to test the effect of various drugs on aggregation, as demonstrated with ROS-inducing paraquat as well as PPIases inhibitory drugs. We have, thus, successfully used this model to obtain preliminary results that can then be further tested in fly systems that more closely resemble the disease.

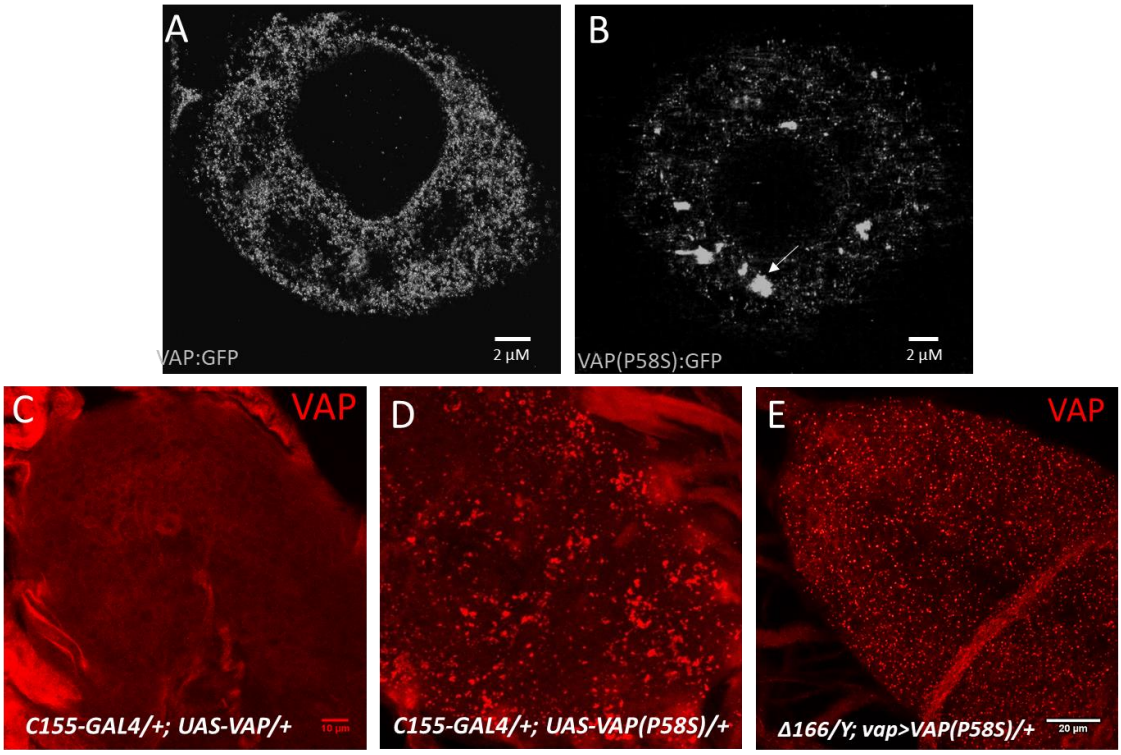

Figure 2: *Drosophila* models of VAP(P58S) aggregation to study ALS8.
A, B: In this thesis, the S2R+ cell culture model has been used to identify modulators of VAP aggregation as well as to study the effect of conformational changes on aggregate formation.
C, D: Using the *UAS-GAL4* system, VAP(P58S) aggregation could be modulated in the third instar larval brain. In our study, we have found the role of ROS in facilitating the degradation of VAP(P58S) aggregates via the ubiquitin-proteasomal system regulated by the mTOR pathway. We also identified a

role of wildtype VAP in the regulation of ROS in the third instar larval brains. We hypothesize this regulation may be mediated via the mTOR pathway.
E: The genomic line expressing VAP(P58S) under the *vap* promoter itself was procured from Tsuda lab (Moustaqim-barrette et al. 2014). When balanced with a functional null of VAP, a large number of aggregates are observed in the third instar larval brains. The flies also develop motor and lifespan defects, thus, phenocopying the ALS condition more closely.

We have utilized two models of the disease in *Drosophila*. The first model is based on the use of *UAS-GAL4* system to overexpress the mutant protein in the brain with the endogenous protein being expressed in the background (Chapter 2). The model serves as a good platform to study aggregation dynamics and genetic interactions that perturb it at the cellular level (Ratnaparkhi et al. 2008; Deivasigamani et al. 2014). The interaction between two ALS loci, SOD1 and VAP could be studied using this system. We found that modulation of ROS via SOD1 could in turn regulate the degradation of VAP(P58S) aggregation. The degradation appeared to be facilitated through the ubiquitin proteasomal system as opposed to autophagy, but could be regulated by the mTOR pathway in an ROS dependent manner. Rapamycin, an inhibitor of mTOR pathway, found be responsible for reducing VAP(P58S) neuroaggregates in our ALS8 *Drosophila* model, is also in clinical trials for ALS (Mandrioli et al. 2018). However, the overexpression model does not appear develop ALS phenotypes such as motor defects and shortened lifespan. There are two possible reasons that can be considered. Firstly, as the mutant protein is expressed only in the brain, it does not lead to development of drastic phenotypes. Secondly, since there is an expression of wildtype protein in the background, the functional threshold levels of VAP are not compromised in this system. Thus, understanding the link between aggregation and ALS pathogenesis using this model is a challenge.

In the second model, established in our laboratory since 2016, the mutant protein is expressed at genomic levels under the *vap* promoter. The lines used were developed in Tsuda laboratory (Moustaqim-barrette et al. 2014) (Chapter 3, Appendix 3, 4). When monitored for VAP(P58S) aggregates, we found fewer and smaller aggregates in the third instar larval brain in this system as compared to the *UAS-GAL4* system. Upon removing the endogenous *vap* gene (*Δ166*) from the background, the number of aggregates increase several fold. Yet these aggregates are smaller in size when compared to the overexpression system. The flies of the genotype, *Δ166;; vap>VAP(P58S)*, show progressive loss of motor function as well as shortened lifespan. Thus,

these flies serve as a much better model for ALS wherein the role of aggregation in disease progression can be studied. This has been addressed in Appendix 3, where we have explored the role of SOD1-modulated ROS in change in aggregation and lifespan. A time dependent change in aggregation in adult flies along with changes in motor defects in response to ROS would be worth investigating. The model is also useful in deciphering the function of VAP mutant protein in flies. With this direction, in Appendix 4, we have identified change in levels of different lipid species in brains of 15 day old flies. These changes demonstrate a loss-of-function of VAP mutant protein in lipid metabolism that are restored with a single copy of wildtype VAP. Finally, the system serves as a good model to validate more genetic interactors of VAP and modulators of VAP aggregation identified in the screens performed in the lab. As described in Chapter 3, prolyl isomerases that can aid in VAP folding, can be identified. Chaperones or prolyl isomerases that can aid VAP fold and, thus, dissolve mutant VAP aggregates in the third instar larval brain can be identified. The effect of solubilizing VAP aggregation on motor and lifespan defects will, in turn, reflect on the role of aggregates in ALS.

References

Blokhuis AM, Groen EJN, Koppers M, et al (2013) Protein aggregation in amyotrophic lateral sclerosis. Acta Neuropathol 125:777–794. doi: 10.1007/s00401-013-1125-6

Deivasigamani S, Verma HK, Ueda R, et al (2014) A genetic screen identifies Tor as an interactor of VAPB in a Drosophila model of amyotrophic lateral sclerosis. Biol Open 3:1127–1138. doi: 10.1242/bio.201410066

Han SM, El Oussini H, Scekic-Zahirovic J, et al (2013) VAPB/ALS8 MSP ligands regulate striated muscle energy metabolism critical for adult survival in caenorhabditis elegans. PLoS Genet 9:e1003738. doi: 10.1371/journal.pgen.1003738

Han SM, Tsuda H, Yang Y, et al (2012) Secreted VAPB/ALS8 major sperm protein domains modulate mitochondrial localization and morphology via growth cone guidance receptors. Dev Cell 22:348–362. doi: S1534-5807(11)00575-2 [pii]10.1016/j.devcel.2011.12.009

Hughes D, Mallucci GR (2018) The unfolded protein response in neurodegenerative disorders - therapeutic modulation of the PERK pathway. FEBS J 1–14. doi: 10.1093/isle/isv094

Kamemura K, Chihara T (2019) Multiple functions of the ER-resident VAP and its extracellular role in neural development and disease. J Biochem 0:1–10. doi: 10.1093/jb/mvz011

Kim S, Leal SS, Ben Halevy D, et al (2010) Structural requirements for VAP-B oligomerization and their implication in amyotrophic lateral sclerosis-associated VAP-B(P56S) neurotoxicity. J Biol Chem 285:13839–49. doi: 10.1074/jbc.M109.097345

Mandrioli J, D'Amico R, Zucchi E, et al (2018) Rapamycin treatment for amyotrophic lateral sclerosis. Medicine (Baltimore) 97:e11119. doi: 10.1097/MD.0000000000011119

Mitne-Neto M, Ramos CR, Pimenta DC, et al (2007) A mutation in human VAP-B--MSP domain, present in ALS patients, affects the interaction with other cellular proteins. Protein Expr Purif 55:139–146. doi: S1046-5928(07)00096-4 [pii]10.1016/j.pep.2007.04.007

Moustaqim-barrette A, Lin YQ, Pradhan S, et al (2014) The amyotrophic lateral sclerosis 8 protein, VAP, is required for ER protein quality control. Hum Mol Genet 23:1975–1989. doi: 10.1093/hmg/ddt594

Murphy SE, Levine TP (2016) VAP, a Versatile Access Point for the Endoplasmic Reticulum: Review and analysis of FFAT-like motifs in the VAPome. Biochim Biophys Acta 1861:952–961. doi: 10.1016/j.bbalip.2016.02.009

Nishimura AL, Mitne-neto M, Silva HCA, et al (2004) A Mutation in the Vesicle-Trafficking Protein VAPB Causes Late-Onset Spinal Muscular Atrophy and Amyotrophic Lateral Sclerosis. 2:822–831

Papiani G, Ruggiano A, Fossati M, et al (2012) Restructured endoplasmic reticulum generated by mutant amyotrophic lateral sclerosis-linked VAPB is cleared by the proteasome. J Cell Sci 125:3601–3611. doi: 10.1242/jcs.102137

Ratnaparkhi A, Lawless GM, Schweizer FE, et al (2008) A Drosophila Model of ALS: Human ALS-Associated Mutation in VAP33A Suggests a Dominant Negative Mechanism. PLoS One 3:e2334. doi: 10.1371/journal.pone.0002334

Sheng Y, Chattopadhyay M, Whitelegge J, Valentine JS (2012) SOD1 Aggregation and ALS : Role of Metallation States and Disulfide. 2560–2572

Shi J, Lua S, Tong JS, Song J (2010) Elimination of the native structure and solubility of the hVAPB MSP domain by the Pro56Ser mutation that causes amyotrophic lateral sclerosis. Biochemistry 49:3887–97. doi: 10.1021/bi902057a

Tsuda H, Han SM, Yang Y, et al (2008) The Amyotrophic Lateral Sclerosis 8 Protein VAPB Is Cleaved, Secreted, and Acts as a Ligand for Eph Receptors. Cell 133:963–977. doi: 10.1016/j.cell.2008.04.039

Vasconcellos LRC, Dutra FF, Siqueira MS, et al (2016) Protein aggregation as a cellular response to oxidative stress induced by heme and iron. Proc Natl Acad Sci 113:E7474–E7482. doi: 10.1073/pnas.1608928113

Wang Q, Johnson JL, Agar NYR, Agar JN (2008) Protein aggregation and protein instability govern familial amyotrophic lateral sclerosis patient survival. PLoS Biol 6:e170. doi: 10.1371/journal.pbio.0060170

Webster CP, Smith EF, Shaw PJ, De Vos KJ (2017) Protein Homeostasis in Amyotrophic Lateral Sclerosis: Therapeutic Opportunities? Front Mol Neurosci 10:1–22. doi:

10.3389/fnmol.2017.00123

Appendix 1

High Throughput RNAi screen conducted offsite at the NCBS-C-CAMP imaging facility, followed by Automated image analysis

A cell-based RNAi screen to identify modulators of VAP(P58S) aggregation

The RNAi screen was performed to identify modulators of aggregation in a *Drosophila* S2R+ cell line expressing VAP(P58S). The screen was conducted at the highthrouput screening facility at C-CAMP, NCBS, Bangalore. dsRNA for 900 genes (Table 1) were synthesized from templates procured from Open Biosystems (RDM1189 and RDM4220) and spotted on sixteen 384 well plates (Fig. 1) by Chromous Biotech, Bangalore. GFP dsRNA, VAP dsRNA, scrambled dsRNA, uninduced and 1000μM $CuSO_4$ treatment were used as controls (Fig. 1). The cells were treated with dsRNA and processed for imaging as described in Materials and methods, Chapter II. The imaging was performed using THERMO Array Scan VTI HCS system in dual channels, the FITC (488nm) channel for imaging VAP(P58S):GFP aggregates and the DAPI (405nm) channel for imaging cell nuclei. With 10 fields per sample and 400 cells per field, in triplicates for each dsRNA knockdown, over 1 lakh images were generated. The screen is explained in detail in the MS thesis by Lokesh Pimpale (Pimpale 2015).

Table 1: List of 900 genes utilized for the screen. List is sorted alphabetically based on gene symbol.

SUBMITTED ID	FBID_KEY	NAME	SYMBOL
CG6778	FBgn0027088	Glycyl-tRNA synthetase	Aats-gly
CG6335	FBgn0027087	Histidyl-tRNA synthetase	Aats-his
CG11198	FBgn0033246	Acetyl-CoA carboxylase	ACC
CG1966	FBgn0027620	ATP-dependent chromatin assembly factor large subunit	Acf
CG10473	FBgn0263198	Acinus	Acn
CG9244	FBgn0010100	Aconitase	Acon
CG9709	FBgn0034629	acyl-Coenzyme A oxidase at 57D distal	Acox57D-d
CG9707	FBgn0034628	acyl-Coenzyme A oxidase at 57D proximal	Acox57D-p
CG7899	FBgn0000032	Acid phosphatase 1	Acph-1
CG8732	FBgn0263120	Acyl-CoA synthetase long-chain	Acsl
CG11994	FBgn0037661	Adenosine deaminase	Ada
CG9638	FBgn0037555	transcriptional Adaptor 2b	Ada2b
CG7098	FBgn0030891	transcriptional Adaptor 3	Ada3
CG5315	FBgn0038984	Adiponectin receptor	AdipoR
CG33138	FBgn0053138	1,4-Alpha-Glucan Branching Enzyme	AGBE

CG15010	FBgn0041171	archipelago	ago
CG13388	FBgn0027932	A kinase anchor protein 200	Akap200
CG4006	FBgn0010379	Akt1	Akt1
CG8057	FBgn0260972	alicorn	alc
CG9556	FBgn0013746	alien	alien
CG17223	FBgn0031491	alpha4GT1	alpha4GT1
CG7158	FBgn0037116	Amyotrophic lateral sclerosis 2 ortholog	Als2
CG6438	FBgn0023179	amontillado	amon
CG3051	FBgn0023169	AMP-activated protein kinase alpha subunit	AMPKalpha
CG17876	FBgn0000078	Amylase distal	Amy-d
CG8465	FBgn0028343	ANKLE2 ortholog	Ankle2
CG12276	FBgn0029512	Activator of SUMO 1	Aos1
CG8376	FBgn0267978	apterous	ap
CG1451	FBgn0015589	APC-like	Apc
CG11419	FBgn0034231	Anaphase Promoting Complex subunit 10	APC10
CG32707	FBgn0052707	Anaphase Promoting Complex subunit 4	APC4
CG14444	FBgn0029879	Anaphase Promoting Complex subunit 7	APC7
CG8385	FBgn0010348	ADP ribosylation factor at 79F	Arf79F
CG5659	FBgn0017418	ariadne 1	ari-1
CG5709	FBgn0025186	ariadne 2	ari-2
CG11579	FBgn0000117	armadillo	arm
CG7843	FBgn0033062	-	Ars2
CG8787	FBgn0261823	Additional sex combs	Asx
CG9200	FBgn0031876	Ada2a-containing complex component 1	Atac1
CG3136	FBgn0033010	Atf6	Atf6
CG10967	FBgn0260945	Autophagy-related 1	Atg1
CG12821	FBgn0040780	Autophagy-related 10	Atg10
CG7053	FBgn0030960	Autophagy-related 101	Atg101
CG7331	FBgn0261108	Autophagy-related 13	Atg13
CG31033	FBgn0039705	Autophagy-related 16	Atg16
CG1347	FBgn0037363	Autophagy-related 17	Atg17
CG7986	FBgn0035850	Autophagy-related 18a	Atg18a
CG8678	FBgn0032935	Autophagy-related 18b	Atg18b
CG1241	FBgn0044452	Autophagy-related 2	Atg2
CG6877	FBgn0036813	Autophagy-related 3	Atg3
CG4428	FBgn0031298	Autophagy-related 4a	Atg4a
CG6194	FBgn0038325	Autophagy-related 4b	Atg4b
CG5429	FBgn0264325	Autophagy-related 6	Atg6
CG5489	FBgn0034366	Autophagy-related 7	Atg7
CG12334	FBgn0038539	Autophagy-related 8b	Atg8b
CG3615	FBgn0034110	Autophagy-related 9	Atg9
CG2503	FBgn0010750	antimeros	atms
CG8322	FBgn0020236	ATP citrate lyase	ATPCL

CG5166	FBgn0041188	Ataxin-2	Atx2
CG2210	FBgn0000150	abnormal wing discs	awd
CG7926	FBgn0026597	Axin	Axn
CG6016	FBgn0033844	bb in a boxcar	bbc
CG7842	FBgn0036691	bad egg	beg
CG18319	FBgn0000173	bendless	ben
CG8536	FBgn0027538	beta4GalNAcTA	beta4GalNAcTA
CG14517	FBgn0039625	beta4GalNAcTB	beta4GalNAcTB
CG9277	FBgn0003887	beta-Tubulin at 56D	betaTub56D
CG3612	FBgn0011211	bellwether	blw
CG7314	FBgn0036199	Bmcp	Bmcp
CG5295	FBgn0036449	brummer	bmm
CG11491	FBgn0283451	broad	br
CG4934	FBgn0000221	brainiac	brn
CG6303	FBgn0266717	BIR repeat containing ubiquitin-conjugating enzyme	Bruce
CG3411	FBgn0004101	blistered	bs
CG9242	FBgn0000239	burgundy	bur
CG13969	FBgn0045064	brain washing	bwa
CG9520	FBgn0032078	Core 1 Galactosyltransferase A	C1GalTA
CG13664	FBgn0039294	Cadherin 96Cb	Cad96Cb
CG4236	FBgn0263979	Chromatin assembly factor 1, p55 subunit	Caf1-55
CG9429	FBgn0005585	Calreticulin	Calr
CG6871	FBgn0000261	Catalase	Cat
CG7037	FBgn0020224	Cbl proto-oncogene ortholog	Cbl
CG7035	FBgn0022942	cap binding protein 80	Cbp80
CG17753	FBgn0010531	Copper chaperone for superoxide dismutase	Ccs
CG1049	FBgn0041342	CTP:phosphocholine cytidylyltransferase 1	Cct1
CG14980	FBgn0035470	Ccz1 ortholog	Ccz1
CG1471	FBgn0039774	Ceramidase	CDase
CG6759	FBgn0025781	Cell division cycle 16 ortholog	Cdc16
CG2508	FBgn0032863	Cell division cycle 23 ortholog	Cdc23
CG8610	FBgn0012058	Cell division cycle 27 ortholog	Cdc27
CG12019	FBgn0011573	Cdc37	Cdc37
CG5971	FBgn0035918	Cdc6	Cdc6
CG32742	FBgn0028360	Cdc7 kinase	Cdc7
CG8203	FBgn0013762	Cyclin-dependent kinase 5	Cdk5
CG5387	FBgn0027491	Cdk5 activator-like protein	Cdk5alpha
CG5179	FBgn0019949	Cyclin-dependent kinase 9	Cdk9
CG7962	FBgn0010350	CDP diglyceride synthetase	CdsA
CG11804	FBgn0029092	ced-6	ced-6
CG16708	FBgn0037315	Ceramide kinase	Cerk
CG7207	FBgn0027569	ceramide transfer protein	cert
CG15645	FBgn0030657	cervantes	cerv

CG10089	FBgn0036369	-	CG10089
CG1024	FBgn0027514	-	CG1024
CG10254	FBgn0027512	-	CG10254
CG10262	FBgn0032813	-	CG10262
CG10635	FBgn0035603	-	CG10635
CG10694	FBgn0039147	-	CG10694
CG10754	FBgn0036314	-	CG10754
CG10862	FBgn0035455	-	CG10862
CG10907	FBgn0036207	-	CG10907
CG11035	FBgn0037544	-	CG11035
CG11070	FBgn0028467	-	CG11070
CG11261	FBgn0036332	-	CG11261
CG11321	FBgn0031857	-	CG11321
CG11337	FBgn0039846	-	CG11337
CG11444	FBgn0029715	-	CG11444
CG11560	FBgn0036249	-	CG11560
CG11594	FBgn0035484	-	CG11594
CG11777	FBgn0033527	-	CG11777
CG11779	FBgn0038683	-	CG11779
CG11811	FBgn0036099	-	CG11811
CG11858	FBgn0039305	-	CG11858
CG12020	FBgn0035273	-	CG12020
CG12096	FBgn0030457	-	CG12096
CG12338	FBgn0033543	-	CG12338
CG12538	FBgn0038157	-	CG12538
CG12746	FBgn0037341	-	CG12746
CG12822	FBgn0033229	-	CG12822
CG13048	FBgn0036593	-	CG13048
CG13063	FBgn0036601	-	CG13063
CG13075	FBgn0036563	-	CG13075
CG13116	FBgn0032139	-	CG13116
CG13296	FBgn0035687	-	CG13296
CG13298	FBgn0035692	-	CG13298
CG13531	FBgn0034786	-	CG13531
CG13532	FBgn0034788	-	CG13532
CG13900	FBgn0035162	-	CG13900
CG13994	FBgn0031772	-	CG13994
CG14006	FBgn0031733	-	CG14006
CG14024	FBgn0031697	-	CG14024
CG14043	FBgn0031659	-	CG14043
CG1409	FBgn0029964	-	CG1409
CG14125	FBgn0036232	-	CG14125
CG1416	FBgn0032961	-	CG1416

CG14207	FBgn0031037	-	CG14207
CG14238	FBgn0039429	-	CG14238
CG14326	FBgn0038528	-	CG14326
CG14435	FBgn0029911	-	CG14435
CG14490	FBgn0034281	-	CG14490
CG14606	FBgn0037485	-	CG14606
CG14715	FBgn0037930	-	CG14715
CG14718	FBgn0037939	-	CG14718
CG14739	FBgn0037987	-	CG14739
CG14740	FBgn0037988	-	CG14740
CG14837	FBgn0035797	-	CG14837
CG15141	FBgn0032635	-	CG15141
CG15160	FBgn0032688	-	CG15160
CG15237	FBgn0033104	-	CG15237
CG15615	FBgn0034159	-	CG15615
CG15676	FBgn0034651	-	CG15676
CG15767	FBgn0029809	-	CG15767
CG15800	FBgn0034904	-	CG15800
CG16817	FBgn0037728	-	CG16817
CG16879	FBgn0028904	-	CG16879
CG16892	FBgn0030122	-	CG16892
CG16935	FBgn0033883	-	CG16935
CG17026	FBgn0036550	-	CG17026
CG17028	FBgn0036552	-	CG17028
CG17029	FBgn0036551	-	CG17029
CG17030	FBgn0035584	-	CG17030
CG17266	FBgn0033089	-	CG17266
CG17327	FBgn0038107	-	CG17327
CG17343	FBgn0032751	-	CG17343
CG17726	FBgn0037880	-	CG17726
CG17760	FBgn0033756	-	CG17760
CG17840	FBgn0031611	-	CG17840
CG17982	FBgn0030006	-	CG17982
CG17985	FBgn0033199	-	CG17985
CG1890	FBgn0039869	-	CG1890
CG2218	FBgn0039767	-	CG2218
CG2574	FBgn0030386	-	CG2574
CG2681	FBgn0024997	-	CG2681
CG2807	FBgn0031266	-	CG2807
CG2852	FBgn0034753	-	CG2852
CG2887	FBgn0030207	-	CG2887
CG2924	FBgn0023528	-	CG2924
CG2964	FBgn0031462	-	CG2964

CG30043	FBgn0050043	-	CG30043
CG30161	FBgn0050161	-	CG30161
CG30350	FBgn0050350	-	CG30350
CG30429	FBgn0050429	-	CG30429
CG30463	FBgn0050463	-	CG30463
CG31098	FBgn0051098	-	CG31098
CG31528	FBgn0051528	-	CG31528
CG31550	FBgn0051550	-	CG31550
CG31769	FBgn0051769	-	CG31769
CG31935	FBgn0051935	-	CG31935
CG32236	FBgn0046793	-	CG32236
CG32437	FBgn0052437	-	CG32437
CG32486	FBgn0266918	-	CG32486
CG6463	FBgn0053493	-	CG33493
CG3356	FBgn0034989	-	CG3356
CG3457	FBgn0024984	-	CG3457
CG3473	FBgn0028913	-	CG3473
CG3476	FBgn0031881	-	CG3476
CG3492	FBgn0035007	-	CG3492
CG3500	FBgn0034849	-	CG3500
CG3511	FBgn0035027	-	CG3511
CG3605	FBgn0031493	-	CG3605
CG4080	FBgn0035983	-	CG4080
CG4164	FBgn0031256	-	CG4164
CG4238	FBgn0031384	-	CG4238
CG4461	FBgn0035982	-	CG4461
CG4627	FBgn0033808	-	CG4627
CG4646	FBgn0033810	-	CG4646
CG4872	FBgn0030799	-	CG4872
CG4887	FBgn0031318	-	CG4887
CG5001	FBgn0031322	-	CG5001
CG5028	FBgn0039358	-	CG5028
CG5071	FBgn0039347	-	CG5071
CG5087	FBgn0035953	-	CG5087
CG5181	FBgn0031909	-	CG5181
CG5285	FBgn0038490	-	CG5285
CG5335	FBgn0034365	-	CG5335
CG5379	FBgn0038956	-	CG5379
CG5440	FBgn0031331	-	CG5440
CG5482	FBgn0034368	-	CG5482
CG5604	FBgn0032208	-	CG5604
CG5790	FBgn0032677	-	CG5790
CG5808	FBgn0027617	-	CG5808

CG5823	FBgn0038515	-	CG5823
CG5828	FBgn0031682	-	CG5828
CG5953	FBgn0032587	-	CG5953
CG6015	FBgn0038927	-	CG6015
CG6048	FBgn0029827	-	CG6048
CG6220	FBgn0033865	-	CG6220
CG6337	FBgn0033873	-	CG6337
CG6345	FBgn0037816	-	CG6345
CG6428	FBgn0029689	-	CG6428
CG6432	FBgn0039184	-	CG6432
CG6439	FBgn0038922	-	CG6439
CG6543	FBgn0033879	-	CG6543
CG6674	FBgn0036063	-	CG6674
CG6734	FBgn0032395	-	CG6734
CG6766	FBgn0032398	-	CG6766
CG6770	FBgn0032400	-	CG6770
CG6885	FBgn0036810	-	CG6885
CG6910	FBgn0036262	-	CG6910
CG6950	FBgn0037955	-	CG6950
CG6966	FBgn0038286	-	CG6966
CG7069	FBgn0038952	-	CG7069
CG7185	FBgn0035872	-	CG7185
CG7220	FBgn0033544	-	CG7220
CG7382	FBgn0031708	-	CG7382
CG7387	FBgn0035852	-	CG7387
CG7409	FBgn0035817	-	CG7409
CG7504	FBgn0035842	-	CG7504
CG7564	FBgn0036734	-	CG7564
CG7656	FBgn0036516	-	CG7656
CG7747	FBgn0034109	-	CG7747
CG7766	FBgn0030087	-	CG7766
CG7768	FBgn0036415	-	CG7768
CG7804	FBgn0036496	-	CG7804
CG8142	FBgn0030871	-	CG8142
CG8160	FBgn0034011	-	CG8160
CG8184	FBgn0030674	-	CG8184
CG8188	FBgn0030863	-	CG8188
CG8219	FBgn0035693	-	CG8219
CG8336	FBgn0036020	-	CG8336
CG8475	FBgn0031995	-	CG8475
CG8771	FBgn0033766	-	CG8771
CG8786	FBgn0036897	-	CG8786
CG8891	FBgn0031663	-	CG8891

CG9014	FBgn0028847	-	CG9014
CG9153	FBgn0035207	-	CG9153
CG9279	FBgn0036882	-	CG9279
CG9391	FBgn0037063	-	CG9391
CG9485	FBgn0034618	-	CG9485
CG9588	FBgn0038166	-	CG9588
CG9650	FBgn0029939	-	CG9650
CG9934	FBgn0032467	-	CG9934
CG9953	FBgn0035726	-	CG9953
CG3924	FBgn0013764	Chip	Chi
CG5686	FBgn0024248	chico	chico
CG4618	FBgn0035589	Charged multivesicular body protein 2b	CHMP2B
CG6198	FBgn0029503	CHORD	CHORD
CG2125	FBgn0004859	cubitus interruptus	ci
CG2028	FBgn0015024	Casein kinase Ialpha	CkIalpha
CG9790	FBgn0037613	Cyclin-dependent kinase subunit 85A	Cks85A
CG4774	FBgn0039360	Cardiolipin synthase	CLS
CG1555	FBgn0000337	cinnabar	cn
CG10965	FBgn0030028	Companion of reaper	Corp
CG11330	FBgn0000351	cortex	cort
CG14724	FBgn0019624	Cytochrome c oxidase subunit 5A	COX5A
CG9603	FBgn0040529	Cytochrome c oxidase subunit 7A	COX7A
CG6692	FBgn0013770	Cysteine proteinase-1	Cp1
CG3474	FBgn0028871	Cuticular protein 35B	Cpr35B
CG4280	FBgn0015924	croquemort	crq
CG32220	FBgn0052220	CMP-sialic acid synthase	Csas
CG4697	FBgn0028838	COP9 signalosome subunit 1a	CSN1a
CG3889	FBgn0027057	COP9 signalosome subunit 1b	CSN1b
CG18332	FBgn0027055	COP9 signalosome subunit 3	CSN3
CG8725	FBgn0027054	COP9 signalosome subunit 4	CSN4
CG14884	FBgn0027053	COP9 signalosome subunit 5	CSN5
CG6932	FBgn0028837	COP9 signalosome subunit 6	CSN6
CG2038	FBgn0028836	COP9 signalosome subunit 7	CSN7
CG6998	FBgn0011760	cut up	ctp
CG1877	FBgn0015509	Cullin 1	Cul1
CG1512	FBgn0032956	Cullin 2	Cul2
CG8711	FBgn0033260	Cullin 4	Cul4
CG1401	FBgn0039632	Cullin 5	Cul5
CG3510	FBgn0000405	Cyclin B	CycB
CG7281	FBgn0004597	Cyclin C	CycC
CG3938	FBgn0010382	Cyclin E	CycE
CG6292	FBgn0025455	Cyclin T	CycT
CG9916	FBgn0004432	Cyclophilin 1	Cyp1

CG4886	FBgn0028382	cyclophilin-33	cyp33
CG14032	FBgn0031693	Cyp4ac1	Cyp4ac1
CG10243	FBgn0033979	Cyp6a19	Cyp6a19
CG9438	FBgn0000473	Cytochrome P450-6a2	Cyp6a2
CG4486	FBgn0015039	Cytochrome P450-9b2	Cyp9b2
CG13892	FBgn0035141	Cyclophilin-like	Cypl
CG2048	FBgn0002413	discs overgrown	dco
CG5370	FBgn0010501	Death caspase-1	Dcp-1
CG9206	FBgn0001108	Dynactin 1, p150 subunit	DCTN1-p150
CG10846	FBgn0040228	Dynactin 5, p25 subunit	DCTN5-p25
CG14813	FBgn0028969	Coat Protein (coatomer) delta	deltaCOP
CG14899	FBgn0038438	Derlin-2	Der-2
CG5925	FBgn0043043	Desaturase 2	Desat2
CG12265	FBgn0264291	Deterin	Det
CG10981	FBgn0037384	degringolade	dgrn
CG14887	FBgn0004087	Dihydrofolate reductase	Dhfr
CG1768	FBgn0011202	diaphanous	dia
CG12284	FBgn0260635	Death-associated inhibitor of apoptosis 1	Diap1
CG1625	FBgn0033447	dilatory	dila
CG3058	FBgn0031601	Dim1	Dim1
CG5602	FBgn0262619	DNA ligase I	DNA-ligI
CG10578	FBgn0263106	DnaJ-like-1	DnaJ-1
CG9828	FBgn0032474	DnaJ homolog	DnaJ-H
CG6349	FBgn0259113	DNA polymerase alpha 180kD	DNApol-alpha180
CG5923	FBgn0005696	DNA polymerase alpha 73kD	DNApol-alpha73
CG5949	FBgn0263600	DNA-polymerase-delta	DNApol-delta
CG17051	FBgn0015379	dodo	dod
CG1616	FBgn0015929	disc proliferation abnormal	dpa
CG9885	FBgn0000490	decapentaplegic	dpp
CG1828	FBgn0002183	dre4	dre4
CG8863	FBgn0038145	DnaJ-like-2	Droj2
CG8091	FBgn0026404	Death regulator Nedd2-like caspase	Dronc
CG3210	FBgn0026479	Dynamin related protein 1	Drp1
CG10810	FBgn0283461	Drosomycin	Drs
CG3929	FBgn0000524	deltex	dx
CG7776	FBgn0000581	Enhancer of Polycomb	E(Pc)
CG6099	FBgn0002629	Enhancer of split m4, Bearded family member	E(spl)m4-BFM
CG8337	FBgn0002732	Enhancer of split malpha, Bearded family member	E(spl)malpha-BFM
CG6474	FBgn0000617	enhancer of yellow 1	e(y)1
CG6502	FBgn0000629	Enhancer of zeste	E(z)
CG4913	FBgn0026441	ENL/AF9-related	ear
CG3525	FBgn0000536	easily shocked	eas

CG1765	FBgn0000546	Ecdysone receptor	EcR
CG3810	FBgn0023511	ER degradation enhancer, mannosidase alpha-like 1	Edem1
CG5682	FBgn0032480	ER degradation enhancer, mannosidase alpha-like 2	Edem2
CG6542	FBgn0027506	Egg-derived tyrosine phosphatase	EDTP
CG4912	FBgn0032198	eEF1delta	eEF1delta
CG6341	FBgn0028737	Elongation factor 1 beta	Ef1beta
CG7425	FBgn0011217	effete	eff
CG12919	FBgn0033483	eiger	egr
CG9946	FBgn0261609	eukaryotic translation Initiation Factor 2alpha	eIF-2alpha
CG4153	FBgn0004926	Eukaryotic initiation factor 2beta	eIF-2beta
CG4035	FBgn0015218	Eukaryotic initiation factor 4E	eIF-4E
CG2677	FBgn0024996	eIF2B-beta	eIF2B-beta
CG10315	FBgn0034858	eIF2B-delta	eIF2B-delta
CG10124	FBgn0035709	eIF4E-4	eIF4E-4
CG10811	FBgn0023213	eukaryotic translation initiation factor 4G	eIF4G
CG18389	FBgn0264490	Ecdysone-induced protein 93F	Eip93F
CG17033	FBgn0036546	early girl	elgi
CG32072	FBgn0052072	Elongase 68alpha	Elo68alpha
CG9291	FBgn0266711	Elongin C	EloC
CG15433	FBgn0031604	Elongator complex protein 3	Elp3
CG13387	FBgn0020497	embargoed	emb
CG9543	FBgn0027496	Coat Protein (coatomer) epsilon	epsilonCOP
CG32703	FBgn0052703	Extracellularly regulated kinase 7	Erk7
CG1333	FBgn0261274	Endoplasmic reticulum oxidoreductin-1-like	Ero1L
CG14941	FBgn0000588	extra sexcombs	esc
CG5202	FBgn0032391	escl	escl
CG12140	FBgn0033465	Electron transfer flavoprotein-ubiquinone oxidoreductase	Etf-QO
CG30502	FBgn0050502	fatty acid 2-hydroylase	fa2h
CG7923	FBgn0029172	Fad2	Fad2
CG1945	FBgn0005632	fat facets	faf
CG10023	FBgn0020440	Focal adhesion kinase	Fak
CG7919	FBgn0028379	farinelli	fan
CG12812	FBgn0037781	Fancl	Fancl
CG9461	FBgn0037760	F-box protein 11	FBXO11
CG8824	FBgn0045063	fused lobes	fdl
CG8971	FBgn0030092	frataxin homolog	fh
CG6226	FBgn0013269	FK506-binding protein 1	FK506-bp1
CG11001	FBgn0013954	FK506-binding protein 2	FK506-bp2
CG9847	FBgn0010470	FK506-binding protein 14 ortholog	Fkbp14
CG4535	FBgn0029174	FK506-binding protein FKBP59	FKBP59
CG4396	FBgn0086675	found in neurons	fne
CG10580	FBgn0011591	fringe	fng
CG3143	FBgn0038197	forkhead box, sub-group O	foxo

CG12389	FBgn0025373	Farnesyl pyrophosphate synthase	Fpps
CG9526	FBgn0031815	farjavit	frj
CG12765	FBgn0033813	fates-shifted	fsd
CG17608	FBgn0026718	fu12	fu12
CG4274	FBgn0001086	fizzy	fzy
CG3033	FBgn0029818	Glycosylphosphatidylinositol anchor attachment 1 ortholog (H. sapiens)	GAA1
CG8893	FBgn0001092	Glyceraldehyde 3 phosphate dehydrogenase 2	Gapdh2
CG4012	FBgn0023081	genghis khan	gek
CG32038	FBgn0266124	ghiberti	ghi
CG6975	FBgn0005198	gigas	gig
CG6963	FBgn0250823	gilgamesh	gish
CG6207	FBgn0036144	GlcAT-P	GlcAT-P
CG3881	FBgn0032135	GlcAT-S	GlcAT-S
CG7254	FBgn0004507	Glycogen phosphorylase	GlyP
CG6904	FBgn0266064	Glycogen synthase	GlyS
CG3493	FBgn0034854	Golgin-245 ortholog (H. sapiens)	Golgin245
CG5520	FBgn0039562	Glycoprotein 93	Gp93
CG9042	FBgn0001128	Glycerol 3 phosphate dehydrogenase	Gpdh
CG32578	FBgn0086448	Gpi1	Gpi1
CG5688	FBgn0026432	Grip163	Grip163
CG31003	FBgn0046332	gasket	gskt
CG8938	FBgn0010226	Glutathione S transferase S1	GstS1
CG17035	FBgn0036545	GXIVsPLA2	GXIVsPLA2
CG8019	FBgn0001179	haywire	hay
CG7471	FBgn0015805	Histone deacetylase 1	HDAC1
CG11734	FBgn0031107	HECT and RLD domain containing protein 2	HERC2
CG14536	FBgn0031950	Homocysteine-induced endoplasmic reticulum protein	Herp
CG1318	FBgn0041630	Hexosaminidase 1	Hexo1
CG1787	FBgn0041629	Hexosaminidase 2	Hexo2
CG2947	FBgn0029676	Hsc/Hsp70-interacting protein related	HIP-R
CG32592	FBgn0030600	highwire	hiw
CG5005	FBgn0022740	HLH54F	HLH54F
CG10367	FBgn0263782	HMG Coenzyme A reductase	Hmgcr
CG4311	FBgn0010611	HMG Coenzyme A synthase	Hmgs
CG13425	FBgn0267791	Heterogeneous nuclear ribonucleoprotein K	HnRNP-K
CG3949	FBgn0015393	hoi-polloi	hoip
CG5198	FBgn0032250	hole-in-one	holn1
CG1594	FBgn0004864	hopscotch	hop
CG12855	FBgn0033973	Hermansky-Pudlak Syndrome 1 ortholog (H. sapiens)	HPS1
CG8937	FBgn0001216	Heat shock protein cognate 1	Hsc70-1
CG7756	FBgn0001217	Heat shock protein cognate 2	Hsc70-2
CG4147	FBgn0001218	Heat shock 70-kDa protein cognate 3	Hsc70-3

CG4264	FBgn0266599	Heat shock protein cognate 4	Hsc70-4
CG8542	FBgn0001220	Heat shock protein cognate 5	Hsc70-5
CG6603	FBgn0026418	Hsc70Cb	Hsc70Cb
CG5748	FBgn0001222	Heat shock factor	Hsf
CG11055	FBgn0034491	Hormone-sensitive lipase ortholog	Hsl
CG4463	FBgn0001224	Heat shock protein 23	Hsp23
CG4183	FBgn0001225	Heat shock protein 26	Hsp26
CG4466	FBgn0001226	Heat shock protein 27	Hsp27
CG12101	FBgn0015245	Heat shock protein 60	Hsp60
CG7235	FBgn0031728	Hsp60C	Hsp60C
CG16954	FBgn0032525	Hsp60D	Hsp60D
CG4167	FBgn0001227	Heat shock gene 67Ba	Hsp67Ba
CG5436	FBgn0001230	Heat shock protein 68	Hsp68
CG1242	FBgn0001233	Heat shock protein 83	Hsp83
CG9484	FBgn0002431	hyperplastic discs	hyd
CG10574	FBgn0028429	Inhibitor-2	I-2
CG4924	FBgn0029079	icln	icln
CG10850	FBgn0041147	imaginal discs arrested	ida
CG9623	FBgn0001250	inflated	if
CG9078	FBgn0001941	infertile crescent	ifc
CG11143	FBgn0025885	Inos	Inos
CG18402	FBgn0283499	Insulin-like receptor	InR
CG4501	FBgn0266375	Inositol 1,4,5-triphosphate kinase 2	IP3K2
CG3028	FBgn0016672	Inositol polyphosphate 1-phosphatase	Ipp
CG31423	FBgn0051423	Ionotropic receptor 94c	Ir94c
CG4583	FBgn0261984	Inositol-requiring enzyme-1	Ire1
CG4715	FBgn0031305	Iris	Iris
CG4900	FBgn0024958	Iron regulatory protein 1A	Irp-1A
CG6342	FBgn0024957	Iron regulatory protein 1B	Irp-1B
CG1063	FBgn0010051	Inositol 1,4,5,-tris-phosphate receptor	Itp-r83A
CG15106	FBgn0034406	Juvenile hormone epoxide hydrolase 3	Jheh3
CG9423	FBgn0027338	karyopherin alpha3	Kap-alpha3
CG11759	FBgn0028421	Kinesin associated protein 3	Kap3
CG1059	FBgn0087013	Karyopherin beta 3	Karybeta3
CG3861	FBgn0261955	knockdown	kdn
CG5575	FBgn0011236	ken and barbie	ken
CG12423	FBgn0040038	-	klhl10
CG3571	FBgn0037978	-	KLHL18
CG12233	FBgn0027291	lethal (1) G0156	l(1)G0156
CG3688	FBgn0001974	lethal (2) 35Bd	l(2)35Bd
CG4533	FBgn0011296	lethal (2) essential for life	l(2)efl
CG5504	FBgn0002174	lethal (2) tumorous imaginal discs	l(2)tid
CG6302	FBgn0010741	lethal (3) 01239	l(3)01239

CG5931	FBgn0263599	lethal (3) 72Ab	l(3)72Ab
CG4162	FBgn0002524	lace	lace
CG5231	FBgn0029158	Lipoic acid synthase	Las
CG4088	FBgn0005654	latheo	lat
CG17280	FBgn0034877	levy	levy
CG10743	FBgn0036376	Liprin-beta	Liprin-beta
CG8798	FBgn0036892	Lon protease	Lon
CG11335	FBgn0039848	lysyl oxidase-like	lox
CG4402	FBgn0034660	lysyl oxidase-like 2	lox2
CG8709	FBgn0263593	Lipin	Lpin
CG8532	FBgn0028582	liquid facets	lqf
CG10374	FBgn0039114	Lipid storage droplet-1	Lsd-1
CG3004	FBgn0264691	-	Lst8
CG3018	FBgn0010602	lesswright	lwr
CG11896	FBgn0038488	mann-cup	m-cup
CG2072	FBgn0026326	-	Mad1
CG11669	FBgn0033296	Maltase A7	Mal-A7
CG14935	FBgn0032382	Maltase B2	Mal-B2
CG3869	FBgn0029870	Mitochondrial assembly regulatory factor	Marf
CG9241	FBgn0032929	Minichromosome maintenance 10	Mcm10
CG7538	FBgn0014861	Minichromosome maintenance 2	Mcm2
CG4206	FBgn0024332	Minichromosome maintenance 3	Mcm3
CG4082	FBgn0017577	Minichromosome maintenance 5	Mcm5
CG4039	FBgn0025815	Minichromosome maintenance 6	Mcm6
CG31991	FBgn0004797	midway	mdy
CG3697	FBgn0002707	meiotic 9	mei-9
CG14228	FBgn0086384	Merlin	Mer
CG1771	FBgn0004456	multiple edematous wings	mew
CG3415	FBgn0030731	peroxisomal Multifunctional enzyme type 2	Mfe2
CG6719	FBgn0264694	merry-go-round	mgr
CG5841	FBgn0263601	mind bomb 1	mib1
CG17492	FBgn0086442	mind bomb 2	mib2
CG11680	FBgn0002774	maleless	mle
CG1866	FBgn0039581	Moca-cyp	Moca-cyp
CG15437	FBgn0027609	modifier of rpr and grim, ubiquitously expressed	morgue
CG3060	FBgn0002791	morula	mr
CG6214	FBgn0032456	Multidrug-Resistance like Protein 1	MRP
CG9378	FBgn0014023	mitochondrial ribosomal protein L47	mRpL47
CG5924	FBgn0032154	mitochondrial DNA helicase	mtDNA-helicase
CG7476	FBgn0035847	methuselah-like 7	mthl7
CG8274	FBgn0013756	Megator	Mtor
CG9342	FBgn0266369	Microsomal triacylglycerol transfer protein	Mtp
CG4389	FBgn0028479	Mitochondrial trifunctional protein alpha subunit	Mtpalpha

CG7109	FBgn0004177	microtubule star	mts
CG1134	FBgn0035483	Mitochondrial E3 ubiquitin protein ligase 1 homologue	Mul1
CG10798	FBgn0262656	Myc	Myc
CG1560	FBgn0004657	myospheroid	mys
CG3936	FBgn0004647	Notch	N
CG14222	FBgn0031043	N(alpha)-acetyltransferase 20	NAA20
CG5330	FBgn0015268	Nucleosome assembly protein 1	Nap1
CG10207	FBgn0016684	Na[+]-dependent inorganic phosphate cotransporter	NaPi-T
CG9172	FBgn0030718	NADH dehydrogenase (ubiquinone) 20 kDa subunit	ND-20
CG2014	FBgn0039669	NADH dehydrogenase (ubiquinone) 20 kDa subunit-like	ND-20L
CG12079	FBgn0266582	NADH dehydrogenase (ubiquinone) 30 kDa subunit	ND-30
CG6020	FBgn0037001	NADH dehydrogenase (ubiquinone) 39 kDa subunit	ND-39
CG6343	FBgn0019957	NADH dehydrogenase (ubiquinone) 42 kDa subunit	ND-42
CG1970	FBgn0039909	NADH dehydrogenase (ubiquinone) 49 kDa subunit	ND-49
CG11913	FBgn0039331	NADH dehydrogenase (ubiquinone) 49 kDa subunit-like	ND-49L
CG11423	FBgn0034251	NADH dehydrogenase (ubiquinone) 51 kDa subunit-like 1	ND-51L1
CG2286	FBgn0017566	NADH dehydrogenase (ubiquinone) 75 kDa subunit	ND-75
CG9160	FBgn0011361	NADH dehydrogenase (ubiquinone) acyl carrier protein	ND-ACP
CG3192	FBgn0029888	NADH dehydrogenase (ubiquinone) ASHI subunit	ND-ASHI
CG15434	FBgn0040705	NADH dehydrogenase (ubiquinone) B8 subunit	ND-B8
CG8844	FBgn0021967	NADH dehydrogenase (ubiquinone) PDSW subunit	ND-PDSW
CG32177	FBgn0052177	Nedd4 family interacting protein	Ndfip
CG10679	FBgn0032725	Nedd8	Nedd8
CG32721	FBgn0027553	NELF-B	NELF-B
CG2245	FBgn0261479	nero	nero
CG9655	FBgn0026630	nessy	nes
CG32635	FBgn0265416	Neuropilin and tolloid-like	Neto
CG11988	FBgn0002932	neuralized	neur
CG3966	FBgn0002936	neither inactivation nor afterpotential A	ninaA
CG9347	FBgn0002937	neither inactivation nor afterpotential B	ninaB
CG6728	FBgn0037896	ninaG	ninaG
CG7917	FBgn0016685	Nucleoplasmin	Nlp
CG3460	FBgn0023542	Nonsense-mediated mRNA 3	Nmd3
CG8362	FBgn0028997	nmdyn-D7	nmdyn-D7
CG3620	FBgn0262738	no receptor potential A	norpA
CG4166	FBgn0013717	non-stop	not
CG5722	FBgn0024320	Niemann-Pick type C-1a	Npc1a
CG4699	FBgn0262527	non-specific lethal 1	nsl1
CG10855	FBgn0035461	nutcracker	ntc
CG6743	FBgn0027868	Nucleoporin 107kD	Nup107
CG6958	FBgn0039004	Nucleoporin 133kD	Nup133
CG4453	FBgn0061200	Nucleoporin 153kD	Nup153
CG4579	FBgn0021761	Nucleoporin 154kD	Nup154

CG4738	FBgn0262647	Nucleoporin 160kD	Nup160
CG11943	FBgn0031078	Nucleoporin 205kD	Nup205
CG7671	FBgn0038609	Nucleoporin 43kD	Nup43
CG8722	FBgn0033247	Nucleoporin at 44A	Nup44A
CG2158	FBgn0033264	Nucleoporin 50kD	Nup50
CG8831	FBgn0033737	Nucleoporin 54kD	Nup54
CG6251	FBgn0034118	Nucleoporin 62kD	Nup62
CG5733	FBgn0034310	Nucleoporin 75kD	Nup75
CG11092	FBgn0027537	Nucleoporin 93kD-1	Nup93-1
CG7262	FBgn0038274	Nucleoporin 93kD-2	Nup93-2
CG12366	FBgn0033901	O-fucosyltransferase 1	O-fut1
CG3573	FBgn0023508	Oculocerebrorenal syndrome of Lowe	Ocrl
CG1795	FBgn0027864	8-oxoguanine DNA glycosylase	Ogg1
CG1133	FBgn0003002	odd paired	opa
CG10667	FBgn0022772	Origin recognition complex subunit 1	Orc1
CG3041	FBgn0015270	Origin recognition complex subunit 2	Orc2
CG1584	FBgn0023180	Origin recognition complex subunit 6	Orc6
CG6708	FBgn0020626	Oxysterol binding protein	Osbp
CG15188	FBgn0037430	Osiris 20	Osi20
CG15589	FBgn0037409	Osiris 24	Osi24
CG12743	FBgn0003023	ovarian tumor	otu
CG18445	FBgn0033476	oysgedart	oys
CG5119	FBgn0265297	-	pAbp
CG9907	FBgn0264255	paralytic	para
CG10523	FBgn0041100	parkin	park
CG10335	FBgn0036271	Porphobilinogen synthase	Pbgs
CG5109	FBgn0003044	Polycomblike	Pcl
CG3291	FBgn0020261	pacman	pcm
CG9193	FBgn0005655	Proliferating cell nuclear antigen	PCNA
CG8279	FBgn0038237	Phosphodiesterase 6	Pde6
CG9009	FBgn0027601	pudgy	pdgy
CG4899	FBgn0011693	Photoreceptor dehydrogenase	Pdh
CG1210	FBgn0020386	Phosphoinositide-dependent kinase 1	Pdk1
CG2087	FBgn0037327	pancreatic eIF-2alpha kinase	PEK
CG6760	FBgn0013563	Peroxin 1	Pex1
CG7864	FBgn0035233	Peroxin 10	Pex10
CG3947	FBgn0037019	Peroxin 16	Pex16
CG5325	FBgn0032407	Peroxin 19	Pex19
CG14815	FBgn0023516	Peroxin 5	Pex5
CG3127	FBgn0250906	Phosphoglycerate kinase	Pgk
CG3895	FBgn0004860	polyhomeotic distal	ph-d
CG10108	FBgn0013725	phyllopod	phyl
CG8979	FBgn0033669	-	PI31

CG2699	FBgn0020622	Pi3K21B	Pi3K21B
CG5373	FBgn0015277	Phosphotidylinositol 3 kinase 59F	Pi3K59F
CG11621	FBgn0015278	Phosphotidylinositol 3 kinase 68D	Pi3K68D
CG4141	FBgn0015279	Pi3K92E	Pi3K92E
CG2929	FBgn0037339	Pi4KIIalpha	Pi4KIIalpha
CG10260	FBgn0267350	Phosphatidylinositol 4-kinase III alpha	PI4KIIIalpha
CG7769	FBgn0260962	piccolo	pic
CG11940	FBgn0261811	pico	pico
CG12077	FBgn0035435	Phosphatidylinositol glycan anchor biosynthesis, class C ortholog (H. sapiens)	PIG-C
CG13089	FBgn0032052	Phosphatidylinositol glycan anchor biosynthesis, class U ortholog (H. sapiens)	PIG-U
CG4523	FBgn0029891	PTEN-induced putative kinase 1	Pink1
CG3682	FBgn0034789	Phosphatidylinositol 4-phosphate 5-kinase at 59B	PIP5K59B
CG9245	FBgn0030670	Phosphatidylinositol synthase	Pis
CG4268	FBgn0016696	Pitslre	Pitslre
CG4574	FBgn0004611	Phospholipase C at 21C	Plc21C
CG6792	FBgn0032401	Promyelocytic leukemia zinc finger ortholog	Plzf
CG8705	FBgn0013726	peanut	pnut
CG14472	FBgn0011230	purity of essence	poe
CG3975	FBgn0283467	-	Pol32
CG9324	FBgn0032884	Pomp	Pomp
CG5684	FBgn0036239	Pop2	Pop2
CG6647	FBgn0004363	porin	porin
CG4909	FBgn0040294	Plenty of SH3s	POSH
CG5650	FBgn0004103	Protein phosphatase 1 at 87B	Pp1-87B
CG17291	FBgn0260439	Protein phosphatase 2A at 29B	Pp2A-29B
CG9952	FBgn0020257	Partner of paired	Ppa
CG5629	FBgn0261285	Phosphopantothenoylcysteine synthetase	Ppcs
CG18110	FBgn0039677	pickpocket 30	ppk30
CG11820	FBgn0039270	Poly-glutamine tract binding protein 1	PQBP1
CG9296	FBgn0032059	Prenyl-binding protein	PrBP
CG18495	FBgn0263121	Proteasome alpha1 subunit	Prosalpha1
CG5266	FBgn0086134	Proteasome alpha2 subunit	Prosalpha2
CG9327	FBgn0261394	Proteasome alpha3 subunit	Prosalpha3
CG1736	FBgn0261395	Proteasome alpha3 subunit, Testis-specific	Prosalpha3T
CG3422	FBgn0004066	Proteasome alpha4 subunit	Prosalpha4
CG17268	FBgn0265606	Proteasome alpha4 subunit, Testis-specific 1	Prosalpha4T1
CG4569	FBgn0017556	Proteasome alpha4 subunit, Testis-specific 2	Prosalpha4T2
CG10938	FBgn0016697	Proteasome alpha5 subunit	Prosalpha5
CG4904	FBgn0250843	Proteasome alpha6 subunit	Prosalpha6
CG5648	FBgn0032492	Proteasome alpha6 subunit, Testis-specific	Prosalpha6T
CG1519	FBgn0023175	Proteasome alpha7 subunit	Prosalpha7
CG8392	FBgn0010590	Proteasome beta1 subunit	Prosbeta1

CG3329	FBgn0023174	Proteasome beta2 subunit	Prosbeta2
CG18341	FBgn0029812	Proteasome beta2 subunit-related 1	Prosbeta2R1
CG12161	FBgn0037296	Proteasome beta2 subunit-related 2	Prosbeta2R2
CG11981	FBgn0026380	Proteasome beta3 subunit	Prosbeta3
CG17331	FBgn0032596	Proteasome beta4 subunit	Prosbeta4
CG17301	FBgn0031442	Proteasome beta4 subunit-related 1	Prosbeta4R1
CG17302	FBgn0031443	Proteasome beta4 subunit-related 2	Prosbeta4R2
CG12323	FBgn0029134	Proteasome beta5 subunit	Prosbeta5
CG9868	FBgn0034842	Proteasome beta5 subunit-related 1	Prosbeta5R1
CG31742	FBgn0051742	Proteasome beta5 subunit-related 2	Prosbeta5R2
CG4097	FBgn0002284	Proteasome beta6 subunit	Prosbeta6
CG12000	FBgn0250746	Proteasome beta7 subunit	Prosbeta7
CG5519	FBgn0261119	Pre-RNA processing factor 19	Prp19
CG7217	FBgn0038570	Peroxiredoxin 5	Prx5
CG3886	FBgn0005624	Posterior sex combs	Psc
CG18803	FBgn0019947	Presenilin	Psn
CG5671	FBgn0026379	Phosphatase and tensin homolog	Pten
CG11212	FBgn0262867	Patched-related	Ptr
CG7660	FBgn0261987	Peroxinectin-like	Pxt
CG7070	FBgn0267385	Pyruvate kinase	PyK
CG13732	FBgn0036730	quijote	qjt
CG31005	FBgn0051005	qless	qless
CG8593	FBgn0019662	quemao	qm
CG9139	FBgn0262937	Rabaptin-5-associated exchange factor for Rab5 ortholog (H. sapiens)	Rabex-5
CG7111	FBgn0020618	Receptor of activated protein kinase C 1	Rack1
CG1836	FBgn0026777	Rad23	Rad23
CG9862	FBgn0034646	Rae1	Rae1
CG11968	FBgn0037647	Ras-related GTP binding A/B ortholog (H. sapiens)	RagA-B
CG3000	FBgn0262699	retina aberrant in pattern	rap
CG4320	FBgn0029840	raptor	raptor
CG9375	FBgn0003205	Ras oncogene at 85D	Ras85D
CG5585	FBgn0036973	Retinoblastoma binding protein 5	Rbbp5
CG17766	FBgn0023510	Rabconnectin-3B	Rbcn-3B
CG11111	FBgn0003218	retinal degeneration B	rdgB
CG10360	FBgn0003231	refractory to sigma P	ref(2)P
CG1591	FBgn0029133	REG	REG
CG9750	FBgn0040075	reptin	rept
CG13624	FBgn0039209	Repressed by TOR	REPTOR
CG5313	FBgn0032244	Replication factor C subunit 3	RfC3
CG6258	FBgn0028700	Replication factor C 38kD subunit	RfC38
CG1081	FBgn0041191	Ras homolog enriched in brain ortholog (H. sapiens)	Rheb
CG8002	FBgn0031006	rapamycin-insensitive companion of Tor	rictor

CG4420	FBgn0030753	rings lost	rngo
CG16788	FBgn0037707	RNA-binding protein S1	RnpS1
CG5371	FBgn0011703	Ribonucleoside diphosphate reductase large subunit	RnrL
CG8975	FBgn0011704	Ribonucleoside diphosphate reductase small subunit	RnrS
CG16982	FBgn0025638	Regulator of cullins 1a	Roc1a
CG16988	FBgn0040291	Regulator of cullins 1b	Roc1b
CG8998	FBgn0044020	Regulator of cullins 2	Roc2
CG6155	FBgn0014877	Roe1	Roe1
CG3180	FBgn0262955	RNA polymerase II 140kD subunit	RpII140
CG3284	FBgn0004855	RNA polymerase II 15kD subunit	RpII15
CG1554	FBgn0003277	RNA polymerase II 215kD subunit	RpII215
CG7885	FBgn0026373	RNA polymerase II 33kD subunit	RpII33
CG2960	FBgn0003941	Ribosomal protein L40	RpL40
CG7762	FBgn0028695	Regulatory particle non-ATPase 1	Rpn1
CG7619	FBgn0015283	Regulatory particle non-ATPase 10	Rpn10
CG18174	FBgn0028694	Regulatory particle non-ATPase 11	Rpn11
CG4157	FBgn0028693	Regulatory particle non-ATPase 12	Rpn12
CG11552	FBgn0036465	Regulatory particle non-ATPase 12-related	Rpn12R
CG13349	FBgn0033886	Regulatory particle non-ATPase 13	Rpn13
CG6789	FBgn0029745	Regulatory particle non-ATPase 13-related	Rpn13R
CG11888	FBgn0028692	Regulatory particle non-ATPase 2	Rpn2
CG1100	FBgn0028690	Regulatory particle non-ATPase 5	Rpn5
CG10149	FBgn0028689	Regulatory particle non-ATPase 6	Rpn6
CG5378	FBgn0028688	Regulatory particle non-ATPase 7	Rpn7
CG3416	FBgn0002787	Regulatory particle non-ATPase 8	Rpn8
CG10230	FBgn0028691	Regulatory particle non-ATPase 9	Rpn9
CG4319	FBgn0011706	reaper	rpr
CG5271	FBgn0003942	Ribosomal protein S27A	RpS27A
CG1341	FBgn0028687	Regulatory particle triple-A ATPase 1	Rpt1
CG5289	FBgn0015282	Regulatory particle triple-A ATPase 2	Rpt2
CG16916	FBgn0028686	Regulatory particle triple-A ATPase 3	Rpt3
CG3455	FBgn0028685	Regulatory particle triple-A ATPase 4	Rpt4
CG7257	FBgn0036224	Regulatory particle triple-A ATPase 4-related	Rpt4R
CG10370	FBgn0028684	Regulatory particle triple-A ATPase 5	Rpt5
CG1489	FBgn0020369	Regulatory particle triple-A ATPase 6	Rpt6
CG7642	FBgn0003308	rosy	ry
CG10539	FBgn0283472	Ribosomal protein S6 kinase	S6k
CG9128	FBgn0283500	Sac1 phosphatase	Sac1
CG12789	FBgn0025697	scavenger receptor acting in neural tissue and majority of rhodopsin is absent	santa-maria
CG12070	FBgn0000416	Saposin-related	Sap-r
CG11006	FBgn0262714	Sin3A-associated protein 130	Sap130
CG1664	FBgn0003321	small bristles	sbr

CG3766	FBgn0011232	scattered	scat
CG8095	FBgn0003328	scab	scb
CG5595	FBgn0003330	Sex combs extra	Sce
CG3576	FBgn0040918	schlank	schlank
CG9495	FBgn0003334	Sex comb on midleg	Scm
CG8885	FBgn0262467	Synthesis of cytochrome c oxidase	Scox
CG7113	FBgn0021765	scully	scu
CG3283	FBgn0014028	Succinate dehydrogenase, subunit B (iron-sulfur)	SdhB
CG7359	FBgn0260855	Sec22 ortholog (S. cerevisiae)	Sec22
CG9539	FBgn0086357	Sec61 alpha subunit	Sec61alpha
CG10130	FBgn0010638	Sec61 beta subunit	Sec61beta
CG14214	FBgn0031049	Sec61 gamma subunit	Sec61gamma
CG9904	FBgn0040336	Seipin	Seipin
CG1403	FBgn0011710	Septin 1	Sep1'
CG16944	FBgn0003360	stress-sensitive B	sesB
CG6987	FBgn0283477	Splicing factor 2	SF2
CG2621	FBgn0003371	shaggy	sgg
CG9617	FBgn0265101	suppressor-of-G2-allele-of-skp1	Sgt1
CG32423	FBgn0052423	alan shepard	shep
CG3722	FBgn0003391	shotgun	shg
CG9198	FBgn0004391	shattered	shtd
CG4735	FBgn0003401	shutdown	shu
CG9949	FBgn0003410	seven in absentia	sina
CG13030	FBgn0259794	sina homologue	sinah
CG1937	FBgn0039875	septin interacting protein 3	sip3
CG7224	FBgn0031971	Starvation-upregulated protein	Sirup
CG32434	FBgn0026179	schizo	siz
CG1747	FBgn0030300	Sphingosine kinase 1	Sk1
CG32484	FBgn0052484	Sphingosine kinase 2	Sk2
CG13701	FBgn0036786	sickle	skl
CG9772	FBgn0037236	-	Skp2
CG16983	FBgn0025637	SKP1-related A	SkpA
CG12227	FBgn0034863	SKP1-related F	SkpF
CG9985	FBgn0016984	skittles	sktl
CG4200	FBgn0003416	small wing	sl
CG5186	FBgn0261477	scruin like at the midline	slim
CG3412	FBgn0283468	supernumerary limbs	slmb
CG8427	FBgn0023167	Small ribonucleoprotein particle protein SmD3	SmD3
CG8571	FBgn0016983	smallminded	smid
CG16725	FBgn0036641	survival motor neuron	Smn
CG32380	FBgn0052380	SMSr	SMSr
CG4494	FBgn0264922	smt3	smt3
CG4943	FBgn0029006	SMAD specific E3 ubiquitin protein ligase	Smurf

CG4528	FBgn0003449	sans fille	snf
CG17299	FBgn0264357	SNF4/AMP-activated protein kinase gamma subunit	SNF4Agamma
CG11793	FBgn0003462	Superoxide dismutase	Sod
CG8905	FBgn0010213	Superoxide dismutase 2 (Mn)	Sod2
CG11153	FBgn0039938	Sox102F	Sox102F
CG13570	FBgn0015544	spaghetti	spag
CG5977	FBgn0039141	spastin	spas
CG11124	FBgn0033170	secretory Phospholipase A2	sPLA2
CG8946	FBgn0010591	Sphingosine-1-phosphate lyase	Sply
CG4804	FBgn0032178	Serpin 31A	Spn31A
CG1865	FBgn0024293	Serpin 43Ab	Spn43Ab
CG1859	FBgn0044011	Serpin 43Ad	Spn43Ad
CG10956	FBgn0034195	Serpin 53F	Spn53F
CG11840	FBgn0031260	Signal peptide peptidase	Spp
CG17689	FBgn0036374	Spt20	Spt20
CG3169	FBgn0037981	Spt3	Spt3
CG12372	FBgn0028683	spt4	spt4
CG6506	FBgn0030874	Spt7	Spt7
CG11274	FBgn0036340	SRm160	SRm160
CG3992	FBgn0003507	serpent	srp
CG6238	FBgn0029157	slingshot	ssh
CG11115	FBgn0037202	Suppressor of Stem-Loop mutation ortholog (S. cerevisiae)	Ssl1
CG4817	FBgn0010278	Structure specific recognition protein	Ssrp
CG8739	FBgn0086784	stambha A	stmA
CG5203	FBgn0027052	STIP1 homology and U-box containing protein 1	STUB1
CG32130	FBgn0086708	starvin	stv
CG4244	FBgn0003557	Suppressor of deltex	Su(dx)
CG4086	FBgn0004465	Suppressor of ref(2)P sterility	Su(P)
CG8068	FBgn0003612	Suppressor of variegation 2-10	Su(var)2-10
CG8013	FBgn0020887	Su(z)12	Su(z)12
CG3905	FBgn0265623	Suppressor of zeste 2	Su(z)2
CG2212	FBgn0003656	swiss cheese	sws
CG6562	FBgn0034691	Synaptojanin	Synj
CG2859	FBgn0028398	TBP-associated factor 10	Taf10
CG3069	FBgn0026324	TBP-associated factor 10b	Taf10b
CG4079	FBgn0011291	TBP-associated factor 11	Taf11
CG10756	FBgn0032847	TBP-associated factor 13	Taf13
CG5444	FBgn0010280	TBP-associated factor 4	Taf4
CG7704	FBgn0010356	TBP-associated factor 5	Taf5
CG31057	FBgn0266579	tau	tau
CG8766	FBgn0026619	Tafazzin	Taz
CG7861	FBgn0033055	Tubulin-specific chaperone E	Tbce
CG9874	FBgn0003687	TATA binding protein	Tbp

CG10327	FBgn0025790	TAR DNA-binding protein-43 homolog	TBPH
CG2331	FBgn0261014	TER94	TER94
CG5193	FBgn0004915	Transcription factor IIB	TfIIB
CG10281	FBgn0010282	Transcription factor IIFalpha	TfIIFalpha
CG6538	FBgn0010421	Transcription factor TFIIFbeta	TfIIFbeta
CG9984	FBgn0010416	TH1	TH1
CG4581	FBgn0025352	Thiolase	Thiolase
CG8846	FBgn0261560	Thor	Thor
CG3234	FBgn0014396	timeless	tim
CG1539	FBgn0082582	tropomodulin	tmod
CG8595	FBgn0034476	Toll-7	Toll-7
CG10123	FBgn0040268	Topoisomerase 3alpha	Top3alpha
CG15104	FBgn0267351	Topoisomerase I-interacting protein	Topors
CG5092	FBgn0021796	Target of rapamycin	Tor
CG3024	FBgn0025615	Torsin	Torsin
CG10387	FBgn0015553	tosca	tos
CG3048	FBgn0026319	TNF-receptor-associated factor 4	Traf4
CG10961	FBgn0265464	TNF-receptor-associated factor 6	Traf6
CG3152	FBgn0026761	Trap1	Trap1
CG8743	FBgn0262516	Transient receptor potential cation channel, mucolipin ortholog	Trpml
CG8651	FBgn0003862	trithorax	trx
CG3181	FBgn0024920	Thymidylate synthase	Ts
CG6147	FBgn0026317	Tsc1	Tsc1
CG11415	FBgn0024361	Tetraspanin 2A	Tsp2A
CG10210	FBgn0039117	twister	tst
CG6235	FBgn0004889	twins	tws
CG13401	FBgn0027780	U26	U26
CG3582	FBgn0017457	U2 small nuclear riboprotein auxiliary factor 38	U2af38
CG9998	FBgn0005411	U2 small nuclear riboprotein auxiliary factor 50	U2af50
CG1782	FBgn0023143	Ubiquitin activating enzyme 1	Uba1
CG7528	FBgn0029113	Ubiquitin activating enzyme 2	Uba2
CG13343	FBgn0263697	Ubiquitin activating enzyme 3	Uba3
CG5788	FBgn0026316	Ubiquitin conjugating enzyme 10	Ubc10
CG6720	FBgn0015320	Ubiquitin conjugating enzyme 2	Ubc2
CG8284	FBgn0015321	Ubiquitin conjugating enzyme 4	Ubc4
CG2013	FBgn0004436	Ubiquitin conjugating enzyme 6	Ubc6
CG4443	FBgn0267384	Ubiquitin conjugating enzyme 7	Ubc7
CG12799	FBgn0017456	Ubiquitin conjugating enzyme 84D	Ubc84D
CG9602	FBgn0267383	Ubiquitin conjugating enzyme 87F	Ubc87F
CG2257	FBgn0029996	Ubiquitin conjugating enzyme E2H	UbcE2H
CG7375	FBgn0035853	Ubiquitin conjugating enzyme E2M	UbcE2M
CG6190	FBgn0061469	Ubiquitin protein ligase E3A	Ube3a
CG14224	FBgn0031057	Ubiquilin	Ubqn

CG9086	FBgn0030809	Ubr1 ubiquitin ligase	Ubr1
CG3431	FBgn0011327	Ubiquitin carboxy-terminal hydrolase L5 ortholog	Uch-L5
CG1950	FBgn0030370	Uch-L5-related	Uch-L5R
CG10640	FBgn0035601	Ubiquitin-conjugating enzyme variant 1A	Uev1A
CG6233	FBgn0036136	Ubiquitin fusion-degradation 1-like	Ufd1-like
CG4347	FBgn0035978	UGP	UGP
CG12359	FBgn0027603	Ulp1	Ulp1
CG2999	FBgn0025726	unc-13	unc-13
CG4169	FBgn0250814	Ubiquinol-cytochrome c reductase core protein 2	UQCR-C2
CG14181	FBgn0035965	USE1 ortholog (S. cerevisiae)	Use1
CG4380	FBgn0003964	ultraspiracle	usp
CG6116	FBgn0032499	UV-resistance associated gene	Uvrag
CG5014	FBgn0029687	VAMP-associated protein of 33kDa ortholog A	Vap-33A
CG13221	FBgn0041174	von Hippel-Lindau	Vhl
CG10682	FBgn0264848	vihar	vih
CG3299	FBgn0004397	Vinculin	Vinc
CG9746	FBgn0260935	Vacuolar protein sorting 15	Vps15
CG2759	FBgn0003996	white	w
CG4448	FBgn0039067	will decrease acetylation	wda
CG5643	FBgn0027492	widerborst	wdb
CG17437	FBgn0040066	will die slowly	wds
CG5675	FBgn0026313	X11L	X11L
CG9433	FBgn0261850	Xeroderma pigmentosum D ortholog (H. sapiens)	Xpd
CG4600	FBgn0040064	yippee interacting protein 2	yip2
CG4005	FBgn0034970	yorkie	yki
CG32685	FBgn0052685	-	ZAP3
CG10267	FBgn0037446	Zinc-finger protein	Zif
CG13189	FBgn0033665	Zinc/iron regulated transporter-related protein 48C	Zip48C
CG10125	FBgn0024177	zero population growth	zpg
CG5847	FBgn0036985	zye	zye

Figure 1: Plate maps of dsRNA spotted on 384-well plates for the S2R+ cell-based screen (Chapter II).
"0c": Uninduced; "500c":500µM $CuSO_4$; "1000c":1000µM $CuSO_4$; "??????": Scrambled dsRNA.

Plate 1, 24 hours

	1	2	3	4	5	6	7	8	9	10	11	12	13	14	15	16	17	18	19	20	21	22	23	24
A	CG17291	CG3500	CG30429	CG11444	CG32685	GFP	CG13116	1000c	CG4319	CG17291	VAPB	CG3766	CG4461	CG30161	CG31742	CG32703	CG14043	CG11811	CG32236	CG13296	CG16725	CG17726	CG17985	CG14718
B	TBPH	CG17301	CG1836	CG10125	CG32177	CG13732	CG10267	CG10207	CG13994	CG2852	CG30429	CG32177	CG13296	CG3284	CG16935	CG15767	500c	CG1877	CG2852	CG3492	CG3000	CG15160	CG3024	CG11330
C	CG32437	CG32486	CG17753	0c	CG30043	CG12822	CG1937	CG17327	CG17753	CG11811	CG10315	CG13387	SOD	CG14715	CG31057	CG12743	CG18341	CG31769	CG14715	CG12822	CG10089	CG2038	TBPH	CG13063
D	CG31769	CG13387	CG17343	CG13063	CG18803	CG3024	CG10327	CG14181	VAPB	CG18332	CG17726	CG10679	CG13732	CG3476	CG10089	CG10267	CG10243	CG10125	CG31528	CG16935	CG15188	CG15767	CG12743	SOD
E	CG32703	GFP	CG3492	CG4486	CG15800	CG2013	CG11777	CG4461	CG32685	CG14125	CG10743	CG13063	CG14006	CG17760	TBPH	CG1836	CG13075	CG4461	CG3457	CG10846	CG1242	CG14326	CG3766	CG14435
F	???????	CG14006	CG3457	CG13221	CG14606	CG10315	CG1877	CG17982	CG3457	CG18174	CG10125	CG11415	???????	CG13116	CG11444	CG16725	VAPB	CG18110	CG3975	CG18174	0c	CG4086	CG17268	CG32437
G	CG14222	CG1625	CG2038	CG15645	CG10679	CG14718	CG32236	CG15237	500c	CG11560	1000c	CG1625	CG14043	CG17302	CG17985	CG14435	CG1736	CG13732	CG2013	CG11415	CG13387	CG13221	CG14125	CG18803
H	CG31057	500c	SOD	CG30350	CG18174	CG11330	CG3000	CG13075	CG17343	CG4086	CG10327	CG14326	CG1866	CG4005	CG10108	CG10243	CG17343	CG31057	CG32177	CG15589	CG18332	CG1836	???????	CG32685
I	CG11415	CG30161	CG14125	CG14032	CG4443	CG15767	CG14715	CG17760	CG32236	CG14444	CG1736	CG1877	CG3492	CG15589	CG15237	CG3500	CG15237	CG14032	CG1560	CG14606	CG11560	CG31742	CG1866	VAPB
J	CG12743	CG10855	CG14444	CG13048	CG1409	CG14326	CG1736	CG15160	CG32437	VAPB	CG14222	CG17301	CG13048	CG3474	GFP	CG3000	CG14837	CG17302	CG13048	CG3284	CG30161	CG1625	CG10207	CG10267
K	VAPB	CG14837	CG10743	CG3284	CG3474	SOD	CG18332	CG15188	CG10846	CG10207	CG18110	CG4443	SOD	CG15160	CG13075	???????	CG11777	CG17301	TBPH	CG13994	CG10743	CG11444	CG1409	CG30429
L	CG18110	CG1866	CG31528	CG14435	CG16725	CG4086	CG3476	CG4012	CG3975	CG32486	CG31003	CG31769	CG15800	CG2038	CG13221	CG17327	CG4005	CG17760	CG17753	CG1865	CG13532	CG14181	GFP	CG15010
M	CG2852	CG17985	CG4005	CG31742	CG1865	CG14043	CG1242	CG10846	CG4486	CG30350	CG1242	CG17268	CG14606	CG11330	CG17982	CG15645	CG10108	CG13116	CG1937	???????	CG10315	CG14006	CG3474	CG31003
N	CG13296	CG10243	CG18341	CG16935	CG15010	CG4319	CG3975	CG1560	TBPH	CG18341	CG18803	CG1937	CG4012	CG11777	CG1560	0c	CG17982	CG10327	CG14222	CG32703	1000c	CG4012	CG17291	CG30350
O	CG13532	CG17726	CG17302	CG10108	CG31003	CG10089	CG11560	CG3766	CG13532	CG2013	CG30043	CG14181	CG1409	CG3024	CG14837	CG15010	CG17327	CG4486	CG14444	CG10679	CG3476	CG4443	CG15800	CG32486
P	1000c	CG13994	CG17268	500c	???????	CG15589	CG11811	GFP	CG14718	CG1865	CG14032	CG12822	CG10855	CG15188	CG31528	GFP	CG10855	CG4319	SOD	CG30043	CG15645	TBPH	CG3500	0c

Plate 1, 36 hours

	1	2	3	4	5	6	7	8	9	10	11	12	13	14	15	16	17	18	19	20	21	22	23	24
A	CG1866	CG18341	CG10108	SOD	CG3474	0c	CG14606	CG15589	CG2852	CG2013	CG11330	CG3766	CG11811	CG17343	CG10089	CG3024	CG1866	TBPH	CG3474	CG14181	CG15589	CG4012	CG31003	CG32703
B	CG32437	0c	CG14222	CG17753	CG30161	CG1836	CG3000	CG11330	CG14006	CG30429	CG14837	CG13994	CG10846	CG14326	CG17985	CG13387	CG10855	CG4461	CG14326	CG17753	CG12822	CG32177	CG11811	CG1242
C	CG18174	CG32177	CG11415	CG13732	CG14032	VAPB	CG10089	CG17982	CG13387	CG18174	CG14006	CG3474	CG31003	CG11560	CG4443	SOD	???????	CG1560	CG17343	CG3766	CG3476	CG17327	CG14222	CG10125
D	CG4461	CG18803	CG10846	CG13116	CG17985	CG4005	CG4443	CG32236	TBPH	CG15188	CG14606	CG1560	1000c	CG15589	CG15010	CG1937	CG10108	CG13994	VAPB	CG14006	CG17301	CG14444	CG14837	CG13063
E	GFP	CG13048	1000c	CG10125	CG3500	CG14125	CG30429	CG3766	???????	CG10315	CG17327	CG2852	CG15237	CG32685	CG11415	CG3000	CG3000	CG15160	CG3492	CG13221	CG1736	CG10679	0c	CG15188
F	CG4086	CG14718	CG3476	CG11777	CG13532	CG32685	CG3457	CG11560	CG14032	CG31057	500c	CG13063	CG1409	CG14435	CG17291	CG17753	CG30350	CG10743	CG2852	GFP	CG10327	CG10846	CG1836	CG14715
G	CG15767	CG17726	CG15188	CG17327	SOD	CG12822	CG17291	CG13296	CG14718	CG17760	CG11777	CG3975	CG17301	CG4461	CG4086	CG10108	CG11330	CG10243	CG32685	CG13048	CG4086	CG4443	CG4005	CG1865
H	CG14326	CG11811	CG17302	CG16725	CG15800	CG10267	???????	CG15645	CG10679	CG4005	CG10207	CG4486	CG13532	0c	CG32236	CG14222	CG1409	CG14032	CG13296	CG14435	CG30043	CG17726	CG30429	500c
I	CG16935	CG15160	CG4012	CG31742	CG18332	CG13221	GFP	CG17760	CG15160	CG11444	CG1866	TBPH	CG32703	CG17302	CG3492	CG31742	CG4319	CG15010	CG13075	CG13532	CG13116	CG3024	CG4486	CG2038
J	500c	CG1242	CG30350	VAPB	CG11444	CG10679	CG3284	CG31003	CG10243	CG3500	CG18341	CG30161	CG3284	CG12743	CG18803	CG10743	SOD	CG3457	GFP	CG11415	CG32236	TBPH	CG17268	CG32486
K	CG1865	CG2013	CG1937	CG17268	CG17301	CG32486	CG14043	CG3492	CG32437	CG1625	CG18110	CG14125	CG10125	CG15800	CG10267	CG10855	CG17760	CG16725	CG10315	CG3975	CG17302	CG10207	CG16935	CG3500
L	CG31057	CG31528	CG2038	CG10315	CG4486	CG10743	CG17343	CG10243	CG13221	VAPB	CG1836	CG31769	CG17726	CG12822	CG18332	CG14715	CG18110	???????	CG17982	CG1625	CG14125	CG31742	CG10089	CG15767
M	CG14444	CG13075	CG1736	CG13063	CG15010	CG31769	CG14181	1000c	CG16725	CG13116	CG3457	SOD	CG15645	CG1877	VAPB	CG13075	CG17291	CG31769	CG3284	1000c	CG11777	CG13732	CG10267	CG14606
N	CG1409	CG1625	SOD	CG3024	CG32703	CG10207	CG30043	CG18110	CG30350	CG17268	CG14043	CG2038	CG15767	CG32486	CG1865	CG13296	GFP	CG15237	CG13387	CG15800	CG14718	CG18332	TBPH	CG1937
O	CG12743	CG1560	???????	CG13994	CG15237	CG4319	CG1877	500c	CG30043	CG4319	CG13048	CG10327	CG31528	CG3476	CG4012	CG16935	CG31057	CG18174	CG31528	CG2013	CG1877	CG17985	CG11560	CG11444
P	TBPH	CG14715	CG14837	CG10327	GFP	CG14435	CG10855	CG3975	CG1736	CG13732	???????	CG14181	CG17982	CG14444	CG1242	CG32177	CG18803	CG30161	CG32437	CG12743	CG15645	CG14043	CG18341	VAPB

Plate 2, 24 hours

	1	2	3	4	5	6	7	8	9	10	11	12	13	14	15	16	17	18	19	20	21	22	23	24
A	CG1950	CG10956	CG12746	CG5924	CG13701	GFP	CG6341	1000c	CG11759	CG1950	VAPB	CG10967	CG11858	CG11777	CG3476	CG10335	CG7217	CG5971	CG10108	CG6345	CG9324	CG2125	CG31935	CG8219
B	TBPH	CG2028	CG30463	CG4715	CG10743	CG6674	CG5014	CG4913	CG6885	CG4157	CG12746	CG10743	CG6345	CG10539	CG9391	CG9172	500c	CG3060	CG4157	CG10938	CG4274	CG8465	CG12265	CG5828
C	CG10360	CG12821	CG9952	0c	CG10965	CG6099	CG31098	CG9543	CG9952	CG5971	CG5092	CG6502	SOD	CG8160	CG13388	CG6048	CG3018	CG10243	CG8160	CG6099	CG4627	CG3889	TBPH	CG6238
D	CG10243	CG6502	CG9638	CG6238	CG3431	CG12265	CG5181	CG7564	VAPB	CG32707	CG2125	CG5186	CG6674	CG10907	CG4627	CG5014	CG4924	CG4715	CG13664	CG9391	CG8571	CG9172	CG6048	SOD
E	CG10335	GFP	CG10938	CG11940	CG9291	CG3455	CG5953	CG11858	CG13701	CG7314	CG5266	CG6238	CG6950	CG9953	TBPH	CG30463	CG6337	CG11858	CG1063	CG5325	CG5977	CG7843	CG10967	CG7917
F	??????	CG6950	CG1063	CG6342	CG8068	CG5092	CG3060	CG31423	CG1063	CG2621	CG4715	CG5847	??????	CG6341	CG5924	CG9324	VAPB	CG3234	CG11001	CG2621	0c	CG11594	CG1945	CG10360
G	CG7776	CG9296	CG3889	CG8998	CG5186	CG8219	CG10108	CG8771	500c	CG5925	1000c	CG9296	CG7217	CG9438	CG31935	CG7917	CG2048	CG6674	CG3455	CG5847	CG6502	CG6342	CG7314	CG3431
H	CG13388	500c	SOD	CG12538	CG2621	CG5828	CG4274	CG6337	CG9638	CG11594	CG5181	CG7843	CG3416	CG11153	CG4646	CG4924	CG9638	CG13388	CG10743	CG8863	CG32707	CG30463	??????	CG13701
I	CG5847	CG11777	CG7314	CG6963	CG11804	CG9172	CG8160	CG9953	CG10108	CG7919	CG2048	CG3060	CG10938	CG8863	CG8771	CG10956	CG8771	CG6963	CG8979	CG8068	CG5925	CG3476	CG3416	VAPB
J	CG6048	CG5733	CG7919	CG6220	CG7254	CG7843	CG2048	CG8465	CG10360	VAPB	CG7776	CG2028	CG6220	CG1081	GFP	CG4274	CG8337	CG9438	CG6220	CG10539	CG11777	CG9296	CG4913	CG5014
K	VAPB	CG8337	CG5266	CG10539	CG1081	SOD	CG32707	CG8571	CG5325	CG4913	CG3234	CG11804	SOD	CG8465	CG6337	??????	CG5953	CG2028	TBPH	CG6885	CG5266	CG5924	CG7254	CG12746
L	CG3234	CG3416	CG13664	CG7917	CG9324	CG11594	CG10907	CG11335	CG11001	CG12821	CG12919	CG10243	CG9291	CG3889	CG6342	CG9543	CG11153	CG9953	CG9952	CG3412	CG6647	CG7564	GFP	CG8392
M	CG4157	CG31935	CG11153	CG3476	CG3412	CG7217	CG5977	CG5325	CG11940	CG12538	CG5977	CG1945	CG8068	CG5828	CG31423	CG8998	CG4646	CG6341	CG31098	??????	CG5092	CG6950	CG1081	CG12919
N	CG6345	CG4924	CG3018	CG9391	CG8392	CG11759	CG11001	CG8979	TBPH	CG3018	CG3431	CG31098	CG11335	CG5953	CG8979	0c	CG31423	CG5181	CG7776	CG10335	1000c	CG11335	CG1950	CG12538
O	CG6647	CG2125	CG9438	CG4646	CG12919	CG4627	CG5925	CG10967	CG6647	CG3455	CG10965	CG7564	CG7254	CG12265	CG8337	CG8392	CG9543	CG11940	CG7919	CG5186	CG10907	CG11804	CG9291	CG12821
P	1000c	CG6885	CG1945	500c	??????	CG8863	CG5971	GFP	CG8219	CG3412	CG6963	CG6099	CG5733	CG8571	CG13664	GFP	CG5733	CG11759	SOD	CG10965	CG8998	TBPH	CG10956	0c

Plate 2, 36 hours

	1	2	3	4	5	6	7	8	9	10	11	12	13	14	15	16	17	18	19	20	21	22	23	24
A	CG3416	CG3018	CG4646	SOD	CG1081	0c	CG8068	CG8863	CG4157	CG3455	CG5828	CG10967	CG5971	CG9638	CG4627	CG12265	CG3416	TBPH	CG1081	CG7564	CG8863	CG11335	CG12919	CG10335
B	CG10360	0c	CG7776	CG9952	CG11777	CG30463	CG4274	CG5828	CG6950	CG12746	CG8337	CG6885	CG5325	CG7843	CG31935	CG6502	CG5733	CG11858	CG7843	CG9952	CG6099	CG10743	CG5971	CG5977
C	CG2621	CG10743	CG5847	CG6674	CG6963	VAPB	CG4627	CG31423	CG6502	CG2621	CG6950	CG1081	CG12919	CG5925	CG11804	SOD	??????	CG8979	CG9638	CG10967	CG10907	CG9543	CG7776	CG4715
D	CG11858	CG3431	CG5325	CG6341	CG31935	CG11153	CG11804	CG10108	TBPH	CG8571	CG8068	CG8979	1000c	CG8863	CG8392	CG31098	CG4646	CG6885	VAPB	CG6950	CG2028	CG7919	CG8337	CG6238
E	GFP	CG6220	1000c	CG4715	CG10956	CG7314	CG12746	CG10967	??????	CG5092	CG9543	CG4157	CG8771	CG13701	CG5847	CG4274	CG4274	CG8465	CG10938	CG6342	CG2048	CG5186	0c	CG8571
F	CG11594	CG8219	CG10907	CG5953	CG6647	CG13701	CG1063	CG5925	CG6963	CG13388	500c	CG6238	CG7254	CG7917	CG1950	CG9952	CG12538	CG5266	CG4157	GFP	CG5181	CG5325	CG30463	CG8160
G	CG9172	CG2125	CG8571	CG9543	SOD	CG6099	CG1950	CG6345	CG8219	CG9953	CG5953	CG11001	CG2028	CG11858	CG11594	CG4646	CG5828	CG4924	CG13701	CG6220	CG11594	CG11804	CG11153	CG3412
H	CG7843	CG5971	CG9438	CG9324	CG9291	CG5014	??????	CG8998	CG5186	CG11153	CG4913	CG11940	CG6647	0c	CG10108	CG7776	CG7254	CG6963	CG6345	CG7917	CG10965	CG2125	CG12746	500c
I	CG9391	CG8465	CG11335	CG3476	CG32707	CG6342	GFP	CG9953	CG8465	CG5924	CG3416	TBPH	CG10335	CG9438	CG10938	CG3476	CG11759	CG8392	CG6337	CG6647	CG6341	CG12265	CG11940	CG3889
J	500c	CG5977	CG12538	VAPB	CG5924	CG5186	CG10539	CG12919	CG4924	CG10956	CG3018	CG11777	CG10539	CG6048	CG3431	CG5266	SOD	CG1063	GFP	CG5847	CG10108	TBPH	CG1945	CG12821
K	CG3412	CG3455	CG31098	CG1945	CG2028	CG12821	CG7217	CG10938	CG10360	CG9296	CG3234	CG7314	CG4715	CG9291	CG5014	CG5733	CG9953	CG9324	CG5092	CG11001	CG9438	CG4913	CG9391	CG10956
L	CG13388	CG13664	CG3889	CG5092	CG11940	CG5266	CG9638	CG4924	CG6342	VAPB	CG30463	CG10243	CG2125	CG6099	CG32707	CG8160	CG3234	??????	CG31423	CG9296	CG7314	CG3476	CG4627	CG9172
M	CG7919	CG6337	CG2048	CG6238	CG8392	CG10243	CG7564	1000c	CG9324	CG6341	CG1063	SOD	CG8998	CG3060	VAPB	CG6337	CG1950	CG10243	CG10539	1000c	CG5953	CG6674	CG5014	CG8068
N	CG7254	CG9296	SOD	CG12265	CG10335	CG4913	CG10965	CG3234	CG12538	CG1945	CG7217	CG3889	CG9172	CG12821	CG3412	CG6345	GFP	CG8771	CG6502	CG9291	CG8219	CG32707	TBPH	CG31098
O	CG6048	CG8979	??????	CG6885	CG8771	CG11759	CG3060	500c	CG10965	CG11759	CG6220	CG5181	CG13664	CG10907	CG11335	CG9391	CG13388	CG2621	CG13664	CG3455	CG3060	CG31935	CG5925	CG5924
P	TBPH	CG8160	CG8337	CG5181	GFP	CG7917	CG5733	CG11001	CG2048	CG6674	??????	CG7564	CG31423	CG7919	CG5977	CG10743	CG3431	CG11777	CG10360	CG6048	CG8998	CG7217	CG3018	VAPB

Plate 3, 24 hours

	TBPH	SOD	VAPB	GFP	0c	500c	1000c	8	9	10	11	12	13	14	15	16	17	18	19	20	21	22	23	24
A	CG14884	CG11943	CG9907	CG15433	CG1100	GFP	CG1859	1000c	CG13349	CG14884	VAPB	CG12161	CG13624	CG9327	CG10149	CG11111	CG3329	CG17331	CG10370	CG2331	CG5808	CG15437	CG7768	CG4535
B	TBPH	CG1489	CG16982	CG1210	CG1024	CG3004	CG12855	CG12323	CG3051	CG8905	CG9907	CG1024	CG2331	CG11115	CG6147	CG5482	500c	CG16983	CG8905	CG11888	CG9206	CG4804	CG9650	CG14490
C	CG1059	CG10694	CG6998	0c	CG9279	CG17840	CG16988	CG6778	CG6998	CG17331	CG1318	CG2503	SOD	CG4402	CG9949	CG1768	CG16916	CG10230	CG4402	CG17840	CG11981	CG8846	TBPH	CG1795
D	CG10230	CG2503	CG6975	CG1795	CG8336	CG9650	CG13189	CG3511	VAPB	CG7899	CG15437	CG13531	CG3004	CG11552	CG11981	CG12855	CG12338	CG1210	CG10123	CG6147	CG4872	CG5482	CG1768	SOD
E	CG11111	GFP	CG11888	CG14238	CG5575	CG8824	CG17266	CG13624	CG1100	CG3493	CG13892	CG1795	CG32423	CG7504	TBPH	CG16982	CG18495	CG13624	CG11212	CG14024	CG1765	CG3966	CG12161	CG4006
F	??????	CG32423	CG11212	CG2072	CG4320	CG1318	CG16983	CG7747	CG11212	CG16879	CG1210	CG1519	??????	CG1859	CG15433	CG5808	VAPB	CG7804	CG12276	CG16879	0c	CG13030	CG14815	CG1059
G	CG3936	CG5686	CG8846	CG5166	CG13531	CG4535	CG10370	CG4886	500c	CG17051	1000c	CG5686	CG3329	CG6226	CG7768	CG4006	CG15106	CG3004	CG8824	CG1519	CG2503	CG2072	CG3493	CG8336
H	CG9949	500c	SOD	CG9847	CG16879	CG14490	CG9206	CG18495	CG6975	CG13030	CG13189	CG3966	CG8274	CG12359	CG12000	CG12338	CG6975	CG9949	CG1024	CG4904	CG7899	CG16982	??????	CG1100
I	CG1519	CG9327	CG3493	CG32635	CG1341	CG5482	CG4402	CG7504	CG10370	CG4097	CG15106	CG16983	CG11888	CG4904	CG4886	CG11943	CG4886	CG32635	CG5071	CG4320	CG17051	CG10149	CG8274	VAPB
J	CG1768	CG14224	CG4097	CG1787	CG3422	CG3966	CG15106	CG4804	CG1059	VAPB	CG3936	CG1489	CG1787	CG11419	GFP	CG9206	CG4618	CG6226	CG1787	CG11115	CG9327	CG5686	CG12323	CG12855
K	VAPB	CG4618	CG13892	CG11115	CG11419	SOD	CG7899	CG4872	CG14024	CG12323	CG7804	CG1341	SOD	CG4804	CG18495	??????	CG17266	CG1489	TBPH	CG3051	CG13892	CG15433	CG3422	CG9907
L	CG7804	CG8274	CG10123	CG4006	CG5808	CG13030	CG11552	CG12765	CG12276	CG10694	CG9916	CG10230	CG5575	CG8846	CG2072	CG6778	CG12359	CG7504	CG6998	CG8002	CG2999	CG3511	GFP	CG4735
M	CG8905	CG7768	CG12359	CG10149	CG8002	CG3329	CG1765	CG14024	CG14238	CG9847	CG1765	CG14815	CG4320	CG14490	CG7747	CG5166	CG12000	CG1859	CG16988	??????	CG1318	CG32423	CG11419	CG9916
N	CG2331	CG12338	CG16916	CG6147	CG4735	CG13349	CG12276	CG5071	TBPH	CG16916	CG8336	CG16988	CG12765	CG17266	CG5071	0c	CG7747	CG13189	CG3936	CG11111	1000c	CG12765	CG14884	CG9847
O	CG2999	CG15437	CG6226	CG12000	CG9916	CG11981	CG17051	CG12161	CG2999	CG8824	CG9279	CG3511	CG3422	CG9650	CG4618	CG4735	CG6778	CG14238	CG4097	CG13531	CG11552	CG1341	CG5575	CG10694
P	1000c	CG3051	CG14815	500c	??????	CG4904	CG17331	GFP	CG4535	CG8002	CG32635	CG17840	CG14224	CG4872	CG10123	GFP	CG14224	CG13349	SOD	CG9279	CG5166	TBPH	CG11943	0c

Plate 3, 36 hours

	TBPH	SOD	VAPB	GFP	0c	500c	1000c	8	9	10	11	12	13	14	15	16	17	18	19	20	21	22	23	24
A	CG8274	CG16916	CG12000	SOD	CG11419	0c	CG4320	CG4904	CG8905	CG8824	CG14490	CG12161	CG17331	CG6975	CG11981	CG9650	CG8274	TBPH	CG11419	CG3511	CG4904	CG12765	CG9916	CG11111
B	CG1059	0c	CG3936	CG6998	CG9327	CG16982	CG9206	CG14490	CG32423	CG9907	CG4618	CG3051	CG14024	CG3966	CG7768	CG2503	CG14224	CG13624	CG3966	CG6998	CG17840	CG1024	CG17331	CG1765
C	CG16879	CG1024	CG1519	CG3004	CG32635	VAPB	CG11981	CG7747	CG2503	CG16879	CG32423	CG11419	CG9916	CG17051	CG1341	SOD	??????	CG5071	CG6975	CG12161	CG11552	CG6778	CG3936	CG1210
D	CG13624	CG8336	CG14024	CG1859	CG7768	CG12359	CG1341	CG10370	TBPH	CG4872	CG4320	CG5071	1000c	CG4904	CG4735	CG16988	CG12000	CG3051	VAPB	CG32423	CG1489	CG4097	CG4618	CG1795
E	GFP	CG1787	1000c	CG1210	CG11943	CG3493	CG9907	CG12161	??????	CG1318	CG6778	CG8905	CG4886	CG1100	CG1519	CG9206	CG9206	CG4804	CG11888	CG2072	CG15106	CG13531	0c	CG4872
F	CG13030	CG4535	CG11552	CG17266	CG2999	CG1100	CG11212	CG17051	CG32635	CG9949	500c	CG1795	CG3422	CG4006	CG14884	CG6998	CG9847	CG13892	CG8905	GFP	CG13189	CG14024	CG16982	CG4402
G	CG5482	CG15437	CG4872	CG6778	SOD	CG17840	CG14884	CG2331	CG4535	CG7504	CG17266	CG12276	CG1489	CG13624	CG13030	CG12000	CG14490	CG12338	CG1100	CG1787	CG13030	CG1341	CG12359	CG8002
H	CG3966	CG17331	CG6226	CG5808	CG5575	CG12855	??????	CG5166	CG13531	CG12359	CG12323	CG14238	CG2999	0c	CG10370	CG3936	CG3422	CG32635	CG2331	CG4006	CG9279	CG15437	CG9907	500c
I	CG6147	CG4804	CG12765	CG10149	CG7899	CG2072	GFP	CG7504	CG4804	CG15433	CG8274	TBPH	CG11111	CG6226	CG11888	CG10149	CG13349	CG4735	CG18495	CG2999	CG1859	CG9650	CG14238	CG8846
J	500c	CG1765	CG9847	VAPB	CG15433	CG13531	CG11115	CG9916	CG12338	CG11943	CG16916	CG9327	CG11115	CG1768	CG8336	CG13892	SOD	CG11212	GFP	CG1519	CG10370	TBPH	CG14815	CG10694
K	CG8002	CG8824	CG16988	CG14815	CG1489	CG10694	CG3329	CG11888	CG1059	CG5686	CG7804	CG3493	CG1210	CG5575	CG12855	CG14224	CG7504	CG5808	CG1318	CG12276	CG6226	CG12323	CG6147	CG11943
L	CG9949	CG10123	CG8846	CG1318	CG14238	CG13892	CG6975	CG12338	CG2072	VAPB	CG16982	CG10230	CG15437	CG17840	CG7899	CG4402	CG7804	??????	CG7747	CG5686	CG3493	CG10149	CG11981	CG5482
M	CG4097	CG18495	CG15106	CG1795	CG4735	CG10230	CG3511	1000c	CG5808	CG1859	CG11212	SOD	CG5166	CG16983	VAPB	CG18495	CG14884	CG10230	CG11115	1000c	CG17266	CG3004	CG12855	CG4320
N	CG3422	CG5686	SOD	CG9650	CG11111	CG12323	CG9279	CG7804	CG9847	CG14815	CG3329	CG8846	CG5482	CG10694	CG8002	CG2331	GFP	CG4886	CG2503	CG5575	CG4535	CG7899	TBPH	CG16988
O	CG1768	CG5071	??????	CG3051	CG4886	CG13349	CG16983	500c	CG9279	CG13349	CG1787	CG13189	CG10123	CG11552	CG12765	CG6147	CG9949	CG16879	CG10123	CG8824	CG16983	CG7768	CG17051	CG15433
P	TBPH	CG4402	CG4618	CG13189	GFP	CG4006	CG14224	CG12276	CG15106	CG3004	??????	CG3511	CG7747	CG4097	CG1765	CG1024	CG8336	CG9327	CG1059	CG1768	CG5166	CG3329	CG16916	VAPB

Plate 4, 24 hours

	1	2	3	4	5	6	7	8	9	10	11	12	13	14	15	16	17	18	19	20	21	22	23	24
A	CG4581	CG4236	CG3525	CG5648	CG3992	GFP	CG6759	1000c	CG4389	CG4581	VAPB	CG4238	CG4501	CG3411	CG3722	CG4035	CG7762	CG5688	CG3881	CG6789	CG2212	CG4909	CG2929	CG9868
B	TBPH	CG4583	CG3936	CG4420	CG3869	CG7281	CG4697	CG4494	CG7476	CG3152	CG3525	CG3869	CG6789	CG4082	CG2218	CG1890	500c	CG1100	CG3152	CG4183	CG3210	CG1333	CG3415	CG5379
C	CG3895	CG3929	CG2574	0c	CG3356	CG6214	CG11111	CG2257	CG2574	CG5688	CG4699	CG6932	SOD	CG9790	CG3573	CG6198	CG3511	CG3810	CG9790	CG6214	CG1100	CG3143	TBPH	CG6428
D	CG3810	CG6932	CG2508	CG6428	CG3048	CG3415	CG5005	CG8739	VAPB	CG3028	CG4909	CG5285	CG7281	CG4164	CG1100	CG4697	CG4569	CG4420	CG3682	CG2218	CG1401	CG1890	CG6198	SOD
E	CG4035	GFP	CG4183	CG4523	CG2087	CG3136	CG5684	CG4501	CG3992	CG8725	CG5289	CG6428	CG7528	CG2887	TBPH	CG3936	CG6708	CG4501	CG4147	CG5370	CG5722	CG9198	CG4238	CG9378
F	??????	CG7528	CG4147	CG6760	CG9772	CG4699	CG1100	CG2924	CG4147	CG3493	CG4420	CG5604	??????	CG6759	CG5648	CG2212	VAPB	CG2947	CG4244	CG3493	0c	CG4280	CG4574	CG3895
G	CG8743	CG32484	CG3143	CG30502	CG5285	CG9868	CG3881	CG1416	500c	CG5675	1000c	CG32484	CG7762	CG2245	CG2929	CG9378	CG4899	CG7281	CG3136	CG5604	CG6932	CG6760	CG8725	CG3048
H	CG3573	500c	SOD	CG3473	CG3493	CG5379	CG3210	CG6708	CG2508	CG4280	CG5005	CG9198	CG3041	CG4264	CG11111	CG4569	CG2508	CG3573	CG3869	CG1471	CG3028	CG3936	??????	CG3992
I	CG5604	CG3411	CG8725	CG7619	CG4428	CG1890	CG9790	CG2887	CG3881	CG9556	CG4899	CG1100	CG4183	CG1471	CG1416	CG4236	CG1416	CG7619	CG1554	CG9772	CG5675	CG3722	CG3041	VAPB
J	CG6198	CG5378	CG9556	CG6233	CG8279	CG9198	CG4899	CG1333	CG3895	VAPB	CG8743	CG4583	CG6233	CG4162	GFP	CG3210	CG1134	CG2245	CG6233	CG4082	CG3411	CG32484	CG4494	CG4697
K	VAPB	CG1134	CG5289	CG4082	CG4162	SOD	CG3028	CG1401	CG5370	CG4494	CG2947	CG4428	SOD	CG1333	CG6708	??????	CG5684	CG4583	TBPH	CG7476	CG5289	CG5648	CG8279	CG3525
L	CG2947	CG3041	CG3682	CG9378	CG2212	CG4280	CG4164	CG4268	CG4244	CG3929	CG3571	CG3810	CG2087	CG3143	CG6760	CG2257	CG4264	CG2887	CG2574	CG3033	CG7207	CG8739	GFP	CG1241
M	CG3152	CG2929	CG4264	CG3722	CG3033	CG7762	CG5722	CG5370	CG4523	CG3473	CG5722	CG4574	CG9772	CG5379	CG2924	CG30502	CG11111	CG6759	CG11111	??????	CG4699	CG7528	CG4162	CG3571
N	CG6789	CG4569	CG3511	CG2218	CG1241	CG4389	CG4244	CG1554	TBPH	CG3511	CG3048	CG11111	CG4268	CG5684	CG1554	0c	CG2924	CG5005	CG8743	CG4035	1000c	CG4268	CG4581	CG3473
O	CG7207	CG4909	CG2245	CG11111	CG3571	CG1100	CG5675	CG4238	CG7207	CG3136	CG3356	CG8739	CG8279	CG3415	CG1134	CG1241	CG2257	CG4523	CG9556	CG5285	CG4164	CG4428	CG2087	CG3929
P	1000c	CG7476	CG4574	500c	??????	CG1471	CG5688	GFP	CG9868	CG3033	CG7619	CG6214	CG5378	CG1401	CG3682	GFP	CG5378	CG4389	SOD	CG3356	CG30502	TBPH	CG4236	0c

Plate 4, 36 hours

	1	2	3	4	5	6	7	8	9	10	11	12	13	14	15	16	17	18	19	20	21	22	23	24
A	CG3041	CG3511	CG11111	SOD	CG4162	0c	CG9772	CG1471	CG3152	CG3136	CG5379	CG4238	CG5688	CG2508	CG1100	CG3415	CG3041	TBPH	CG4162	CG8739	CG1471	CG4268	CG3571	CG4035
B	CG3895	0c	CG8743	CG2574	CG3411	CG3936	CG3210	CG5379	CG7528	CG3525	CG1134	CG7476	CG5370	CG9198	CG2929	CG6932	CG5378	CG4501	CG9198	CG2574	CG6214	CG3869	CG5688	CG5722
C	CG3493	CG3869	CG5604	CG7281	CG7619	VAPB	CG1100	CG2924	CG6932	CG3493	CG7528	CG4162	CG3571	CG5675	CG4428	SOD	??????	CG1554	CG2508	CG4238	CG4164	CG2257	CG8743	CG4420
D	CG4501	CG3048	CG5370	CG6759	CG2929	CG4264	CG4428	CG3881	TBPH	CG1401	CG9772	CG1554	1000c	CG1471	CG1241	CG11111	CG11111	CG7476	VAPB	CG7528	CG4583	CG9556	CG1134	CG6428
E	GFP	CG6233	1000c	CG4420	CG4236	CG8725	CG3525	CG4238	??????	CG4699	CG2257	CG3152	CG1416	CG3992	CG5604	CG3210	CG3210	CG1333	CG4183	CG6760	CG4899	CG5285	0c	CG1401
F	CG4280	CG9868	CG4164	CG5684	CG7207	CG3992	CG4147	CG5675	CG7619	CG3573	500c	CG6428	CG8279	CG9378	CG4581	CG2574	CG3473	CG5289	CG3152	GFP	CG5005	CG5370	CG3936	CG9790
G	CG1890	CG4909	CG1401	CG2257	SOD	CG6214	CG4581	CG6789	CG9868	CG2887	CG5684	CG4244	CG4583	CG4501	CG4280	CG11111	CG5379	CG4569	CG3992	CG6233	CG4280	CG4428	CG4264	CG3033
H	CG9198	CG5688	CG2245	CG2212	CG2087	CG4697	??????	CG30502	CG5285	CG4264	CG4494	CG4523	CG7207	0c	CG3881	CG8743	CG8279	CG7619	CG6789	CG9378	CG3356	CG4909	CG3525	500c
I	CG2218	CG1333	CG4268	CG3722	CG3028	CG6760	GFP	CG2887	CG1333	CG5648	CG3041	TBPH	CG4035	CG2245	CG4183	CG3722	CG4389	CG1241	CG6708	CG7207	CG6759	CG3415	CG4523	CG3143
J	500c	CG5722	CG3473	VAPB	CG5648	CG5285	CG4082	CG3571	CG4569	CG4236	CG3511	CG3411	CG4082	CG6198	CG3048	CG5289	SOD	CG4147	GFP	CG5604	CG3881	TBPH	CG4574	CG3929
K	CG3033	CG3136	CG11111	CG4574	CG4583	CG3929	CG7762	CG4183	CG3895	CG32484	CG2947	CG8725	CG4420	CG2087	CG4697	CG5378	CG2887	CG2212	CG4699	CG4244	CG2245	CG4494	CG2218	CG4236
L	CG3573	CG3682	CG3143	CG4699	CG4523	CG5289	CG2508	CG4569	CG6760	VAPB	CG3936	CG3810	CG4909	CG6214	CG3028	CG9790	CG2947	??????	CG2924	CG32484	CG8725	CG3722	CG1100	CG1890
M	CG9556	CG6708	CG4899	CG6428	CG1241	CG3810	CG8739	1000c	CG2212	CG6759	CG4147	SOD	CG30502	CG1100	VAPB	CG6708	CG4581	CG3810	CG4082	1000c	CG5684	CG7281	CG4697	CG9772
N	CG8279	CG32484	SOD	CG3415	CG4035	CG4494	CG3356	CG2947	CG3473	CG4574	CG7762	CG3143	CG1890	CG3929	CG3033	CG6789	GFP	CG1416	CG6932	CG2087	CG9868	CG3028	TBPH	CG11111
O	CG6198	CG1554	??????	CG7476	CG1416	CG4389	CG1100	500c	CG3356	CG4389	CG6233	CG5005	CG3682	CG4164	CG4268	CG2218	CG3573	CG3493	CG3682	CG3136	CG1100	CG2929	CG5675	CG5648
P	TBPH	CG9790	CG1134	CG5005	GFP	CG9378	CG5378	CG4244	CG4899	CG7281	??????	CG8739	CG2924	CG9556	CG5722	CG3869	CG3048	CG3411	CG3895	CG6198	CG30502	CG7762	CG3511	VAPB

Plate 5, 24 hours

	TBPH	SOD	VAPB	GFP	0c	500c	1000c	8	9	10	11	12	13	14	15	16	17	18	19	20	21	22	23	24
A	CG8091	CG7425	CG6766	CG5519	CG7224	GFP	CG5949	1000c	CG7842	CG8091	VAPB	CG7642	CG7923	CG6719	CG7037	CG7235	CG6603	CG5629	CG7111	CG6116	CG4167	CG8188	CG5489	CG1782
B	TBPH	CG8142	CG8536	CG5087	CG7109	CG6302	CG5295	CG5119	CG6438	CG15141	CG6766	CG7109	CG6116	CG7257	CG4200	CG3947	500c	CG8532	CG15141	CG7387	CG6258	CG2699	CG6728	CG5436
C	CG7113	CG7220	CG4774	0c	CG6349	CG5748	CG8542	CG4466	CG4774	CG5629	CG5313	CG6190	SOD	CG1771	CG6877	CG5709	CG8284	CG7053	CG1771	CG5748	CG4934	CG6235	TBPH	CG5841
D	CG7053	CG6190	CG4600	CG5841	CG6155	CG6728	CG5315	CG1133	VAPB	CG5659	CG8188	CG5330	CG6302	CG7382	CG4934	CG5295	CG5203	CG5087	CG6966	CG4200	CG2759	CG3947	CG5709	SOD
E	CG7235	GFP	CG7387	CG7986	CG4080	CG6194	CG5602	CG7923	CG7224	CG1049	CG5335	CG5841	CG6542	CG5001	TBPH	CG8536	CG5923	CG7923	CG7331	CG5373	CG5682	CG1403	CG7642	CG1512
F	??????	CG6542	CG7331	CG6016	CG1747	CG5313	CG8532	CG5429	CG7331	CG8203	CG5087	CG5440	??????	CG5949	CG5519	CG4167	VAPB	CG5643	CG7656	CG8203	0c	CG7769	CG8057	CG7113
G	CG1347	CG4141	CG6235	CG3697	CG5330	CG1782	CG7111	CG3291	500c	CG5520	1000c	CG4141	CG6603	CG4463	CG5489	CG1512	CG8184	CG6302	CG6194	CG5440	CG6190	CG6016	CG1049	CG6155
H	CG6877	500c	SOD	CG6734	CG8203	CG5436	CG6258	CG5923	CG4600	CG7769	CG5315	CG1403	CG5823	CG7660	CG4943	CG5203	CG4600	CG6877	CG7109	CG3615	CG5659	CG8536	??????	CG7224
I	CG5440	CG6719	CG1049	CG6562	CG7861	CG3947	CG1771	CG5001	CG7111	CG1616	CG8184	CG8532	CG7387	CG3615	CG3291	CG7425	CG3291	CG6562	CG3620	CG1747	CG5520	CG7037	CG5823	VAPB
J	CG5709	CG5387	CG1616	CG5788	CG6720	CG1403	CG8184	CG2699	CG7113	VAPB	CG1347	CG8142	CG5788	CG7375	GFP	CG6258	CG1966	CG4463	CG5788	CG7257	CG6719	CG4141	CG5119	CG5295
K	VAPB	CG1966	CG5335	CG7257	CG7375	SOD	CG5659	CG2759	CG5373	CG5119	CG5643	CG7861	SOD	CG2699	CG5923	??????	CG5602	CG8142	TBPH	CG6438	CG5335	CG5519	CG6720	CG6766
L	CG5643	CG5823	CG6966	CG1512	CG4167	CG7769	CG7382	CG7756	CG7656	CG7220	CG6792	CG7053	CG4080	CG6235	CG6016	CG4466	CG7660	CG5001	CG4774	CG5671	CG6207	CG1133	GFP	CG2681
M	CG15141	CG5489	CG7660	CG7037	CG5671	CG6603	CG5682	CG5373	CG7986	CG6734	CG5682	CG8057	CG1747	CG5436	CG5429	CG3697	CG4943	CG5949	CG8542	??????	CG5313	CG6542	CG7375	CG6792
N	CG6116	CG5203	CG8284	CG4200	CG2681	CG7842	CG7656	CG3620	TBPH	CG8284	CG6155	CG8542	CG7756	CG5602	CG3620	0c	CG5429	CG5315	CG1347	CG7235	1000c	CG7756	CG8091	CG6734
O	CG6207	CG8188	CG4463	CG4943	CG6792	CG4934	CG5520	CG7642	CG6207	CG6194	CG6349	CG1133	CG6720	CG6728	CG1966	CG2681	CG4466	CG7986	CG1616	CG5330	CG7382	CG7861	CG4080	CG7220
P	1000c	CG6438	CG8057	500c	??????	CG3615	CG5629	GFP	CG1782	CG5671	CG6562	CG5748	CG5387	CG2759	CG6966	GFP	CG5387	CG7842	SOD	CG6349	CG3697	TBPH	CG7425	0c

Plate 5, 36 hours

	TBPH	SOD	VAPB	GFP	0c	500c	1000c	8	9	10	11	12	13	14	15	16	17	18	19	20	21	22	23	24
A	CG5823	CG8284	CG4943	SOD	CG7375	0c	CG1747	CG3615	CG15141	CG6194	CG5436	CG7642	CG5629	CG4600	CG4934	CG6728	CG5823	TBPH	CG7375	CG1133	CG3615	CG7756	CG6792	CG7235
B	CG7113	0c	CG1347	CG4774	CG6719	CG8536	CG6258	CG5436	CG6542	CG6766	CG1966	CG6438	CG5373	CG1403	CG5489	CG6190	CG5387	CG7923	CG1403	CG4774	CG5748	CG7109	CG5629	CG5682
C	CG8203	CG7109	CG5440	CG6302	CG6562	VAPB	CG4934	CG5429	CG6190	CG8203	CG6542	CG7375	CG6792	CG5520	CG7861	SOD	??????	CG3620	CG4600	CG7642	CG7382	CG4466	CG1347	CG5087
D	CG7923	CG6155	CG5373	CG5949	CG5489	CG7660	CG7861	CG7111	TBPH	CG2759	CG1747	CG3620	1000c	CG3615	CG2681	CG8542	CG4943	CG6438	VAPB	CG6542	CG8142	CG1616	CG1966	CG5841
E	GFP	CG5788	1000c	CG5087	CG7425	CG1049	CG6766	CG7642	??????	CG5313	CG4466	CG15141	CG3291	CG7224	CG5440	CG6258	CG6258	CG2699	CG7387	CG6016	CG8184	CG5330	0c	CG2759
F	CG7769	CG1782	CG7382	CG5602	CG6207	CG7224	CG7331	CG5520	CG6562	CG6877	500c	CG5841	CG6720	CG1512	CG8091	CG4774	CG6734	CG5335	CG15141	GFP	CG5315	CG5373	CG8536	CG1771
G	CG3947	CG8188	CG2759	CG4466	SOD	CG5748	CG8091	CG6116	CG1782	CG5001	CG5602	CG7656	CG8142	CG7923	CG7769	CG4943	CG5436	CG5203	CG7224	CG5788	CG7769	CG7861	CG7660	CG5671
H	CG1403	CG5629	CG4463	CG4167	CG4080	CG5295	??????	CG3697	CG5330	CG7660	CG5119	CG7986	CG6207	0c	CG7111	CG1347	CG6720	CG6562	CG6116	CG1512	CG6349	CG8188	CG6766	500c
I	CG4200	CG2699	CG7756	CG7037	CG5659	CG6016	GFP	CG5001	CG2699	CG5519	CG5823	TBPH	CG7235	CG4463	CG7387	CG7037	CG7842	CG2681	CG5923	CG6207	CG5949	CG6728	CG7986	CG6235
J	500c	CG5682	CG6734	VAPB	CG5519	CG5330	CG7257	CG6792	CG5203	CG7425	CG8284	CG6719	CG7257	CG5709	CG6155	CG5335	SOD	CG7331	GFP	CG5440	CG7111	TBPH	CG8057	CG7220
K	CG5671	CG6194	CG8542	CG8057	CG8142	CG7220	CG6603	CG7387	CG7113	CG4141	CG5643	CG1049	CG5087	CG4080	CG5295	CG5387	CG5001	CG4167	CG5313	CG7656	CG4463	CG5119	CG4200	CG7425
L	CG6877	CG6966	CG6235	CG5313	CG7986	CG5335	CG4600	CG5203	CG6016	VAPB	CG8536	CG7053	CG8188	CG5748	CG5659	CG1771	CG5643	??????	CG5429	CG4141	CG1049	CG7037	CG4934	CG3947
M	CG1616	CG5923	CG8184	CG5841	CG2681	CG7053	CG1133	1000c	CG4167	CG5949	CG7331	SOD	CG3697	CG8532	VAPB	CG5923	CG8091	CG7053	CG7257	1000c	CG5602	CG6302	CG5295	CG1747
N	CG6720	CG4141	SOD	CG6728	CG7235	CG5119	CG6349	CG5643	CG6734	CG8057	CG6603	CG6235	CG3947	CG7220	CG5671	CG6116	GFP	CG3291	CG6190	CG4080	CG1782	CG5659	TBPH	CG8542
O	CG5709	CG3620	??????	CG6438	CG3291	CG7842	CG8532	500c	CG6349	CG7842	CG5788	CG5315	CG6966	CG7382	CG7756	CG4200	CG6877	CG8203	CG6966	CG6194	CG8532	CG5489	CG5520	CG5519
P	TBPH	CG1771	CG1966	CG5315	GFP	CG1512	CG5387	CG7656	CG8184	CG6302	??????	CG1133	CG5429	CG1616	CG5682	CG7109	CG6155	CG6719	CG7113	CG5709	CG3697	CG6603	CG8284	VAPB

Plate 6, 24 hours

	TBPH	SOD	VAPB	GFP	0c	500c	1000c	8	9	10	11	12	13	14	15	16	17	18	19	20	21	22	23	24
A	CG14899	CG31991	CG11968	CG9014	CG12334	GFP	CG9241	1000c	CG14228	CG14899	VAPB	CG13343	CG14517	CG11820	CG12070	CG12366	CG9588	CG9078	CG12140	CG9347	CG10578	CG31033	CG10961	CG9885
B	TBPH	CG14980	CG16817	CG8610	CG12101	CG9461	CG8709	CG8678	CG9484	CG11621	CG11968	CG12101	CG9347	CG12389	CG10635	CG10473	500c	CG16954	CG11621	CG13089	CG11734	CG10023	CG11840	CG8938
C	CG12227	CG12284	CG10811	0c	CG11793	CG9139	CG17030	CG10682	CG10811	CG9078	CG8711	CG9375	SOD	CG9862	CG12019	CG9128	CG16708	CG12077	CG9862	CG9139	CG8593	CG11321	TBPH	CG9160
D	CG12077	CG9375	CG32130	CG9160	CG11143	CG11840	CG8766	CG9623	VAPB	CG11035	CG31033	CG8786	CG9461	CG12812	CG8593	CG8709	CG8705	CG8610	CG12020	CG10635	CG10130	CG10473	CG9128	SOD
E	CG12366	GFP	CG13089	CG14536	CG10523	CG11261	CG32592	CG14517	CG12334	CG9617	CG8798	CG9160	CG9520	CG10850	TBPH	CG16817	CG9193	CG14517	CG12423	CG8885	CG9086	CG9707	CG13343	CG9709
F	??????	CG9520	CG12423	CG9342	CG9828	CG8711	CG16954	CG10862	CG12423	CG15676	CG8610	CG8971	??????	CG9241	CG9014	CG10578	VAPB	CG10981	CG13401	CG15676	0c	CG14214	CG14739	CG12227
G	CG9655	CG32434	CG11321	CG10367	CG8786	CG9885	CG12140	CG10210	500c	CG9042	1000c	CG32434	CG9588	CG10640	CG10961	CG9709	CG15104	CG9461	CG11261	CG8971	CG9375	CG9342	CG9617	CG11143
H	CG12019	500c	SOD	CG11896	CG15676	CG8938	CG11734	CG9193	CG32130	CG14214	CG8766	CG9707	CG11070	CG13570	CG8595	CG8705	CG32130	CG12019	CG12101	CG10254	CG11035	CG16817	??????	CG12334
I	CG8971	CG11820	CG9617	CG9526	CG14472	CG10473	CG9862	CG10850	CG12140	CG9746	CG15104	CG16954	CG13089	CG10254	CG10210	CG31991	CG10210	CG9526	CG10260	CG9828	CG9042	CG12070	CG11070	VAPB
J	CG9128	CG8937	CG9746	CG9153	CG9602	CG9707	CG15104	CG10023	CG12227	VAPB	CG9655	CG14980	CG9153	CG12799	GFP	CG11734	CG9934	CG10640	CG9153	CG12389	CG11820	CG32434	CG8678	CG8709
K	VAPB	CG9934	CG8798	CG12389	CG12799	SOD	CG11035	CG10130	CG8885	CG8678	CG10981	CG14472	SOD	CG10023	CG9193	??????	CG32592	CG14980	TBPH	CG9484	CG8798	CG9014	CG9602	CG11968
L	CG10981	CG11070	CG12020	CG9709	CG10578	CG14214	CG12812	CG14207	CG13401	CG12284	CG11988	CG12077	CG10523	CG11321	CG9342	CG10682	CG13570	CG10850	CG10811	CG11055	CG9429	CG9623	GFP	CG9985
M	CG11621	CG10961	CG13570	CG12070	CG11055	CG9588	CG9086	CG8885	CG14536	CG11896	CG9086	CG14739	CG9828	CG8938	CG10862	CG10367	CG8595	CG9241	CG17030	??????	CG8711	CG9520	CG12799	CG11988
N	CG9347	CG8705	CG16708	CG10635	CG9985	CG14228	CG13401	CG10260	TBPH	CG16708	CG11143	CG17030	CG14207	CG32592	CG10260	0c	CG10862	CG8766	CG9655	CG12366	1000c	CG14207	CG14899	CG11896
O	CG9429	CG31033	CG10640	CG8595	CG11988	CG8593	CG9042	CG13343	CG9429	CG11261	CG11793	CG9623	CG9602	CG11840	CG9934	CG9985	CG10682	CG14536	CG9746	CG8786	CG12812	CG14472	CG10523	CG12284
P	1000c	CG9484	CG14739	500c	??????	CG10254	CG9078	GFP	CG9885	CG11055	CG9526	CG9139	CG8937	CG10130	CG12020	GFP	CG8937	CG14228	SOD	CG11793	CG10367	TBPH	CG31991	0c

Plate 6, 36 hours

	TBPH	SOD	VAPB	GFP	0c	500c	1000c	8	9	10	11	12	13	14	15	16	17	18	19	20	21	22	23	24
A	CG11070	CG16708	CG8595	SOD	CG12799	0c	CG9828	CG10254	CG11621	CG11261	CG8938	CG13343	CG9078	CG32130	CG8593	CG11840	CG11070	TBPH	CG12799	CG9623	CG10254	CG14207	CG11988	CG12366
B	CG12227	0c	CG9655	CG10811	CG11820	CG16817	CG11734	CG8938	CG9520	CG11968	CG9934	CG9484	CG8885	CG9707	CG10961	CG9375	CG8937	CG14517	CG9707	CG10811	CG9139	CG12101	CG9078	CG9086
C	CG15676	CG12101	CG8971	CG9461	CG9526	VAPB	CG8593	CG10862	CG9375	CG15676	CG9520	CG12799	CG11988	CG9042	CG14472	SOD	??????	CG10260	CG32130	CG13343	CG12812	CG10682	CG9655	CG8610
D	CG14517	CG11143	CG8885	CG9241	CG10961	CG13570	CG14472	CG12140	TBPH	CG10130	CG9828	CG10260	1000c	CG10254	CG9985	CG17030	CG8595	CG9484	VAPB	CG9520	CG14980	CG9746	CG9934	CG9160
E	GFP	CG9153	1000c	CG8610	CG31991	CG9617	CG11968	CG13343	??????	CG8711	CG10682	CG11621	CG10210	CG12334	CG8971	CG11734	CG11734	CG10023	CG13089	CG9342	CG15104	CG8786	0c	CG10130
F	CG14214	CG9885	CG12812	CG32592	CG9429	CG12334	CG12423	CG9042	CG9526	CG12019	500c	CG9160	CG9602	CG9709	CG14899	CG10811	CG11896	CG8798	CG11621	GFP	CG8766	CG8885	CG16817	CG9862
G	CG10473	CG31033	CG10130	CG10682	SOD	CG9139	CG14899	CG9347	CG9885	CG10850	CG32592	CG13401	CG14980	CG14517	CG14214	CG8595	CG8938	CG8705	CG12334	CG9153	CG14214	CG14472	CG13570	CG11055
H	CG9707	CG9078	CG10640	CG10578	CG10523	CG8709	??????	CG10367	CG8786	CG13570	CG8678	CG14536	CG9429	0c	CG12140	CG9655	CG9602	CG9526	CG9347	CG9709	CG11793	CG31033	CG11968	500c
I	CG10635	CG10023	CG14207	CG12070	CG11035	CG9342	GFP	CG10850	CG10023	CG9014	CG11070	TBPH	CG12366	CG10640	CG13089	CG12070	CG14228	CG9985	CG9193	CG9429	CG9241	CG11840	CG14536	CG11321
J	500c	CG9086	CG11896	VAPB	CG9014	CG8786	CG12389	CG11988	CG8705	CG31991	CG16708	CG11820	CG12389	CG9128	CG11143	CG8798	SOD	CG12423	GFP	CG8971	CG12140	TBPH	CG14739	CG12284
K	CG11055	CG11261	CG17030	CG14739	CG14980	CG12284	CG9588	CG13089	CG12227	CG32434	CG10981	CG9617	CG8610	CG10523	CG8709	CG8937	CG10850	CG10578	CG8711	CG13401	CG10640	CG8678	CG10635	CG31991
L	CG12019	CG12020	CG11321	CG8711	CG14536	CG8798	CG32130	CG8705	CG9342	VAPB	CG16817	CG12077	CG31033	CG9139	CG11035	CG9862	CG10981	??????	CG10862	CG32434	CG9617	CG12070	CG8593	CG10473
M	CG9746	CG9193	CG15104	CG9160	CG9985	CG12077	CG9623	1000c	CG10578	CG9241	CG12423	SOD	CG10367	CG16954	VAPB	CG9193	CG14899	CG12077	CG12389	1000c	CG32592	CG9461	CG8709	CG9828
N	CG9602	CG32434	SOD	CG11840	CG12366	CG8678	CG11793	CG10981	CG11896	CG14739	CG9588	CG11321	CG10473	CG12284	CG11055	CG9347	GFP	CG10210	CG9375	CG10523	CG9885	CG11035	TBPH	CG17030
O	CG9128	CG10260	??????	CG9484	CG10210	CG14228	CG16954	500c	CG11793	CG14228	CG9153	CG8766	CG12020	CG12812	CG14207	CG10635	CG12019	CG15676	CG12020	CG11261	CG16954	CG10961	CG9042	CG9014
P	TBPH	CG9862	CG9934	CG8766	GFP	CG9709	CG8937	CG13401	CG15104	CG9461	??????	CG9623	CG10862	CG9746	CG9086	CG12101	CG11143	CG11820	CG12227	CG9128	CG10367	CG9588	CG16708	VAPB

Plate 7, 24 hours

	TBPH	SOD	VAPB	GFP	0c	500c	1000c	8	9	10	11	12	13	14	15	16	17	18	19	20	21	22	23	24
A	CG10124	CG8975	CG7766	CG4311	CG8427	GFP	CG3576	1000c	CG9750	CG10124	VAPB	CG9242	CG9946	CG7538	CG8019	CG8475	CG11006	CG32380	CG8362	CG9245	CG6343	CG10387	CG6871	CG5198
B	TBPH	CG10262	CG10667	CG17299	CG8322	CG11124	CG18319	CG17492	CG15615	CG7359	CG7766	CG8322	CG9245	CG32742	CG6432	CG6020	500c	CG10754	CG7359	CG8893	CG7409	CG5371	CG7671	CG11198
C	CG8376	CG8385	CG6538	0c	CG7471	CG17035	CG10756	CG6463	CG6538	CG32380	CG18389	CG32578	SOD	CG5193	CG7926	CG32072	CG10580	CG8095	CG5193	CG17035	CG17033	CG7262	TBPH	CG31005
D	CG8095	CG32578	CG6474	CG31005	CG7069	CG7671	CG18402	CG11491	VAPB	CG6910	CG10387	CG18445	CG11124	CG8891	CG17033	CG18319	CG17608	CG17299	CG8013	CG6432	CG5585	CG6020	CG32072	SOD
E	CG8475	GFP	CG8893	CG9984	CG8651	CG7158	CG7864	CG9946	CG8427	CG10374	CG9539	CG31005	CG10810	CG6692	TBPH	CG10667	CG9904	CG9946	CG8722	CG12789	CG7962	CG4380	CG9242	CG4533
F	??????	CG10810	CG8722	CG9009	CG6303	CG18389	CG10754	CG6743	CG8722	CG10574	CG17299	CG8732	??????	CG3576	CG4311	CG6343	VAPB	CG6904	CG9277	CG10574	0c	CG9485	CG9998	CG8376
G	CG10798	CG6335	CG7262	CG6015	CG18445	CG5198	CG8362	CG5650	500c	CG8946	1000c	CG6335	CG11006	CG6439	CG6871	CG4533	CG10281	CG11124	CG7158	CG8732	CG32578	CG9009	CG10374	CG7069
H	CG7926	500c	SOD	CG7704	CG10574	CG11198	CG7409	CG9904	CG6474	CG9485	CG18402	CG4380	CG7035	CG9423	CG17223	CG17608	CG6474	CG7926	CG8322	CG5790	CG6910	CG10667	??????	CG8427
I	CG8732	CG7538	CG10374	CG32038	CG9874	CG6020	CG5193	CG6692	CG8362	CG5504	CG10281	CG10754	CG8893	CG5790	CG5650	CG8975	CG5650	CG32038	CG5931	CG6303	CG8946	CG8019	CG7035	VAPB
J	CG32072	CG13969	CG5504	CG5231	CG32220	CG4380	CG10281	CG5371	CG8376	VAPB	CG10798	CG10262	CG5231	CG8831	GFP	CG7409	CG5202	CG6439	CG5231	CG32742	CG7538	CG6335	CG17492	CG18319
K	VAPB	CG5202	CG9539	CG32742	CG8831	SOD	CG6910	CG5585	CG12789	CG17492	CG6904	CG9874	SOD	CG5371	CG9904	??????	CG7864	CG10262	TBPH	CG15615	CG9539	CG4311	CG32220	CG7766
L	CG6904	CG7035	CG8013	CG4533	CG6343	CG9485	CG8891	CG9433	CG9277	CG8385	CG7885	CG8095	CG8651	CG7262	CG9009	CG6463	CG9423	CG6692	CG6538	CG6958	CG6770	CG11491	GFP	CG9603
M	CG7359	CG6871	CG9423	CG8019	CG6958	CG11006	CG7962	CG12789	CG9984	CG7704	CG7962	CG9998	CG6303	CG11198	CG6743	CG6015	CG17223	CG3576	CG10756	??????	CG18389	CG10810	CG8831	CG7885
N	CG9245	CG17608	CG10580	CG6432	CG9603	CG9750	CG9277	CG5931	TBPH	CG10580	CG7069	CG10756	CG9433	CG7864	CG5931	0c	CG6743	CG18402	CG10798	CG8475	1000c	CG9433	CG10124	CG7704
O	CG6770	CG10387	CG6439	CG17223	CG7885	CG17033	CG8946	CG9242	CG6770	CG7158	CG7471	CG11491	CG32220	CG7671	CG5202	CG9603	CG6463	CG9984	CG5504	CG18445	CG8891	CG9874	CG8651	CG8385
P	1000c	CG15615	CG9998	500c	??????	CG5790	CG32380	GFP	CG5198	CG6958	CG32038	CG17035	CG13969	CG5585	CG8013	GFP	CG13969	CG9750	SOD	CG7471	CG6015	TBPH	CG8975	0c

Plate 7, 36 hours

	TBPH	SOD	VAPB	GFP	0c	500c	1000c	8	9	10	11	12	13	14	15	16	17	18	19	20	21	22	23	24
A	CG7035	CG10580	CG17223	SOD	CG8831	0c	CG6303	CG5790	CG7359	CG7158	CG11198	CG9242	CG32380	CG6474	CG17033	CG7671	CG7035	TBPH	CG8831	CG11491	CG5790	CG9433	CG7885	CG8475
B	CG8376	0c	CG10798	CG6538	CG7538	CG10667	CG7409	CG11198	CG10810	CG7766	CG5202	CG15615	CG12789	CG4380	CG6871	CG32578	CG13969	CG9946	CG4380	CG6538	CG17035	CG8322	CG32380	CG7962
C	CG10574	CG8322	CG8732	CG11124	CG32038	VAPB	CG17033	CG6743	CG32578	CG10574	CG10810	CG8831	CG7885	CG8946	CG9874	SOD	??????	CG5931	CG6474	CG9242	CG8891	CG6463	CG10798	CG17299
D	CG9946	CG7069	CG12789	CG3576	CG6871	CG9423	CG9874	CG8362	TBPH	CG5585	CG6303	CG5931	1000c	CG5790	CG9603	CG10756	CG17223	CG15615	VAPB	CG10810	CG10262	CG5504	CG5202	CG31005
E	GFP	CG5231	1000c	CG17299	CG8975	CG10374	CG7766	CG9242	??????	CG18389	CG6463	CG7359	CG5650	CG8427	CG8732	CG7409	CG7409	CG5371	CG8893	CG9009	CG10281	CG18445	0c	CG5585
F	CG9485	CG5198	CG8891	CG7864	CG6770	CG8427	CG8722	CG8946	CG32038	CG7926	500c	CG31005	CG32220	CG4533	CG10124	CG6538	CG7704	CG9539	CG7359	GFP	CG18402	CG12789	CG10667	CG5193
G	CG6020	CG10387	CG5585	CG6463	SOD	CG17035	CG10124	CG9245	CG5198	CG6692	CG7864	CG9277	CG10262	CG9946	CG9485	CG17223	CG11198	CG17608	CG8427	CG5231	CG9485	CG9874	CG9423	CG6958
H	CG4380	CG32380	CG6439	CG6343	CG8651	CG18319	??????	CG6015	CG18445	CG9423	CG17492	CG9984	CG6770	0c	CG8362	CG10798	CG32220	CG32038	CG9245	CG4533	CG7471	CG10387	CG7766	500c
I	CG6432	CG5371	CG9433	CG8019	CG6910	CG9009	GFP	CG6692	CG5371	CG4311	CG7035	TBPH	CG8475	CG6439	CG8893	CG8019	CG9750	CG9603	CG9904	CG6770	CG3576	CG7671	CG9984	CG7262
J	500c	CG7962	CG7704	VAPB	CG4311	CG18445	CG32742	CG7885	CG17608	CG8975	CG10580	CG7538	CG32742	CG32072	CG7069	CG9539	SOD	CG8722	GFP	CG8732	CG8362	TBPH	CG9998	CG8385
K	CG6958	CG7158	CG10756	CG9998	CG10262	CG8385	CG11006	CG8893	CG8376	CG6335	CG6904	CG10374	CG17299	CG8651	CG18319	CG13969	CG6692	CG6343	CG18389	CG9277	CG6439	CG17492	CG6432	CG8975
L	CG7926	CG8013	CG7262	CG18389	CG9984	CG9539	CG6474	CG17608	CG9009	VAPB	CG10667	CG8095	CG10387	CG17035	CG6910	CG5193	CG6904	??????	CG6743	CG6335	CG10374	CG8019	CG17033	CG6020
M	CG5504	CG9904	CG10281	CG31005	CG9603	CG8095	CG11491	1000c	CG6343	CG3576	CG8722	SOD	CG6015	CG10754	VAPB	CG9904	CG10124	CG8095	CG32742	1000c	CG7864	CG11124	CG18319	CG6303
N	CG32220	CG6335	SOD	CG7671	CG8475	CG17492	CG7471	CG6904	CG7704	CG9998	CG11006	CG7262	CG6020	CG8385	CG6958	CG9245	GFP	CG5650	CG32578	CG8651	CG5198	CG6910	TBPH	CG10756
O	CG32072	CG5931	??????	CG15615	CG5650	CG9750	CG10754	500c	CG7471	CG9750	CG5231	CG18402	CG8013	CG8891	CG9433	CG6432	CG7926	CG10574	CG8013	CG7158	CG10754	CG6871	CG8946	CG4311
P	TBPH	CG5193	CG5202	CG18402	GFP	CG4533	CG13969	CG9277	CG10281	CG11124	??????	CG11491	CG6743	CG5504	CG7962	CG8322	CG7069	CG7538	CG8376	CG32072	CG6015	CG11006	CG10580	VAPB

Plate 8, 24 hours

	TBPH	SOD	VAPB	GFP	0c	500c	1000c	8	9	10	11	12	13	14	15	16	17	18	19	20	21	22	23	24
A	CG17026	CG4528	CG3612	CG13298	CG4153	GFP	CG5109	1000c	CG14935	CG17026	VAPB	CG4738	CG16788	CG3460	CG3924	CG4166	CG17876	CG14724	CG33138	CG6251	CG1594	CG17280	CG2859	CG7185
B	TBPH	CG17028	CG8844	CG11423	CG3949	CG9244	CG11680	CG11579	CG9495	CG3192	CG3612	CG3949	CG6251	CG4169	CG1828	CG1451	500c	CG15434	CG3192	CG4453	CG3283	CG2158	CG3582	CG31550
C	CG4079	CG4088	CG2286	0c	CG3299	CG6506	CG9200	CG2014	CG2286	CG14724	CG11779	CG6543	SOD	CG7098	CG3886	CG14887	CG17689	CG3938	CG7098	CG6506	CG11092	CG3181	TBPH	CG5028
D	CG3938	CG6543	CG2210	CG5028	CG3127	CG3582	CG11913	CG1591	VAPB	CG2964	CG17280	CG11994	CG9244	CG4396	CG11092	CG11680	CG11669	CG11423	CG3905	CG1828	CG4448	CG1451	CG14887	SOD
E	CG4166	GFP	CG4453	CG16892	CG1555	CG3180	CG13900	CG16788	CG4153	CG17766	CG12079	CG5028	CG11274	CG2677	TBPH	CG8844	CG4579	CG16788	CG4206	CG12096	CG14813	CG3861	CG4738	CG4039
F	??????	CG11274	CG4206	CG5595	CG7070	CG11779	CG15434	CG2807	CG4206	CG17437	CG11423	CG12372	??????	CG5109	CG13298	CG1594	VAPB	CG2960	CG4817	CG17437	0c	CG4912	CG16944	CG4079
G	CG3169	CG1584	CG3181	CG1664	CG11994	CG7185	CG33138	CG5179	500c	CG13425	1000c	CG1584	CG17876	CG1970	CG2859	CG4039	CG17029	CG9244	CG3180	CG12372	CG6543	CG5595	CG17766	CG3127
H	CG3886	500c	SOD	CG3605	CG17437	CG31550	CG3283	CG4579	CG2210	CG4912	CG11913	CG3861	CG3069	CG4887	CG11337	CG11669	CG2210	CG3886	CG3949	CG6987	CG2964	CG8844	??????	CG4153
I	CG12372	CG3460	CG17766	CG14740	CG14941	CG1451	CG7098	CG2677	CG33138	CG5444	CG17029	CG15434	CG4453	CG6987	CG5179	CG4528	CG5179	CG14740	CG1539	CG7070	CG13425	CG3924	CG3069	VAPB
J	CG14887	CG12233	CG5444	CG3510	CG32721	CG3861	CG17029	CG2158	CG4079	VAPB	CG3169	CG17028	CG3510	CG4347	GFP	CG3283	CG5271	CG1970	CG3510	CG4169	CG3460	CG1584	CG11579	CG11680
K	VAPB	CG5271	CG12079	CG4169	CG4347	SOD	CG2964	CG4448	CG12096	CG11579	CG2960	CG14941	SOD	CG2158	CG4579	??????	CG13900	CG17028	TBPH	CG9495	CG12079	CG13298	CG32721	CG3612
L	CG2960	CG3069	CG3905	CG4039	CG1594	CG4912	CG4396	CG4900	CG4817	CG4088	CG3688	CG3938	CG1555	CG3181	CG5595	CG2014	CG4887	CG2677	CG2286	CG3058	CG8787	CG1591	GFP	CG6292
M	CG3192	CG2859	CG4887	CG3924	CG3058	CG17876	CG14813	CG12096	CG16892	CG3605	CG14813	CG16944	CG7070	CG31550	CG2807	CG1664	CG11337	CG5109	CG9200	??????	CG11779	CG11274	CG4347	CG3688
N	CG6251	CG11669	CG17689	CG1828	CG6292	CG14935	CG4817	CG1539	TBPH	CG17689	CG3127	CG9200	CG4900	CG13900	CG1539	0c	CG2807	CG11913	CG3169	CG4166	1000c	CG4900	CG17026	CG3605
O	CG8787	CG17280	CG1970	CG11337	CG3688	CG11092	CG13425	CG4738	CG8787	CG3180	CG3299	CG1591	CG32721	CG3582	CG5271	CG6292	CG2014	CG16892	CG5444	CG11994	CG4396	CG14941	CG1555	CG4088
P	1000c	CG9495	CG16944	500c	??????	CG6987	CG14724	GFP	CG7185	CG3058	CG14740	CG6506	CG12233	CG4448	CG3905	GFP	CG12233	CG14935	SOD	CG3299	CG1664	TBPH	CG4528	0c

Plate 8, 36 hours

	TBPH	SOD	VAPB	GFP	0c	500c	1000c	8	9	10	11	12	13	14	15	16	17	18	19	20	21	22	23	24
A	CG3069	CG17689	CG11337	SOD	CG4347	0c	CG7070	CG6987	CG3192	CG3180	CG31550	CG4738	CG14724	CG2210	CG11092	CG3582	CG3069	TBPH	CG4347	CG1591	CG6987	CG4900	CG3688	CG4166
B	CG4079	0c	CG3169	CG2286	CG3460	CG8844	CG3283	CG31550	CG11274	CG3612	CG5271	CG9495	CG12096	CG3861	CG2859	CG6543	CG12233	CG16788	CG3861	CG2286	CG6506	CG3949	CG14724	CG14813
C	CG17437	CG3949	CG12372	CG9244	CG14740	VAPB	CG11092	CG2807	CG6543	CG17437	CG11274	CG4347	CG3688	CG13425	CG14941	SOD	??????	CG1539	CG2210	CG4738	CG4396	CG2014	CG3169	CG11423
D	CG16788	CG3127	CG12096	CG5109	CG2859	CG4887	CG14941	CG33138	TBPH	CG4448	CG7070	CG1539	1000c	CG6987	CG6292	CG9200	CG11337	CG9495	VAPB	CG11274	CG17028	CG5444	CG5271	CG5028
E	GFP	CG3510	1000c	CG11423	CG4528	CG17766	CG3612	CG4738	??????	CG11779	CG2014	CG3192	CG5179	CG4153	CG12372	CG3283	CG3283	CG2158	CG4453	CG5595	CG17029	CG11994	0c	CG4448
F	CG4912	CG7185	CG4396	CG13900	CG8787	CG4153	CG4206	CG13425	CG14740	CG3886	500c	CG5028	CG32721	CG4039	CG17026	CG2286	CG3605	CG12079	CG3192	GFP	CG11913	CG12096	CG8844	CG7098
G	CG1451	CG17280	CG4488	CG2014	SOD	CG6506	CG17026	CG6251	CG7185	CG2677	CG13900	CG4817	CG17028	CG16788	CG4912	CG11337	CG31550	CG11669	CG4153	CG3510	CG4912	CG14941	CG4887	CG3058
H	CG3861	CG14724	CG1970	CG1594	CG1555	CG11680	??????	CG1664	CG11994	CG4887	CG11579	CG16892	CG8787	0c	CG33138	CG3169	CG32721	CG14740	CG6251	CG4039	CG3299	CG17280	CG3612	500c
I	CG1828	CG2158	CG4900	CG3924	CG2964	CG5595	GFP	CG2677	CG2158	CG13298	CG3069	TBPH	CG4166	CG1970	CG4453	CG3924	CG14935	CG6292	CG4579	CG8787	CG5109	CG3582	CG16892	CG3181
J	500c	CG14813	CG3605	VAPB	CG13298	CG11994	CG4169	CG3688	CG11669	CG4528	CG17689	CG3460	CG4169	CG14887	CG3127	CG12079	SOD	CG4206	GFP	CG12372	CG33138	TBPH	CG16944	CG4088
K	CG3058	CG3180	CG9200	CG16944	CG17028	CG4088	CG17876	CG4453	CG4079	CG1584	CG2960	CG17766	CG11423	CG1555	CG11680	CG12233	CG2677	CG1594	CG11779	CG4817	CG1970	CG11579	CG1828	CG4528
L	CG3886	CG3905	CG3181	CG11779	CG16892	CG12079	CG2210	CG11669	CG5595	VAPB	CG8844	CG3938	CG17280	CG6506	CG2964	CG7098	CG2960	??????	CG2807	CG1584	CG17766	CG3924	CG11092	CG1451
M	CG5444	CG4579	CG17029	CG5028	CG6292	CG3938	CG1591	1000c	CG1594	CG5109	CG4206	SOD	CG1664	CG15434	VAPB	CG4579	CG17026	CG3938	CG4169	1000c	CG13900	CG9244	CG11680	CG7070
N	CG32721	CG1584	SOD	CG3582	CG4166	CG11579	CG3299	CG2960	CG3605	CG16944	CG17876	CG3181	CG1451	CG4088	CG3058	CG6251	GFP	CG5179	CG6543	CG1555	CG7185	CG2964	TBPH	CG9200
O	CG14887	CG1539	??????	CG9495	CG5179	CG14935	CG15434	500c	CG3299	CG14935	CG3510	CG11913	CG3905	CG4396	CG4900	CG1828	CG3886	CG17437	CG3905	CG3180	CG15434	CG2859	CG13425	CG13298
P	TBPH	CG7098	CG5271	CG11913	GFP	CG4039	CG12233	CG4817	CG17029	CG9244	??????	CG1591	CG2807	CG5444	CG14813	CG3949	CG3127	CG3460	CG4079	CG14887	CG1664	CG17876	CG17689	VAPB

The genes were categorized into 9 categories, ALS loci, ALS related genes, VAP genetic interactors, mTOR pathway, VAP motif interactors, lipid biosynthesis, unfolded protein response, ubiquitin proteasomal system and autophagy (Table 2), as described in Chapter II.

Table 2: 900 genes, utilized for the screen, classified and listed into 10 categories associated with ALS or VAP or proteostasis.

ALS Loci	ALS related genes	VAP Genetic interactors	mTOR Pathway	Motif interactors	Lipid Biosynthesis	Unfolded protein Response	Ubiquitin Proteasomal System	Autophagy
20	**36**	**273**	**22**	**34**	**92**	**123**	**212**	**88**
CG9279	CG9907	CG9998	CG8846	CG9378	CG9985	CG9916	CG9952	CG9862
CG9206	CG9650	CG9984	CG8274	CG8739	CG9904	CG9847	CG9949	CG9746
CG7919	CG8905	CG9953	CG8002	CG8279	CG9709	CG9828	CG9934	CG9623
CG7804	CG8824	CG9946	CG6998	CG7476	CG9707	CG9617	CG9885	CG9539
CG7504	CG8160	CG9874	CG6975	CG7281	CG9655	CG9588	CG9868	CG9375
CG7158	CG6963	CG9750	CG6147	CG6760	CG9526	CG9429	CG9790	CG9241
CG5977	CG6778	CG9638	CG5686	CG6708	CG9520	CG8971	CG9772	CG9193
CG5166	CG5575	CG9603	CG5092	CG6428	CG9347	CG8937	CG9602	CG8938
CG5014	CG4872	CG9543	CG4320	CG6214	CG9342	CG8885	CG9556	CG8743
CG4618	CG4804	CG9495	CG4006	CG6198	CG9245	CG8863	CG9484	CG8722
CG31528	CG4402	CG9485	CG3493	CG5722	CG9160	CG8798	CG9461	CG8678
CG2999	CG3766	CG9438	CG3051	CG5688	CG9128	CG8542	CG9327	CG8595
CG17840	CG32635	CG9433	CG3004	CG5684	CG9078	CG8336	CG9324	CG8532
CG16725	CG32423	CG9423	CG2503	CG5675	CG9042	CG8203	CG9291	CG8142
CG15433	CG31057	CG9391	CG2072	CG5379	CG9009	CG7861	CG9242	CG8091
CG14224	CG30429	CG9296	CG14024	CG5285	CG8946	CG7768	CG9198	CG8068
CG13531	CG18803	CG9277	CG12855	CG5005	CG8766	CG7756	CG9153	CG8057
CG12338	CG1865	CG9244	CG1210	CG4699	CG8732	CG7619	CG9139	CG7986
CG11793	CG1859	CG9200	CG11804	CG31935	CG8709	CG7387	CG9086	CG7359
CG10327	CG1795	CG9172	CG10967	CG31423	CG8593	CG7382	CG9014	CG7331
	CG1787	CG8975	CG1081	CG31098	CG8536	CG7257	CG8998	CG7224
	CG17753	CG8893	CG10539	CG30463	CG7962	CG7235	CG8979	CG7111
	CG1768	CG8891		CG17726	CG7923	CG6792	CG8787	CG7109
	CG14718	CG8844		CG16879	CG7864	CG6766	CG8786	CG7053
	CG14490	CG8831		CG15106	CG7842	CG6734	CG8725	CG6877
	CG13189	CG8771		CG14815	CG7660	CG6719	CG8711	CG6770
	CG1318	CG8571		CG14238	CG7642	CG6603	CG8705	CG6542
	CG12284	CG8475		CG13624	CG7113	CG6302	CG8651	CG6349
	CG11940	CG8465		CG11943	CG6728	CG6226	CG8610	CG6258
	CG11759	CG8427		CG11212	CG6562	CG6155	CG8392	CG6235
	CG11594	CG8385		CG11115	CG6207	CG5808	CG8337	CG6194
	CG11335	CG8376		CG1059	CG6016	CG5748	CG8284	CG6116

	CG11153	CG8362		CG1024	CG5315	CG5682	CG8188	CG5949
	CG10956	CG8322		CG10123	CG5295	CG5520	CG8184	CG5923
	CG1063	CG8219			CG5231	CG5504	CG7769	CG5671
	CG10335	CG8095			CG4934	CG5482	CG7762	CG5643
		CG8019			CG4899	CG5436	CG7747	CG5602
		CG8013			CG4774	CG5387	CG7656	CG5489
		CG7926			CG4600	CG5330	CG7528	CG5429
		CG7917			CG4581	CG5289	CG7425	CG5373
		CG7899			CG4574	CG5119	CG7375	CG5370
		CG7885			CG4389	CG5071	CG7220	CG5335
		CG7843			CG4311	CG5001	CG7037	CG5313
		CG7776			CG4200	CG4886	CG6966	CG4533
		CG7766			CG4162	CG4735	CG6932	CG4428
		CG7704			CG3947	CG4583	CG6789	CG4280
		CG7671			CG3881	CG4535	CG6759	CG4268
		CG7564			CG3682	CG4523	CG6720	CG4141
		CG7538			CG3620	CG4501	CG6438	CG4082
		CG7471			CG3576	CG4466	CG6303	CG3992
		CG7409			CG3573	CG4463	CG6233	CG3936
		CG7314			CG3525	CG4461	CG6190	CG3722
		CG7262			CG3415	CG4380	CG6099	CG3615
		CG7254			CG32578	CG4264	CG5841	CG3411
		CG7217			CG32484	CG4236	CG5823	CG32592
		CG7207			CG32380	CG4183	CG5788	CG3143
		CG7185			CG32220	CG4167	CG5709	CG31033
		CG7098			CG32072	CG4164	CG5659	CG3041
		CG7070			CG32038	CG4153	CG5648	CG2699
		CG7069			CG31991	CG4147	CG5629	CG2621
		CG7035			CG31005	CG4035	CG5604	CG2245
		CG6987			CG30502	CG3966	CG5595	CG18402
		CG6958			CG3033	CG3895	CG5519	CG18389
		CG6950			CG3028	CG3869	CG5440	CG1771
		CG6910			CG2929	CG3810	CG5378	CG1765
		CG6904			CG2212	CG3511	CG5271	CG17299
		CG6885			CG18445	CG3492	CG5266	CG17291
		CG6871			CG17608	CG3457	CG5203	CG16944
		CG6743			CG1747	CG3291	CG5186	CG1616
		CG6692			CG17223	CG32236	CG5087	CG15615
		CG6674			CG17035	CG32130	CG4943	CG1560
		CG6647			CG16708	CG3210	CG4909	CG14980
		CG6543			CG1471	CG3152	CG4904	CG14214
		CG6538			CG14517	CG3136	CG4697	CG14207
		CG6506			CG13969	CG30350	CG4569	CG13701

		CG6502			CG13401	CG3024	CG4494	CG1347
		CG6474			CG13089	CG2947	CG4443	CG12821
		CG6463			CG12789	CG2887	CG4420	CG1241
		CG6439			CG12389	CG2852	CG4319	CG12334
		CG6432			CG12140	CG2087	CG4274	CG11968
		CG6345			CG12077	CG1966	CG4244	CG11491
		CG6343			CG12070	CG1937	CG4238	CG11006
		CG6342			CG11621	CG1890	CG4166	CG10810
		CG6341			CG11198	CG1866	CG4157	CG10798
		CG6337			CG11143	CG17266	CG4097	CG10473
		CG6335			CG11124	CG17051	CG4080	CG10360
		CG6292			CG11111	CG16954	CG4005	CG10130
		CG6251			CG11055	CG16916	CG3929	CG10023
		CG6238			CG1049	CG16817	CG3905	
		CG6220			CG10374	CG15767	CG3889	
		CG6048			CG10367	CG15676	CG3886	
		CG6020			CG10260	CG14899	CG3697	
		CG6015				CG1489	CG3571	
		CG5971				CG14715	CG3473	
		CG5953				CG14536	CG3455	
		CG5931				CG14228	CG3431	
		CG5925				CG1416	CG3422	
		CG5924				CG1409	CG3416	
		CG5847				CG13892	CG3412	
		CG5828				CG13664	CG3356	
		CG5790				CG13570	CG3329	
		CG5733				CG1341	CG32707	
		CG5650				CG1333	CG32486	
		CG5585				CG12919	CG32434	
		CG5444				CG1242	CG3234	
		CG5371				CG12366	CG32177	
		CG5325				CG12101	CG31742	
		CG5202				CG12020	CG3060	
		CG5198				CG12019	CG3048	
		CG5193				CG11888	CG3018	
		CG5181				CG11858	CG3000	
		CG5179				CG11840	CG2960	
		CG5109				CG11820	CG2924	
		CG5028				CG11777	CG2759	
		CG4924				CG1133	CG2681	
		CG4913				CG11035	CG2574	
		CG4912				CG11001	CG2508	
		CG4900				CG1100	CG2331	

		CG4887				CG10907	CG2257	
		CG4817				CG10811	CG2218	
		CG4738				CG10635	CG2125	
		CG4715				CG10578	CG2048	
		CG4646				CG10210	CG2038	
		CG4627					CG2028	
		CG4579					CG2013	
		CG4528					CG1950	
		CG4486					CG1945	
		CG4453					CG1877	
		CG4448					CG18495	
		CG4396					CG1836	
		CG4347					CG18341	
		CG4206					CG18332	
		CG4169					CG18319	
		CG4088					CG18174	
		CG4086					CG1782	
		CG4079					CG17492	
		CG4039					CG17437	
		CG4012					CG1736	
		CG3975					CG17343	
		CG3949					CG17331	
		CG3938					CG17302	
		CG3924					CG17301	
		CG3861					CG17268	
		CG3688					CG17033	
		CG3612					CG17030	
		CG3605					CG16988	
		CG3582					CG16983	
		CG3510					CG16982	
		CG3500					CG1591	
		CG3476					CG15800	
		CG3474					CG15645	
		CG3460					CG1554	
		CG33138					CG15437	
		CG3299					CG15237	
		CG3284					CG1519	
		CG3283					CG15141	
		CG32742					CG1512	
		CG32721					CG15104	
		CG32703					CG15010	
		CG32685					CG14884	
		CG32437					CG14739	

		CG3192					CG14472	
		CG3181					CG14444	
		CG3180					CG14435	
		CG31769					CG1403	
		CG3169					CG1401	
		CG31550					CG13732	
		CG3127					CG13349	
		CG31003					CG13343	
		CG3069					CG13221	
		CG3058					CG13030	
		CG30161					CG12812	
		CG30043					CG12799	
		CG2964					CG12765	
		CG2859					CG12743	
		CG2807					CG12423	
		CG2677					CG12359	
		CG2286					CG12323	
		CG2210					CG12276	
		CG2158					CG12265	
		CG2014					CG12227	
		CG1970					CG12161	
		CG1828					CG12096	
		CG18110					CG12000	
		CG17985					CG11988	
		CG17982					CG11981	
		CG17876					CG11896	
		CG17766					CG11734	
		CG17760					CG11579	
		CG17689					CG11552	
		CG17327					CG11419	
		CG17280					CG1134	
		CG17029					CG11330	
		CG17028					CG11321	
		CG17026					CG11261	
		CG16935					CG11070	
		CG16892					CG10981	
		CG16788					CG10961	
		CG1664					CG10938	
		CG1625					CG10862	
		CG1594					CG10855	
		CG1584					CG10850	
		CG15589					CG10694	
		CG1555					CG10682	

		CG15434					CG10679	
		CG1539					CG10640	
		CG15188					CG10523	
		CG15160					CG10370	
		CG14941					CG10254	
		CG14935					CG10230	
		CG14887					CG10149	
		CG14837					CG10108	
		CG14813						
		CG14740						
		CG14724						
		CG14606						
		CG1451						
		CG14326						
		CG14222						
		CG14181						
		CG14125						
		CG14043						
		CG14032						
		CG14006						
		CG13994						
		CG13900						
		CG13532						
		CG13425						
		CG13388						
		CG13387						
		CG13298						
		CG13296						
		CG13116						
		CG13075						
		CG13063						
		CG13048						
		CG12822						
		CG12746						
		CG12538						
		CG12372						
		CG12233						
		CG12079						
		CG11994						
		CG11913						
		CG11811						
		CG11779						
		CG11680						

		CG11669						
		CG11560						
		CG11444						
		CG11423						
		CG11415						
		CG11337						
		CG11274						
		CG11092						
		CG10965						
		CG10846						
		CG10756						
		CG10754						
		CG10743						
		CG10667						
		CG10580						
		CG10574						
		CG10387						
		CG10315						
		CG10281						
		CG10267						
		CG10262						
		CG10243						
		CG10207						
		CG10125						
		CG10124						
		CG10089						

High throughput data analysis

Images from the FITC and DAPI channels for each sample were read using the Bio-Formats MATLAB toolbox (Linkert et al. 2010) and were processed using custom MATLAB script (See below) (Dey et al. 2014). The segmentation was done using the DAPI images and the extraction of pixel intensities was done on the FITC channel. Illumination correction was performed as a pre-processing step on the DAPI Images and individual nuclei were segmented after a contrast stretching routine was applied. The identified objects were further filtered for outliers, based on a size-based cutoffs and the individual 8-connected components were labelled as separate nuclei. Under 20x magnification we estimated the cellular radius to be around 10 pixels corresponding to 5 μm. Thus, labelled cellular objects (ROIs), were obtained by dilating the centroids of each nuclei

by 10 pixels. Around 400 ROIs were obtained from each field consistent with manually counted cells in these images. The resultant ROI's were further filtered for clumps and out of focus objects. The GFP intensities were obtained for these ROI's post a local background correction of the FITC images (with a disk size of 3 pixels). Average and total intensities were calculated from the pixel data obtained from every cell/ROI from these FITC images. A Kolmogorov-Smirnov-like (KS) statistic was used to assign Z-scores to each gene on plate as reported by (Dey et al. 2014). A statistically significant threshold was obtained for the triplicate data using monte-carlo simulations. Genes were classified as hits, if it occurred two or more times above a given Z-score threshold. The false positive rates for both parameters at both time points was zero. The false negative rates for average intensity for 24 hours- time point was 0.2523 and for 36 hours- time point was 0.361. The false negative rates for total intensity for 24 hours- time point was 0.3838 and for 36 hours- time point was 0.3164. We identified 150 genes using average cell intensity and 85 genes using total cell intensity as parameters (Chapter II), with an overlap of 57 genes (Table 3)

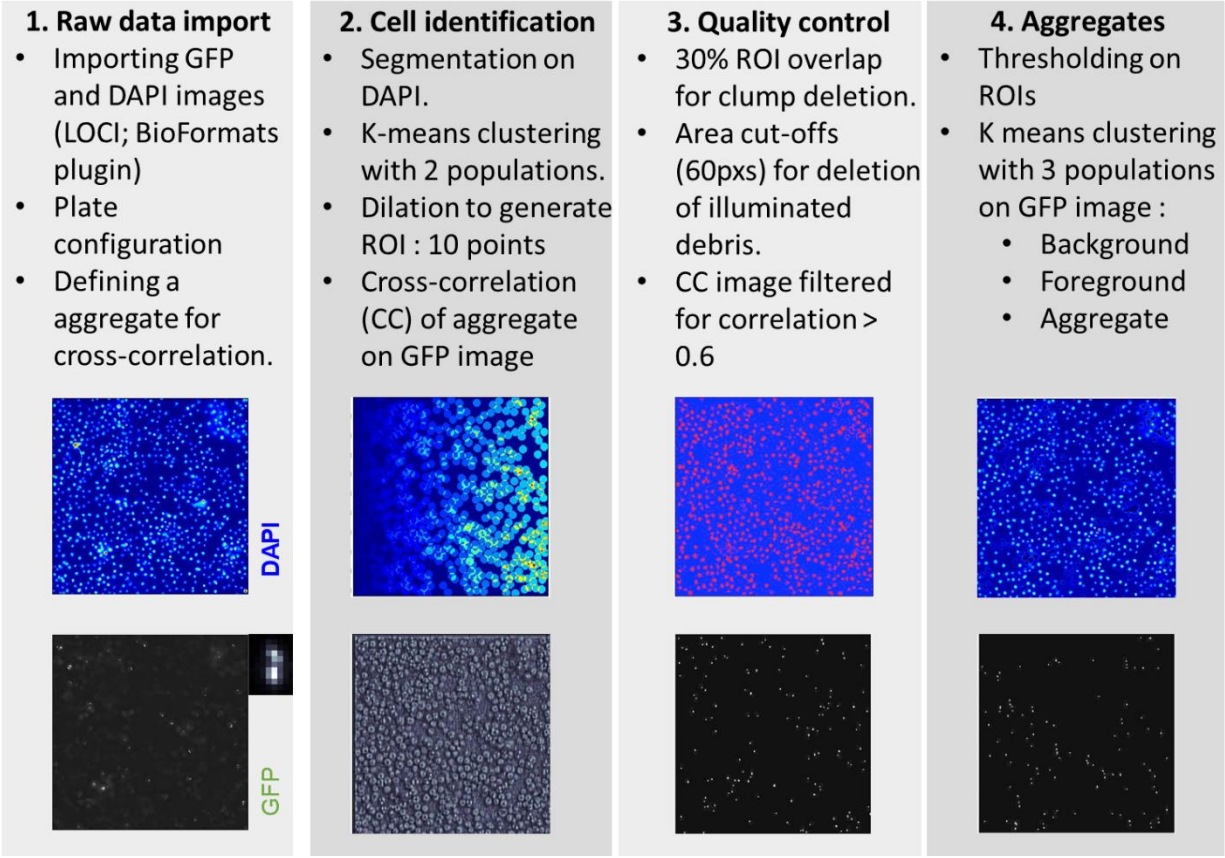

Figure 2: Workflow of the steps executed for image analysis using an automated MATLAB script. Figure contributed by Lokesh Pimpale. (Dey et al. 2014)

MATLAB code (Source: Balaji Ramalingam)

```
%Screen : Girish's Screen (VAP aggregation at 24,36 and 48 hours)
%Author : Balaji
%Last edited : 04/07/2014

%Init
clear all;close all;

%Params
%96 well ids
wellvec={'A','B','C','D','E','F','G','H','I','J','K','L','M','N','O','P','Q','R','S','T','U','V','W','X','Y','Z'};
%params
masterdir = '/Users/bramalingam/Google Drive';
slashtype='/';
timepoints = {'24 HRS' '36 HRS'};
subdirec = dir ([masterdir slashtype 'Plate*']);
cntr = 1;
for i = 1:length(subdirec)
   platedir = [subdirec(i).folder slashtype subdirec(i).name];
   for j = 1:2
      timedir = [platedir slashtype timepoints{j}];
      platenamedir = dir([timedir slashtype 'MFGTMP_*']);
      platenamedir = [platenamedir.folder slashtype platenamedir.name];
      inputdirvec{cntr,1} = platenamedir; %#ok<*SAGROW>
      platename = [subdirec(i).name '_' timepoints{j}];
      inputdirvec{cntr,2} = platename;
      cntr = cntr + 1;
   end
end
keyboard
batchlength = 1;
disks = [3 7 11];
%inputdir
for j1=1:length(inputdirvec)

   inputdir = inputdirvec{j1,1};
   if exist(inputdir) == 0
      continue
   end
   %Resultmat
   idx1=findstr(slashtype,inputdir); %#ok<*FSTR>
   resultdir = inputdirvec{j1,2};
   if exist(resultdir) == 0
      mkdir(resultdir)
   end

   %path
   filepath1=fuf([inputdir slashtype '*d0.C01'],'detail');
```

```
 %Read GFP
filepath=filepath1{1};
reader = bfGetReader(filepath);

welldatamat=[];namevec={};wellcounter = 1;
for i=1:reader.getSeriesCount()

   reader.setSeries(i-1)
   gfp1= bfGetPlane(reader, 2);

   for gf = 1:length(disks)
      gfp{gf,1} = imtophat(gfp1,strel('disk',disks(gf)));
      gfp{gf,2} = bwlabel(imbinarize(gfp{gf,1},graythresh(gfp{gf,1})));
   end

   %Read DAPI
   dapi=bfGetPlane(reader, 1); %corrected read location

   %wellID & %FieldID
   dapi = imadjust(dapi);
   wellsrch='_';
   metadata = reader.getSeriesUsedFiles();
   metadata= char(metadata(1));
   idx1=max(findstr(wellsrch,metadata));
   wellid = metadata(idx1+1:idx1+3);
   fieldnumber=str2double(metadata(idx1+5:idx1+6));
   wellx=strmatch(wellid(1),wellvec,'exact'); %#ok<*MATCH3>
   welly=str2double(wellid(2:3));
   wellid_check = (wellx-1)*24 + welly;
   if wellid_check ~= wellcounter
      save([resultdir '/' num2str(wellcounter) '.mat'],'welldatamat','namevec');
      welldatamat = [];
      namevec={};
      wellcounter = wellcounter + 1;
   end
   %Threshold dapi
   img1 = imbinarize(dapi,graythresh(dapi));
   img2=bwareaopen(bwlabel(img1),300);
   pixidx=intersect(find(img1==1),find(img2==0));
   finimg=zeros(size(dapi,1),size(dapi,2));
   finimg(pixidx)=1;
   finimg=imclearborder(bwareaopen(finimg,5));
   clearvars img1 img2 pixidx;

   nucleus = finimg;
   nucleus = bwlabel(bwmorph(nucleus,'shrink',Inf));
   zerovec1=imdilate(nucleus,strel('disk',11));
   zerovec1(finimg>0) = 0;
   L = watershed(zerovec1);
   clearvars finimg dapi centvec idx idx2 nucleus;
   for idx = 1:max(L(:))
      idx2 = find(L==idx);
      if length(idx2)<1000
```

```
            gfpvec = [];
            for gf = 1:length(disks)
               idx3 = find(gfp{gf,2}>0);
               idx3 = intersect(idx2,idx3);
               if isempty(idx3)
                  meanandsumvec = [0 0];
               else
                  meanandsumvec = [mean(gfp{gf,1}(idx3)) sum(gfp{gf,1}(idx3))];
               end
               gfpvec = [gfpvec mean(gfp{gf,1}(idx2)) sum(gfp{gf,1}(idx2)) meanandsumvec...
                  sum(gfp{gf,2}(idx2)>0)/length(idx2) length(unique(gfp{gf,2}(idx2)))-1];
            end
            welldatamat=[welldatamat ; wellx welly fieldnumber ...
               length(idx2)  gfpvec]; %#ok<*AGROW>
            namevec=[namevec ; [wellid '_' num2str(fieldnumber)]];
         end
      end

      disp([j1 wellx welly fieldnumber])
   end
   save([resultdir '/' num2str(wellcounter) '.mat'],'welldatamat','namevec');
end
```

Table 3: List of 57 common modifiers of VAP(P58S) aggregation, along with their human orthologs.

Category	Genes	Name	Symbol	Human orthologs
ALS loci	CG11793	Superoxide dismutase 1	Sod1	SOD1 SOD3
	CG10327	TAR DNA-binding protein-43 homolog	TBPH	TARDBP
ALS related genes	CG11940	pico	pico	RAPH1 APBB1IP GRB10 GRB7 GRB14
VAP interactors	CG9750	reptin	rept	RUVBL2
	CG9200	Ada2a-containing complex component 1	Atac1	ZZZ3
	CG9172	NADH dehydrogenase (ubiquinone) 20 kDa subunit	ND-20	NDUFS7 TSG101 UEVLD
	CG8095	scab	scb	POLR2C
	CG7766	-	CG7766	MCM2
	CG7538	Minichromosome maintenance 2	Mcm2	HDAC1 HDAC2 HDAC3
	CG7217	Peroxiredoxin 5	Prx5	HSD17B10
	CG6292	Cyclin T	CycT	CCNT1 CCNT2 CCNK CCNQ
	CG6048	-	CG6048	HABP2 KLK14 KLK10 AZU1 CFD PRSS55

	CG5179	Cyclin-dependent kinase 9	Cdk9	CDK9 CDK13 CDK12
	CG4817	Structure specific recognition protein	Ssrp	SSRP1
	CG4646	-	CG4646	C1orf123
	CG4528	sans fille	snf	SNRPA SNRPB2
	CG4347	UGP	UGP	UGP2
	CG4206	Minichromosome maintenance 3	Mcm3	MCM3
	CG3688	RNA guanine-7 methyltransferase	Rnmt	RNMT
	CG3605	Splicing factor 3b subunit 2	Sf3b2	SF3B2
	CG3299	Vinculin	Vinc	VCL
	CG32703	Extracellularly regulated kinase 7	Erk7	MAPK15 MAPK11 MAPK13 MAPK7 MAPK1 MAPK14 MAPK12 MAPK3
	CG3192	NADH dehydrogenase (ubiquinone) ASHI subunit	ND-ASHI	NDUFB8
	CG2964	-	CG2964	PKM PKLR
	CG17689	Spt20	Spt20	SUPT20H SUPT20HL2 SUPT20HL1
	CG14935	Maltase B2	Mal-B2	SLC3A1 SLC3A2
	CG14837	-	CG14837	
	CG14813	Coat Protein (coatomer) delta	deltaCOP	ARCN1
	CG10743	Liprin-beta	Liprin-beta	PPFIBP2 PPFIBP1
Motif Interactors	CG6198	CHORD	CHORD	CHORDC1 ITGB1BP2
	CG4699	non-specific lethal 1	nsl1	KANSL1 KANSL1L
Unfolded Protein Response	CG6155	Roe1	Roe1	GRPEL1 GRPEL2
	CG5330	Nucleosome assembly protein 1	Nap1	NAP1L1 NAP1L4 NAP1L3 NAP1L2 NAP1L5
	CG4463	Heat shock protein 23	Hsp23	HSPB2 CRYAB HSPB1 HSPB6 CRYAA CRYAA2 HSPB8 HSPB3 HSPB9 HSPB7
	CG1242	Heat shock protein 83	Hsp83	HSP90AA1 HSP90AB1 HSP90B1 HSP90AA4P
Ubiquitin Proteasomal System	CG9242	burgundy	bur	GMPS
	CG7037	Cbl proto-oncogene	Cbl	SRSF1 SRSF9 SRSF6 SRSF5 SRSF4
	CG5186	scruin like at the midline	slim	KLHDC10
	CG4943	SMAD specific E3 ubiquitin protein ligase	Smurf	SMURF2 SMURF1 ITCH NEDD4L NEDD4 WWP2 WWP1
	CG4166	non-stop	not	USP22 USP27X USP51 USP3
	CG3455	Regulatory particle triple-A ATPase 4	Rpt4	PSMC6
	CG32486	-	CG32486	CYHR1

	CG3234	timeless	tim	TIMELESS
	CG3018	lesswright	lwr	UBE2I
	CG2960	Ribosomal protein L40	RpL40	UBA52
	CG2038	COP9 signalosome subunit 7	CSN7	COPS7B COPS7A
	CG18341	Proteasome beta2 subunit-related 1	Prosbeta2R1	PSMB7 PSMB10
	CG17437	will die slowly	wds	WDR5 WDR5B
	CG1736	Proteasome alpha3 subunit, Testis-specific	Prosalpha3T	PSMA4
	CG12265	Deterin	Det	BIRC5 BIRC7 BIRC3 XIAP BIRC2 BIRC8 BIRC6 NAIP
	CG10938	Proteasome alpha5 subunit	Prosalpha5	PSMA5
	CG10108	phyllopod	phyl	MAG
Autophagy	CG6116	UV-resistance associated gene	Uvrag	UVRAG
	CG5602	DNA ligase 1	DNAlig1	LIG1
	CG5489	Autophagy-related 7	Atg7	ATG7
	CG16944	stress-sensitive B	sesB	SLC25A4 SLC25A5 SLC25A6 SLC25A31
	CG10360	refractory to sigma P	ref(2)P	SQSTM1

Acknowledgements

Lokesh Pimpale performed the screen at the high throughput screening facility at C-CAMP, NCBS, Bangalore. At NCBS, we thank MS Shahab Uddin, Lokavya Kurup and Vandana for technical assistance during the execution of the screen; Dr. Kausik Chakraborty, IGIB, for advice on the analysis of the screen. Balaji Ramalingam is thanked for writing the MATLAB code for the analysis of the screen.

References

Dey G, Gupta GD, Ramalingam B, et al (2014) Exploiting cell-to-cell variability to detect cellular perturbations. PLoS One 9:. doi: 10.1371/journal.pone.0090540

Linkert M, Rueden CT, Allan C, et al (2010) Metadata matters: Access to image data in the real world. J Cell Biol 189:777–782. doi: 10.1083/jcb.201004104

Pimpale L (2015) A high throughput RNAi screen to identify modifiers of ALS8 aggregation using automated computational image analysis. Master's thesis, IISER Pune

Appendix 2

An in-house RNAi screen to identify modifiers of VAP(P58S):GFP aggregation in S2R+ cells

As described in chapter II, we performed an RNAi screen to identify modifiers of VAP(P58S) aggregation and protein levels a stable S2R+ cell line expressing the mutant protein. The materials and methods for dsRNA treatment, processing of cells, imaging and analysis, as well as western blotting, are detailed in Chapter II.

A

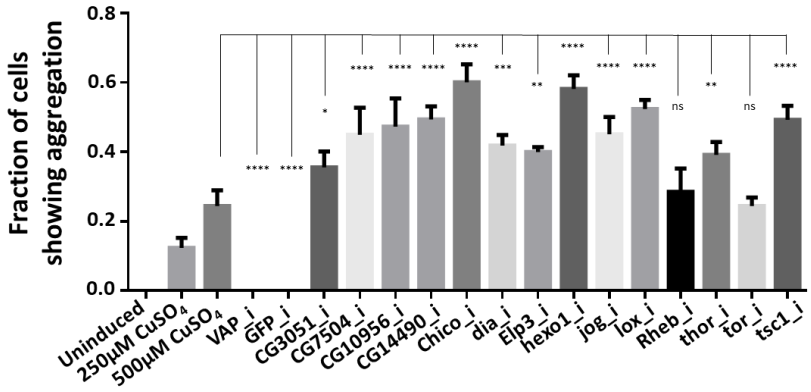

B

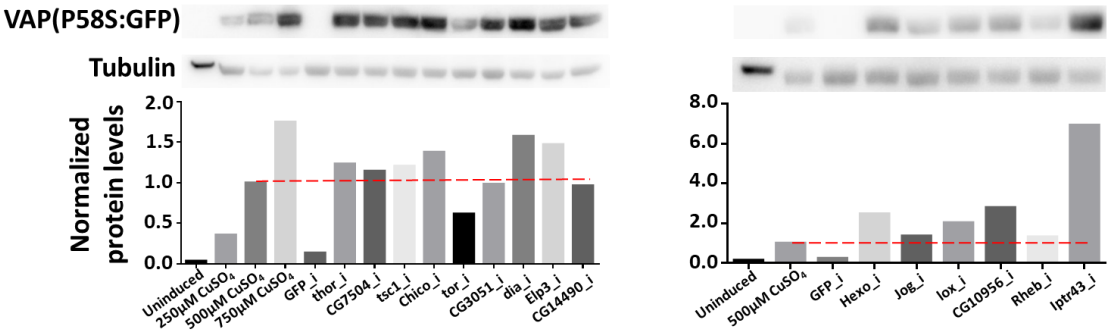

C

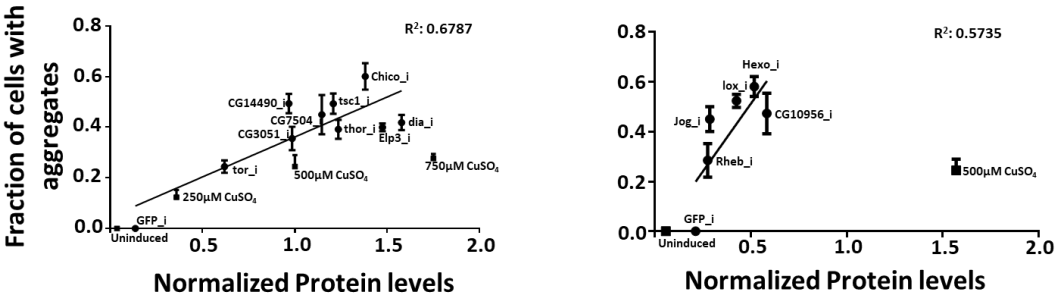

Figure 1: Validation of targets

A: Validation of targets: Graph plots for Fraction of cells showing aggregation in response to knockdown of individual targets from categories: ALS Loci, ALS related genes and mTOR pathway. ANOVA P value: ****<0.0001. Fisher's LSD multiple comparison test ** < 0.01, ***< 0.001, **** < 0.0001, ns: not significant

B: Western blot showing change in levels of expression of P58S-GFP protein normalized over tubulin, upon knockdown of individual target genes from categories: ALS Loci, ALS related genes and mTOR pathway.

C: Correlation between fraction of cells showing aggregation and protein level of VAP(P58S:GFP).

We checked whether change in aggregation was accompanied by a change in VAP(P58S:GFP) protein levels using western blots. The change in normalized protein level (Fig. 1B) for each target knockdown was found to be consistent with the corresponding change in aggregation kinetics (Fig. 1A) and the two parameters were strongly correlated (Fig. C). Since, expression is controlled under an exogenous inducible promoter using a fixed concentration of $CuSO_4$, the possibility of transcriptional change in gene expression of VAP(P58S:GFP) as a result of RNAi was eliminated. This meant that increase in aggregation could be attributed to an accumulation of VAP(P58S:GFP) protein and decrease in aggregation could be caused due to its degradation.

Acknowledgements

Dr. Nagaraj Balasubramaniam is thanked for access to the Invitrogen™ EVOS™ FL Auto Imaging System by Thermo Fisher Scientific.

Appendix 3

SOD1 activity modulates VAP(P58S) aggregation dynamics in a genomic *Drosophila* model of ALS8

Summary

Protein aggregates are an important feature in neurodegenerative disease. These cellular inclusions are found in neurons of ALS patients, both sporadic and familial, and are also seen when mutant ALS loci are expressed in animal models. We have previously used an overexpression system to model VAP(P58S) aggregation in *Drosophila*. We found that activity of SOD1/ALS1, TOR signaling and wild type VAP modulates ROS levels that govern the formation and/or clearance of the aggregates formed by the ALS8 causative locus, *VAPB*, in the third instar larval brain. Our findings support one of the earliest models proposed for ALS, which incorporate oxidative stress as a central feature of the disease. The relationships between loci, as detailed in our study, allow insight into the mechanisms by which a neuronal cell could regulate proteostasis. We now use a genomic system expressing the VAP(P58S) under the *vap* promoter in a *vap* null background, in order to better model the ALS disease using flies. In this study, we observe microaggregates of VAP(P58S) in the third instar larval brains, and validate the effect of SOD1 and ROS in the animal. Our study will help uncovers critical regulatory networks that would be affected during the initiation, progression and onset of motor neuron disease.

Introduction

Drosophila models in ALS8 have been traditionally developed using the UAS-GAL4 system to express the *Drosophila* ortholog of VAP, VAP(P58S) and other VAP mutants such as VAP(T48I) and VAP(V260I) (Ratnaparkhi et al. 2008; Chen et al. 2010b; Sanhueza et al. 2014), as well as the human ortholog, hVAP and hVAP(P56S) (Chai et al. 2008). Overexpression VAP(P58S), VAP(T48I) and VAP(V260I), in the *Drosophila* homolog, VAP33a (thereafter mentioned as VAP), led to the formation of cellular puncta (Ratnaparkhi et al. 2008; Chen et al. 2010b; Sanhueza et al. 2014). Colocalization of tagged VAP and VAP(P58S) protein suggested a dominant negative effect of VAP(P58S) that interacts with and sequesters the wildtype VAP into its ubiquitinated aggregates (Ratnaparkhi et al. 2008). A number of VAP null mutants have also been generated using P-element excision, creating complete deletions such as Δ20 and Δ448 and

a partial deletion, Δ166 (Pennetta et al. 2002). In 2013, constructs of the genomic region of VAP as well as VAP containing the P58S mutation, were generated and site-specifically inserted into the 3rd chromosome to generate transgenic flies expressing VAP or its mutation under its own promoter (Moustaqim-barrette et al. 2013). Both the wildtype and the mutant genomic construct could rescue the lethality associated with VAP null mutant. While wildtype VAP could rescue the entire length of the *Drosophila* lifespan, the VAP(P58S) genomic rescued flies survived only up to 25 – 30 days post eclosion. Curiously, when expressed at endogenous levels, the heterozygous combination of one copy each of wildtype and mutant construct could survive as long as wildtype flies. The expression of VAP(P58S) at endogenous level does not compromise the functional VAP protein unlike its overexpression using the UAS-GAL4 system. It appears that the threshold of VAP(P58S) as well as VAP protein level determines the extent of degeneration in the fly. This suggests that the reduction in lifespan of VAP(P58S) genomic-rescued flies is a result of partial loss-of-function of VAP(P58S) mutant protein.

Results

VAP(P58S) forms aggregates in third instar larval brains

We generated balanced lines rescuing Δ166 mutant with genomic constructs of VAP or VAP(P58S). We observed similar motor and lifespan defects in these rescued lines as reported previously (Moustaqim-barrette et al. 2013). We investigated whether VAP(P58S) mutation leads to aggregation in third instar male larval brains of *Δ166/Y; vap>VAP(P58S)/+* . Using anti-VAP antibody staining, we observed high intensity puncta distributed in the neuronal cell bodies of the ventral nerve cord. We also observed membrane/non-aggregated staining marking the cell bodies in the ventral nerve cord suggesting that not all of the mutant protein succumbs to aggregation (Fig. 1A). With an interest in estimating the aggregation dynamics of VAP(P58S), we devised analysis methods using ImageJ and Huygen Professional software to measure various parameters such as aggregation density, aggregation size and total intensity (Fig. 1C).

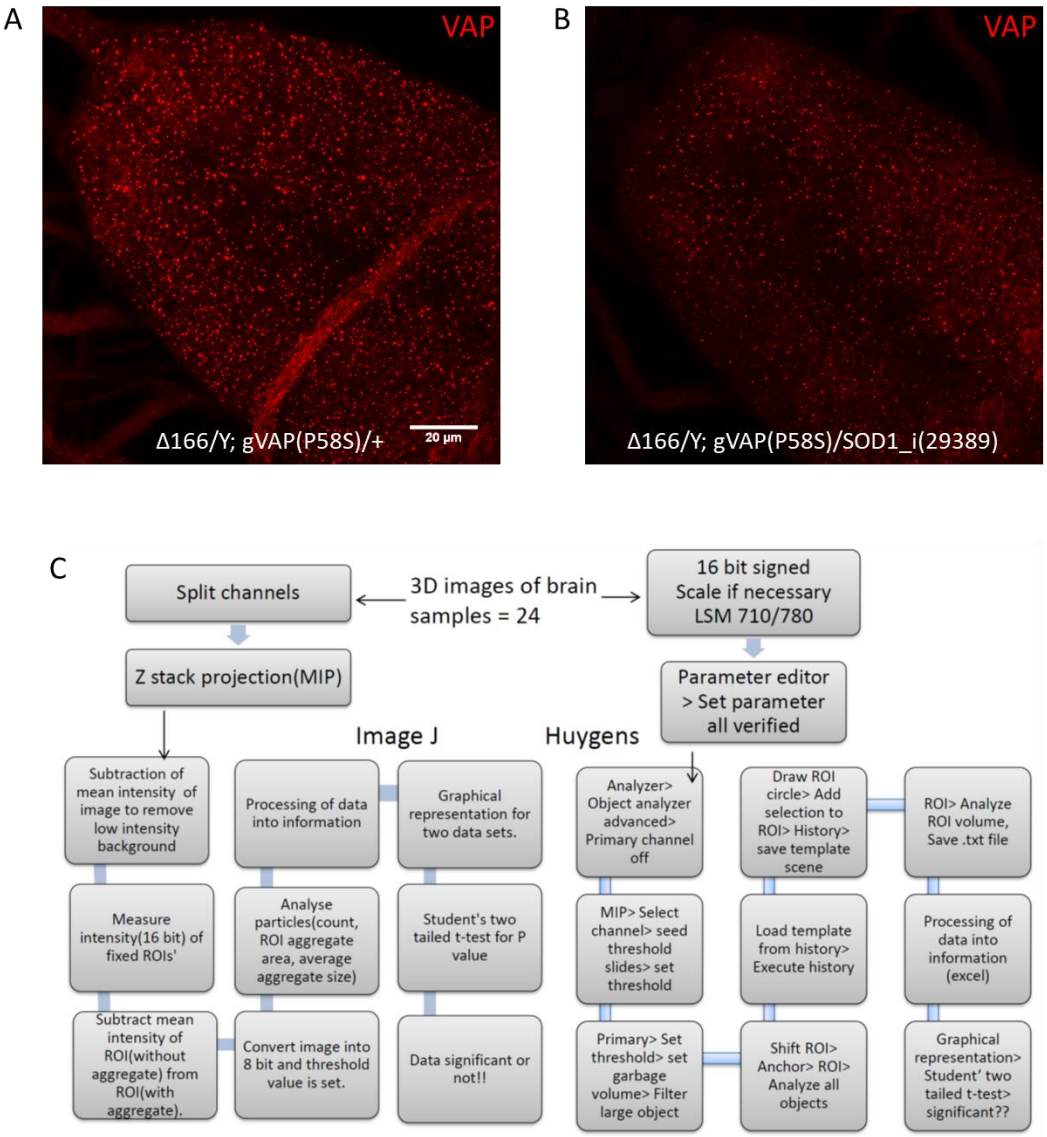

Figure 1: VAP(P58S) expressed under the vap promotor aggregates in the third instar larval brain.
A: Ventral nerve cords of the third instar larval brains of *Δ166/Y; gVAP(P58S)/+* stained with VAP antibody show punctate staining in the cell body.
B: With neuronal SOD1 knockdown, the VAP(P58S) puncta appear to be smaller, scantier and less intense in *Δ166/Y; gVAP(P58S)/SOD1_i(29389)* larval brains.
C: Flowchart depicting the methodology used for image processing and analysis of VAP(P58S) aggregation using two softwares: Image J and Huygen Professional.

SOD1 modulates VAP(P58S) aggregation levels in a genomic fly model

SOD1 knockdown in the *C155-GAL4/+; UAS-VAP(P58S)* genotype led to a reduction in aggregation density in the ventral nerve cord of third instar larval brains. We found that this reduction was triggered due to the build-up of oxidative stress that initiated proteasomal clearance mechanisms in the cell. We performed a similar knockdown of SOD1 in the genomic rescue line balanced with a neuronal driver on the second chromosome, *Δ166/Y; elav-GAL4/cyo; vap>VAP(P58S)/vap>VAP(P58S)*, and observed the aggregation levels in the ventral nerve cords of third instar male larval brains of the genotype, *Δ166/Y; elav-GAL4/+; vap>VAP(P58S)/UAS-SOD1i_(29389)* (Fig. 1B). We found that the aggregation density (Fig. 2A, 3A), average aggregation size (Fig. 2C, 3C), total aggregation area per ROI (Fig. 2D) and aggregation intensity per ROI (Fig. 2B, 3B) were reduced as compared to the control, *Δ166/Y; elav-GAL4/+; vap>VAP(P58S)/+*. Further studies exploring the role of ROS in these flies will be performed to understand the genetic interaction between the two ALS loci, SOD1 and VAP in this *Drosophila* model.

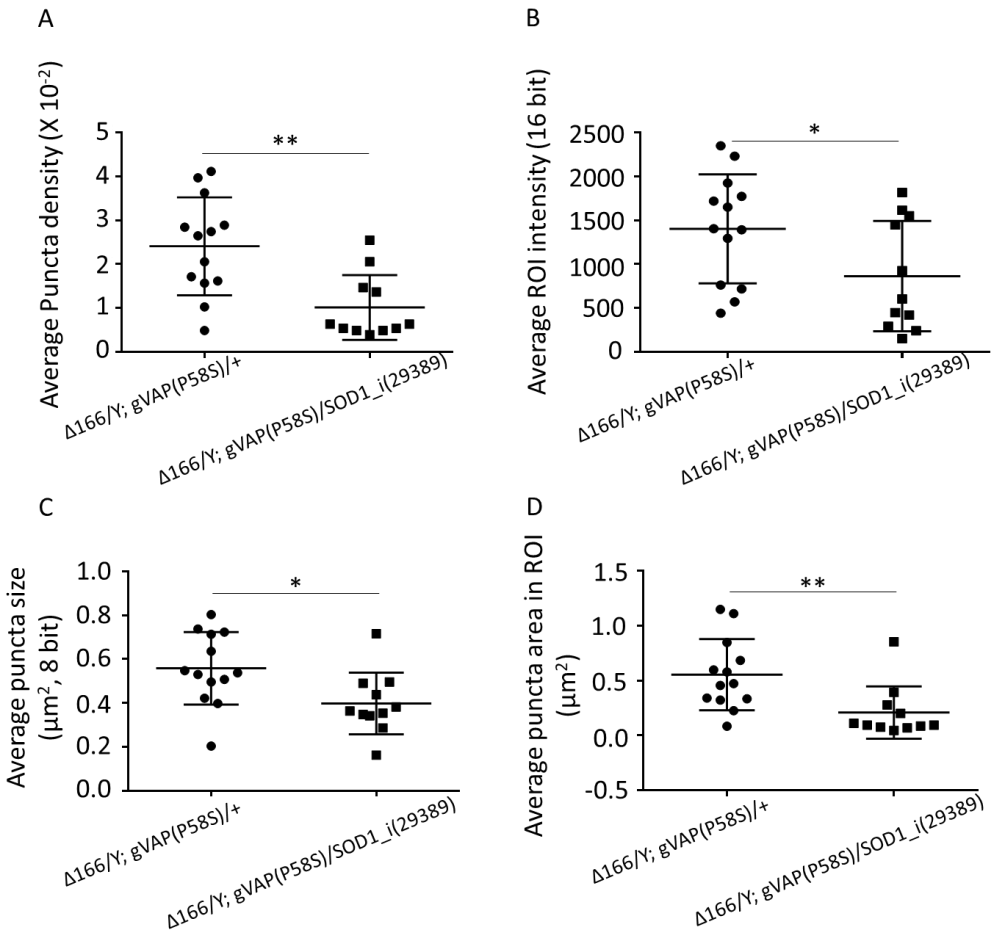

Figure 2: SOD1 knockdown reduces VAP(P58S) aggregation in the third instar larval brain.
A-D: Aggregation levels of VAP(P58S) are measured by immunostaining against VAP in the ventral nerve cord of the third instar larval brain using the ImageJ software. A neuron-specific knockdown of SOD1 in a fly expressing VAP(P58S) under the *vap* promoter leads to a reduction in average puncta density (**A**), average ROI intensity (**B**), average puncta size (**C**) and average puncta area occupied in the ROI (**D**), as measured using maximum intensity projections of immunofluorescent images.

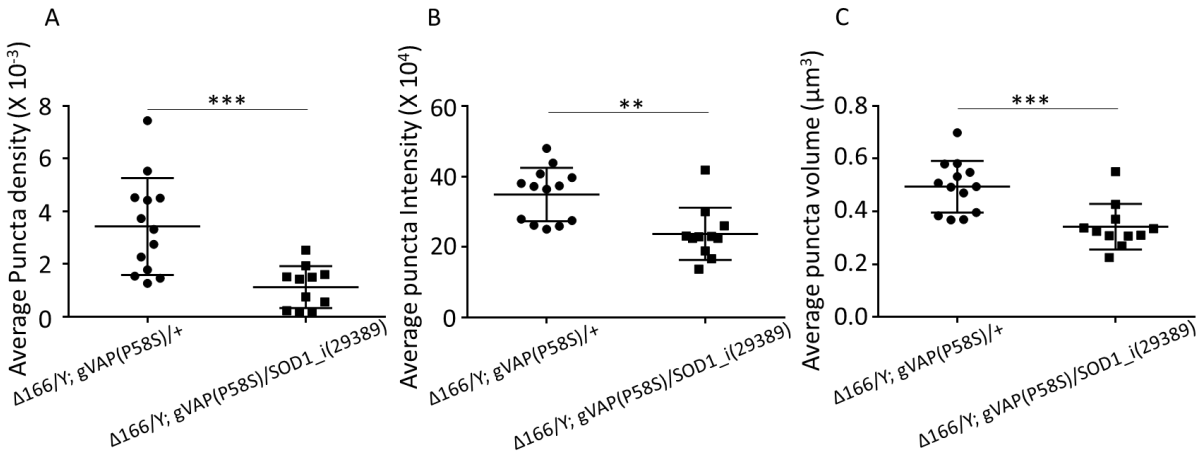

Figure 3: SOD1 knockdown reduces VAP(P58S) aggregation in the third instar larval brain.
A-C: Aggregation levels of VAP(P58S) are measured by immunostaining against VAP in the ventral nerve cord of the third instar larval brain using the Huygen Professional software. A neuron-specific knockdown of SOD1 in a fly expressing VAP(P58S) under the *vap* promoter leads to a reduction in average puncta density (**A**), average puncta intensity (**B**) and average puncta volume (**C**), as measured using three dimensional maximum intensity projections of immunofluorescent images.

SOD1 modulates the lifespan of ALS8 genomic fly model in a muscle-specific manner

We tested the effect of SOD1 on the genomic rescue line balanced with a muscle driver on the second chromosome, *Δ166/Y; mhc-GAL4 mhc-RFP/cyo; vap>VAP(P58S)/vap>VAP(P58S)*. While muscle-specific *SOD1* overexpression did not appear to cause a significant change, muscle-specific knockdown of *SOD1* led to a marginal decrease in lifespan of the flies. However, a heterozygous SOD1 null mutant, SOD1-X^{69}/+, did not appear to have a significant effect on the lifespan of the *Δ166/Y; mhc-GAL4 mhc-RFP/+; vap>VAP(P58S)/SOD1-X^{69}* flies (Fig. 4).

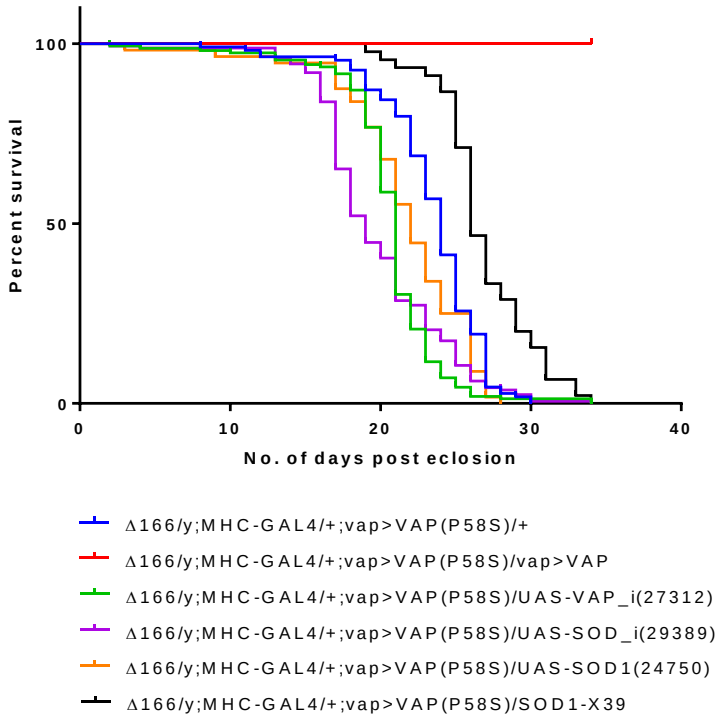

Figure 4: Muscle-specific changes in SOD1 levels affect the lifespan of genomic VAP(P58S) rescue line.

Kaplan- Meier survival analysis curve showing the percentage survival of males from each test genotype compared with negative control, *Δ166/y;MHC-GAL4/+;vap>VAP(P58S)/+* (blue), and positive control, *Δ166/y;MHC-GAL4/+; vap>VAP(P58S)/vap>VAP* (red). (Log Rank test, P value ****≤0.0001). In this preliminary experiment, approximately 50-150 male flies were counted for each genotype. SOD1 knockdown (UAS-SOD1_i(20389)) (purple) in the muscle could marginally worsen the lifespan of the flies with a decrease in median survival from 24 days (n=109) of control to 19 days (n=161). SOD1 overexpression (UAS-SOD1(24750)) (orange), SOD1 null heterozygous (SOD1-X39) (black) and VAP knockdown (UAS-VAP_i(27312)) (green) in the muscle did not appear to change the lifespan of the flies with a median survival of 22 days (n=56), 26 days (n=45) and 21 days (n=155), respectively. Number in parenthesis indicates the BDSC stock number.

ROS levels are affected in the ALS8 genomic fly model

Since ROS could affect the aggregation levels of VAP(P58S) in the larval brain and the lifespan of the ALS8 fly model through the muscle, we wanted to explore whether ROS could be affected in these flies. We measured the level of oxidized proteins using the OxyBlot kit (Materials and methods, Chapter II) in whole fly lysates of 15 day old male wildtype CS, *Δ166/Y; vap>VAP(P58S)/+* and *Δ166/Y; vap>VAP/+*. To our surprise, we found that the level of oxidized

proteins was lower in the mutant rescue line as compared to the wildtype rescue line which was comparable to the CS control (Fig. 5). This result, and our earlier data regarding the role of VAP in regulating ROS levels, suggested a possible loss-of-function phenotype for VAP(P58S).

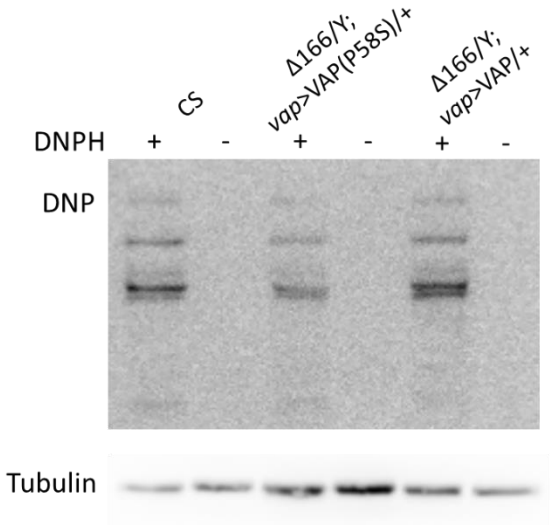

Figure 5: ROS levels are lowered in the *Drosophila* ALS8 model.
Lysates of 5 flies of each genotype were tested for levels of oxidized proteins using the OxyBlot kit. The flies expressing the mutant protein, but not wildtype protein, appeared to show lower levels of ROS.

Discussion

We have previously established a genetic interaction between SOD1 and VAP. We have found SOD1 to be a suppressor of wildtype VAP phenotype in an RNAi screen (Deivasigamani et al. 2014). Using the overexpression brain aggregation model, *C155-GAL4; UAS-VAP(P58S)*, we have observed that *SOD1* knockdown reduces of VAP(P58S) aggregation. In this system, we found that *SOD1* knockdown initiates an ROS-mediated clearance of VAP(P58S) via the proteasomal degradative mechanism. In the ALS8 genomic model, we see a similar reduction in puncta levels with *SOD1* knockdown. The mechanism for the reduction in aggregation levels in this system is still unclear at this point. Via immunostaining, we observe two kinds of distribution of the protein- the aggregated form and the soluble form. It is possible that the reduction in aggregation is attributed to either dissociation of the aggregates or active clearance. In order to understand the mechanism, using solubility assays, we would be measuring the fractions of soluble and the

aggregated level of the protein. It would also be worth exploring *vap* transcript levels in response to ROS in this system.

ROS appears to be lower in the ALS8 genomic model as compared to wildtype flies. Previously, it has been reported that owing to lower ATP levels and disrupted mitochondrial activity, VAP null mutant of *C. elegans* shows lower ROS levels (Han et al, 2012). We have observed that overexpression of VAP in larval brains, increases ROS, suggesting a role for VAP in modulating ROS. It can be hypothesized that VAP(P58S) may not possess this function. Interestingly, a muscle specific increase in ROS using *SOD1* knockdown, but not a ubiquitous increase in ROS using a heterozygous SOD1 null mutation, could reduce the lifespan of the ALS8 genomic line even further. Further evaluation of the interplay between ROS and VAP(P58S) in a cell specific manner will shed more light on the nature of the interaction between SOD1 and VAP. Using this model, we have found that VAP(P58S), expressed at endogenous levels, may be a partially functional allele of VAP that causes ALS-like phenotypes in the fly. Deciphering the role of VAP(P58S) in this model as well as the consequences of the aggregation of this protein will help us in understanding disease progression.

Acknowledgements

Aparna Thulasidharan is thanked for the initial observation of VAP(P58S) aggregation in *Δ166/Y;; vap>VAP(P58S)/+*. Lovleen Kumar Garg is thanked for the analysis of aggregation using ImageJ and Huygen Professional Software.

References

Chai A, Withers J, Koh YH, et al (2008) hVAPB, the causative gene of a heterogeneous group of motor neuron diseases in humans, is functionally interchangeable with its Drosophila homologue DVAP-33A at the neuromuscular junction. Hum Mol Genet 17:266–280. doi: 10.1093/hmg/ddm303

Chen H-J, Anagnostou G, Chai A, et al (2010) Characterization of the Properties of a Novel Mutation in VAPB in Familial Amyotrophic Lateral Sclerosis. J Biol Chem 285:40266–40281. doi: 10.1074/jbc.M110.161398

Deivasigamani S, Verma HK, Ueda R, et al (2014) A genetic screen identifies Tor as an interactor of VAPB in a Drosophila model of amyotrophic lateral sclerosis. Biol Open 3:1127–38. doi: 10.1242/bio.201410066

Moustaqim-barrette A, Lin YQ, Pradhan S, et al (2013) The Amyotrophic Lateral Sclerosis 8 protein , VAP , is required for ER protein quality control Department of Neurology and Neurosurgery , Montreal Neurological Institute , McGill University , Montreal , Department of Molecular and Human Genetics Howard Hu. 1–47

Pennetta G, Hiesinger PR, Fabian-Fine R, et al (2002) Drosophila VAP-33A directs bouton formation at neuromuscular junctions in a dosage-dependent manner. Neuron 35:291–306

Ratnaparkhi A, Lawless GM, Schweizer FE, et al (2008) A Drosophila model of ALS: Human ALS-associated mutation in VAP33A suggests a dominant negative mechanism. PLoS One 3:e2334. doi: 10.1371/journal.pone.0002334

Sanhueza M, Zechini L, Gillespie T, Pennetta G (2014) Gain-of-function mutations in the ALS8 causative gene VAPB have detrimental effects on neurons and muscles. Biol Open 3:59–71. doi: 10.1242/bio.20137070

Appendix 4

Understanding the role of VAP in lipid metabolism in a *Drosophila* model of ALS8

Summary

ER is the seat of synthesis of proteins and lipid in the cell. VAP proteins are involved in maintaining ER homeostasis in the cell. Loss of VAP leads to ER stress accompanied with accumulation of misfolded and aggregated proteins. VAP is also known to play a role in lipid homeostasis. In the absence of VAP, proteins involved in lipid biosynthesis become mislocalized. Transport of lipids from the ER to the Golgi bodies and the plasma membrane is disrupted in ALS8 fly and cell culture models. In order to understand the effect of lipid metabolism in ALS, in our study, we identify differences in lipid profiles between adult fly brains expressing wildtype and mutant VAP by performing a mass spectrometry analysis. Our results speculate partial functions attributed to VAP(P58S) in regulating lipids in the fly.

Introduction

A genomic model for ALS8, expressing VAP(P58S) under its own promoter, in the lack of endogenous VAP, causes motor and lifespan defects in the fly (Described in Chapter III and Appendix II). ER stress is observed in the adult brain cortex of the fly as identified by misfolded and mislocalized proteins of the ER (Moustaqim-barrette et al. 2014). VAP appears to be involved in lipid homeostasis by mediating lipid transport between organelles, by interacting with proteins involved in lipid biosynthesis such as Nir2, Oxysterol-binding protein (OSBP), Ceramide transfer protein (CERT) and via the FFAT domain (Peretti et al. 2008; Forrest et al. 2013; Yadav et al. 2018). VAP performs this function by tethering membranes of different organelles with the ER membrane, forming membrane contact sites. Breakdown of membrane-contact sites can cause ER stress, oxidative stress, problems in calcium homeostasis and metabolism (Peretti et al. 2008; Han et al. 2012; Yadav et al. 2018). Loss of VAP and subsequent defects in lipid transport also cause changes in ER and Golgi morphology (Peretti et al. 2008). ER stress and *Drosophila* osbp localization in the ALS8 flies could be rescued by the overexpression of human OSPB in the nervous system.

Results

We isolated and compared lipids from brain lysates of 15 day old flies of Canton-S, *Δ166/Y;vap>VAP/+, Δ166/Y;vap>VAP(P58S)/+* and *Δ166/Y;vap>VAP/vap>VAP(P58S)* by LC-MS/MS lipidomics, as described in Chapter II.

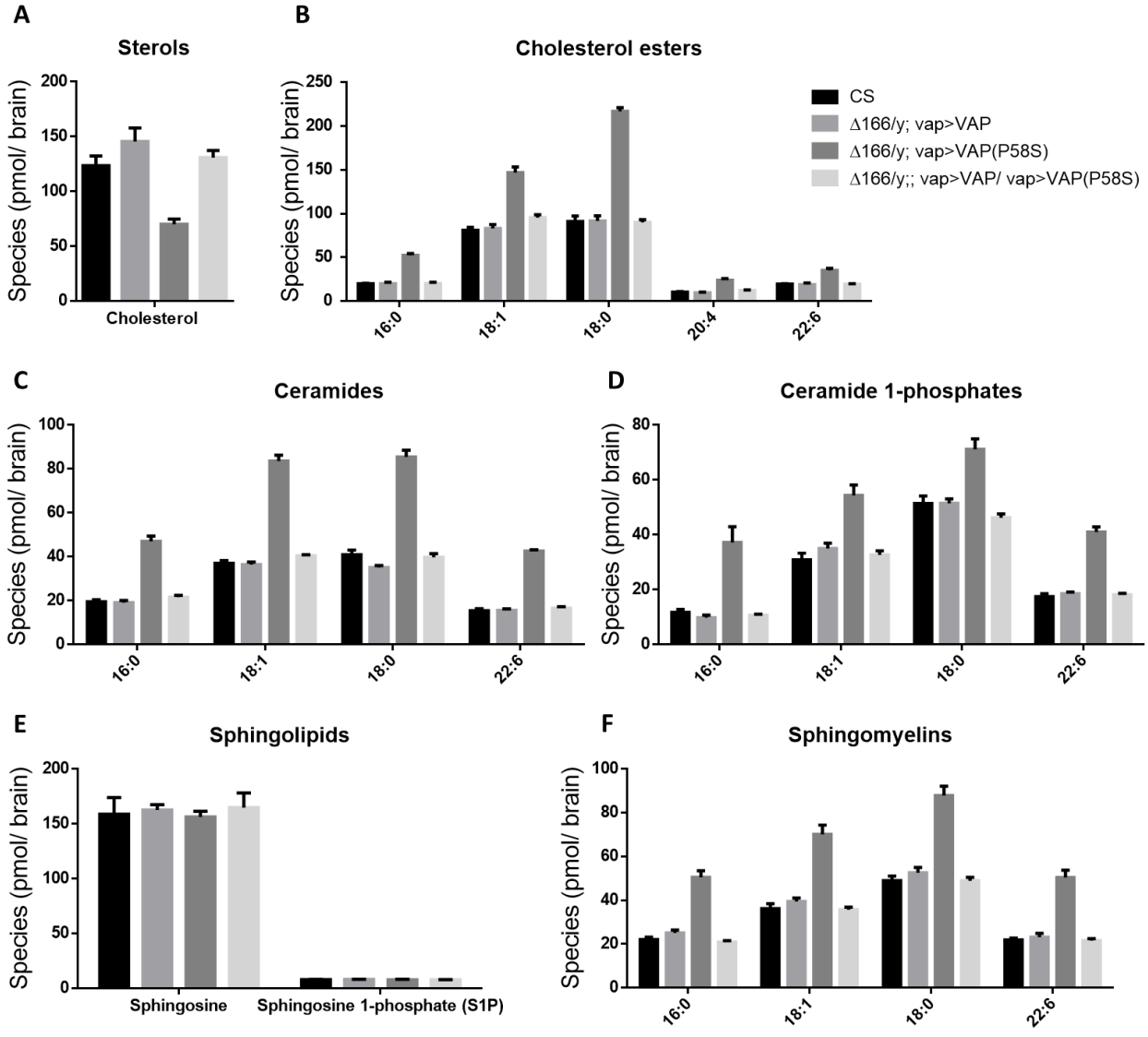

Figure 1: Changes in lipid profiles in the adult fly brain
Levels of cholesterol (**A**) and cholesterol esters (**B**) change in *Δ166/Y;vap>VAP(P58S)/+*. Ceramides (**C**), ceramide 1-phosphates (**D**) and sphinogomyelins (**F**) increase in *Δ166/Y;vap>VAP(P58S)/+*, but did not change for sphingosine and sphingosine 1-phosphate as compared to CS control (**E**). Levels of all these lipids remains equivalent between CS, *Δ166/Y;vap>VAP/+,* and the heterozygous rescue, *Δ166/Y;vap>VAP/vap>VAP(P58S).* N=5, n=2 for each genotype. (Statistics in Table 1)

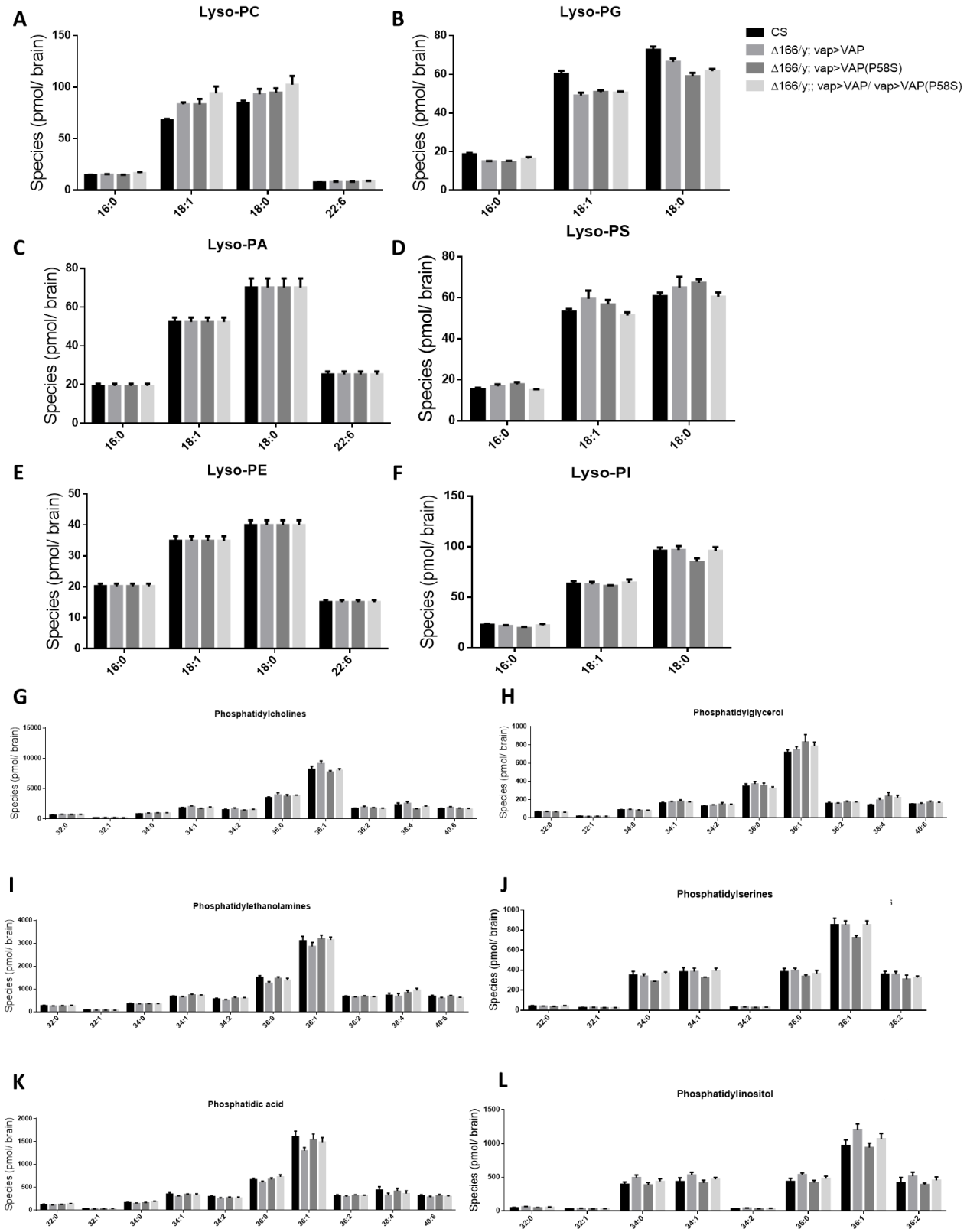
A
Lyso-PC
Species (pmol/ brain)
16:0
18:1
18:0
22:6
B
Lyso-PG
CS
Δ166/y; vap>VAP
Δ166/y; vap>VAP(P58S)
Δ166/y;; vap>VAP/ vap>VAP(P58S)
C
Lyso-PA
D
Lyso-PS
E
Lyso-PE
F
Lyso-PI
G
Phosphatidylcholines
H
Phosphatidylglycerol
I
Phosphatidylethanolamines
J
Phosphatidylserines
K
Phosphatidic acid
L
Phosphatidylinositol

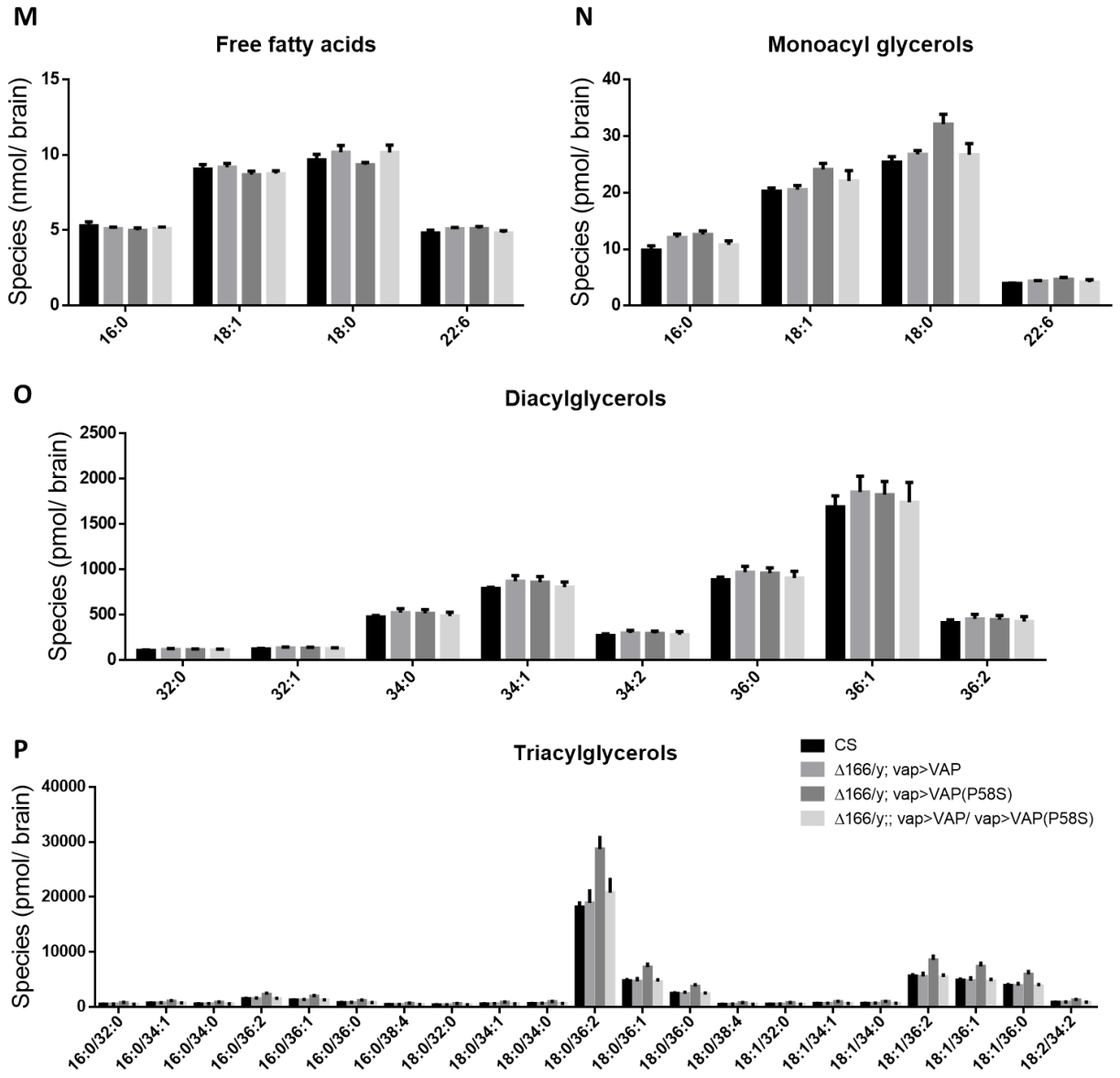

Figure 2: Changes in lipid profiles of the adult fly brain

Levels of phospholipids and its derivatives, lyso-phospholipids, do not change significantly between genotypes. Levels of free fatty acids and diacylglycerols, did not significantly change between wildtype VAP, VAP(P58S) and the heterozygous condition, while monoacylglycerols and triacylglycerols were significantly upregulated in VAP(P58S) as compared to CS. N=5, n=2 for each genotype. (Statistics in Table 1)

Table 1: LC-MS quantitation of the different lipids in 15 day old male adult *Drosophila* brain of CS and *Δ166/Y;vap>VAP(P58S)/+*.

Unpaired t-test. * p < 0.05,** p < 0.01, *** p < 0.001, ****p < 0.0001. Internal Controls used are in red.

Lipid Class	Species targeted	CS	Δ166/Y;;vap> VAP(P58S)	SEM	N	P value
Sterols	Cholesterol	123.602	70.066	9.97645	5	0.00067
	Cholesterol d7 (IS) (1000 pmol)					
Sphingolipids	Sphingosine	158.958	156.426	15.9503	5	0.87781
	17:1 Sphingosine (IS) (1000 pmol)					
	Sphingosine 1-phosphate (S1P)	7.95	7.808	0.39765	5	0.73025
	17:1 S1P (IS) (100 pmol)					
Ceramides	16:0	19.418	47.028	2.64931	5	< 0.0001
	18:1	36.972	83.654	2.95893	5	< 0.0001
	18:0	40.886	85.46	3.72467	5	< 0.0001
	22:6	15.41	42.666	1.02356	5	< 0.0001
	25:0 (IS) (100 pmol)					
Sphingomyelins	16:0	22.092	50.546	3.21331	5	< 0.0001
	18:1	36.2	70.098	4.85723	5	0.00012
	18:0	49	87.856	4.75395	5	< 0.0001
	22:6	21.952	50.438	3.41295	5	< 0.0001
	12:0 (IS) (100 pmol)					
Free fatty acids	16:0	5.312	4.996	0.30439	5	0.32955
	18:1	9.068	8.698	0.38152	5	0.36055
	18:0	9.682	9.362	0.38434	5	0.42923
	22:6	4.818	5.102	0.24318	4	0.27649
	17:1 (IS) (1 nmol)					
Monoacyl glycerols (MAG)	16:0	9.838	12.628	1.00069	5	0.02363
	18:1	20.272	24.11	1.22069	5	0.01372
	18:0	25.408	32.14	2.00656	5	0.01001
	22:6	3.94	4.688	0.3549	5	0.06812
	20:4 (d5-glycerol) IS (100 pmol)					
Cholesterol esters	16:0	19.886	52.328	2.20122	5	< 0.0001
	18:1	80.842	147.072	7.11331	5	< 0.0001
	18:0	91.174	216.99	7.4336	5	< 0.0001

	20:4	10.292	23.802	2.07339	5	0.00018
	22:6	19.51	35.346	2.25966	5	0.00011
	19:0 (IS) (100 pmol)					
Ceramide 1-phosphates	16:0	11.696	37.236	5.79717	5	0.00227
	18:1	30.812	54.378	4.50295	5	0.00079
	18:0	51.424	71.14	4.70065	5	0.00302
	22:6	17.434	41.006	2.19499	5	< 0.0001
	12:0 (IS) (100 pmol)					
Phosphatidylcholines (PC)	32:0	628.212	711.046	55.9976	5	0.17734
	32:1	180.852	199.776	23.6041	5	0.44587
	34:0	816.118	961.894	60.3242	5	0.04208
	34:1	1819.1	1710.57	94.4569	5	0.28377
	34:2	1482.29	1405.77	125.385	5	0.55861
	36:0	3511.78	3733.49	309.545	5	0.49421
	36:1	8225.52	7728.77	541.585	5	0.38584
	36:2	1714.37	1791.73	97.6716	5	0.4512
	38:4	2326.2	1621.72	331.106	5	0.06603
	40:6	1704.1	1680.71	121.697	5	0.85235
	37:4 (IS) (1000 pmol)					
Phosphatidylethanolamine (PE)	32:0	265.242	248.852	25.9196	5	0.54481
	32:1	79.646	71.918	6.06113	5	0.23809
	34:0	354.954	347.808	21.4105	5	0.74714
	34:1	679.088	734.454	46.1754	5	0.26482
	34:2	558.632	597.712	60.3513	5	0.53542
	36:0	1499.99	1461.53	105.541	5	0.72496
	36:1	3109.2	3195.31	252.917	5	0.74228
	36:2	670.47	669.014	43.1075	5	0.97388
	38:4	721.858	833.912	137.247	5	0.43788
	40:6	677.552	684.978	54.3529	5	0.8947
	37:4 (IS) (1000 pmol)					
Phosphatidic acid (PA)	32:0	118.768	121.55	12.5371	5	0.82995
	32:1	34.874	33.606	2.77189	5	0.65952
	34:0	162.676	160.438	12.6638	5	0.86412
	34:1	352.44	343.522	31.9209	5	0.78704

	34:2	297.018	269.316	26.481	5	0.32609
	36:0	664.362	671.34	44.2857	5	0.8787
	36:1	1601.65	1538.81	177.984	5	0.73313
	36:2	320.928	322.744	24.9255	5	0.94371
	38:4	438.834	412.598	97.1487	5	0.79395
	40:6	322.632	321.5	27.1055	5	0.96771
	37:4 (IS) (1000 pmol)					
Phosphatidylglycerol (PG)	32:0	66.186	62.748	5.10509	5	0.51964
	32:1	19.382	18.206	2.3381	5	0.62854
	34:0	87.86	82.572	7.59177	5	0.50582
	34:1	161.792	183.86	17.6426	5	0.24634
	34:2	129.454	150.482	18.117	5	0.27923
	36:0	349.86	354.964	36.8651	5	0.89331
	36:1	720.104	833.974	85.2196	5	0.21824
	36:2	159.176	172.816	17.1329	5	0.44893
	38:4	142.97	238.902	41.0155	5	0.0475
	40:6	152.3	172.316	13.3438	5	0.172
	37:4 (IS) (1000 pmol)					
Phosphatidylserine (PS)	32:0	42.408	34.758	5.26005	5	0.18393
	32:1	25.886	23.79	1.99113	5	0.32325
	34:0	352.874	286.754	34.4026	5	0.09084
	34:1	382.608	323.638	43.0836	5	0.20828
	34:2	30.846	27.042	2.46228	5	0.16095
	36:0	384.668	338.192	37.1862	5	0.24669
	36:1	854.914	724.418	66.871	5	0.0868
	36:2	359.662	311.132	50.175	5	0.36176
	37:4 (IS) (100 pmol)					
Phosphatidylinositol (PI)	32:0	48.394	46.718	7.33772	5	0.82506
	32:1	29.816	28.614	3.3468	5	0.72878
	34:0	397.564	387.87	49.8778	5	0.85074
	34:1	436.874	418.576	68.5851	5	0.79638
	34:2	35.4	33.86	4.25592	5	0.72684
	36:0	439.21	422.366	54.3965	5	0.76474
	36:1	970.734	940.922	104.638	5	0.78295
	36:2	422.786	393.146	76.7535	5	0.70944

	37:4 (IS) (100 pmol)					
Lyso-PC	16:0	14.672	14.536	0.6999	5	0.85077
	18:1	68.096	83.348	5.44837	5	0.02322
	18:0	84.596	94.718	4.79812	5	0.06792
	22:6	7.524	7.89	0.46267	5	0.45172
	17:1 (IS) (100 pmol)					
Lyso-PE	16:0	20.198	20.198	1.13977	5	> 0.9999
	18:1	34.912	34.912	2.0361	5	> 0.9999
	18:0	39.998	39.998	2.17457	5	> 0.9999
	22:6	15.056	15.056	0.99394	5	> 0.9999
	17:1 (IS) (100 pmol)					
Lyso-PA	16:0	19.316	19.316	1.63329	5	> 0.9999
	18:1	52.396	52.396	3.12222	5	> 0.9999
	18:0	70.198	70.198	6.61749	5	> 0.9999
	22:6	25.228	25.228	2.14932	5	> 0.9999
	17:1 (IS) (100 pmol)					
Lyso-PG	16:0	18.636	14.664	0.85701	5	0.00168
	18:1	60.14	50.85	2.02258	5	0.00177
	18:0	72.764	58.948	2.46404	5	0.00051
	17:1 (IS) (100 pmol)					
Lyso-PS	16:0	15.35	17.782	1.28968	5	0.09605
	18:1	53.242	56.752	2.49913	5	0.19779
	18:0	60.766	67.258	2.47682	5	0.0306
	17:1 (IS) (100 pmol)					
Lyso-PI	16:0	22.78	19.53	1.4634	5	0.05711
	18:1	63.42	61.12	2.51389	5	0.38698
	18:0	96.05	85.254	4.63121	5	0.04808
	17:1 (IS) (100 pmol)					
Triacylglycerols (TAG)	16:0/32:0	509.414	773.096	64.5083	5	0.0035
	16:0/34:1	722.98	1097.2	91.553	5	0.0035
	16:0/34:0	558.77	847.996	70.7568	5	0.0035
	16:0/36:2	1527.74	2318.52	193.461	5	0.0035
	16:0/36:1	1277.68	1939.02	161.796	5	0.0035
	16:0/36:0	777.404	1179.8	98.4443	5	0.0035
	16:0/38:4	437.344	663.72	55.3822	5	0.0035

	18:0/32:0	395.844	600.74	50.1263	5	0.0035
	18:0/34:1	558.126	847.022	70.6766	5	0.0035
	18:0/34:0	629.696	955.64	79.7393	5	0.0035
	18:0/36:2	18177.2	28702.1	2252.01	5	0.0016
	18:0/36:1	4772.29	7242.51	604.326	5	0.0035
	18:0/36:0	2468.29	3745.91	312.565	5	0.0035
	18:0/38:4	492.272	747.078	62.3368	5	0.0035
	18:1/32:0	508.844	772.226	64.4358	5	0.0035
	18:1/34:1	635.124	963.874	80.4283	5	0.0035
	18:1/34:0	643.982	977.318	81.5484	5	0.0035
	18:1/36:2	5642.12	8562.58	714.475	5	0.0035
	18:1/36:1	4873.5	7396.11	617.142	5	0.0035
	18:1/36:0	3930.1	5964.38	497.677	5	0.0035
	18:2/34:2	851.62	1292.43	107.843	5	0.0035
	17:0/34:1 (IS) (1000 pmol)					
Diacylglycerols (DAG)	32:0	108.008	116.6	9.95454	5	0.4132
	32:1	123.204	132.892	11.8082	5	0.43572
	34:0	475.398	516.43	44.9683	5	0.38819
	34:1	791.156	859.524	62.6835	5	0.30717
	34:2	272.826	295.304	30.2549	5	0.47876
	36:0	885.826	958.34	66.7929	5	0.30926
	36:1	1692.24	1826.68	190.4	5	0.5002
	36:2	412.706	447.318	54.9424	5	0.54628
	32:0 (d5-glycerol) (IS) (1000 pmol)					
	Unpaired t-test					
	* $p < 0.05$,** $p < 0.01$, *** $p < 0.001$, ****$p < 0.0001$					
	Internal Controls used are in RED					

Discussion

Alterations in lipid metabolism have been identified in mice model of Alzheimer's disease, leading to a change in ceramides, sphingomyelins as well as cholesterol in response to amyloid β aggregation and membrane-associated oxidative stress progressively in the disease (Fig. 3) (Cutler et al. 2004). We found similar changes in lipid levels in our study in the ALS8 *Drosophila* model.

Storage lipid levels changed in the brain of *Δ166/Y;vap>VAP(P58S)/+* as compared to the wildtype controls. Overall, there was no significant difference between lipid levels of Canton-S, *Δ166/Y;vap>VAP/+,* and the heterozygous rescue, *Δ166/Y;vap>VAP/vap>VAP(P58S).* While cholesterols decreased between wildtype and mutant genotypes, cholesterol esters increased. Moreover, free fatty acids that are generated with hydrolysis of cholesterol esters to cholesterol, did not appear to change. This indicated that the interconversion of cholesterol esters and cholesterol is regulated by VAP and that regulation is perturbed in presence of VAP(P58S). Ceramide levels and its downstream derivatives, ceramide 1-phosphate as well as sphingomyelins increased in presence of the mutation. There was also a change in levels of triacylglycerols and monoacylglycerols, but not diacylglycelrol levels. It points to an increase in flux of ceramide production in the cell. A subcellular localization of the lipids in the neurons would provide a clearer picture of the regulation of this pathway. Moreover, the localization and interaction of CERT, OSBP and sphingomyelin synthase (SMS) with VAP(P58S) would also help understand the disease condition. As seen in the mice model of Alzheimer's disease, it would be worth looking at the accompanying changes in levels of ROS in the ALS8 fly brain as well.

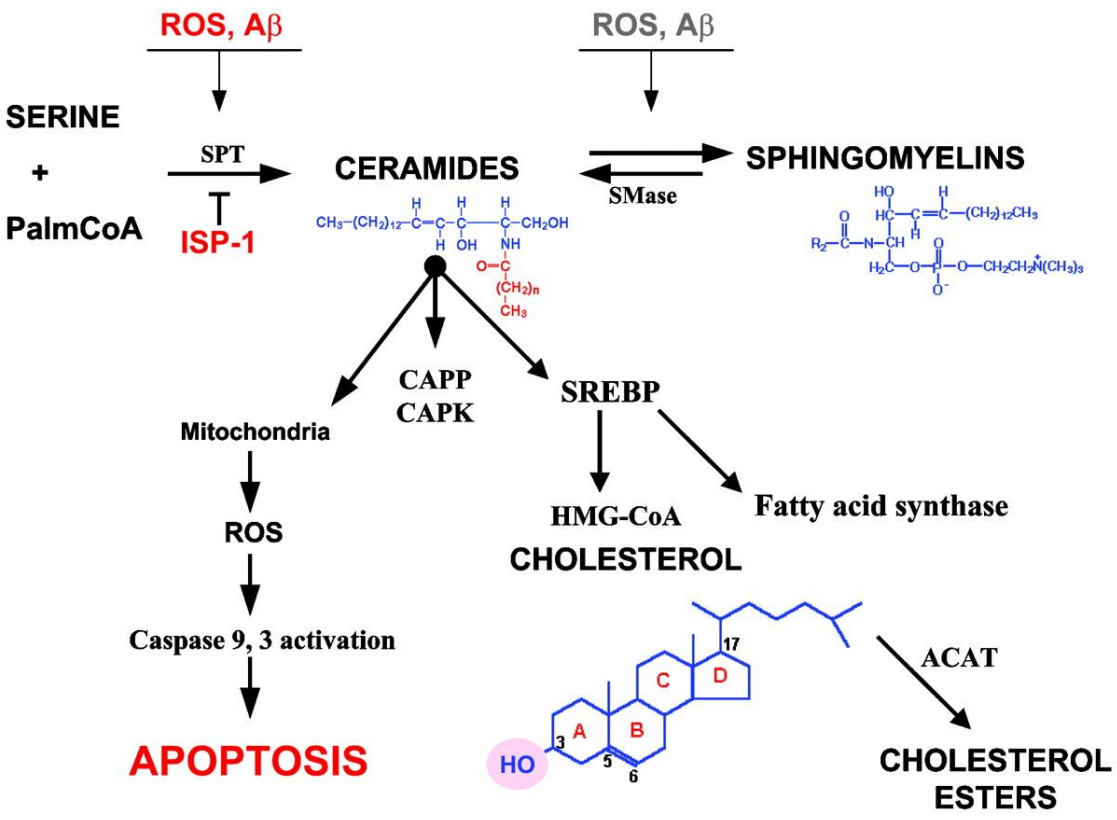

Figure 3: Effect of Amyloid β aggregation and membrane associated oxidative stress on lipid metabolism.
Reproduced from (Cutler et al. 2004). Changes in lipid content in the brain have been observed in case of other neurodegenerative diseases as well. The presence of Amyloid β aggregation in the Alzheimer's disease mice model causes an increase in membrane-associated oxidative stress. This change is correlated with an accumulation of ceramides and cholesterol in an age dependent manner, with an initial increase and subsequent decline of sphingomyelins. Altered lipid metabolism together with ROS could lead to neuronal death. In our ALS8 model, we find an upregulation of ceramides and sphingomyelins, but a downregulation in cholesterol levels, indicating that there the interconversion between these lipids may be affected in neurodegeneration.

VAP downregulation causes a disruption of in PIP2 conversion as well as PI4P regulation as the plasma membrane and the Golgi bodies, respectively (Peretti et al. 2008; Yadav et al. 2018). However, we did not observe a change in phospholipids in the mutant brain. The dysregulation of different lipids by VAP(P58S) in the brain could be restored by a single copy of wildtype VAP in the heterozygous flies. Taken together, the results and literature, indicate that VAP(P58S) may be a partially functional allele. The partial function may allow for the flies to develop and grow to adult stages. With age and the aggregation-prone nature of the protein, VAP(P58S) may become dysfunctional and lead to disease phenotypes. A time-based lipidomics study would further help justify this hypothesis. Moreover, it would be interesting to check whether restoring the lipid levels to wildtype, by genetically manipulating levels of lipid biosynthesis genes, could rescue disease phenotypes as well.

Acknowledgements

Dr. Siddhesh Kamat helped design the experiment. Aparna Thulasidharan and Neena Dhiman is thanked for help with adult brain dissections. Neelay Mehendale and Shabnam Patil are thanked for technical assistance with the mass spectrometry experiments.

References

Cutler RG, Kelly J, Storie K, et al (2004) Involvement of oxidative stress-induced abnormalities in ceramide and cholesterol metabolism in brain aging and Alzheimer's disease. Proc Natl Acad Sci 101:2070–2075. doi: 10.1073/pnas.0305799101

Forrest S, Chai A, Sanhueza M, et al (2013) Increased levels of phosphoinositides cause neurodegeneration in a Drosophila model of amyotrophic lateral sclerosis. Hum Mol Genet 22:2689–2704. doi: 10.1093/hmg/ddt118

Han SM, Tsuda H, Yang Y, et al (2012) Secreted VAPB/ALS8 Major Sperm Protein Domains Modulate Mitochondrial Localization and Morphology via Growth Cone Guidance Receptors. Dev Cell 22:348–362. doi: 10.1016/j.devcel.2011.12.009

Moustaqim-barrette A, Lin YQ, Pradhan S, et al (2014) The amyotrophic lateral sclerosis 8 protein, VAP, is required for ER protein quality control. Hum Mol Genet 23:1975–1989. doi: 10.1093/hmg/ddt594

Peretti D, Dahan N, Shimoni E, et al (2008) Coordinated Lipid Transfer between the Endoplasmic Reticulum and the Golgi Complex Requires the VAP Proteins and Is Essential for Golgi-mediated Transport. 19:3871–3884. doi: 10.1091/mbc.E08

Yadav S, Thakur R, Georgiev P, et al (2018) RDGBα localization and function at membrane contact sites is regulated by FFAT–VAP interactions. J Cell Sci 131:jcs207985. doi: 10.1242/jcs.207985

Appendix 5

Reagents

Antibody Production

The antibody for VAP was raised against the central coiled coil region (CCD) of the protein in two rabbits by Abexome Biosciences (Yadav et al. 2018).

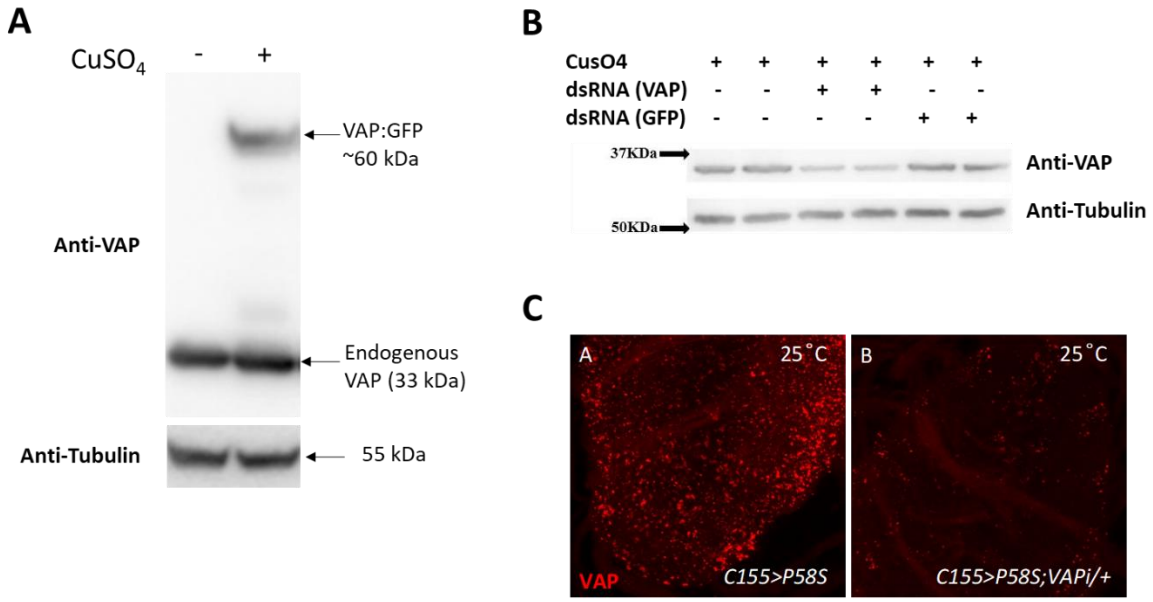

Figure 1: Validation of dVAP-A antibody (Reproduced from Suppl. Fig 1 (Yadav et al. 2018))
A: S2R+ stable cell line expressing VAP:GFP. On induction (+) by 0.5 mM CuSO4, the VAP:GFP fusion can be seen at 60 kD. The antibody also cross-reacts with endogenous VAP (33 kDa). Antibody dilutions used are Anti-VAP (1:20,000), Anti-Tubulin (1:20,000).
B: Reduction of VAP-A transcripts by dsRNA leads to a decrease of VAP protein. 20 ug/ml dsRNA was added to S2R+ cells, 48 hours before VAP induction. This led to a 50% decrease in VAP levels (lane 3 & 4).
C: VAP-A(P58S), when expressed in larval brain shows inclusions/protein aggregates in neurons, when stained with anti-dVAP antibody. These inclusions are not seen when VAPA(wt) is overexpressed (data not shown). These aggregates can be reduced by reducing protein levels by VAP specific RNAi. Antibody dilution used is 1:1000 (Anti-dVAP-A)

Abexome Biosciences Pvt Ltd
78/1, 2nd Main Road, Raghavendra Layout
Off Tumkur Road, Yeshwanthpur, Bangalore 560022
Tel: +91 80 2337 5476/77 Fax: +91 80 2337 5469

Implementation Report: Polyclonal Antibody

Project Title	Development of polyclonal antibodies against VAP CCD			Project Code	SP1112-077		
Date Initiated	19 Aug 11	Updated on	05 Jan 12	Lab Record No.	48-111-2011	Page No.	1-

1. Project Specification

SN	Deliverable
1	Pre immune sera
2	Hyper immune sera
3	Purified antibody

2. Materials

2.1 Materials Received

SN	Name	Type	Amount (mg)	Volume (ml)	Concentration (mg/ml)	Purpose
1	VAP CCD (GST-tagged protein leaved with Thrombin)	Protein (MGAAGGGSAGANTSSASAEALESKPKLSSEDKFKPSNLLETSESLDLLSGEIKALRECNIELRRENLHLKDQITRFRSSPAVKQVNEPYAPVLAE)	6	2	3	Polyclonal antibody generation

2.2 Material Usage

2.2.1 Material Name:

VAP CCD

SN	Experiment	Quantity (mg)
1	Antigen purification	0.69
2	Prescreening	0.05
3	Immunization	2.1
4	Titer check	0.08
5	Dot Blot	0.03
6	Western blot	0.1

3. Project Timelines

3.1 Target Dates

- Date of Initiation: 23 Aug 11
- Immunization Schedule

Parameter	Immunization	1st Booster	2nd Booster	3rd Booster	4th booster
Dosage (mg)	300	150	300	300	300
Timeline (Approximate Dates)	28 Sep 11	12 Oct 11	25 Oct 11	08 Nov 11	21 Dec 11

3.2 Project Steps with Timeline

Step No	Description	Start Date	End Date	Remarks
1	Prescreening	26 Sep 11	27 Sep 11	

2	Immunization	28 Sep 11	28 Sep 11	
3	Booster 1	11 Oct 11	11 Oct 11	
4	Titer check	21 Oct 11	21 Oct 11	
5	Booster 2	25 Oct 11	25 Oct 11	
6	Titer check	04 Nov 11	04 Nov 11	If titer is acceptable can go to Step 11.
7	Booster 3	08 Nov 11	08 Nov 11	
8	Titer check	18 Nov 11	18 Nov 11	If titer is acceptable can go to Step 11.
9	Booster 4	21 Dec 11	21 Dec 11	
10	Titer check	31 Dec 11	31 Dec 11	If titer is acceptable can go to Step 11.
11	Production bleed			To be decided
12	Antibody purification			
13	Characterization of the product			
14	Delivery to customer			

4. Experimental Results

DEFINITIONS USED IN THE DOCUMENT

No Antigen Control	In ELISA, wells where antigen is not added
No Antibody Control	In ELISA, wells where no antibody is added
ELISA control	In ELISA, wells where Rabbit IgG is coated
HIS	Hyper Immune Sera
PIS	Pre Immune Sera

4.1 Antigen Preparation

4.1.1 Dialysis

Steps	Dialysis Buffer	Duration
1	Salinated 50mM Phosphate Buffer, 150 mM NaCl, pH 7.4	Overnight with 4 buffer changes

4.1.2 Antigen Quantitation

Sl No	Parameter	Concentration (mg/ml)
1	BCA Estimation	1.18

4.1.3 SDS-PAGE Image

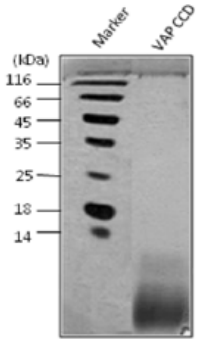

Figure 1: SDS-PAGE analysis for the VAP CCD protein. Marker from MBI Fermentas, Cat. No. SM0431.

Conclusion: The VAP CCD protein (10 µg) was loaded onto a 15 % SDS-PAGE. There was a smear observed at < 14 kDa. The expected band size was 10 kDa.

4.2 Pre-screening

4.2.1 ELISA details

Antigen, Antigen concentration	VAP CCD Protein, 200 ng/well
Primary Antibody	Diluted Serum as given in the Table below
Secondary Antibody	Goat Anti-Rabbit-HRP, C0008-02, Abexome

4.2.2 Pre-screening Results

Host ID	OD @ 450 nm				If selected
	1/125	1/250	1/500	No Ag control	
RB446	0.097	0.070	0.060	0.057	Yes
R48	0.275	0.211	0.170	0.066	No
RB456	0.179	0.126	0.107	0.070	Yes
W1	0.181	0.142	0.111	0.053	No
No Ab Control	0.054				

4.2.3 Conclusion

Host RB446 and RB456 were selected.

4.3 Immunization

4.3.1 Host Details

S N	Parameter	Value	
		RB446	RB456
1	Species	NZ White Rabbits	
2	Number of Hosts Used	2	
3	Age	261 days	285 days
4	Gender	Male	Male

4.3.2 Immunization Records

Stage	Immunization	1st Booster	2nd Booster	3rd Booster	4th Booster
Date	28 Sep 11	11 Oct 11	25 Oct 11	08 Nov 11	21 Dec 11
Antigen Dosage (µg)	300	150	300	300	300
Antigen: Adjuvant	1:1	1:1	1:1	1:1	1:1
Type of Adjuvant	FCA	FIA	FIA	FIA	FIA
Route of Administration	S/C	S/C	S/C	S/C	S/C
Total Volume Injected (µl)x Number of sites	250 X 2	250 X 2	250 X 2	250 X 2	250 X 2

4.4 Titer Check Results

Titer of the sera for the experimental animals was checked by ELISA. The experimental details are given below.

Parameter	Value
Amount of Antigen coated	VAP CCD Protein, 200 ng/well
Amount of Sera used	Serially diluted starting from 1/100 for further 5 dilutions.
Secondary Antibody	Goat Anti-Rabbit-HRP, C0008-02, Abexome

4.4.1 ELISA Results

Titer of an antisera is calculated by Endpoint method ie the minimum dilution above the antigen blank where no fluctuation of the reading is observed.

Guidance for Titer Values in Rabbits

Protein	Peptide	Small Molecule	Grade
<10,000	<5,000	<1,000	**Low**
10,000- 50,000	5,000-20,000	1,500-3,000	**Medium**
50,000-1,00,000	20,000-50,000	3,000-5,000	**Good**

>1,00,000	>50,000	>5,000	**High**

Host	Booster I	Booster II	Booster III	Booster IV
RB446	Medium	Good	Good	Good
RB456	Low	Medium	Good	Good

4.5 Detection sensitivity by Western

4.5.1 Western analysis of recombinant VAP-CCD

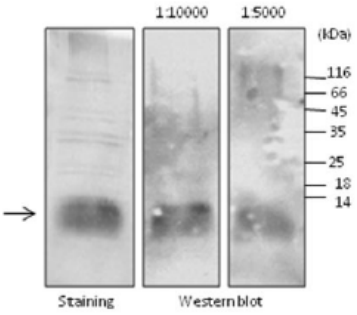

Figure 2: Western blot analysis with Antisera.

Antigen: VAPCCD Protein, 2 µg for western blot and 10 µg for staining. The protein was run on a 15 % SDS-PAGE and transferred on PVDF membrane for 30 min, blocked with 5 % Skimmed milk in 50 mM phosphate buffer, 150 mM NaCl pH 7.4.
Primary Antibody: Antisera 4th booster, RB446 at 1/5,000 and 1/10,000 dilution.
Incubation in Primary Antibody: 4 hr at RT.
Secondary Antibody: Goat Anti-Rabbit IgG-HRP, 1000X, C0008-02, Abexome.
Development: ECL, 2 min exposure.
Conclusion: The Antisera from 4th booster, RB446 could detect the VAPCCD protein at the expected molecular weight

4.5.2 Western analysis of native extract

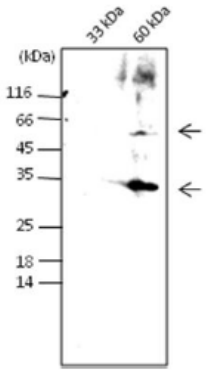

Figure 3: Western blot analysis with Antisera.
Antigen: 18 µl of each of the Lysate were run on a 15 % SDS-PAGE and transferred on NC membrane for 1hr, blocked with 5 % Skimmed milk in 50 mM phosphate buffer, 150 mM NaCl pH 7.4.
Primary Antibody: Antisera 4th booster, RB446 at 1/10,000 dilution.
Incubation in Primary Antibody: 4 hr at RT.
Secondary Antibody: Goat Anti-Rabbit IgG-HRP, 1000X, C0008-02, Abexome.
Development: ECL, 1 min exposure.

Conclusion
The Antisera from 4th booster, RB446 could detect the native protein at ~35 kDa with an extra band at ~66 kDa in the '60 kDa' lysate provided. There was no signal observed in 33 kDa lysate provided (Figure 3).

4.6 Future plan of Work

- Purification of antibody from 4th booster antisera from RB446
- Western analysis of recombinant and native protein with the purified antibody
- One more booster after 28 days of last booster

5. Raw Data

5.1 Titer check

RB446		1st booster			2nd booster			3rd booster		4th booster		
Dilution of the sera	PIS	HIS	HIS-PIS	PIS	HIS	HIS-PIS	PIS	HIS	HIS-PIS	PIS	HIS	HIS-PIS
100	0.363	2.750	2.386	0.393	2.825	2.431	0.290	2.574	2.284	0.219	2.884	2.557
1000	0.002	1.329	1.326	0.045	2.020	1.976	0.000	2.258	2.258	0.000	2.826	2.748
10000	0.000	0.317	0.317	0.000	0.517	0.517	0.000	1.110	1.110	0.000	1.910	1.910
100000	0.000	0.092	0.092	0.000	0.134	0.134	0.000	0.299	0.299	0.000	0.497	0.497
1000000	0.000	0.064	0.064	0.000	0.096	0.096	0.000	0.161	0.161	0.000	0.135	0.135
Anitgen ©		0.086			0.068		0.000	0.171			0.113	

RB456		1st booster			2nd booster			3rd booster		4th booster		
Dilution of the sera	PIS	HIS	HIS-PIS	PIS	HIS	HIS-PIS	PIS	HIS	HIS-PIS	PIS	HIS	HIS-PIS
100	0.323	0.929	0.606	0.456	2.895	2.439	0.431	2.572	2.141	0.328	2.868	2.540
1000	0.000	0.183	0.183	0.070	1.790	1.720	0.000	2.376	2.376	0.078	2.759	2.681
10000	0.000	0.078	0.078	0.005	0.374	0.369	0.000	1.181	1.181	0.000	1.717	1.717
100000	0.000	0.063	0.063	0.000	0.120	0.120	0.000	0.285	0.285	0.000	0.395	0.395
1000000	0.000	0.062	0.062	0.000	0.094	0.094	0.000	0.151	0.151	0.000	0.119	0.119
Anitgen ©		0.182			0.100		0.000	0.134			0.120	

_____
Quality Analysis By:
Scientist
Date: 05 Jan 12

_____
Approved by:
Project Lead
Date: 05 Jan 12

Table 1: List of Fly lines

Gene	Source	Fly ID	Genotype
CG5014 (VAP33a)	(Ratnaparkhi et al. 2008)	-	*y[1]; UAS-VAP/Cyo*
		-	*y[1]; UAS-VAP(P58S)/Cyo*
	(Deivasigamani et al. 2014)		*C155-GAL4/C155-GAL4; UAS-VAP/Cyo*
			C155-GAL4/C155-GAL4; UAS-VAP(P58S)/Cyo
	(Moustaqim-barrette et al. 2014)	-	*vap>VAP/Tb*
		-	*vap>VAP(P58S)/Tb*
	(Pennetta et al. 2002)	-	*Δ166/FM7a*
	In-house	-	*Δ166/FM7a; vap>VAP(P58S)/Tb*
		-	*Δ166/FM7a; if/Cyo; vap>VAP(P58S)/Tb*
		-	*Δ166/FM7a; elav-GAL4/Cyo; vap>VAP(P58S)/Tb*
		-	*Δ166/FM7a; mhc-GAL4 mhc-RFP/cyo; vap>VAP(P58S)/Tb*
GAL4	BDSC	8765	*P{GAL4-elav.L}2/CyO*
	BDSC	38464	*w[*]; P{w[+mC]=Mhc-RFP.F3-580}2, P{w[+mC]=Mhc-GAL4.F3-580}2/SM6b*
	BDSC	458	*P{w[+mW.hs]=GawB}elav[C155]*
CG11793 (SOD1)	BDSC	29389	*y[1] v[1]; P{TRiP.JF03321}attP2*
	BDSC	36804	*y[1] sc[*] v[1]; P{TRiP.GL01016}attP40*
	BDSC	34616	*y[1] sc[*] v[1]; P{TRiP.HMS01291}attP2*
	BDSC	24750	*w[1]; P{UAS-Sod1.A}B37*
	BDSC	33605	*w[1118]; P{UAS-Sod1}12.1*

	DGRC	-	*w[*]; p{w[+mC]=UAS-SOD1-FLAG-HA}attP2*
CG8905 (SOD2)	BDSC	25969	*y[1] v[1]; P{TRiP.JF01989}attP2*
	BDSC	24494	*w[1]; P{UAS-Sod2.M}UM83*
CG6871 (Catalase)	BDSC	34020	*y[1] sc[*] v[1]; P{TRiP.HMS00990}attP2*
	BDSC	24621	*w[1]; P{UAS-Cat.A}2*
CG5092 (Tor)	BDSC	35578	*y[1] sc[*] v[1]; P{TRiP.GL00156}attP2*
CG11299 (Sestrin)	BDSC	64027	*y[1] sc[*] v[1]; P{TRiP.HMS05363}attP40*
CG3143 (Foxo)	BDSC	43633	*w1118; P{UASp-foxo.GFP}3*
CG5808	DGRC	-	*w[*]; p{w[+mC]=UAS-CG5808-FLAG-HA}attP2*
CG8336	BDSC	24728	*w[1118]; Mi{ET1}Or67b[MB04909] CG8336[MB04909]*
	DGRC	-	*w[*]; p{w[+mC]=UAS-CG8336-FLAG-HA}attP2*
CG1866 (moca-cyp)	BDSC	16389	*y[1] w[67c23]; P{w[+mC] y[+mDint2]=EPgy2}Moca-cyp[EY06157]*
CG9916 (cyclophillin 1)	BDSC	33950	*y[1] sc[*] v[1]; P{y[+t7.7] v[+t1.8]=TRiP.HMS00902}attP2*
CG13892	VDRC	v107406	*P{KK107406}VIE-260B*
CG11777	VDRC	v108775	*P{KK108775}VIE-260B*
CG7768	DGRC	-	*w[*]; p{w[+mC]=UAS-CG7768-FLAG-HA}attP2*
CG3511	DGRC	-	*w[*]; p{w[+mC]=UAS-CG3511-FLAG-HA}attP2*

CG4535 (FKbp59)	BDSC	19999	*y[1] w[67c23]; P{w[+mC] y[+mDint2]=EPgy2}FKBP59[EY03538]*
CG14715	BDSC	32608	*w[1118]; P{w[+mC]=EP}CG14715[G6908]*
CG6226 (FK506 BP-1, FKBP39)	BDSC	32348	*y[1] sc[*] v[1]; P{y[+t7.7] v[+t1.8]=TRiP.HMS00339}attP2*
CG5482	VDRC	v4991	*w[1118]; P{GD2071}v4991*
CG11858	VDRC	v108489	*P{KK108489}VIE-260B*

References

Deivasigamani S, Verma HK, Ueda R, et al (2014) A genetic screen identifies Tor as an interactor of VAPB in a Drosophila model of amyotrophic lateral sclerosis. Biol Open 3:1127–38. doi: 10.1242/bio.201410066

Moustaqim-barrette A, Lin YQ, Pradhan S, et al (2014) The amyotrophic lateral sclerosis 8 protein, VAP, is required for ER protein quality control. Hum Mol Genet 23:1975–1989. doi: 10.1093/hmg/ddt594

Pennetta G, Hiesinger PR, Fabian-Fine R, et al (2002) Drosophila VAP-33A directs bouton formation at neuromuscular junctions in a dosage-dependent manner. Neuron 35:291–306

Ratnaparkhi A, Lawless GM, Schweizer FE, et al (2008) A Drosophila model of ALS: Human ALS-associated mutation in VAP33A suggests a dominant negative mechanism. PLoS One 3:e2334. doi: 10.1371/journal.pone.0002334

Yadav S, Thakur R, Georgiev P, et al (2018) RDGBα localization and function at membrane contact sites is regulated by FFAT–VAP interactions. J Cell Sci 131:jcs207985. doi: 10.1242/jcs.207985

Appendix 6

Statistics for LC-MS of oxidized lipids from third instar larval brain

Table 1: Details of the MRM transitions for the different phospholipids measured.

Lipid Class	Species targeted	Precursor Ion Mass	Product Ion Mass	Declustering Potential	Entrance Potential	Collision Energy (V)	Collision Exit Potential	Ionization Mode
Phosphatidyl cholines (PC)	32:0	734.6	184	170	10	45	15	Positive
	32:1	732.6	184	170	10	45	15	Positive
	34:0	762.6	184	170	10	45	15	Positive
	34:1	760.6	184	170	10	45	15	Positive
	34:2	758.6	184	170	10	45	15	Positive
	36:0	790.6	184	170	10	45	15	Positive
	36:1	788.6	184	170	10	45	15	Positive
	36:2	786.6	184	170	10	45	15	Positive
	ox-36:2	802.6	184	150	10	40	12	Positive
	hy-36:2	804.6	184	150	10	40	12	Positive
	36:4	782.6	184	170	10	45	15	Positive
	ox-36:4	798.6	184	150	10	40	12	Positive
	hy-36:4	800.6	184	150	10	40	12	Positive
	38:4	810.6	184	170	10	45	15	Positive
	ox-38:4	826.6	184	150	10	40	12	Positive
	hy-38:4	828.6	184	150	10	40	12	Positive
	38:5	808.6	184	170	10	45	15	Positive

	ox-38:5	824.6	184	150	10	40	12	Positive
	hy-38:5	826.6	184	150	10	40	12	Positive
	40:7	832.6	184	170	10	45	15	Positive
	ox-40:7	848.6	184	150	10	40	12	Positive
	hy-40:7	850.6	184	150	10	40	12	Positive
	40:6	834.6	184	170	10	45	15	Positive
	ox-40:6	850.6	184	150	10	40	12	Positive
	hy-40:6	852.6	184	150	10	40	12	Positive
	37:4 (Internal Standard)	796.6	184	170	10	45	15	Positive
Phosphatidyl ethanolamin e (PE)	32:0	692.5	551.6	150	10	50	10	Positive
	32:1	690.5	549.6	150	10	50	10	Positive
	34:0	720.5	579.6	150	10	50	10	Positive
	34:1	718.5	577.6	150	10	50	10	Positive
	34:2	716.5	575.6	150	10	50	10	Positive
	36:0	748.5	607.6	150	10	50	10	Positive
	36:1	746.5	605.6	150	10	50	10	Positive
	36:2	744.5	603.6	150	10	50	10	Positive
	ox-36:2	760.5	619.6	135	10	40	10	Positive
	hy-36:2	762.5	621.6	135	10	40	10	Positive
	36:4	740.5	599.6	150	10	50	10	Positive
	ox-36:4	756.5	615.6	135	10	40	10	Positive
	hy-36:4	758.5	617.6	135	10	40	10	Positive

	38:5	766.5	625.6	150	10	50	10	Positive
	ox-38:5	782.5	641.6	135	10	40	10	Positive
	hy-38:5	784.5	643.6	135	10	40	10	Positive
	38:4	768.5	627.6	150	10	50	10	Positive
	ox-38:4	784.5	643.6	135	10	40	10	Positive
	hy-38:4	786.5	645.6	135	10	40	10	Positive
	40:7	790.5	649.6	150	10	50	10	Positive
	ox-40:7	806.5	665.6	135	10	40	10	Positive
	hy-40:7	808.5	667.6	135	10	40	10	Positive
	40:6	792.5	651.6	150	10	50	10	Positive
	ox-40:6	808.5	667.6	135	10	40	10	Positive
	hy-40:6	810.5	669.6	135	10	40	10	Positive
	37:4 (Internal Standard)	754.5	613.6	150	10	50	10	Positive
Phosphatidic acid (PA)	32:0	647.5	255.3	-65	-10	-45	-10	Negative
	32:1	645.5	255.3	-65	-10	-45	-10	Negative
	34:0	675.5	255.3	-65	-10	-45	-10	Negative
	34:1	673.5	255.3	-65	-10	-45	-10	Negative
	34:2	671.5	255.3	-65	-10	-45	-10	Negative
	36:0	703.5	283.3	-65	-10	-45	-10	Negative
	36:1	701.5	283.3	-65	-10	-45	-10	Negative
	36:2	699.5	281.3	-65	-10	-45	-10	Negative
	ox-36:2	715.5	281.3	-50	-10	-40	-10	Negative
	hy-36:2	717.7	281.3	-50	-10	-40	-10	Negative

	36:4	695.5	255.3	-65	-10	-45	-10	Negative
	ox-36:4	711.5	255.3	-50	-10	-40	-10	Negative
	hy-36:4	713.5	255.3	-50	-10	-40	-10	Negative
	38:4	723.5	283.3	-65	-10	-45	-10	Negative
	ox-38:4	739.5	283.3	-50	-10	-40	-10	Negative
	hy-38:4	741.5	283.3	-50	-10	-40	-10	Negative
	40:6	747.5	283.3	-65	-10	-45	-10	Negative
	ox-40:6	763.5	283.3	-50	-10	-40	-10	Negative
	hy-40:6	765.5	283.3	-50	-10	-40	-10	Negative
	37:4 (Internal Standard)	709.5	269.3	-65	-10	-45	-10	Negative
Phosphatidyl serine (PS)	32:0	734.5	255.3	-120	-10	-52	-11	Negative
	32:1	732.6	255.3	-120	-10	-52	-11	Negative
	34:0	762.6	255.3	-120	-10	-52	-11	Negative
	34:1	760.6	255.3	-120	-10	-52	-11	Negative
	34:2	758.6	255.3	-120	-10	-52	-11	Negative
	36:0	790.6	283.3	-120	-10	-52	-11	Negative
	36:1	788.6	283.3	-120	-10	-52	-11	Negative
	36:2	786.6	281.3	-120	-10	-52	-11	Negative
	ox-36:2	802.6	281.3	-100	-10	-45	-11	Negative
	hy-36:2	804.6	281.3	-100	-10	-45	-11	Negative
	36:4	782.6	255.3	-120	-10	-52	-11	Negative
	ox-36:4	798.6	255.3	-100	-10	-45	-11	Negative
	hy-36:4	800.6	255.3	-100	-10	-45	-11	Negative

	38:5	808.5	281.3	-120	-10	-52	-11	Negative
	ox-38:5	824.6	281.3	-100	-10	-45	-11	Negative
	hy-38:5	826.6	281.3	-100	-10	-45	-11	Negative
	38:4	810.6	283.3	-120	-10	-52	-11	Negative
	ox-38:4	826.6	283.3	-100	-10	-45	-11	Negative
	hy-38:4	828.6	283.3	-100	-10	-45	-11	Negative
	40:7	832.6	281.3	-120	-10	-52	-11	Negative
	ox-40:7	848.6	281.3	-100	-10	-45	-11	Negative
	hy-40:7	850.6	281.3	-100	-10	-45	-11	Negative
	40:6	834.6	283.3	-120	-10	-52	-11	Negative
	ox-40:6	850.6	283.3	-100	-10	-45	-11	Negative
	hy-40:6	852.6	283.3	-100	-10	-45	-11	Negative
	37:4 (Internal Standard)	796.6	269.3	-120	-10	-52	-11	Negative

Table 2: LC-MS quantitation of the different phospholipids for different genotypes and paraquat treatment.
Unpaired t-test, control: C155-GAL4, * p < 0.05, ** p < 0.01, *** p < 0.001, ****p < 0.0001

Phosphatidylserine (PS) (pmol/ brain)						Lipid Class	
40:7	38:5	hy-40:7	ox-40:7	hy-38:5	ox-38:5	Species	
283.4	366.3	1.13	0.89	0.56	1.23	Mean	C155-GAL4
36.7	41.2	0.097	0.051	0.046	0.11	SEM	
4	4	4	4	4	4	N	
297.6	349.5	11.23	9.91	4.39	8.81	Mean	C155-GAL4 + 5mM Paraquat
32.4	37.6	1.12	0.92	0.32	0.78	SEM	
4	4	4	4	4	4	N	
0.781535	0.773432	0.00010631	< 0.0001	< 0.0001	< 0.0001	P-value	
302.2	378.6	0.93	0.69	0.43	0.89	Mean	C155-GAL4; UAS-VAP(P58S)
35.6	31.2	0.12	0.078	0.033	0.078	SEM	
4	4	4	4	4	4	N	
0.723591	0.819388	0.24254	0.0755142	0.0614109	0.0452042	P-value	
288.6	351.2	8.94	8.12	1.81	7.65	Mean	C155-GAL4; UAS-VAP(P58S) + 5mM Paraquat
29.1	34.8	0.98	0.91	0.23	0.65	SEM	
4	4	4	4	4	4	N	
0.924962	0.786176	0.00021353	0.00021323	0.00177943	< 0.0001	P-value	
298.7	367.3	2.92	3.34	2.2	4.5	Mean	C155-GAL4; UAS-VAP(P58S); UAS-SOD1_i(29389)
28.7	33.6	0.19	0.23	0.29	0.32	SEM	
4	4	4	4	4	4	N	
0.753767	0.985603	0.00015600	< 0.0001	0.00139963	< 0.0001	P-value	
291.7	379.8	2.77	2.36	1.56	3.91	Mean	C155-GAL4; UAS-VAP
29.8	32.1	0.23	0.22	0.43	0.34	SEM	
4	4	4	4	4	4	N	
0.864997	0.804452	0.00059603	0.00062646	0.060072	0.00029064	P-value	

Phosphatidylcholine (PC) (pmol/ brain)			Phosphatidylethanolamine (PE) (pmol/brain)							
40:7	**38:4**	**38:5**	**40:7**	**38:4**	**38:5**	**hy-40:7**	**ox-40:7**	**ox-38:4**	**hy-38:5**	**ox-38:5**
591.2	**567.8**	**616.6**	**443.1**	**489.3**	**512.3**	**0.26**	**0.13**	**0.49**	**0.18**	**0.23**
54.4	**58.6**	**67.8**	**45.6**	**41.2**	**43.1**	**0.035**	**0.028**	**0.056**	**0.029**	**0.031**
4	**4**	**4**	**4**	**4**	**4**	**4**	**4**	**4**	**4**	**4**
556.7	**575.6**	**623.4**	**459.1**	**477.6**	**501.4**	**3.39**	**1.89**	**3.56**	**3.26**	**1.92**
52.3	**55.6**	**65.4**	**34.9**	**56.7**	**51.4**	**0.34**	**0.12**	**0.31**	**0.34**	**0.12**
4	**4**	**4**	**4**	**4**	**4**	**4**	**4**	**4**	**4**	**4**
0.661575	**0.925441**	**0.944297**	**0.789879**	**0.872907**	**0.87625**	**< 0.0001**	**< 0.0001**	**< 0.0001**	**0.00010357**	**< 0.0001**
536.9	**551.5**	**617.8**	**488.3**	**432.5**	**518.7**	**0.17**	**0.23**	**0.41**	**0.12**	**0.18**
54.3	**55.6**	**65.7**	**42.4**	**45.4**	**51.7**	**0.033**	**0.032**	**0.049**	**0.011**	**0.021**
4	**4**	**4**	**4**	**4**	**4**	**4**	**4**	**4**	**4**	**4**
0.498133	**0.841291**	**0.996737**	**0.495222**	**0.389943**	**0.927344**	**0.110534**	**0.0569181**	**0.323646**	**0.101214**	**0.230187**
513.2	**554.6**	**665.4**	**478.3**	**491.8**	**495.6**	**3.91**	**1.55**	**1.34**	**1.89**	**1.21**
54.4	**69.5**	**61.9**	**43.4**	**47.8**	**51.3**	**0.32**	**0.13**	**0.09**	**0.11**	**0.12**
4	**4**	**4**	**4**	**4**	**4**	**4**	**4**	**4**	**4**	**4**
0.348132	**0.888838**	**0.611896**	**0.596291**	**0.969684**	**0.811484**	**< 0.0001**	**< 0.0001**	**0.00020082**	**< 0.0001**	**0.00021707**
523.4	**504.6**	**651.8**	**475.6**	**492.3**	**516.6**	**2.08**	**0.95**	**2.08**	**2.21**	**1.09**
51.6	**52.3**	**71.8**	**48.9**	**51.4**	**56.8**	**0.13**	**0.07**	**0.18**	**0.16**	**0.12**
4	**4**	**4**	**4**	**4**	**4**	**4**	**4**	**4**	**4**	**4**
0.39654	**0.44816**	**0.730771**	**0.644157**	**0.965154**	**0.953869**	**< 0.0001**	**< 0.0001**	**0.00015153**	**< 0.0001**	**0.00044410**
533.5	**513.2**	**605.6**	**455.9**	**499.6**	**504.6**	**1.78**	**0.81**	**1.76**	**1.89**	**1.11**
52.3	**55.6**	**66.5**	**45.6**	**59.8**	**55.6**	**0.3**	**0.06**	**0.12**	**0.09**	**0.11**
4	**4**	**4**	**4**	**4**	**4**	**4**	**4**	**4**	**4**	**4**
0.468216	**0.520649**	**0.906213**	**0.84922**	**0.891851**	**0.916411**	**0.00237435**	**< 0.0001**	**< 0.0001**	**< 0.0001**	**0.00025136**

Phosphatidic acid (PA) (pmol/ brain)				
40:6	**40:7**	**38:4**	**38:5**	**40:6**
391.8	**353.6**	**268.9**	**321.2**	**778.3**
34.2	**31.3**	**27.8**	**34.5**	**89.1**
4	**4**	**4**	**4**	**4**
381.4	**346.8**	**235.6**	**332.6**	**791.3**
39.5	**37.6**	**29.6**	**31.4**	**79.6**
4	**4**	**4**	**4**	**4**
0.847335	**0.89258**	**0.432883**	**0.812576**	**0.916574**
399.3	**367.8**	**271.4**	**316.4**	**788.7**
31.3	**36.5**	**28.1**	**34.5**	**71.8**
4	**4**	**4**	**4**	**4**
0.881301	**0.789012**	**0.958773**	**0.918008**	**0.935159**
387.6	**377.5**	**271.5**	**335.2**	**760.9**
31.6	**35.6**	**29.2**	**36.5**	**78.1**
4	**4**	**4**	**4**	**4**
0.930848	**0.630709**	**0.949998**	**0.788397**	**0.887986**
382.4	**377.4**	**275.6**	**326.6**	**767.8**
31.4	**36.5**	**21.3**	**34.5**	**78.3**
4	**4**	**4**	**4**	**4**
0.844873	**0.634237**	**0.851172**	**0.914245**	**0.932188**
266.4	**279.3**	**267.2**	**333.2**	**778.4**
25.6	**28.2**	**29.2**	**35.4**	**76.5**
4	**4**	**4**	**4**	**4**
0.0254203	**0.125357**	**0.963446**	**0.818018**	**0.998043**

Table 2: LC-MS quantitation of the different phospholipids for *Tor* knockdown
Unpaired t-test, control: C155-GAL4, * $p < 0.05$, ** $p < 0.01$, *** $p < 0.001$, ****$p < 0.0001$

Lipid Class	Phosphatidylserine (PS) (pmol/ brain)																
Species	40:7	38:5	hy-40:7	ox-40:7	hy-38:5	ox-38:5	C155-GAL4			C155-GAL4; UAS-TOR_i(35578)				C155-GAL4; UAS-VAP(P58S)				C155-GAL4; UAS-VAP(P58S); UAS-TOR_i(35578)			
	Mean	Mean	Mean	Mean	Mean	Mean	Mean	SEM	N	Mean	SEM	N	P-value	Mean	SEM	N	P-value	Mean	SEM	N	P-value
	288.6	314.3	0.75	0.51	0.23	0.91	29.4	24.3	3	278.5	33.2	4	0.8361	298.5	29.5	4	0.8278	277.6	31.3	3	0.8172
			0.09	0.07	0.06	0.15	0.09	0.07	0.06	1.89	0.21	0.16	0.15	0.78	0.09	0.07	0.05	2.44	0.25	0.24	0.21
			3	3	3	3	3	3	3	4	4	4	4	4	4	4	4	3	3	3	3
			0.8171	0.0071	0.0048	0.0113	0.6478	0.1484	0.7068	0.0032	0.0048	0.0113	0.6528	0.5092	0.0093	0.0040	0.0243	0.0060			

Phosphatidylcholine (PC) (pmol/ brain)			Phosphatidylethanolamine (PE) (pmol/brain)							
40:7	**38:4**	**38:5**	**40:7**	**38:4**	**38:5**	**hy-40:7**	**ox-40:7**	**ox-38:4**	**hy-38:5**	**ox-38:5**
589.5	**655.2**	**678.6**	**455.6**	**514.2**	**456.9**	**0.08**	**0.08**	**0.17**	**0.12**	**0.09**
59.5	**71.3**	**67.8**	**43.6**	**55.6**	**51.3**	**0.04**	**0.02**	**0.04**	**0.029**	**0.03**
3	**3**	**3**	**3**	**3**	**3**	**3**	**3**	**3**	**3**	**3**
567.3	**681.3**	**685.4**	**467.5**	**544.3**	**451.3**	**0.61**	**0.32**	**0.65**	**0.56**	**0.45**
54.3	**76.5**	**68.7**	**45.6**	**51.6**	**55.4**	**0.08**	**0.04**	**0.06**	**0.06**	**0.05**
4	**4**	**4**	**4**	**4**	**4**	**4**	**4**	**4**	**4**	**4**
0.7957	**0.8193**	**0.9480**	**0.8622**	**0.7111**	**0.9458**	**0.0032**	**0.0050**	**0.0017**	**0.0020**	**0.0025**
577.4	**655.7**	**693.4**	**442.6**	**566.6**	**467.5**	**0.09**	**0.09**	**0.14**	**0.15**	**0.11**
60.4	**65.1**	**65.5**	**34.9**	**75.4**	**54.6**	**0.02**	**0.01**	**0.03**	**0.03**	**0.02**
4	**4**	**4**	**4**	**4**	**4**	**4**	**4**	**4**	**4**	**4**
0.8945	**0.9961**	**0.8841**	**0.8231**	**0.6233**	**0.8971**	**0.7771**	**0.5761**	**0.4111**	**0.2712**	**0.4617**
589.5	**617.8**	**673.4**	**429.6**	**533.2**	**456.6**	**0.42**	**0.48**	**0.29**	**0.33**	**0.34**
55.6	**65.4**	**68.7**	**45.2**	**56.7**	**45.6**	**0.05**	**0.05**	**0.03**	**0.06**	**0.05**
3	**3**	**3**	**3**	**3**	**3**	**3**	**3**	**3**	**3**	**3**
0.9954	**0.7202**	**0.9565**	**0.7044**	**0.8245**	**0.9989**	**0.2796**	**0.2116**	**0.0273**	**0.1461**	**0.1976**

	Phosphatidic acid (PA) (pmol/ brain)			
	40:6	**38:5**	**38:4**	**40:7**
566.3	**344.2**	**312.4**	**233.5**	**235.6**
54.4	**26.6**	**43.2**	**23.5**	**27.6**
3	**3**	**3**	**3**	**3**
549.7	**359.8**	**301.2**	**256.3**	**241.2**
61.5	**35.8**	**34.5**	**35.7**	**23.4**
4	**4**	**4**	**4**	**4**
0.8543	**0.7576**	**0.8453**	**0.6453**	**0.8826**
515.4	**367.5**	**305.6**	**247.8**	**235.6**
54.2	**35.8**	**34.1**	**26.6**	**24.1**
4	**4**	**4**	**4**	**4**
0.5451	**0.6483**	**0.9048**	**0.7187**	**1.0000**
563.5	**356.7**	**341.2**	**255.6**	**241.3**
57.8	**38.9**	**34.5**	**27.6**	**25.6**
3	**3**	**3**	**3**	**3**
0.9783	**0.7994**	**0.6322**	**0.5684**	**0.8929**

Acknowledgements

Dr. Siddhesh Kamat helped design the experiment. Shubham Singh and Shabnam Patil are thanked for technical assistance with the mass spectrometry experiments.

© 2019. Published by The Company of Biologists Ltd | Disease Models & Mechanisms (2019) 12, dmm033803. doi:10.1242/dmm.033803

RESEARCH ARTICLE

SOD1 activity threshold and TOR signalling modulate VAP(P58S) aggregation via reactive oxygen species-induced proteasomal degradation in a *Drosophila* model of amyotrophic lateral sclerosis

Kriti Chaplot[1], Lokesh Pimpale[1,*], Balaji Ramalingam[2], Senthilkumar Deivasigamani[1,‡], Siddhesh S. Kamat[1] and Girish S. Ratnaparkhi[1,§]

ABSTRACT

Familial amyotrophic lateral sclerosis (ALS) is an incurable, late-onset motor neuron disease, linked strongly to various causative genetic loci. *ALS8* codes for a missense mutation, P56S, in VAMP-associated protein B (VAPB) that causes the protein to misfold and form cellular aggregates. Uncovering genes and mechanisms that affect aggregation dynamics would greatly help increase our understanding of the disease and lead to potential therapeutics. We developed a quantitative high-throughput *Drosophila* S2R+ cell-based kinetic assay coupled with fluorescent microscopy to score for genes involved in the modulation of aggregates of the fly orthologue, VAP(P58S), fused with GFP. A targeted RNA interference screen against 900 genes identified 150 hits that modify aggregation, including the ALS loci *Sod1* and *TDP43* (also known as *TBPH*), as well as genes belonging to the mTOR pathway. Further, a system to measure the extent of VAP(P58S) aggregation in the *Drosophila* larval brain was developed in order to validate the hits from the cell-based screen. In the larval brain, we find that reduction of SOD1 levels or decreased mTOR signalling reduces aggregation, presumably by increasing the levels of cellular reactive oxygen species (ROS). The mechanism of aggregate clearance is, primarily, proteasomal degradation, which appears to be triggered by an increase in ROS. We have thus uncovered an interesting interplay between SOD1, ROS and mTOR signalling that regulates the dynamics of VAP aggregation. Mechanistic processes underlying such cellular regulatory networks will lead to better understanding of the initiation and progression of ALS.

This article has an associated First Person interview with the first author of the paper.

KEY WORDS: ALS, Autophagy, UPS, Aggregate, Rapamycin, MG132

INTRODUCTION

Amyotrophic lateral sclerosis (ALS) is a progressive, fatal neurodegenerative disease characterized by loss of motor neurons, resulting in muscular atrophy, gradual paralysis and, ultimately, death of the patient within 2-5 years post-diagnosis (Cleveland and Rothstein, 2001; Tarasiuk et al., 2012). Most often, the disease occurs sporadically (sporadic ALS). However, in ∼10% of the cases, the disease occurs due to inheritance of altered gene(s) (familial ALS). *SOD1* (also known as *ALS1*), coding for superoxide dismutase 1, was the first causative locus to be discovered (Deng et al., 1993; Rosen et al., 1993), with more than 170 SOD1 mutations attributed to the diseased state. Since then, about 50 potential genetic loci (Taylor et al., 2016) have been identified in ALS through genome-wide association, linkage and sequencing studies. Recent studies have emphasized the oligogenic basis for ALS (Deivasigamani et al., 2014; van Blitterswijk et al., 2012), suggesting that ALS loci may be a part of a gene regulatory network (GRN) that breaks down late in the life of a diseased individual. At the cellular level, several hallmarks of ALS include breakdown of cellular homeostasis (Cluskey and Ramsden, 2001), endoplasmic reticulum (ER) stress, unfolded protein response, aggregation, oxidative stress, mitochondrial dysfunction and autophagy. Although several studies have demonstrated the wide range of consequences of the genetic alterations on cellular function, no clear unifying mechanism has emerged that might explain the pathogenesis of the disease (Andersen and Al-Chalabi, 2011; Mulligan and Chakrabartty, 2013; Taylor et al., 2016; Turner et al., 2013; Walker and Atkin, 2011).

In 2004, Mayana Zatz's group (Nishimura et al., 2004) discovered a novel causative genetic locus, VAMP-associated protein B (VAPB), termed as ALS8, in a large Brazilian family whose members succumbed to ALS and/or spinal muscular atrophy. The point mutation of P56S was identified in the N-terminal, major sperm protein (MSP) domain of VAPB (Nishimura et al., 2004). VAPB is an integral membrane protein present in the ER membrane, ER-Golgi intermediate compartment, mitochondrial-associated membrane and the plasma membrane, implicated in important functions in the cell such as vesicular trafficking, ER structure maintenance, lipid biosynthesis, microtubule organization, mitochondrial mobility and calcium homeostasis (Lev et al., 2008; Murphy and Levine, 2016). Recent studies have highlighted its critical role in membrane contact sites (Alpy et al., 2013; Gomez-Suaga et al., 2017b; Metz et al., 2017; Yadav et al., 2018; Zhao et al., 2018). The *Drosophila* orthologue of VAPB is VAP33A/CG5014 (herein referred to as VAP) and has been used to develop models for ALS (Chai et al., 2008; Deivasigamani et al., 2014; Moustaqim-Barrette et al., 2014; Ratnaparkhi et al., 2008; Sanhueza et al., 2015). We have previously identified a *Drosophila* VAP gene regulatory network consisting of 406 genes, including a novel interaction with the mTOR pathway (Deivasigamani et al., 2014). The ALS8 mutation can also alter the physical interaction of VAP with other proteins, including FFAT motif-containing proteins

[1]Department of Biology, Indian Institute of Science Education and Research, Pune 411008, India. [2]Oxford Nanoimaging Ltd, Oxford OX2 8TA, UK. *Biotechnology Center, Technische Universität Dresden, Tatzberg 47/49, 01307 Dresden, Germany. ‡Neurobiology and Epigenetics Unit, European Molecular Biology Laboratory, Adriano Buzzati-Traverso Campus, Via Ramarini 32, 00015 Monterotondo, Italy.

§Author for correspondence (girish@iiserpune.ac.in)

S.D., 0000-0001-8464-5620; S.S.K., 0000-0001-6132-7574; G.S.R., 0000-0001-7615-3140

This is an Open Access article distributed under the terms of the Creative Commons Attribution License (https://creativecommons.org/licenses/by/4.0), which permits unrestricted use, distribution and reproduction in any medium provided that the original work is properly attributed.

Received 11 July 2018; Accepted 7 January 2019

Disease Models & Mechanisms (2019) 12, dmm033803. doi:10.1242/dmm.033803

(Loewen et al., 2003; Murphy and Levine, 2016), impairing cellular functions (De Vos et al., 2012; Huttlin et al., 2015; Moustaqim-Barrette et al., 2014). Ubiquitinated cellular aggregates (Papiani et al., 2012; Ratnaparkhi et al., 2008) are seen on VAP mutant expression and are capable of sequestering the wild-type VAP protein in a dominant-negative manner (Ratnaparkhi et al., 2008; Teuling et al., 2007). In *Drosophila*, neuronal overexpression of VAP(P58S), and subsequent formation of aggregates, in the background of endogenous VAP appears to lead to only mild neurodegenerative phenotypes, such as flight defects, compared with the more severe phenotypes associated with wild-type VAP neuronal overexpression (Ratnaparkhi et al., 2008; Tsuda et al., 2008). Previously, we have used the UAS-GAL4 system to study the interaction between VAP and mTOR signalling using the neuromuscular junction (NMJ) phenotype associated with neuronally overexpressed VAP(P58S) (Deivasigamani et al., 2014). The functional consequence of neuronal VAP(P58S) aggregation in this system is not fully understood, and its contribution to disease remains elusive.

In this study, we identify 150 genetic modifiers of VAP(P58S) aggregation by conducting a directed S2R+ cell-based RNA interference (RNAi) screen, targeting 900 unique genes belonging to different categories that are associated either with ALS or VAP function or proteostasis. We used the previously described [C155-Gal4;UAS-VAP(P58S)] system (Deivasigamani et al., 2014; Ratnaparkhi et al., 2008) to validate one such modifier, SOD1, *in vivo*, in the third-instar larval brain of *Drosophila*, by measuring changes in aggregation of VAP(P58S) in response to modulation of *Sod1* levels. Our data indicate that clearance of VAP(P58S) aggregates via the proteasomal machinery is enhanced by inducing reactive oxygen species (ROS) due to loss of SOD1 function. We also find a similar clearance of aggregates, attributed to proteasomal degradation, with mTOR downregulation, accompanied by elevated ROS. We find that wild-type VAP, but not mutant VAP, elevates ROS. Accumulated ROS result in inhibition of endogenous *VAP* transcription, a phenomenon that may directly affect familial as well as sporadic ALS pathogenesis.

RESULTS

A *Drosophila* S2R+ cell culture model to study VAP(P58S) aggregation

C-terminal and N-terminal fusions of VAP and VAP(P58S) with GFP were used to transfect cells and generate stable S2R+ lines, as described in the Materials and Methods (Fig. 1A; Fig. S1A). VAP:GFP showed a non-nuclear, reticular localization in the cell with <10% of the transfected (GFP-positive) cells showing high intensity

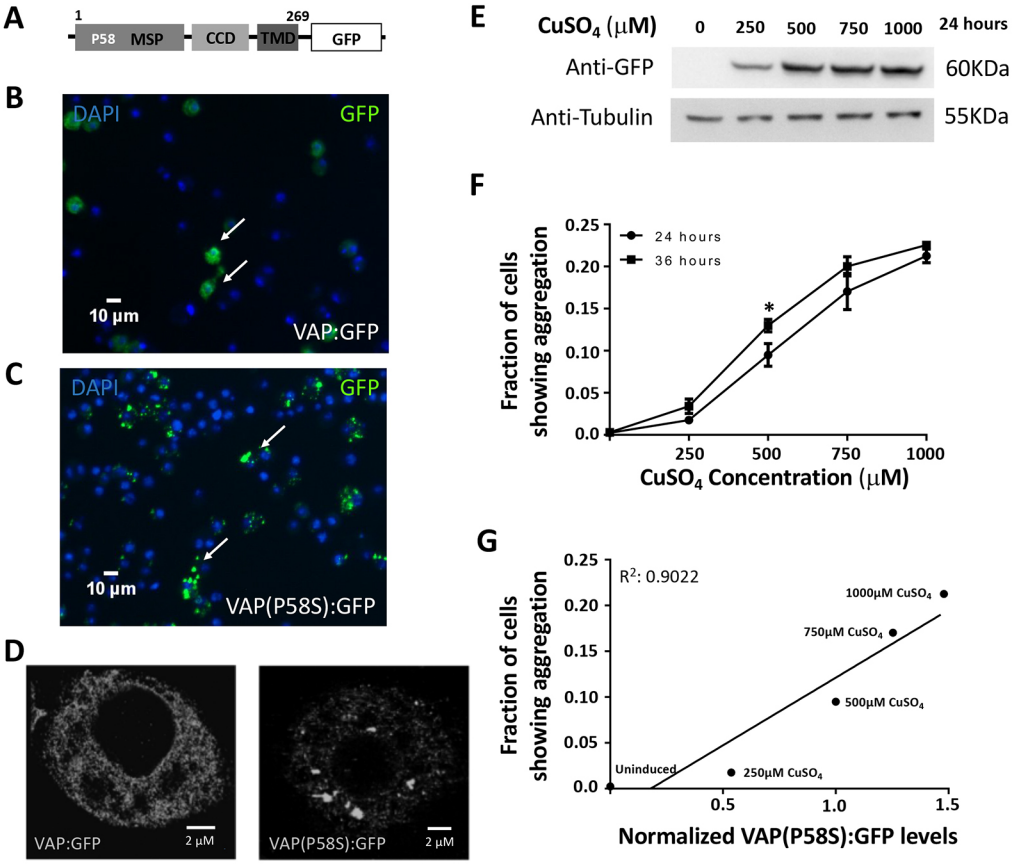

Fig. 1. A *Drosophila* cell culture model to study VAP(P58S) aggregation. (A) VAP:GFP and VAP(P58S):GFP, when expressed in S2R+ cells, allow efficient visualization of VAP protein in the cell by epifluorescence. (B,C) In stable cell lines, expression of *VAP(P58S):GFP*, under an inducible metallothionein promoter results in aggregation (C), unlike wild-type VAP:GFP (B). GFP is visualized by epifluorescence and chromatin by DAPI, post-fixation. Arrows indicate cells expressing VAP:GFP (B) or VAP(P58S):GFP (C). (D) A super-resolution image, using Ground State Depletion microscopy, showing GFP inclusions formed in cells expressing VAP(P58S):GFP but not in VAP:GFP. (E) VAP(P58S):GFP protein levels in cells increase with increasing $CuSO_4$ concentration at 24 h post-induction. (F) The increase in the fraction of S2R+ cells showing GFP-positive inclusions increases with increasing $CuSO_4$ concentration. At 500 mM $CuSO_4$, inclusions significantly increase between 24 h and 36 h. Student's *t*-test (*$P<0.05$). (G) A linear correlation between the fraction of cells showing aggregation, measured using microscopy, plotted against relative VAP(P58S):GFP protein levels, as quantified by western blotting, at 24 h post-induction. Error bars indicate s.d.

Disease Models & Mechanisms (2019) 12, dmm033803. doi:10.1242/dmm.033803

puncta (Fig. 1B; Fig. S1A). In contrast, >80% of the GFP-positive VAP(P58S):GFP cells showed distinct high-intensity puncta with little or no background staining within the cell (Fig. 1C; Fig. S1A). Super-resolution imaging confirmed that VAP appeared to be reticular, while VAP(P58S) was found in inclusion bodies (Fig. 1D). In contrast, GFP, when expressed, showed a uniform cytoplasmic signal (Fig. S1B). Both N-terminal GFP fusions, GFP:VAP and GFP:VAP(P58S), showed puncta formation at levels comparable to VAP(P58S):GFP, and hence were not used further in the study (Fig. S1A). All further experiments (see below) were carried out with stable lines expressing VAP:GFP or VAP(P58S):GFP, which showed expected/relevant localization and levels of aggregation.

An S2R+ cell-based reverse-genetics screen developed to identify modifiers of VAP(P58S) aggregation

In an attempt to identify genetic modifiers of VAP(P58S) aggregation kinetics, we conducted a focused S2R+ cell-based RNAi screen, targeting 900 unique genes belonging to nine different categories or families associated with ALS or VAP function. We generated stable S2R+ cell lines expressing VAP(P58S):GFP under a Cu^{2+}-induced promoter. The inducible cell culture system allowed us to increase the VAP(P58S):GFP protein levels in the cell with increasing copper sulphate ($CuSO_4$) concentrations (250, 500, 750 and 1000 µM) at 24 h post-induction (Fig. 1E). Using fluorescence microscopy, we found a linear relationship between the $CuSO_4$ concentrations and the fraction of

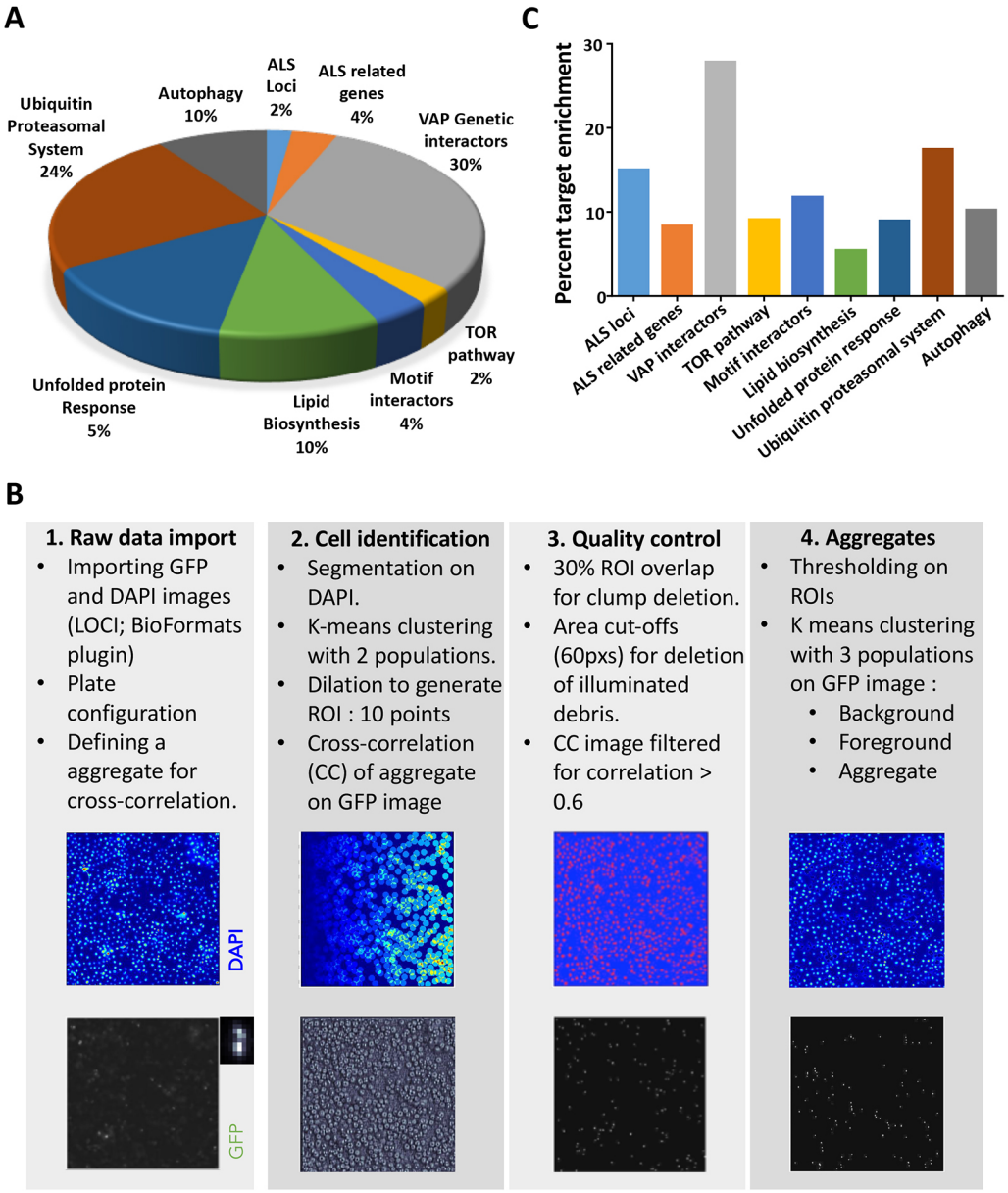

Fig. 2. A targeted dsRNA screen in S2R+ cells to discover modifiers of VAP(P58S):GFP aggregation. (A) dsRNAs for 900 genes (Table S1A) were chosen for knockdown. GO representation indicates the categories of genes chosen and percentage (%) for each category. Genes were categorized as indicated (Table S1A,B). (B) Workflow of the steps executed for image analysis using an automated MATLAB script (Dey et al., 2014). Steps are detailed in the Materials and Methods. (C) The end result of the screen is a list of 150 genes identified, based on average cell intensity, which have been found to modify aggregation of VAP(P58S):GFP. Graph indicates the percentage of genes identified as targets within each gene category. Genes are listed in Table S1C.

Disease Models & Mechanisms (2019) 12, dmm033803. doi:10.1242/dmm.033803

cells showing VAP(P58S):GFP aggregates that also increased with time (24 h and 36 h) post-induction (Fig. 1F). The concentration-dependent increase in relative levels of VAP(P58S):GFP correlated with an increase in the fraction of cells showing aggregates (Fig. 1G), indicating the propensity of the mutant protein to aggregate. Early time points (12-16 h) gave very few cells with aggregates, while non-linearity, high confluency and cell death became a concern at time points beyond 48 h and concentrations greater than 750 µM. The aggregation kinetics curve was used to define the extent of aggregation in the cell culture system and select optimum parameters to conduct the RNAi screen. Keeping a modest confluency and well-separated cells for ease of imaging, the screen was performed at a fixed concentration of 500 µM $CuSO_4$ at 24 h and 36 h post-induction.

We chose 900 genes (Table S1A), based on their availability in the Open Biosystems Library (see Materials and Methods), to screen for modifiers that could change aggregation levels of VAP(P58S):GFP. A Gene Ontology (GO) chart (Fig. 2A) represents the biological process associated with these 900 genes, as defined by FlyBase. The genes were selected and categorized (Table S1B) on the following basis. First, known *Drosophila* orthologues of ALS loci (20 genes) and ALS-related genes (36 genes) as tabulated in the online ALS database (ALSOD) were chosen. The next category included 273 genes from a VAP *Drosophila* GRN consisting of 406 genes (Deivasigamani et al., 2014). As *Mtor* was identified as a major interactor of *VAP* in our previous study (Deivasigamani et al., 2014), we chose 22 genes of the extended mTOR pathway. To explore the functional aspects of VAP(P58S), we also screened genes involved in lipid biosynthesis (92 genes) and FFAT motif interactors of VAP (34 genes). In order to identify a role of proteostasis in aggregation, we screened genes involved in the unfolded protein response (123 genes), ubiquitin proteasomal pathway (212 genes) and autophagy (88 genes).

The images collected at the end of the screen (detailed in the Materials and Methods) were analysed by an automated MATLAB analysis (see Materials and Methods; Fig. 2B). Based on average cell intensity, 150 targets (Table S1C) and, based on total cell intensity, 85 targets (Table S1D) that modulated VAP(P58S):GFP aggregation kinetics were identified; 57 genes were found to be overlapping for both parameters, increasing confidence in our analysis (Table S1E). The percentage of genes identified as modulators from each category are plotted in Fig. 2C and Fig. S1C, as percent target enrichment. ALS loci, notably *Sod1* and *TDP43* (also known as *TBPH*), were found as interesting modulators perturbing VAP(P58S):GFP aggregation. Targets belonging to the VAP genetic network, as defined by Deivasigamani et al. (2014), were also enriched. As identified earlier (Deivasigamani et al., 2014), components of the mTOR pathway also appeared to be key regulators of VAP(P58S):GFP aggregation. Less than 10% of genes screened belonging to families associated with lipid biosynthesis and motif interactors were identified as targets. Interestingly, genes related to the ubiquitin proteasomal system (UPS), such as ubiquitin ligases and proteasome components, were enriched, as were the autophagy-related genes, *Atg7* and *Atg3*. From the unfolded protein response category, along with chaperones such as the heat shock proteins *Hsp60C*, *Hsp23* and *Hsp83*, we also identified a few peptidyl prolyl isomerases as targets. Overall, in our primary targeted screen, we found various genetic interactors of wild-type VAP as modulators of VAP(P58S) aggregation as well. Importantly, the uncovering of two ALS loci, *Sod1* and *TDP43*, mTOR pathway genes such as *Rheb* and *S6k*, and genes enriched in the UPS as modulators of VAP(P58S) aggregation dynamics, led us to develop an *in vivo* model to validate these genes and to understand mechanisms underlying these interactions in *Drosophila*.

A model system for measuring VAP(P58S) aggregation in the *Drosophila* larval brain

In order to validate targets from the screen *in vivo*, we used the *UAS-GAL4* system to specifically overexpress wild-type *VAP* or *VAP(P58S)* in the brain using a pan-neuronal driver, *C155* (*elav*) (Deivasigamani et al., 2014; Ratnaparkhi et al., 2008). Based on anti-VAP immunostaining, unlike wild-type VAP (Fig. S2A), mutant VAP(P58S) formed distinct cellular puncta and could be used as a model to study aggregation in the animal (Fig. S2B-D). These aggregates have been shown to be ubiquitinated and dominant negative when expressed in muscle (Ratnaparkhi et al., 2008). To develop a methodology for quantitation of aggregates in the brain (described in the Materials and Methods), we used temperature as a means to increase GAL4 activity, which would increase VAP(P58S) dosage and, possibly, aggregation. An increase in mean VAP(P58S) aggregation density was observed with increasing temperature, which was significant between 18°C and 25°C, but not significant between 25°C and 28°C (Fig. S2H). Neuronal knockdown of VAP, using RNAi, in *C155-GAL4/+; UAS-VAP(P58S)/+* flies, at each temperature (Fig. S2E-G), led to a significant decrease in the corresponding aggregation density of the ventral nerve cord (Fig. S2H). The above experiments suggested that, at 25°C, we could quantify changes in VAP(P58S) aggregation density in the brain of the larvae and, thereafter, we used this system to further validate modifiers of aggregation identified from the cell-based screen.

Drosophila SOD1 is a modifier of VAP(P58S) aggregation

SOD1, the first known ALS locus (Rosen et al., 1993), has been implicated in sporadic as well as familial cases and was our first choice for validation of the S2R+ based screen in *Drosophila*. We previously identified *Sod1* as a genetic interactor of *VAP* in a fly-based reverse genetics screen (Deivasigamani et al., 2014). Here, we individually knocked down *Sod1* using three independent RNAi lines in the *C155-GAL4/+; UAS-VAP(P58S)/+* background and observed a significant decrease in aggregation density in the ventral nerve cord (Fig. 3A,B; Fig. S3A,C,D). This threefold decrease in VAP aggregates was comparable to the reduction seen with VAP knockdown (Fig. 3B). Likewise, we overexpressed *Sod1* in the *C155-GAL4/+; UAS-VAP(P58S)/+* background. Here, however, we did not find a significant change in aggregation density (Fig. 3C,D; Fig. S3B,C,E). Taken together, these results suggest a need for a threshold level of *Sod1* to maintain VAP(P58S) inclusions.

Oxidative stress reduces VAP(P58S) aggregation

Enzymatically, SOD1 metabolizes superoxide species to hydrogen peroxide, thereby preventing oxidative stress. A loss of function of SOD1 would, in principle, increase ROS. We tested whether a chemical mimic, paraquat, which increases cellular ROS (Castello et al., 2007; Cochemé et al., 2011; Drechsel and Patel, 2008), could phenocopy the effect of *Sod1* knockdown. We treated the VAP(P58S):GFP stable line with non-lethal concentrations of 10 mM and 20 mM paraquat for 4 h prior to $CuSO_4$ induction and found that paraquat could significantly reduce the fraction of cells showing GFP-positive aggregates (Fig. 4A; Fig. S4A) in a dose-dependent manner. Similarly, larvae with the genotype *C155-GAL4/+; UAS-VAP(P58S)/+* hatched,

Disease Models & Mechanisms (2019) 12, dmm033803. doi:10.1242/dmm.033803

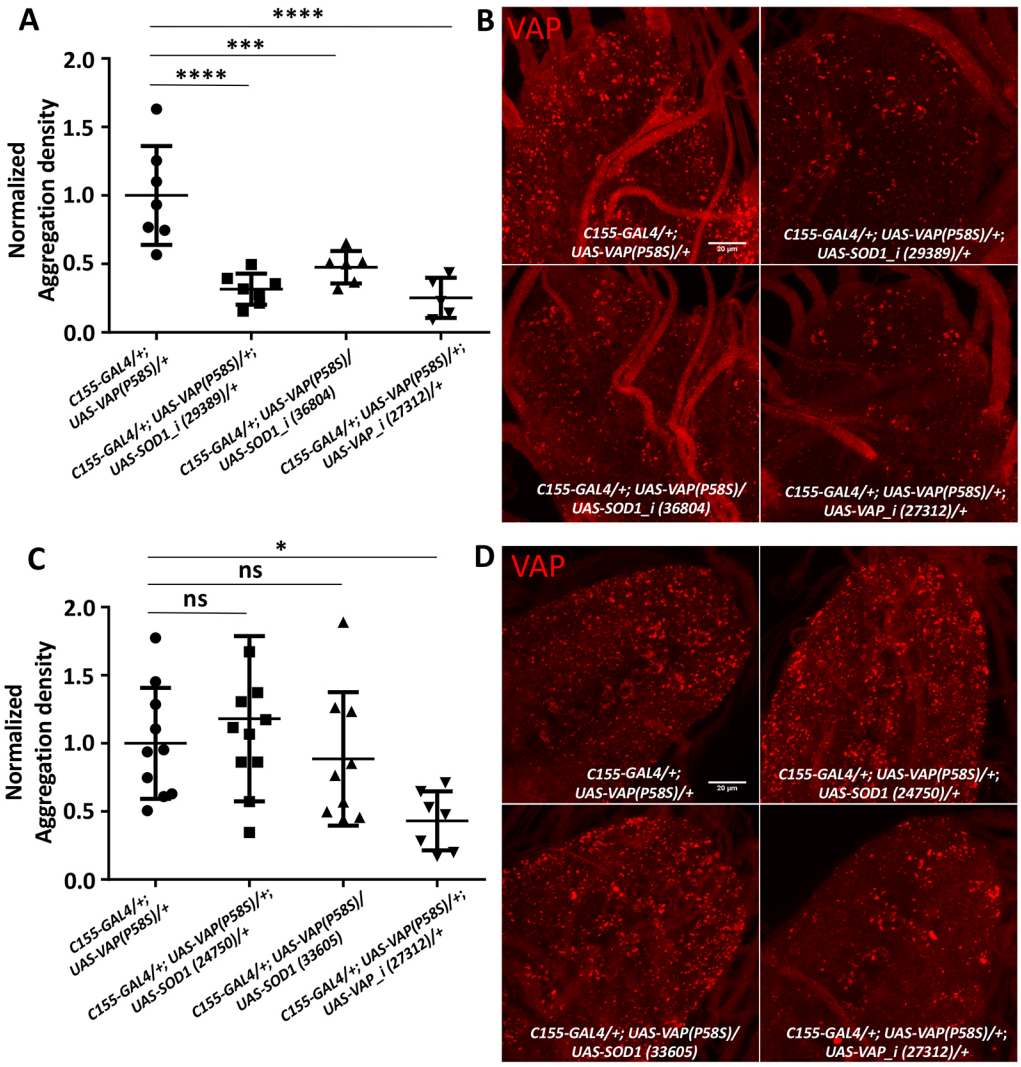

Fig. 3. *Sod1* knockdown reduces VAP(P58S) aggregation in larval brains. (A) *Sod1* knockdown in the nervous system decreases aggregation density in the ventral nerve cord. VAP knockdown also reduces aggregation due to reduction in VAP and VAP(P58S) protein expression. The '*_i*' appended to a gene name indicates an RNAi line. ANOVA (****P<0.0001). Numbers in brackets indicate BDSC stock numbers. (B) Representative images of the ventral nerve cord showing aggregation of VAP(P58S) with *Sod1* knockdown (29389 and 36804) and with *VAP* knockdown (27312). (C) *Sod1* overexpression does not affect aggregation density in the ventral nerve cord. ANOVA (P=0.0208). (D) Representative images of the ventral nerve cord showing aggregation of VAP(P58S) with *Sod1* overexpression (24750 and 33605) and with *VAP* knockdown (27312). All images were taken at the same magnification. Fisher's LSD multiple comparison (*P<0.05, ***P<0.001, ****P<0.0001; ns, not significant). Error bars indicate s.d.

fed and grown on a non-lethal concentration of 5 mM paraquat at 25°C showed a decrease in aggregation density in the third-instar larval brain, reminiscent of the *Sod1* knockdown phenotype (Fig. 4B; Fig. S4B). We also checked the effect of other ROS scavenging genes, such as *Sod2* and *Catalase*, on VAP(P58S) aggregation. Knockdown of both these genes resulted in a drastic reduction in aggregation density in the ventral nerve cord of *C155-GAL4/+; UAS-VAP(P58S)/+* larval brains (Fig. 4C). As seen with SOD1, overexpression of SOD2 did not change aggregation density; however, Catalase overexpression resulted in a fractional increase in aggregation density (Fig. 4C). These results strongly suggest ROS-dependent maintenance and/or stability of VAP(P58S) aggregates.

To confirm whether feeding of paraquat and loss of SOD1 function led to an increase in ROS levels in the larval brain, we measured the levels of oxidized phospholipids, using quantitative mass spectrometry (MS)-based lipidomics (Kamat et al., 2015; Kory et al., 2017; Pathak et al., 2018; Tyurina et al., 2000). On feeding *C155-GAL4/+* larvae with 5 mM paraquat, we enriched and detected nine oxidized polyunsaturated fatty acids (PUFAs), belonging to the phosphatidylserine (PS) and phosphatidylethanolamine (PE) (Fig. 4D; Table S2) families of phospholipids, which were significantly elevated in larval brains, compared with the unfed control. PUFA-containing oxidatively damaged phospholipids showed a mass addition of +16 (denoted as 'ox-', likely an epoxide across the double bond) or +18 (denoted as 'hy-', likely the addition of water across the double bond) to the parent phospholipid, as a consequence of addition of different ROS. Of note, the parent or precursor phospholipids did not change in concentration, and the concentrations of the oxidized phospholipids were less than 1% of the parent or precursor phospholipids. We found a similar elevation in concentrations of oxidized phospholipids in *C155-GAL4/+; UAS-VAP(P58S)/+; UAS-SOD1_i/+*, but not in *C155-GAL4/+; UAS-VAP(P58S)/+*, which was equivalent to the *C155-GAL4/+* control (Fig. 4D; Table S2). This elevation in oxidized phospholipids was found to be inversely correlated with the corresponding fold change in aggregation density (Fig. S4C). Interestingly, we found that overexpression of *VAP* had a curious effect of increasing the oxidation of lipids, indicating that wild-type VAP has a cryptic, yet important, role in regulating ROS levels. Taken together, these results indicate that ROS initiate processes that aid clearance of VAP(P58S) aggregates and are, in turn, regulated by VAP wild-type levels in the cell (Fig. 4E).

ROS activate proteasomal machinery

We further investigated protein degradative mechanisms that may be activated in response to ROS, leading to the clearance of VAP(P58S) aggregates. In order to test whether the proteasomal machinery was responsible for reduction in aggregation, we

Disease Models & Mechanisms (2019) 12, dmm033803. doi:10.1242/dmm.033803

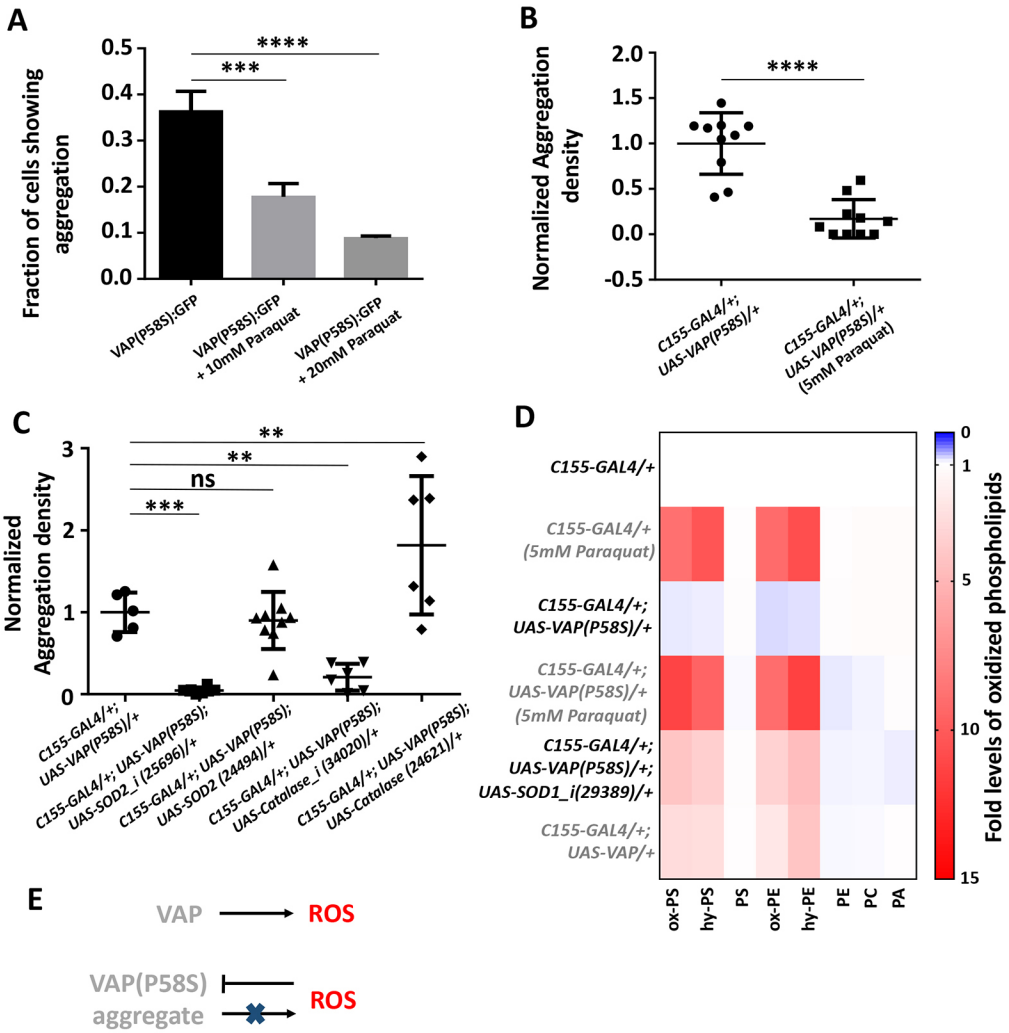

Fig. 4. Increase in ROS leads to decrease in VAP(P58S) aggregation levels. (A) 4 h paraquat treatment prior to inducing VAP(P58S):GFP in stable S2R+ cell line reduces the fraction of cells showing aggregation observed 24 h post-induction. ANOVA (****$P<0.0001$), Fisher's LSD multiple comparison test (***$P<0.001$, ****$P<0.0001$). Representative images are shown in Fig. S4A. (B) Paraquat feeding decreases aggregation density in the ventral nerve cord of third-instar larval brains in *C155-GAL4/+; UAS-VAP(P58S)/+* flies. Student's *t*-test (****$P<0.0001$). Representative images are shown in Fig. S4B. (C) *Sod2* or *Catalase* knockdown reduces aggregation density. Overexpression of *Sod2* does not change aggregation density; however, overexpression of *Catalase* increases aggregation density. The '*_i*' appended to a gene name indicates an RNAi line. ANOVA (****$P<0.0001$), Fisher's LSD multiple comparison test (**$P<0.01$, ***$P<0.001$; ns, not significant). (D) Heat map depicting the change in levels of oxidized phospholipids normalized to *C155-GAL4/+*, quantified using MS in response to ROS generated in third-instar larval brains ($n=4$) for the listed genotypes. *Sod1* knockdown as well as VAP overexpression appears to increase cellular ROS levels. Statistical tests are described in Table S2. (E) Model depicting the effects of overexpression of wild-type and mutant VAP on ROS. Error bars indicate s.d.

hatched, fed and grew larvae on food containing a proteasomal inhibitor, 5 µM MG132. Larval brains were dissected at the wandering third-instar stage and analysed for aggregation density. As expected, unfed *C155-GAL4/+; UAS-VAP(P58S)/+; UAS-SOD1_i/+* showed reduced aggregation density (Fig. 5C), compared with unfed control (Fig. 5A,E). Upon MG132 feeding, *C155-GAL4/+; UAS-VAP(P58S)/+; UAS-SOD1_i/+* showed a complete recovery/retention of VAP(P58S) aggregation (Fig. 5D, E). Fed *C155-GAL4/+; UAS-VAP(P58S)/+; UAS-SOD1_i/+* also showed an enhanced aggregation density compared with fed *C155-GAL4/+; UAS-VAP(P58S)/+* (Fig. 5B,E). Aggregates in the presence of ROS (with *Sod1* knockdown) and proteasomal inhibition (with MG132) appeared to be predominantly smaller, scattered and mislocalized around the nuclear membrane/ER compared with the respective controls (Fig. 5D′). The localization of the aggregates suggests that they may be residing in a juxtanuclear quality control compartment (JUNQ)-like compartment (Ogrodnik et al., 2014). These results indicate that the proteasomal machinery is facilitated in the presence of ROS for active degradation of VAP(P58S) aggregates (Fig. 5F). However, fed *C155-GAL4/+; UAS-VAP(P58S)/+* larvae (Fig. 5A) did not show accumulation of aggregation, compared with unfed control (Fig. 5B,E), indicating that other mechanisms could be at play to maintain the aggregation density.

mTOR downregulation, but not autophagy, lowers VAP(P58S) aggregation

We examined whether aggregates could be cleared via autophagy in the third-instar larval brain. mTOR downregulation is known to activate autophagy (Noda and Ohsumi, 1998), and this could be achieved chemically, by feeding rapamycin (Heitman et al., 1991), and genetically, by *Tor* knockdown. Upon feeding *C155-GAL4/+; UAS-VAP(P58S)/+* larvae with 200 nM rapamycin as described before (Deivasigamani et al., 2014), we observed a drastic clearance of aggregates in the ventral nerve cord compared with unfed controls (Fig. 6A-C). When *Tor* transcripts were reduced using RNAi in *C155-GAL4/+; UAS-VAP(P58S)/+*, a similar decrease in aggregation density was found (Fig. 6D-F). To verify the effect of mTOR downregulation on aggregates, we induced autophagy by overexpressing Atg1 in *C155-GAL4/+; UAS-VAP(P58S)/+* larval brains as described before (Deivasigamani et al., 2014; Shen and Ganetzky, 2009). Validation of the UAS-Atg1 line is described in the Materials and Methods. With overexpression of Atg1, however, we did not observe a change in aggregation density (Fig. 6G-I; Fig. S4D,E), suggesting that mTOR signalling might perturb downstream effectors other than Atg1, which may affect VAP(P58S) aggregation dynamics (Fig. 6J). The data also raise the possibility of an autophagy-independent pathway.

Disease Models & Mechanisms (2019) 12, dmm033803. doi:10.1242/dmm.033803

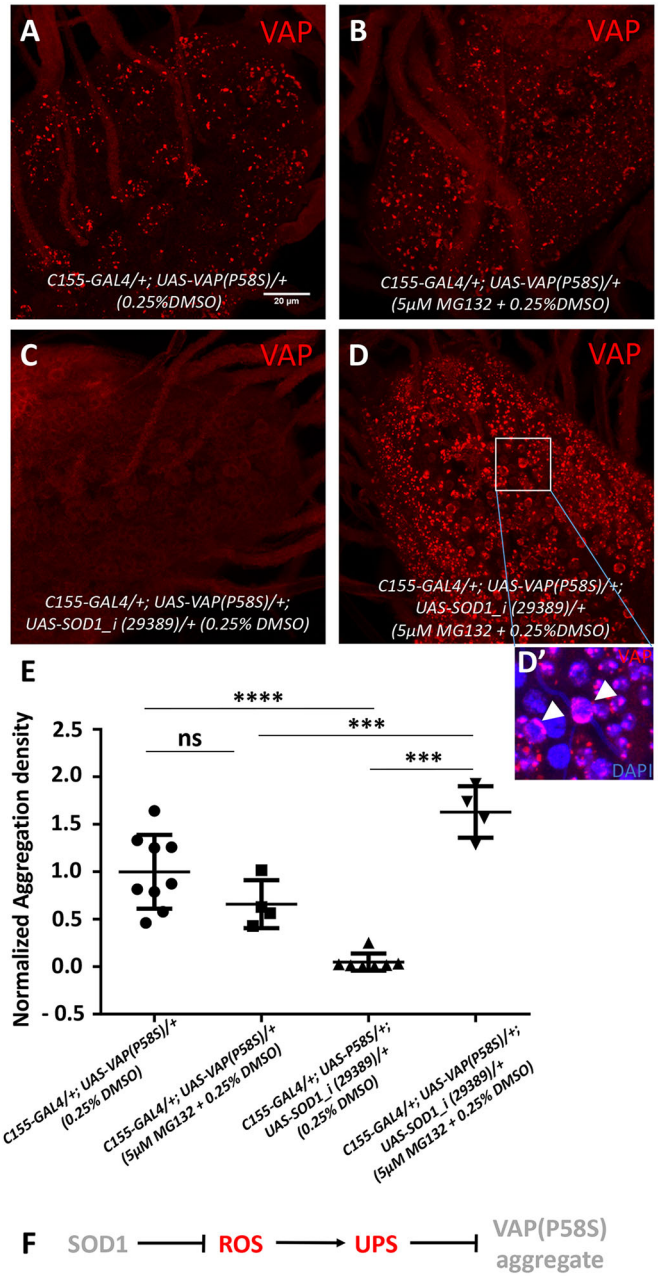

Fig. 5. ROS activates proteasomal machinery. (A,B) MG132 feeding of *C155-GAL4/+; UAS-VAP(P58S)/+*, to inhibit proteasomal machinery, does not accumulate VAP aggregates. (C-D′) MG132 feeding of *C155-GAL4/+; UAS-VAP(P58S)/+; UAS-SOD1_i (29,389)/+*, leads to a dramatic accumulation of VAP aggregates. The aggregates, in the presence of ROS and MG132, seem to be localized around the nuclear membrane (arrowheads) as depicted in the inset (D′). (E) Plot showing a significant decrease in aggregation density in the ventral nerve cord in *C155-GAL4/+; UAS-VAP(P58S); UAS-SOD1_i (29,389)/+* compared with *C155-GAL4/+; UAS-VAP(P58S)/+* control. This decrease is rescued by feeding 5 µM MG132 and is significantly higher than that in the *C155-GAL4/+; UAS-VAP(P58S)/+* control, both unfed and fed with MG132. All images were taken at the same magnification. ANOVA (*****P*<0.0001), Fisher's LSD multiple comparison test (****P*<0.001, *****P*<0.0001; ns, not significant). (F) Model depicting the role of SOD1-regulated ROS in activating proteasomal degradation of VAP(P58S) protein/aggregates. Error bars indicate s.d.

mTOR inhibition promotes proteasomal clearance of VAP(P58S) aggregation via ROS

We first decided to check whether clearance of aggregates with mTOR inhibition correlated with an increase in ROS, as in the case of *Sod1* knockdown. We found that levels of several species of oxidized phospholipids were indeed higher with *Tor* knockdown, with or without neuronal overexpression of VAP(P58S), in third-instar larval brains, with levels similar to those observed upon *Sod1* knockdown (Fig. 7A). mTOR pathway downregulation has recently been shown to activate not only autophagy but also ubiquitin proteasomal machinery (Zhao et al., 2015) via the Mpk1/ERK5 (also known as MAPK7) pathway in yeast and humans (Rousseau and Bertolotti, 2016). We tested whether ROS upregulation with *Tor* knockdown could be inducing proteasomal clearance of VAP(P58S) aggregation by feeding *C155-GAL4/+; UAS-VAP(P58S)/+; UAS-TOR_i/+* with 5 µM MG132 (Fig. 7B-E). Although there was a significant decrease in aggregation density with *Tor* knockdown (Fig. 7D), we found only a slight recovery of aggregation in MG132-fed animals (Fig. 7E) compared with unfed *C155-GAL4/+; UAS-VAP(P58S)/+* control larvae (Fig. 7C). This recovery appeared to be far less dramatic than that seen in the case of *Sod1* knockdown. Taken together, these results indicate that, in the context of ROS, proteasomal degradation could be the major pathway responsible for clearance of VAP(P58S) aggregation (Fig. 7F), although other downstream effectors of mTOR signalling, including autophagy, cannot be conclusively ruled out as additional mechanisms.

We also explored the possible relationship between *VAP* and ROS at a transcriptional level. Larvae of the control, *C155-GAL4/+* genotype were hatched and fed on 5 mM paraquat, and the brains were dissected at the wandering third-instar larval stage. The levels of endogenous *VAP* and *Sod1* mRNA, in response to ROS, were measured using quantitative PCR in control larval brains. We found that endogenous *VAP* mRNA levels were lowered in the presence of high levels of ROS (Fig. 7G), whereas *Sod1* mRNA levels remained unchanged (Fig. 7H). This result may indicate the presence of a negative-feedback loop wherein VAP overexpression leads to accumulation of ROS (Fig. 4C), which, in turn, downregulates endogenous *VAP* transcription (Fig. 7I). This phenomenon merits detailed investigation in future studies.

DISCUSSION

A targeted RNAi screen uncovers SOD1, TDP43 and TOR signalling elements as targets to understand dynamics of VAP(P58S) aggregation

Drosophila S2R+ cell-based whole-genome RNAi screens serve as powerful tools due to the relative ease with which transcript knockdown can be achieved (Echeverri and Perrimon, 2006). Similar systems have been used for identifying modifiers of aggregation of Huntingtin protein (Zhang et al., 2010). Our screen was aimed at enriching genes that are known players in ALS, VAP interactors and proteostasis. First and foremost, we found ALS loci *Sod1* and *TDP43* as modifiers of VAP(P58S) aggregation, which we had previously identified as VAP genetic interactors (Deivasigamani et al., 2014). In this study, we have explored the interaction between *Sod1* and *VAP*, while *TDP43* also serves as an exciting candidate for further investigation. TDP43 has been shown to perturb membrane-associated mitochondrial (Turner et al., 2008) sites that are maintained by VAPB-PTPIP51 interactions in mammalian cell culture (Stoica et al., 2014). Additionally, TDP43 proteinopathy has been identified in motor neurons of mice models of VAP(P58S) aggregation (Tudor et al., 2010). TDP43-driven neurodegeneration has also been shown to be modulated by oxidative stress-related MAP kinase pathways in a *Drosophila* screen (Zhan et al., 2015) and associated with the Nrf2 (also known as Nfe2l2)-dependent antioxidant pathway (Moujalled et al., 2017). In addition to *Sod1*, we have also identified other ROS-related

Disease Models & Mechanisms (2019) 12, dmm033803. doi:10.1242/dmm.033803

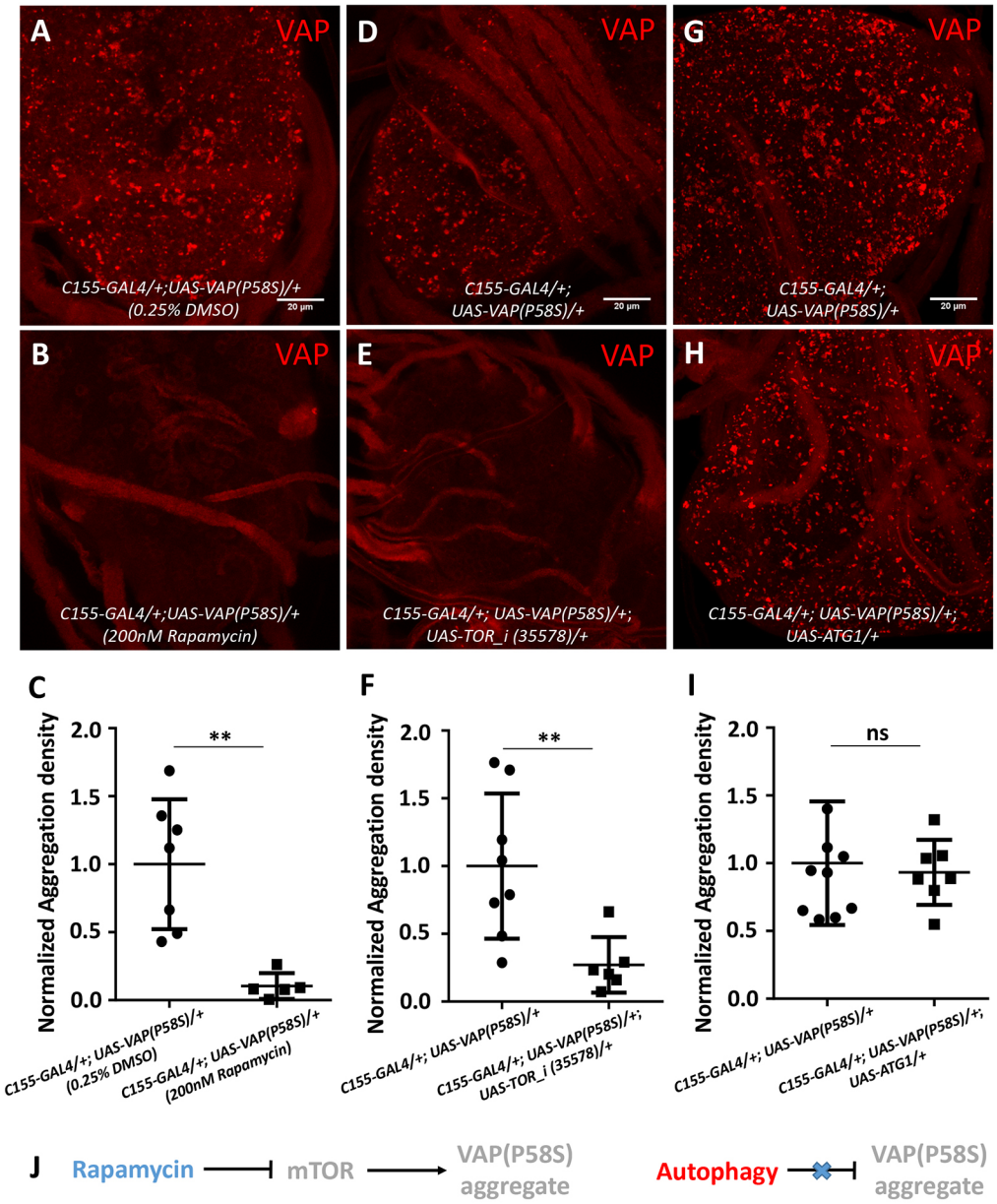

Fig. 6. mTOR downregulation, but not autophagy, reduces VAP(P58S) aggregation. (A-C) Rapamycin feeding decreases aggregation density in the ventral nerve cord of third-instar larval brains in *C155-GAL4/+; UAS-VAP(P58S)/+* flies. (D-F) Neuronal *Tor* knockdown decreases aggregation density in the ventral nerve cord. The '*_i*' appended to a gene name indicates an RNAi line. (G-I) Neuronal overexpression of Atg1 did not affect the aggregation density in the ventral nerve cord. All images were taken at the same magnification. Student's *t*-test (***P*<0.01; ns, not significant). (J) Model depicting mTOR-regulated clearance of aggregates, independent of autophagy. Error bars indicate s.d.

genes – such as *peroxiredoxin V*, *NADH dehydrogenase*, *cytochrome c oxidase* – coding for proteins that localize to the mitochondria, perturbation of which will lead to oxidative stress, potentially affecting the aggregation kinetics of VAP(P58S).

Second, we enriched a subset of targets involved in protein degradation, the UPS and autophagy, an *in vivo* validation of which would shed light on the how these aggregates are compartmentalized and managed in the neurons. Third, this screen highlighted specific chaperones that could be involved in the misfolding and formation of VAP(P58S) aggregates, providing insight into the initiation of the disease condition. Most importantly, through our previous study (Deivasigamani et al., 2014), and our cell-based screen followed by subsequent experimentation, we have established mTOR signalling as a strong modulator of VAP(P58S) aggregation. mTOR signalling responds and integrates signals from nutrients, growth factors, energy and stress, and regulates cellular proteostasis, thus contributing to age-related neurodegenerative diseases (Perluigi et al., 2015), making it an attractive target for further investigation in ALS pathogenesis. Indeed, rapamycin, a mTORC1 inhibitor, is now being used for phase-II clinical trials for ALS (Mandrioli et al., 2018). Lastly, through our screen, targeting processes involved in neurodegeneration, we have identified interactions that point towards a role for VAP as a contributor to a common GRN, in agreement with several examples in the literature (Deivasigamani et al., 2014; Paillusson et al., 2017; Prause et al., 2013; Stoica et al., 2014, 2016; Tudor et al., 2010; van Blitterswijk et al., 2012). When we compared our list of targets with the results from another fly-based screen for VAP(P58S)-induced eye degeneration (Sanhueza et al., 2015), we only found one overlap, *Atg7*, a gene coding for a E1-like ubiquitin-activating enzyme with a role in autophagy (Mizushima and Komatsu, 2011). This lack of significant overlap could possibly be because of differences in sets of genes screened, cell types and phenotypes visualized.

A ROS-dependant physiological mechanism that triggers proteasomal clearance of VAP(P58S) aggregation

In our study, we have used a dosage-dependent pan-neuronal GAL4 expression of VAP(P58S) in order to study changes in aggregation

Disease Models & Mechanisms (2019) 12, dmm033803. doi:10.1242/dmm.033803

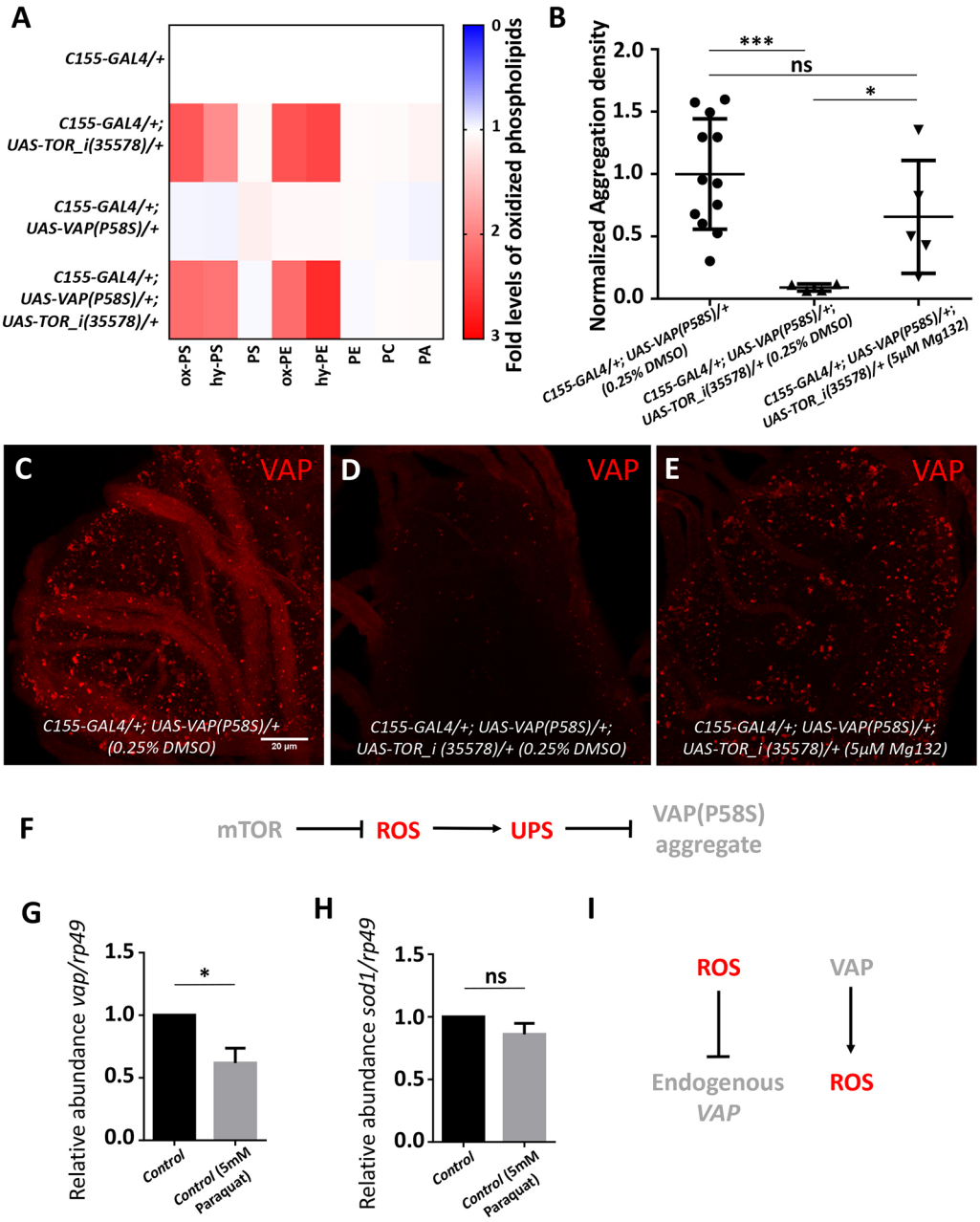

Fig. 7. mTOR inhibition induces ROS and promotes proteasomal degradation of VAP(P58S) protein/aggregates. (A) Heat map depicting change in levels of oxidized phospholipids with *Tor* knockdown normalized to *C155-GAL4/+*, quantified using MS in response to ROS generated in third-instar larval brains (n=3-4) for the listed genotypes. Statistical tests are described in Table S2. (B) Plot showing a significant decrease in aggregation density in the ventral nerve cord in *C155-GAL4/+; UAS-VAP(P58S); UAS-TOR_i (35,578)/+* compared with *C155-GAL4/+; UAS-VAP(P58S)/+* control. This decrease is partially rescued by feeding 5 µM MG132. ANOVA (P=0.0042), Fisher's LSD multiple comparison test (*P<0.05, ***P<0.001; ns, not significant). (C-E) Representative images of third-instar larval brains showing the partial recovery of aggregates upon 5 µM MG132 feeding in *C155-GAL4/+; UAS-VAP(P58S)/+; UAS-TOR_i (35,578)/+* larvae. All images were taken at the same magnification. (F) Model depicting the role of mTOR-regulated ROS in activating proteasomal degradation of VAP(P58S) protein/aggregates. (G) Relative mRNA levels of *VAP* in the *C155-GAL4* control larval brain are lowered upon feeding animals 5 mM paraquat, suggesting that high levels of ROS may negatively regulate *VAP* transcripts. Student's *t*-test (*P<0.05). (H) Relative mRNA levels of *Sod1* in the *C155-GAL4* control larval brain do not change upon feeding 5 mM paraquat (ns, not significant). (I) Model depicting the differential relationship of ROS with VAP. Error bars indicate s.d.

in the third-instar larval brain. We found two targets, SOD1 and mTOR (Deivasigamani et al., 2014), the downregulation of which led to a decrease in VAP(P58S) aggregation accompanied by oxidative stress. We identified a role of ROS in upregulating the proteasomal machinery, thereby facilitating the degradation of misfolded VAP(P58S) protein/aggregates (integrated model, Fig. 8A). However, in the absence of ROS, we did not find any change in aggregation density upon pharmacological proteasomal inhibition. This is consistent with the cell culture studies that point towards the downregulation of the UPS due to VAP(P58S) aggregation, signifying a dominant-negative effect on wild-type VAP function (Genevini et al., 2014; Gkogkas et al., 2008; Kanekura et al., 2006; Papiani et al., 2012). Overexpression of VAP(P58S), or loss of VAP, in *Drosophila* has been shown to enhance ER stress in the adult brain and might be a result of suspended proteasomal degradation (Moustaqim-Barrette et al., 2014; Tsuda et al., 2008). In mice, VAP(P56S) aggregates have been shown to represent an ER quality control compartment that develops as a result of a debilitated ER-associated degradation (ERAD) pathway (Kuijpers et al., 2013). Indeed, VAP has been shown to interact with the unfolded protein response sensor AFT6 in mice and the ERAD complex, thereby regulating proteostasis and lipid homeostasis in HeLa cell lines (Gkogkas et al., 2008; Ernst et al., 2016). Studies in mammalian cell lines suggest that VAP(P56S) is ubiquitinated, aggregates on the ER membrane and is cleared by the AAA+ valosin-containing protein (VCP)/p97, which interacts with Fas-associated factor 1 (FAF1) and may use the FFAT motif in FAF1 as an adapter to interact with VAP (Baron et al., 2014; Papiani et al., 2012). In *Drosophila*, VAP has been shown to be essential for ER homeostasis by maintaining lipid transport, whereas the mutant VAP flies show accumulation of ubiquitinated and membrane proteins in neuronal cells (Moustaqim-Barrette et al., 2014). Hence, although ER stress is built up with VAP(P58S) aggregation, it does not lead to

Disease Models & Mechanisms (2019) 12, dmm033803. doi:10.1242/dmm.033803

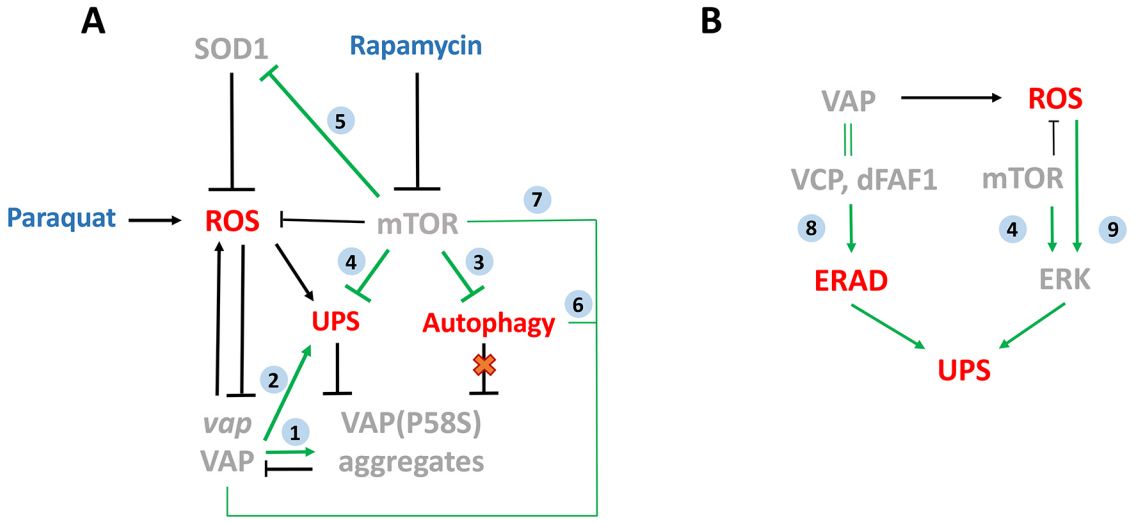

Fig. 8. An integrated model for ROS mediated clearance of VAP(P58S) aggregates via UPS. (A) Model depicting novel relationships of SOD1- and mTOR-induced ROS with VAP and VAP(P58S) aggregates. Clearance of VAP(P58S) protein/aggregates appears to be primarily via the UPS, triggered by ROS, which are, in turn, regulated by cellular pathways such as the mTOR pathway, SOD1 and VAP activity. Autophagy does not appear to be a major contributor to aggregate clearance, under the conditions of our experiment. (B) A hypothetical model proposing the possible link between VAP, ROS and UPS. VAP could regulate the UPS via the ERAD pathway due to its interaction with VCP via dFAF1/Caspar. ROS could be the connecting link between the mTOR pathway and ERK pathway, which together regulate the components of the proteasomal machinery. The link between VAP and ROS that we have demonstrated could modulate proteasomal activity in the cell. Gray italic text, gene; gray upper-case non-italic text, proteins; red text, cellular mechanisms; blue text, drugs; black arrows, experimental evidence/this study; green arrows, relationship described in the literature. Numbers in blue circles indicate research papers: (1) Ratnaparkhi et al., 2008; (2) Kanekura et al., 2006; Kuijpers et al., 2013; (3) Noda and Ohsumi, 1998; Perluigi et al., 2015; (4) Zhao et al., 2015; Rousseau and Bertolotti, 2016; (5) Sun et al., 2012; Tsang et al., 2018; (6) Gomez-Suaga et al., 2017a,b; Zhao et al., 2018; Wu et al., 2018; (7) Deivaisigamani et al., 2014; (8) Baron et al., 2014; Papiani et al., 2012; (9) Cavanaugh et al., 2006; Su et al., 2014.

subsequent oxidative stress, as shown in our results. This suggests that ROS enhances the proteasomal degradation of VAP(P58S) through an ER stress-independent mechanism. Although neuronal VAP(P58S) aggregates appeared to be non-toxic to flies, our study highlights the effects of ROS on the dynamics of VAP(P58S), from misfolded protein to aggregate formation and subsequent clearance.

TOR signalling regulates VAP(P58S) dynamics by UPS-dependent and Atg1-independent mechanisms

We previously identified the mTOR pathway as a strong regulator of both VAP and VAP(P58S) phenotypes at the NMJ (Deivasigamani et al., 2014). Here, we have shown that inhibition of the mTOR pathway also reduces VAP(P58S) aggregation levels in third-instar larval brains in the presence of ROS. mTOR pathway downregulation is known to activate autophagy (Noda and Ohsumi, 1998), a process that has been shown to reduce mutant huntingtin fragments (Ravikumar et al., 2004) and amyloid-β levels (Spilman et al., 2010) in mice models. The role of VAP in autophagy is unclear. With *VAP* (also known as *Vapb*) knockdown in mammalian cell culture, autophagy is upregulated due to the loss of calcium homeostasis that arises with the disruption of ER-mitochondrial contact sites (Gomez-Suaga et al., 2017a,b). This upregulation appears to be dependent on beclin-1, which has a role in autophagosome formation (Wu et al., 2018). However, VAP is also suggested to have a role in autophagosomal biogenesis through direct interaction with the ULK1/FIP200 (also known as RB1CC1) complex (Zhao et al., 2018). Previously, we have observed that neuronal overexpression of VAP or Atg1 reduces bouton size at the NMJ, an effect that is exacerbated in combination (Deivasigamani et al., 2014). On the other hand, Atg1 overexpression rescues the large bouton size associated with VAP(P58S) overexpression in the third-instar larval brains (Deivasigamani et al., 2014). In this study, however, we do not observe any clearance of VAP(P58S) aggregates with overexpression of Atg1 alone (Fig. 8A).

Mtor and *Sod1* have been shown to be genetic interactors in *Drosophila*, with mTOR inhibition enhancing the lifespan defect incurred with *Sod1* knockdown (Sun et al., 2012). Recently, mTOR has been directly shown to regulate SOD1 activity by its phosphorylation based on nutrient availability in yeast and mammalian cells (Tsang et al., 2018). Although this phosphorylation site does not appear to be conserved in *Drosophila*, this study demonstrates the role of mTOR pathway in regulating ROS via SOD1. mTOR inhibition, specifically, mTORC1, has also been shown to activate proteasomal degradation independent of its other targets, such as 4EBP, S6K and Ulk (Cavanaugh et al., 2006; Zhao et al., 2015). An evolutionarily conserved regulation of components of proteasomal assembly by mTORC1 via Mpk1/ERK5 has been reported in yeast and mammalian cell culture (Rousseau and Bertolotti, 2016). ERK5 signalling has been implicated in neuroprotective roles in response to mild levels of oxidative stress (Cavanaugh et al., 2006; Su et al., 2014). These studies suggest that ROS regulation by mTOR inhibition via SOD1 and ERK5 serves as a plausible mechanism for the proteasomal degradation of VAP(P58S) protein/aggregation and, by extension, the rescue of the VAP(P58S) NMJ phenotype (Deivasigamani et al., 2014) (Fig. 8B).

Increase in ROS by VAP, but not VAP(P58S), expression

SOD1-associated elevation in ROS levels and oxidative stress is suggested as a plausible factor of motor neuron death in ALS (Barber et al., 2006; Saccon et al., 2013). Teuling et al. (2007) have shown that VAPB protein levels decrease in an age-dependent manner in a mouse model of SOD1-G93A, providing the first evidence of a link between *Sod1* and *VAP/Als8*. We now find that overexpressed VAP, unlike VAP(P58S), promotes the accumulation

Disease Models & Mechanisms (2019) 12, dmm033803. doi:10.1242/dmm.033803

of ROS in the system. This is consistent with a study that shows lowered ROS in a *vpr-1* (VAP orthologue) mutant of *Caenorhabditis elegans* in response to increased mitochondrial connectivity and altered function (Han et al., 2012). VAP neuronal overexpression in *Drosophila* has also been shown to increase bouton number (Pennetta et al., 2002) similar to the SOD1 mutant phenotype at the NMJ (Milton et al., 2011), and is correlated with increased ROS in both scenarios. VAP may be important in regulating pathways that respond to changes in ROS levels, such as mTOR and ERK pathways that can regulate the UPS (Rousseau and Bertolotti, 2016). VAP also modulates ERAD (and the UPS), via its interaction with VCP and FAF1 (Baron et al., 2014; Papiani et al., 2012). We hypothesize that the interaction between VAP and ROS could lead to crosstalk between these pathways, regulating global proteostasis (hypothetical model, Fig. 8B).

ROS may regulate VAP levels by regulating VAP transcription

In our study, we have found that, in the presence of ROS, *VAP* transcription is downregulated in wild-type flies. We had previously shown that *Sod1* knockdown rescues the VAP macrochaetae phenotype (Deivasigamani et al., 2014), which may be a consequence of excessive ROS accumulation, and subsequent downregulation of VAP levels and function. Two independent studies (Kim et al., 2016; Qiu et al., 2013) that overexpressed VAPB in *Sod1* (SOD1-G93A) mice, as an attempt at rescuing ALS defects, found contradictory observations, owing mainly to differences in expression levels of the protein. *VAPB* mRNA levels are known to be lowered in the spinal cords of patients with sporadic ALS (Anagnostou et al., 2010), as well as in induced pluripotent stem cell-derived motor neurons from ALS8 patients (Mitne-Neto et al., 2007). Based on our results, and taking into consideration earlier observations (Anagnostou et al., 2010; Deivasigamani et al., 2014; Teuling et al., 2007), we propose that a possible ALS disease scenario could include increased ROS, resulting in downregulation of VAP at the transcript level (integrated model, Fig. 8A). It remains to be tested whether ROS-activated pathways, such as MAP kinase pathways or the mTOR pathway, could directly control VAP expression. This VAP/ROS regulation that we have uncovered could have significant implications in ALS pathogenesis for both sporadic and familial ALS.

In summary, we find that the dynamics of VAP(P58S) neural aggregates in *Drosophila*, a species intimately linked to disease in the human context, is sensitive to levels of ROS. Change in the physiological levels of ROS appear to dictate the equilibrium between the aggregated and non-aggregated forms. The cellular levels of ROS are themselves dictated by well-characterized regulatory mechanisms that include ROS generators and scavengers. As shown in this study, TOR signalling and VAP/VAP(P58S) expression levels would contribute to the extent of aggregation, and may act as regulatory feedback loops to regulate physiological ROS levels. SOD1, VAP/ALS8, TOR and ROS appear to be part of a physiological regulatory circuit that maintains levels of VAP(P58S) aggregates.

MATERIALS AND METHODS

Generation of constructs and dsRNA

The complementary DNA (cDNA) sequences of VAP and VAP(P58S) mutant were cloned into *pRM-GFP* plasmid (Bhaskar et al., 2000) to generate both N- and C-terminal GFP fusions, using the *Eco*R1 restriction site. The pRM-GFP vector has GFP cloned into pRM-HA3 vector at the *Bam*HI site. We used 500 µM CuSO4 to drive expression in S2R+ cells after transient transfections. Double-strand RNA (dsRNA) for the secondary screen was generated using a MEGAscript® T7 Kit (AM1333) by Thermo Fisher Scientific. The template for dsRNA was generated using cDNA as a template, prepared from flies. Primers for the template were ordered from Sigma-Aldrich.

Handling of Schneider cells

Drosophila S2R+ cells, a kind gift from Dr Satyajit Mayor [National Centre for Biological Sciences (NCBS), Bangalore, India] were maintained in Schneider cell medium (21720-024, Gibco) with 10% heat-inactivated fetal bovine serum (FBS; 10270, Gibco). Batches of cells were frozen in 10% dimethyl sulfoxide (DMSO; D2650, Sigma-Aldrich) and stored in liquid nitrogen following the DRSC protocol (http://www.flyrnai.org/DRSC-PRC.html). In general, after reviving, cells were discarded after 25-30 passages. Cells were maintained at 23°C and split every 4 days at a ratio of 1:5.

Cell culture and generation of S2R+ stable lines

Stable S2R+ cell lines were generated by co-transfecting with pRM-HA3 constructs of VAP:GFP, VAP(P58S):GFP or GFP along with pCo-Hygro in 20:1 ratio, using Effectene (Qiagen) and/or Mirus TransIT 2020 (MIR 5400), and selected under 250 µg/ml hygromycin (Sigma-Aldrich) for 10-15 passages. Stable as well as transiently transfected cell lines were induced to express the gene of interest under a metallothionein promoter using increasing concentrations (250, 500, 750 and 1000 µM) of $CuSO_4$ and analysed at 12, 24, 36 and 48 h post-induction. Transient transfection assays were performed using Mirus TransIT-2020 (MIR 5400) transfection reagent. The protocol for the dsRNA knockdown assay was modified from Rogers and Rogers (2008). Fixation, 4′,6-diamidino-2-phenylindole (DAPI) staining and imaging were performed using an EVOS FL Auto Cell Imaging system. Super-resolution images of fixed VAP:GFP and VAP(P58S):GFP cells were acquired using a Leica SR GSD 3D system.

Western blotting

Cells were centrifuged at 604 ***g*** for 5 min in an Eppendorf 5414R centrifuge. The pellet was resuspended in 20 µl supernatant and boiled with 1× SDS dye at 95°C. Samples were centrifuged again at 12,045 ***g*** for 10 min. Cell extracts were separated by 12% SDS-PAGE and transferred onto 0.45 µm polyvinylidene fluoride membrane (Millipore). Membranes were blocked for 1 h in 5% skimmed milk in 1× TBS containing 0.1% Tween 20 at room temperature, and probed with 1:10,000 diluted mouse anti-Tubulin (T6074, Sigma-Aldrich) and 1:5000 diluted mouse anti-GFP (Roche Life Science) overnight at 4°C (12 h). Anti-rabbit and anti-mouse secondary antibodies conjugated to horseradish peroxide (Pierce) were used at a dilution of 1:10,000 for 1 h at room temperature. Blots were developed with Immobilon Chemiluminescent Substrate (LuminataClassico Western HRP substrate from Millipore) using a LAS4000 Fuji imaging system.

S2R+ cell culture imaging and analysis

Cell culture images were taken using 20× air objective DAPI (405 nm) and GFP (488 nm) channels to image nuclei and GFP-tagged protein/aggregates in each field, respectively, using an EVOS FL Auto Cell Imaging System. DAPI and GFP channel images were processed using ImageJ 1.48V. Macro scripts were recorded to quantify the total number of cells and number of cells showing aggregates. Total numbers of cells were quantified by converting the DAPI channel image to 8-bit, subtracting the measured mean intensity to remove background, converting greyscale to Binary, using watershed function for segmentation, and analysing particles of size 10-500 and circularity 1. Number of cells showing aggregates were quantified by converting the GFP channel image to 8-bit. Rolling ball background subtraction with 0.3 radius was used to integrate aggregates belonging to the same cell, based on proximity, as one object; the image was converted to Binary, and objects of size 10-500 were counted using ‘analyze particles’ tool.

GO analysis

The list of genes and GO information was obtained based on FlyBase (http://flybase.org) (Marygold et al., 2013) entries. Genes were categorized manually in the broad categories of ALS genes, VAP interactome (Deivasigamani et al., 2014) and proteostasis. Lists of ALS loci and ALS-related genes were obtained from ALSOD (http://alsod.iop.kcl.ac.uk) (Wroe

Disease Models & Mechanisms (2019) 12, dmm033803. doi:10.1242/dmm.033803

et al., 2008). The *Drosophila melanogaster* homologues of these ALS genes were identified using Ensembl biomart tool (http://asia.ensembl.org/biomart/martview) and FlyBase batch download tool. Human orthologues of the target genes listed in Table S1C-E were identified using FlyBase batch download tool.

High-throughput screen and image acquisition

The screen was performed at the screening facility at the Centre for Cellular and Molecular Platforms (C-CAMP), NCBS (http://ccamp.res.in/HTS-HCI). dsRNA for the high-throughput screen was generated and plated into sixteen 384-well plates by Chromous Biotech (Bangalore, India) in preparation for the experiment. The library used as a template for generating dsRNAs was procured from Open Biosystems (RDM1189 and RDM4220). Cells (50 µl; 3×10^6/ml) were plated in each well for the 384-well flat-bottom plates obtained from Corning. Each target dsRNA knockdown experiment was performed in triplicate, randomly arranged in the 384-well plate. The cells were treated with 10 µg/ml dsRNA for 48 h, followed by induction with 500 µM $CuSO_4$. The cells were fixed and imaged at 24 h and 36 h post-induction with $CuSO_4$. Fixation was performed with 4% paraformaldehyde in 1× PBS, after which cells were washed twice with 1× PBS, treated with 0.05 µg/ml DAPI and washed twice with 1× PBS. Each plate contained seven negative controls occupying 42 wells, and 114 unique genes were screened in each plate. A few genes were kept as overlap between multiple plates to check for their consistency and reproducibility. Imaging for the high-throughput screen was performed by an Array Scan VTI HCS system (Thermo Fisher Scientific). Dual-channel images from ten fields in each well were captured using a 20× air objective and an EMCCD camera. The fluorescein isothiocyanate (FITC; 488 nm) channel was used for imaging VAP(P58S):GFP aggregates, and the DAPI (405 nm) channel was used for imaging cell nuclei. Ten fields were imaged in each well and ∼400 cells were imaged per field. In well triplicates, ∼12,000 cells were imaged for each dsRNA knockdown.

High-throughput data analysis

Images from the FITC and DAPI channels in each site were read using the Bio-Formats MATLAB toolbox (Linkert et al., 2010) and were processed using custom MATLAB scripts (Dey et al., 2014). The segmentation was performed using the DAPI images, and the extraction of pixel intensities was done on the FITC channel. Illumination correction was performed as a pre-processing step on the DAPI images, and individual nuclei were segmented after a contrast stretching routine was applied. The identified objects were further filtered for outliers, based on a size-based cutoff, and the individual eight connected components were labelled as separate nuclei. Under 20× magnification, we estimated the cellular radius to be ∼10 pixels, corresponding to 5 µm. Thus, labelled cellular objects (ROIs) were obtained by dilating the centroids of each nuclei by 10 pixels. Around 400 ROIs were obtained from each field, consistent with manually counted cells in these images. The resultant ROIs were further filtered for clumps and out-of-focus objects. The GFP intensities were obtained for these ROIs following a local background correction of the FITC images (with a disk size of 3 pixels). Average and total intensities were calculated from the pixel data obtained from every cell/ROI from these FITC images. A Kolmogorov–Smirnov-like statistic was used to assign *Z*-scores to each gene on plate as reported by Dey et al. (2014). A statistically significant threshold was obtained for the triplicate data using Monte Carlo simulations. Genes were classified as hits if they occurred two or more times above a given *Z*-score threshold. The false-positive rate for both parameters at both time points was zero. The false-negative rate for average intensity for the 24-h time point was 0.2523 and for the 36-h time point was 0.361. The false-negative rate for total intensity for the 24-h time point was 0.3838 and for the 36-h time point was 0.3164.

Fly husbandry and brain aggregation assay

D. melanogaster lines were maintained on standard corn meal agar medium. *UAS-GAL4* system (Brand and Perrimon, 1993) was used for overexpression of transgenes. *UAS-VAP* wild type, *UAS-VAP(P58S)* and *C155-GAL4* lines used for fly experiments have been described earlier (Deivasigamani et al., 2014; Ratnaparkhi et al., 2008). Canton S flies were used as wild-type control. *UAS-VAP_i* (27312), *UAS-SOD1_i* (34616, 29389, 36804) and *UAS-TOR_i* (35578) (where the suffix '*_i*' indicates an RNAi line), and *UAS-SOD1* (24750, 33605), were obtained from Bloomington *Drosophila* Stock Centre (BDSC). Clone for UAS-FLAG-HA-tagged SOD1 in pUASt vector was obtained – for expression in *Drosophila* – from *Drosophila* Genome Research Centre (DGRC) and injected in the NCBS C-CAMP transgenic facility. Two independent *UAS-Atg1* lines were used for our experiments. One line (Mohseni et al., 2009; Scott et al., 2007) was procured from BDSC (51654), while the other was kindly provided by Dr Chen (Academia Sinica, Taipei, Taiwan). Both lines were validated in the wing and thorax using *ptc-GAL4* as described (Chen et al., 2008). Briefly, expression of the two Atg1 lines in the *ptc* domain results in missing anterior cross veins and loss of thoracic bristles. Additionally, expression of both lines using *actin-GAL4* also caused early lethality. Atg1 overexpression in the larval brain using BDSC 51654 has been shown to increase LysoTracker staining in the larval brain hemisphere, indicating activation of autophagy (Shen and Ganetzky, 2009). The readout of autophagy in our experiments is thus indirect and not based on specific cellular markers. For all genetic crosses, experiments were set at 18°C, 25°C or 28°C, as indicated. Brains were dissected from third-instar larvae and processed for immunostaining assay. For fixation, 4% paraformaldehyde containing 0.1% Triton X-100 was used, followed by washes with 1× PBS. Blocking treatment and washes were performed with 0.3% Triton X-100 with 2% bovine serum albumin. Brains were stained with 1:500 diluted anti-VAP antibody (Yadav et al., 2018) and 1:1000 anti-rabbit secondary (Invitrogen) was used. *Z*-stacks of five to ten brains for each sample were imaged under a 63× oil objective of a Ziess LSM 710 confocal microscope. The number of aggregates were quantified per μm^3 of the ventral nerve cord, defined as 'aggregation density', using the Huygen professional software. The high-intensity puncta were considered as aggregates. An arbitrary threshold was set for controls as well as for test samples that achieved removing low-intensity background signal emitted by the tissue, along with separation of high-intensity puncta that were adjacent to one another. An object filter was used to remove objects of size greater than 1000 pixels, and garbage size smaller than 10 pixels was excluded. Three 3D region of interests of fixed size were drawn along the tip of the ventral nerve cord and the number of aggregates were counted from each of these ROIs and averaged for each animal. The volume (in μm^3) of ROI depicting the thickness of the brain tissue was measured as the range of the *z*-stack of the image. The aggregation density obtained for each brain was normalized to the mean of the control group, *C155-GAL4; UAS-VAP(P58S)* (+0.25% DMSO, in the case of DMSO-soluble drug experiments) and plotted as 'normalized aggregation density' in each graph. Student's *t*-test and one-way ANOVA with Fisher's least significance difference (LSD) multiple comparison test were used to measure statistical significance using GraphPad Prism 7.

Drug treatment

Cells were exposed to 10 mM and 20 mM paraquat dichloride hydrate (500 mM, 36541, Sigma-Aldrich) for 24 h prior to protein induction with 500 µM $CuSO_4$. Fixation, DAPI staining and imaging were performed using an EVOS FL Auto Cell Imaging System. For flies, 10-12 virgins were placed with CS males for each genotype, and animals were allowed to mate for 24 h and transferred to standard cornmeal fly medium containing paraquat (5 mM), MG132 (5 µM), rapamycin (200 nM) or DMSO (0.25%).

Lipid extraction and targeted LC-MS lipidomics

All MS quantitation phospholipid standards were purchased from Avanti Polar Lipids (Alabaster, AL, USA). The brain samples were washed with PBS (three times), and transferred into a glass vial using 1 ml PBS. Then, 3 ml of 2:1 (vol/vol) $CHCl_3$: MeOH with the internal standard mix (1 nmol 17:1 free fatty acids, 100 pmol each of 17:0-20:4 PS, 17:0-20:4 phosphatidylcholine, 17:0-20:4 PE and 17:0-20:4 phosphatidylalanine) was added, and the mixture was vigorously vortexed. The two phases were separated by centrifugation at 2800 ***g*** for 5 min. The organic phase (bottom) was removed, 50 µl formic acid was added to acidify the aqueous homogenate (to enhance extraction of phospholipids) and $CHCl_3$ was added to make up 4 ml volume. The mixture was vortexed and separated using centrifugation as described above. Both the organic extracts were pooled and dried under a stream of N_2. The lipidome

was re-solubilized in 200 µl of 2:1 (vol/vol) $CHCl_3$: MeOH, and 20 µl was used for the targeted liquid chromatography (LC)-MS analysis. All the phospholipid species analysed in this study were quantified using the multiple reaction monitoring (MRM) high-resolution scanning method on a Sciex X500R QTOF LC-MS with an Exion-LC series quaternary pump. All data were acquired and analysed using SciexOS software as described before (Pathak et al., 2018). LC separation was achieved using a Gemini 5U C-18 column (Phenomenex, 5 µm, 50×4.6 mm) coupled to a Gemini guard column (Phenomenex, 4×3 mm, Phenomenex security cartridge). The LC solvents were as follows: for positive mode: buffer A, 95:5 (vol/vol) H_2O: MeOH +0.1% formic acid+10 mM ammonium formate; and buffer B, 60:35:5 (vol/vol) iPrOH: MeOH: H_2O+0.1% formic acid+10 mM ammonium formate; for negative mode: buffer A, 95:5 (vol/vol) H_2O: MeOH+0.1% ammonium hydroxide; and buffer B, 60:35:5 (vol/vol) iPrOH: MeOH: H_2O+0.1% ammonium hydroxide. All the MS-based lipid estimations was performed using an electrospray ion source, using the following MS parameters: ion source=turbo spray, collision gas=medium, curtain gas=20 l/min, ion spray voltage=4500 V, temperature=400°C. A typical LC run consisted of 55 min, with the following solvent run sequence post-injection: 0.3 ml/min of 0% buffer B for 5 min, 0.5 ml/min of 0% buffer B for 5 min, 0.5 ml/min linear gradient of buffer B from 0 to 100% over 25 min, 0.5 ml/min of 100% buffer B for 10 min, and re-equilibration with 0.5 ml/min of 0% buffer B for 10 min. A detailed list of all the species targeted in this MRM study, describing the precursor parent ion mass and adduct, and the product ion targeted, can be found in Table S2. All the endogenous lipid species were quantified by measuring the area under the curve in comparison to the respective internal standard, and then normalizing to the number of larval brains. All oxidized phospholipids detected were normalized to the corresponding non-oxidized phospholipid internal standard. All data are represented as mean±s.e.m. of at least four biological replicates per genotype.

mRNA isolation, cDNA preparation and quantitative reverse transcription PCR

Approximately 1 µg mRNA was isolated from 12-18 third-instar larval brains using a Direct-zol™ RNA MicroPrep Kit (R2062) from Zymo Research. The cDNA reaction was carried out using a High Capacity cDNA Reverse Transcriptase Kit (4368814) by Applied Biosystems. The quantitative PCR reaction was carried out using KAPA SYBR FAST (KK4602) by Sigma-Aldrich and Replex Mastercycler by Eppendorf. The experiment was carried out in three biological replicates with technical triplicates.

Regulatory oversight

All experimental protocols were considered and approved by the Indian Institutes of Science Education and Research (IISER) Institutional Biosafety Committee (IBSC). The IBSC is overseen by the Review Committee on Genetic Manipulation, Department of Biotechnology, Government of India.

Acknowledgements

The S2R+ screen was carried out as a paid service at the NCBS C-CAMP high-throughput screening facility. At NCBS, we thank Dr Satyajit Mayor for his support; Shahab Uddin, Lokavya Kurup and Vandana for technical assistance during the execution of the screen; and Kausik Chakraborty, Institute of Genomics and Integrative Biology, for advice on the analysis of the screen. We thank the BDSC, supported by NIH grant P40OD018537, for fly stocks; DGRC, supported by NIH grant 2P40OD010949, for vectors and clones; and the TRiP collection at Harvard Medical School (NIH/NIGMS R01-GM084947) for providing transgenic RNAi fly stocks. We thank IISER Microscopy/Confocal Facility and Dr Nagaraj Balasubramaniam for access to the EVOS system; Shubham Singh and Shabnam Patil for technical assistance with the MS experiments; Anuradha Ratnaparkhi and Girish Deshpande for discussions and comments; and Richa Rikhy for helpful discussions.

Competing interests

The authors declare no competing or financial interests.

Author contributions

Conceptualization: G.S.R.; Methodology: K.C., L.P., B.R., S.D., S.S.K., G.S.R.; Software: B.R.; Validation: K.C., L.P.; Formal analysis: K.C., L.P., B.R., S.S.K., G.S.R.; Investigation: K.C., L.P., S.S.K., G.S.R.; Resources: K.C., S.D., G.S.R.; Data curation: B.R.; Writing - original draft: K.C., B.R., S.D., G.S.R.; Writing - review & editing: K.C., S.S.K., G.S.R.; Visualization: G.S.R.; Supervision: S.S.K., G.S.R.; Project administration: G.S.R.; Funding acquisition: G.S.R.

Funding

This work was supported by the Department of Science and Technology, Ministry of Science and Technology (EMR/2014/000367 to G.S.R.; ECR/2016/001261 to S.S.K.; Fund for Improvement of S&T Infrastructure Development Grant to the IISER Pune Biology Department); the Department of Biotechnology, Ministry of Science and Technology (BT/PR8636/AGR/36/786/2013); the DBT India Alliance (IA/I/15/2/502058 to S.S.K.); and the Council of Scientific and Industrial Research (research fellowships to K.C. and S.D.). K.C. is an awardee of a DMM travel grant.

Data availability

The raw images of the S2R+ screen are available in the EBI Biostudies database (https://www.ebi.ac.uk/biostudies) with accession number S-BSST211.

Supplementary information

Supplementary information available online at
http://dmm.biologists.org/lookup/doi/10.1242/dmm.033803.supplemental

References

Alpy, F., Rousseau, A., Schwab, Y., Legueux, F., Stoll, I., Wendling, C., Spiegelhalter, C., Kessler, P., Mathelin, C., Rio, M.-C. et al. (2013). STARD3 or STARD3NL and VAP form a novel molecular tether between late endosomes and the ER. *J. Cell Sci.* **126**, 5500-5512.

Anagnostou, G., Akbar, M. T., Paul, P., Angelinetta, C., Steiner, T. J. and de Belleroche, J. (2010). Vesicle associated membrane protein B (VAPB) is decreased in ALS spinal cord. *Neurobiol. Aging* **31**, 969-985.

Andersen, P. M. and Al-Chalabi, A. (2011). Clinical genetics of amyotrophic lateral sclerosis: what do we really know? *Nat. Rev. Neurol.* **7**, 603-615.

Barber, S. C., Mead, R. J. and Shaw, P. J. (2006). Oxidative stress in ALS: a mechanism of neurodegeneration and a therapeutic target. *Biochim. Biophys. Acta* **1762**, 1051-1067.

Baron, Y., Pedrioli, P. G., Tyagi, K., Johnson, C., Wood, N. T., Fountaine, D., Wightman, M. and Alexandru, G. (2014). VAPB/ALS8 interacts with FFAT-like proteins including the p97 cofactor FAF1 and the ASNA1 ATPase. *BMC Biol.* **12**, 39.

Bhaskar, V., Valentine, S. A. and Courey, A. J. (2000). A functional interaction between dorsal and components of the Smt3 conjugation machinery. *J. Biol. Chem.* **275**, 4033-4040.

Brand, A. H. and Perrimon, N. (1993). Targeted gene-expression as a means of altering cell fates and generating dominant phenotypes. *Development* **118**, 401-415.

Castello, P. R., Drechsel, D. A. and Patel, M. (2007). Mitochondria are a major source of paraquat-induced reactive oxygen species production in the brain. *J. Biol. Chem.* **282**, 14186-14193.

Cavanaugh, J. E., Jaumotte, J. D., Lakoski, J. M. and Zigmond, M. J. (2006). Neuroprotective role of ERK1/2 and ERK5 in a dopaminergic cell line under basal conditions and in response to oxidative stress. *J. Neurosci. Res.* **84**, 1367-1375.

Chai, A., Withers, J., Koh, Y. H., Parry, K., Bao, H., Zhang, B., Budnik, V. and Pennetta, G. (2008). hVAPB, the causative gene of a heterogeneous group of motor neuron diseases in humans, is functionally interchangeable with its Drosophila homologue DVAP-33A at the neuromuscular junction. *Hum. Mol. Genet.* **17**, 266-280.

Chen, G.-C., Lee, J. Y., Tang, H.-W., Debnath, J., Thomas, S. M. and Settleman, J. (2008). Genetic interactions between Drosophila melanogaster Atg1 and paxillin reveal a role for paxillin in autophagosome formation. *Autophagy* **4**, 37-45.

Cleveland, D. W. and Rothstein, J. D. (2001). From charcot to lou gehrig: deciphering selective motor neuron death in als. *Nat. Rev. Neurosci.* **2**, 806-819.

Cluskey, S. and Ramsden, D. B. (2001). Mechanisms of neurodegeneration in amyotrophic lateral sclerosis. *Mol. Pathol.* **54**, 386-392.

Cochemé, H. M., Quin, C., McQuaker, S. J., Cabreiro, F., Logan, A., Prime, T. A., Abakumova, I., Patel, J. V., Fearnley, I. M., James, A. M. et al. (2011). Measurement of H2O2 within living Drosophila during aging using a ratiometric mass spectrometry probe targeted to the mitochondrial matrix. *Cell Metab.* **13**, 340-350.

Deivasigamani, S., Verma, H. K., Ueda, R., Ratnaparkhi, A. and Ratnaparkhi, G. S. (2014). A genetic screen identifies Tor as an interactor of VAPB in a Drosophila model of amyotrophic lateral sclerosis. *Biol. Open* **3**, 1127-1138.

Deng, H. X., Hentati, A., Tainer, J. A., Iqbal, Z., Cayabyab, A., Hung, W. Y., Getzoff, E. D., Hu, P., Herzfeldt, B., Roos, R. P. et al. (1993). Amyotrophic lateral sclerosis and structural defects in Cu,Zn superoxide dismutase. *Science* **261**, 1047-1051.

De Vos, K. J., Morotz, G. M., Stoica, R., Tudor, E. L., Lau, K.-F., Ackerley, S., Warley, A., Shaw, C. E. and Miller, C. C. (2012). VAPB interacts with the mitochondrial protein PTPIP51 to regulate calcium homeostasis. *Hum. Mol. Genet.* **21**, 1299-1311.

Dey, G., Gupta, G. D., Ramalingam, B., Sathe, M., Mayor, S. and Thattai, M. (2014). Exploiting cell-to-cell variability to detect cellular perturbations. *PLoS ONE* **9**, e90540.

Drechsel, D. A. and Patel, M. (2008). Role of reactive oxygen species in the neurotoxicity of environmental agents implicated in Parkinson's disease. *Free Radic. Biol. Med.* **44**, 1873-1886.

Echeverri, C. J. and Perrimon, N. (2006). High-throughput RNAi screening in cultured cells: a user's guide. *Nat. Rev. Genet.* **7**, 373-384.

Ernst, W. L., Shome, K., Wu, C. C., Gong, X., Frizzell, R. A. and Aridor, M. (2016). VAMP-associated proteins (VAP) as receptors that couple cystic fibrosis transmembrane conductance regulator (CFTR) proteostasis with lipid homeostasis. *J. Biol. Chem.* **291**, 5206-5220.

Genevini, P., Papiani, G., Ruggiano, A., Cantoni, L., Navone, F. and Borgese, N. (2014). Amyotrophic lateral sclerosis-linked mutant VAPB inclusions do not interfere with protein degradation pathways or intracellular transport in a cultured cell model. *PLoS ONE* **9**, e113416.

Gkogkas, C., Middleton, S., Kremer, A. M., Wardrope, C., Hannah, M., Gillingwater, T. H. and Skehel, P. (2008). VAPB interacts with and modulates the activity of ATF6. *Hum. Mol. Genet.* **17**, 1517-1526.

Gomez-Suaga, P., Paillusson, S. and Miller, C. C. J. (2017a). ER-mitochondria signaling regulates autophagy. *Autophagy* **13**, 1250-1251.

Gomez-Suaga, P., Paillusson, S., Stoica, R., Noble, W., Hanger, D. P. and Miller, C. C. J. (2017b). The ER-mitochondria tethering complex VAPB-PTPIP51 regulates autophagy. *Curr. Biol.* **27**, 371-385.

Han, S. M., Tsuda, H., Yang, Y., Vibbert, J., Cottee, P., Lee, S.-J., Winek, J., Haueter, C., Bellen, H. J. and Miller, M. A. (2012). Secreted VAPB/ALS8 major sperm protein domains modulate mitochondrial localization and morphology via growth cone guidance receptors. *Dev. Cell* **22**, 348-362.

Heitman, J., Movva, N. R. and Hall, M. N. (1991). Targets for cell cycle arrest by the immunosuppressant rapamycin in yeast. *Science* **253**, 905-909.

Huttlin, E. L., Ting, L., Bruckner, R. J., Gebreab, F., Gygi, M. P., Szpyt, J., Tam, S., Zarraga, G., Colby, G., Baltier, K. et al. (2015). The BioPlex network: a systematic exploration of the human interactome. *Cell* **162**, 425-440.

Kamat, S. S., Camara, K., Parsons, W. H., Chen, D.-H., Dix, M. M., Bird, T. D., Howell, A. R. and Cravatt, B. F. (2015). Immunomodulatory lysophosphatidylserines are regulated by ABHD16A and ABHD12 interplay. *Nat. Chem. Biol.* **11**, 164-171.

Kanekura, K., Nishimoto, I., Aiso, S. and Matsuoka, M. (2006). Characterization of amyotrophic lateral sclerosis-linked P56S mutation of vesicle-associated membrane protein-associated protein B (VAPB/ALS8). *J. Biol. Chem.* **281**, 30223-30233.

Kim, J. Y., Jang, A., Reddy, R., Yoon, W. H. and Jankowsky, J. L. (2016). Neuronal overexpression of human VAPB slows motor impairment and neuromuscular denervation in a mouse model of ALS. *Hum. Mol. Genet.* **25**, 4661-4673.

Kory, N., Grond, S., Kamat, S. S., Li, Z., Krahmer, N., Chitraju, C., Zhou, P., Fröhlich, F., Semova, I., Ejsing, C. et al. (2017). Mice lacking lipid droplet-associated hydrolase, a gene linked to human prostate cancer, have normal cholesterol ester metabolism. *J. Lipid Res.* **58**, 226-235.

Kuijpers, M., van Dis, V., Haasdijk, E. D., Harterink, M., Vocking, K., Post, J. A., Scheper, W., Hoogenraad, C. C. and Jaarsma, D. (2013). Amyotrophic lateral sclerosis (ALS)-associated VAPB-P56S inclusions represent an ER quality control compartment. *Acta Neuropathol. Commun.* **1**, 24.

Lev, S., Ben Halevy, D., Peretti, D. and Dahan, N. (2008). The VAP protein family: from cellular functions to motor neuron disease. *Trends Cell Biol.* **18**, 282-290.

Linkert, M., Rueden, C. T., Allan, C., Burel, J.-M., Moore, W., Patterson, A., Loranger, B., Moore, J., Neves, C., Macdonald, D. et al. (2010). Metadata matters: access to image data in the real world. *J. Cell Biol.* **189**, 777-782.

Loewen, C. J., Roy, A. and Levine, T. P. (2003). A conserved ER targeting motif in three families of lipid binding proteins and in Opi1p binds VAP. *EMBO J.* **22**, 2025-2035.

Mandrioli, J., D'Amico, R., Zucchi, E., Gessani, A., Fini, N., Fasano, A., Caponnetto, C., Chiò, A., Dalla Bella, E., Lunetta, C. et al. (2018). Rapamycin treatment for amyotrophic lateral sclerosis: Protocol for a phase II randomized, double-blind, placebo-controlled, multicenter, clinical trial (RAP-ALS trial). *Medicine (Baltim.)* **97**, e11119.

Marygold, S. J., Leyland, P. C., Seal, R. L., Goodman, J. L., Thurmond, J., Strelets, V. B. and Wilson, R. J. (2013). FlyBase: improvements to the bibliography. *Nucleic Acids Res.* **41**, D751-D757.

Metz, J., Castro, I. G. and Schrader, M. (2017). Peroxisome motility measurement and quantification assay. *Bio. Protoc.* **7**, e2536.

Milton, V. J., Jarrett, H. E., Gowers, K., Chalak, S., Briggs, L., Robinson, I. M. and Sweeney, S. T. (2011). Oxidative stress induces overgrowth of the Drosophila neuromuscular junction. *Proc. Natl. Acad. Sci. USA* **108**, 17521-17526.

Mitne-Neto, M., Ramos, C. R. R., Pimenta, D. C., Luz, J. S., Nishimura, A. L., Gonzales, F. A., Oliveira, C. C. and Zatz, M. (2007). A mutation in human VAP-B–MSP domain, present in ALS patients, affects the interaction with other cellular proteins. *Protein Expr. Purif.* **55**, 139-146.

Mizushima, N. and Komatsu, M. (2011). Autophagy: renovation of cells and tissues. *Cell* **147**, 728-741.

Mohseni, N., McMillan, S. C., Chaudhary, R., Mok, J. and Reed, B. H. (2009). Autophagy promotes caspase-dependent cell death during Drosophila development. *Autophagy* **5**, 329-338.

Moujalled, D., Grubman, A., Acevedo, K., Yang, S., Ke, Y. D., Moujalled, D. M., Duncan, C., Caragounis, A., Perera, N. D., Turner, B. J. et al. (2017). TDP-43 mutations causing amyotrophic lateral sclerosis are associated with altered expression of RNA-binding protein hnRNP K and affect the Nrf2 antioxidant pathway. *Hum. Mol. Genet.* **26**, 1732-1746.

Moustaqim-Barrette, A., Lin, Y. Q., Pradhan, S., Neely, G. G., Bellen, H. J. and Tsuda, H. (2014). The amyotrophic lateral sclerosis 8 protein, VAP, is required for ER protein quality control. *Hum. Mol. Genet.* **23**, 1975-1989.

Mulligan, V. K. and Chakrabartty, A. (2013). Protein misfolding in the late-onset neurodegenerative diseases: common themes and the unique case of amyotrophic lateral sclerosis. *Proteins* **81**, 1285-1303.

Murphy, S. E. and Levine, T. P. (2016). VAP, a versatile access point for the endoplasmic reticulum: review and analysis of FFAT-like motifs in the VAPome. *Biochim. Biophys. Acta* **1861**, 952-961.

Nishimura, A. L., Mitne-Neto, M., Silva, H. C. A., Richieri-Costa, A., Middleton, S., Cascio, D., Kok, F., Oliveira, J. R. M., Gillingwater, T., Webb, J. et al. (2004). A mutation in the vesicle-trafficking protein VAPB causes late-onset spinal muscular atrophy and amyotrophic lateral sclerosis. *Am. J. Hum. Genet.* **75**, 822-831.

Noda, T. and Ohsumi, Y. (1998). Tor, a phosphatidylinositol kinase homologue, controls autophagy in yeast. *J. Biol. Chem.* **273**, 3963-3966.

Ogrodnik, M., Salmonowicz, H., Brown, R., Turkowska, J., Sredniawa, W., Pattabiraman, S., Amen, T., Abraham, A. C., Eichler, N., Lyakhovetsky, R. et al. (2014). Dynamic JUNQ inclusion bodies are asymmetrically inherited in mammalian cell lines through the asymmetric partitioning of vimentin. *Proc. Natl. Acad. Sci. USA* **111**, 8049-8054.

Paillusson, S., Gomez-Suaga, P., Stoica, R., Little, D., Gissen, P., Devine, M. J., Noble, W., Hanger, D. P. and Miller, C. C. J. (2017). alpha-Synuclein binds to the ER-mitochondria tethering protein VAPB to disrupt Ca(2+) homeostasis and mitochondrial ATP production. *Acta Neuropathol.* **134**, 129-149.

Papiani, G., Ruggiano, A., Fossati, M., Raimondi, A., Bertoni, G., Francolini, M., Benfante, R., Navone, F. and Borgese, N. (2012). Restructured endoplasmic reticulum generated by mutant amyotrophic lateral sclerosis-linked VAPB is cleared by the proteasome. *J. Cell Sci.* **125**, 3601-3611.

Pathak, D., Mehendale, N., Singh, S., Mallik, R. and Kamat, S. S. (2018). Lipidomics suggests a new role for ceramide synthase in phagocytosis. *ACS Chem. Biol.* **13**, 2280-2287.

Pennetta, G., Hiesinger, P. R., Fabian-Fine, R., Meinertzhagen, I. A. and Bellen, H. J. (2002). Drosophila VAP-33A directs bouton formation at neuromuscular junctions in a dosage-dependent manner. *Neuron* **35**, 291-306.

Perluigi, M., Di Domenico, F. and Butterfield, D. A. (2015). mTOR signaling in aging and neurodegeneration: At the crossroad between metabolism dysfunction and impairment of autophagy. *Neurobiol. Dis.* **84**, 39-49.

Prause, J., Goswami, A., Katona, I., Roos, A., Schnizler, M., Bushuven, E., Dreier, A., Buchkremer, S., Johann, S., Beyer, C. et al. (2013). Altered localization, abnormal modification and loss of function of Sigma receptor-1 in amyotrophic lateral sclerosis. *Hum. Mol. Genet.* **22**, 1581-1600.

Qiu, L., Qiao, T., Beers, M., Tan, W., Wang, H., Yang, B. and Xu, Z. (2013). Widespread aggregation of mutant VAPB associated with ALS does not cause motor neuron degeneration or modulate mutant SOD1 aggregation and toxicity in mice. *Mol. Neurodegener* **8**, 1.

Ratnaparkhi, A., Lawless, G. M., Schweizer, F. E., Golshani, P. and Jackson, G. R. (2008). A drosophila model of ALS: human ALS-associated mutation in VAP33A suggests a dominant negative mechanism. *PLoS ONE* **3**, e2334.

Ravikumar, B., Vacher, C., Berger, Z., Davies, J. E., Luo, S., Oroz, L. G., Scaravilli, F., Easton, D. F., Duden, R., O'Kane, C. J. et al. (2004). Inhibition of mTOR induces autophagy and reduces toxicity of polyglutamine expansions in fly and mouse models of Huntington disease. *Nat. Genet.* **36**, 585-595.

Rogers, S. L. and Rogers, G. C. (2008). Culture of Drosophila S2 cells and their use for RNAi-mediated loss-of-function studies and immunofluorescence microscopy. *Nat. Protoc.* **3**, 606-611.

Rosen, D. R., Siddique, T., Patterson, D., Figlewicz, D. A., Sapp, P., Hentati, A., Donaldson, D., Goto, J., O'Regan, J. P., Deng, H.-X. et al. (1993). Mutations in Cu/Zn superoxide dismutase gene are associated with familial amyotrophic lateral sclerosis. *Nature* **362**, 59-62.

Rousseau, A. and Bertolotti, A. (2016). An evolutionarily conserved pathway controls proteasome homeostasis. *Nature* **536**, 184-189.

Saccon, R. A., Bunton-Stasyshyn, R. K., Fisher, E. M. and Fratta, P. (2013). Is SOD1 loss of function involved in amyotrophic lateral sclerosis? *Brain* **136**, 2342-2358.

Sanhueza, M., Chai, A., Smith, C., McCray, B. A., Simpson, T. I., Taylor, J. P. and Pennetta, G. (2015). Network analyses reveal novel aspects of ALS pathogenesis. *PLoS Genet.* **11**, e1005107.

Scott, R. C., Juhász, G. and Neufeld, T. P. (2007). Direct induction of autophagy by Atg1 inhibits cell growth and induces apoptotic cell death. *Curr. Biol.* **17**, 1-11.

Shen, W. and Ganetzky, B. (2009). Autophagy promotes synapse development in Drosophila. *J. Cell Biol.* **187**, 71-79.

Spilman, P., Podlutskaya, N., Hart, M. J., Debnath, J., Gorostiza, O., Bredesen, D., Richardson, A., Strong, R. and Galvan, V. (2010). Inhibition of mTOR by rapamycin abolishes cognitive deficits and reduces amyloid-beta levels in a mouse model of Alzheimer's disease. *PLoS ONE* **5**, e9979.

Stoica, R., De Vos, K. J., Paillusson, S., Mueller, S., Sancho, R. M., Lau, K.-F., Vizcay-Barrena, G., Lin, W.-L., Xu, Y.-F., Lewis, J. et al. (2014). ER-mitochondria associations are regulated by the VAPB-PTPIP51 interaction and are disrupted by ALS/FTD-associated TDP-43. *Nat. Commun.* **5**, 3996.

Stoica, R., Paillusson, S., Gomez-Suaga, P., Mitchell, J. C., Lau, D. H. W., Gray, E. H., Sancho, R. M., Vizcay-Barrena, G., De Vos, K. J., Shaw, C. E. et al. (2016). ALS/FTD-associated FUS activates GSK-3beta to disrupt the VAPB-PTPIP51 interaction and ER-mitochondria associations. *EMBO Rep.* **17**, 1326-1342.

Su, C., Sun, F., Cunningham, R. L., Rybalchenko, N. and Singh, M. (2014). ERK5/KLF4 signaling as a common mediator of the neuroprotective effects of both nerve growth factor and hydrogen peroxide preconditioning. *Age (Dordr)* **36**, 9685.

Sun, X., Komatsu, T., Lim, J., Laslo, M., Yolitz, J., Wang, C., Poirier, L., Alberico, T. and Zou, S. (2012). Nutrient-dependent requirement for SOD1 in lifespan extension by protein restriction in Drosophila melanogaster. *Aging Cell* **11**, 783-793.

Tarasiuk, J., Kułakowska, A., Drozdowski, W., Kornhuber, J. and Lewczuk, P. (2012). CSF markers in amyotrophic lateral sclerosis. *J. Neural. Transm.* **119**, 747-757.

Taylor, J. P., Brown, R. H., Jr. and Cleveland, D. W. (2016). Decoding ALS: from genes to mechanism. *Nature* **539**, 197-206.

Teuling, E., Ahmed, S., Haasdijk, E., Demmers, J., Steinmetz, M. O., Akhmanova, A., Jaarsma, D. and Hoogenraad, C. C. (2007). Motor neuron disease-associated mutant vesicle-associated membrane protein-associated protein (VAP) B recruits wild-type VAPs into endoplasmic reticulum-derived tubular aggregates. *J. Neurosci.* **27**, 9801-9815.

Tsang, C. K., Chen, M., Cheng, X., Qi, Y., Chen, Y., Das, I., Li, X., Vallat, B., Fu, L. W., Qian, C. N. et al. (2018). SOD1 phosphorylation by mTORC1 couples nutrient sensing and redox regulation. *Mol. Cell* **70**, 502-515 e8.

Tsuda, H., Han, S. M., Yang, Y., Tong, C., Lin, Y. Q., Mohan, K., Haueter, C., Zoghbi, A., Harati, Y., Kwan, J. et al. (2008). The amyotrophic lateral sclerosis 8 protein VAPB is cleaved, secreted, and acts as a ligand for Eph receptors. *Cell* **133**, 963-977.

Tudor, E. L., Galtrey, C. M., Perkinton, M. S., Lau, K. F., De Vos, K. J., Mitchell, J. C., Ackerley, S., Hortobágyi, T., Vámos, E., Leigh, P. N. et al. (2010). Amyotrophic lateral sclerosis mutant vesicle-associated membrane protein-associated protein-B transgenic mice develop TAR-DNA-binding protein-43 pathology. *Neuroscience* **167**, 774-785.

Turner, B. J., Baumer, D., Parkinson, N. J., Scaber, J., Ansorge, O. and Talbot, K. (2008). TDP-43 expression in mouse models of amyotrophic lateral sclerosis and spinal muscular atrophy. *BMC Neurosci.* **9**, 104.

Turner, M. R., Hardiman, O., Benatar, M., Brooks, B. R., Chio, A., de Carvalho, M., Ince, P. G., Lin, C., Miller, R. G., Mitsumoto, H. et al. (2013). Controversies and priorities in amyotrophic lateral sclerosis. *Lancet Neurol.* **12**, 310-322.

Tyurina, Y. Y., Shvedova, A. A., Kawai, K., Tyurin, V. A., Kommineni, C., Quinn, P. J., Schor, N. F., Fabisiak, J. P. and Kagan, V. E. (2000). Phospholipid signaling in apoptosis: peroxidation and externalization of phosphatidylserine. *Toxicology* **148**, 93-101.

van Blitterswijk, M., van Es, M. A., Hennekam, E. A., Dooijes, D., van Rheenen, W., Medic, J., Bourque, P. R., Schelhaas, H. J., van der Kooi, A. J., de Visser, M. et al. (2012). Evidence for an oligogenic basis of amyotrophic lateral sclerosis. *Hum. Mol. Genet.* **21**, 3776-3784.

Walker, A. K. and Atkin, J. D. (2011). Stress signaling from the endoplasmic reticulum: a central player in the pathogenesis of amyotrophic lateral sclerosis. *IUBMB Life* **63**, 754-763.

Wroe, R., Wai-Ling Butler, A., Andersen, P. M., Powell, J. F. and Al-Chalabi, A. (2008). ALSOD: the Amyotrophic Lateral Sclerosis Online Database. *Amyotroph Lateral Scler.* **9**, 249-250.

Wu, D., Hao, Z., Ren, H. and Wang, G. (2018). Loss of VAPB regulates autophagy in a Beclin 1-dependent manner. *Neurosci. Bull.* **34**, 1037-1046.

Yadav, S., Thakur, R., Georgiev, P., Deivasigamani, S., Krishnan, H., Ratnaparkhi, G. and Raghu, P. (2018). RDGBalpha localization and function at membrane contact sites is regulated by FFAT-VAP interactions. *J. Cell Sci.* **131**, jcs207985.

Zhan, L., Xie, Q. and Tibbetts, R. S. (2015). Opposing roles of p38 and JNK in a Drosophila model of TDP-43 proteinopathy reveal oxidative stress and innate immunity as pathogenic components of neurodegeneration. *Hum. Mol. Genet.* **24**, 757-772.

Zhang, S., Binari, R., Zhou, R. and Perrimon, N. (2010). A Genomewide RNA Interference Screen for Modifiers of Aggregates Formation by Mutant Huntingtin in Drosophila. *Genetics* **184**, 1165-1179.

Zhao, J., Zhai, B., Gygi, S. P. and Goldberg, A. L. (2015). mTOR inhibition activates overall protein degradation by the ubiquitin proteasome system as well as by autophagy. *Proc. Natl. Acad. Sci. USA* **112**, 15790-15797.

Zhao, Y. G., Liu, N., Miao, G., Chen, Y., Zhao, H. and Zhang, H. (2018). The ER contact proteins VAPA/B interact with multiple autophagy proteins to modulate autophagosome biogenesis. *Curr. Biol.* **28**, 1234-1245.

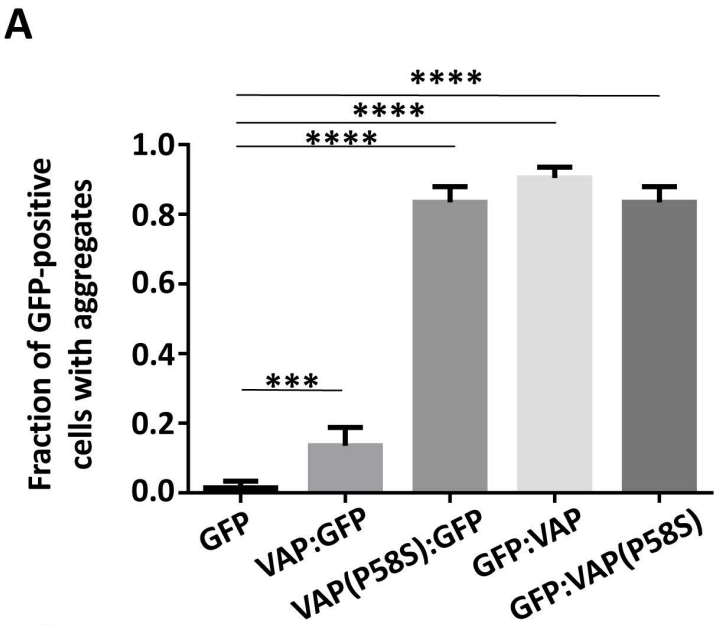

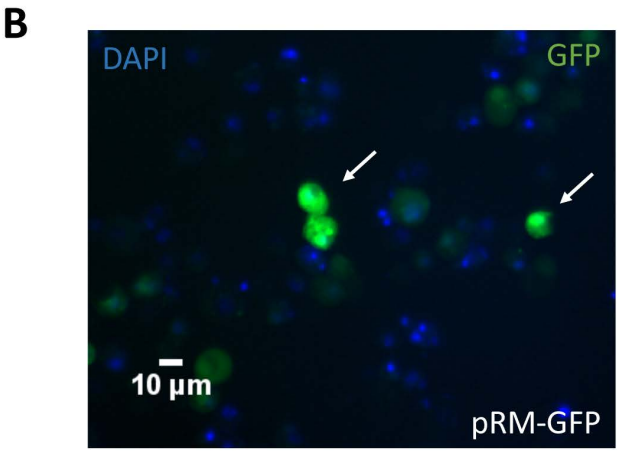

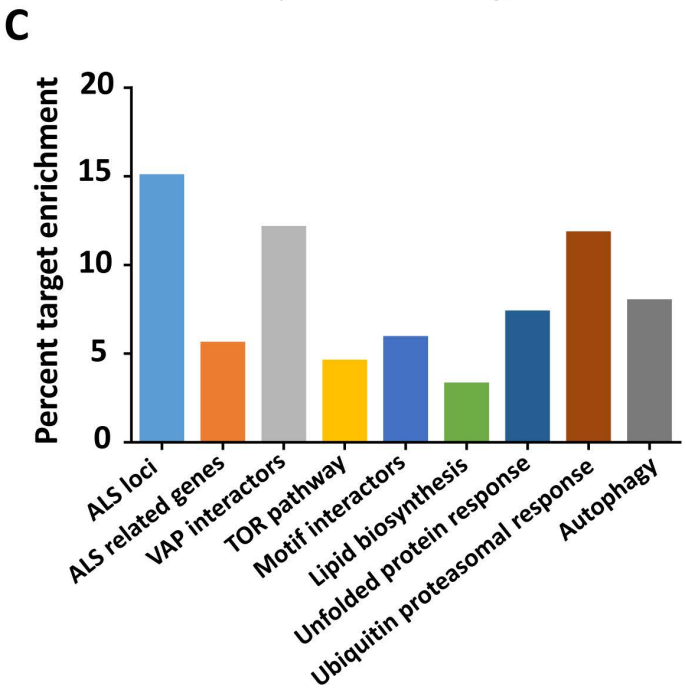

FIGURE S1:

A: Fraction of GFP-positive cells showing aggregates plotted for S2R+ cells transiently transfected with C-terminal or N-terminal tagged GFP constructs of VAP or VAP(P58S) as also only GFP construct at 24 hours post 500µM $CuSO_4$ induction. Unlike C-terminal tagged VAP, N-terminal tagged VAP forms, mutant and wild type, both aggregate. as GFP, when expressed alone does not aggregate or form puncta. ANOVA (P-value: ****<0.0001) Fisher's LSD multiple comparison test (P-values, ***<0.001, ****<0.0001).

B: Homogenous cytoplasmic expression of GFP in S2R+ cells.

C: A list of 85 genes identified based on total cell intensity as a parameter. Based on the analysis of the S2R+ screen, these genes modify aggregation of VAP(P58S):GFP. Graph displays the percent fold enrichment of targets within each gene category. Genes are listed in *Suppl. Table 1D.*

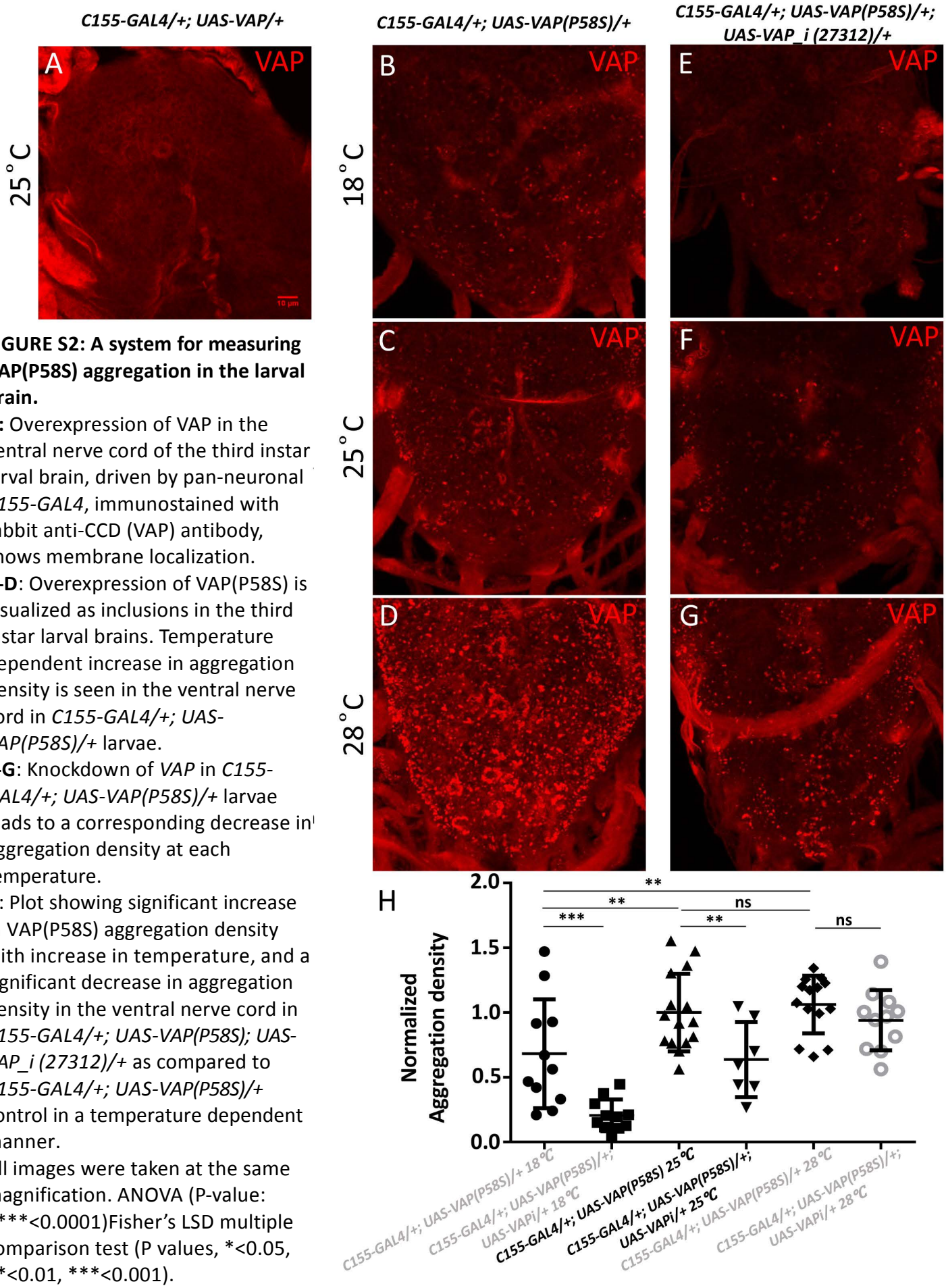

FIGURE S2: A system for measuring VAP(P58S) aggregation in the larval brain.

A: Overexpression of VAP in the ventral nerve cord of the third instar larval brain, driven by pan-neuronal *C155-GAL4*, immunostained with rabbit anti-CCD (VAP) antibody, shows membrane localization.

B-D: Overexpression of VAP(P58S) is visualized as inclusions in the third instar larval brains. Temperature dependent increase in aggregation density is seen in the ventral nerve cord in *C155-GAL4/+; UAS-VAP(P58S)/+* larvae.

E-G: Knockdown of *VAP* in *C155-GAL4/+; UAS-VAP(P58S)/+* larvae leads to a corresponding decrease in aggregation density at each temperature.

H: Plot showing significant increase in VAP(P58S) aggregation density with increase in temperature, and a significant decrease in aggregation density in the ventral nerve cord in *C155-GAL4/+; UAS-VAP(P58S); UAS-VAP_i (27312)/+* as compared to *C155-GAL4/+; UAS-VAP(P58S)/+* control in a temperature dependent manner.

All images were taken at the same magnification. ANOVA (P-value: ****<0.0001)Fisher's LSD multiple comparison test (P values, *<0.05, **<0.01, ***<0.001).

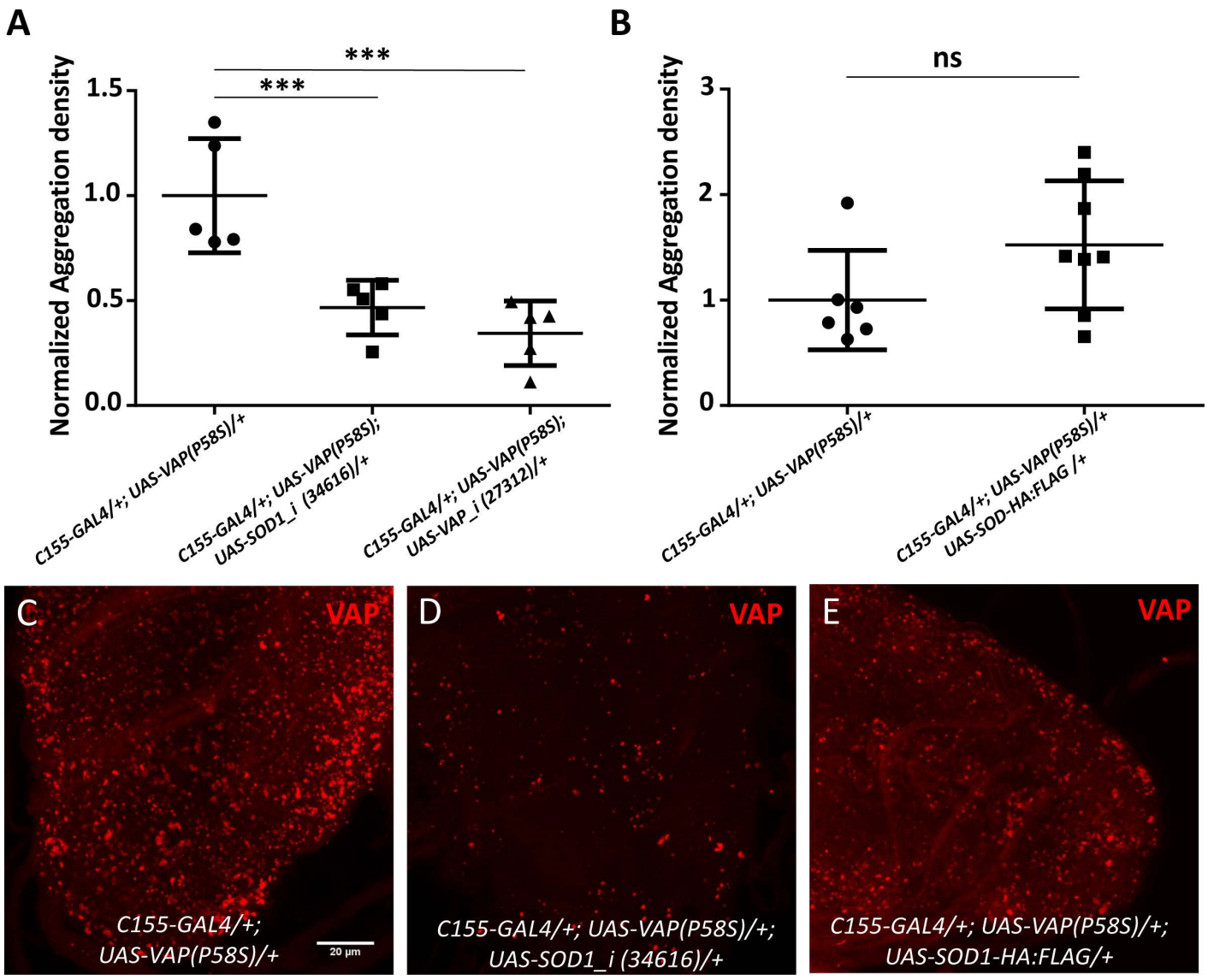

FIGURE S3: SOD1 modulates VAP(P58S) aggregation density in the third instar larval brain

A: *SOD1* knockdown decreases aggregation density. ANOVA (P-value ***, 0.0004) Fisher's LSD multiple comparison test (P-value, ***<0.001)

B: *SOD1:HA:Flag* overexpression does not affect aggregation density. Student's t test (P-value: 0.1066)

C, D, E: Representative images of the ventral nerve cord showing aggregation of VAP(P58S) **(C)**, with *SOD1* knockdown **(D)**, and with *SOD1-HA:Flag* overexpression **(E).** All images were taken at the same magnification. The '*_i*' appended to the gene name indicates a RNAi line with the number in brackets denoting a unique BDSC number. ANOVA (P-value: ****<0.0001) Fisher's LSD multiple comparison test (P-value, **<0.01, ***<0.001).

Disease Models & Mechanisms • Supplementary information

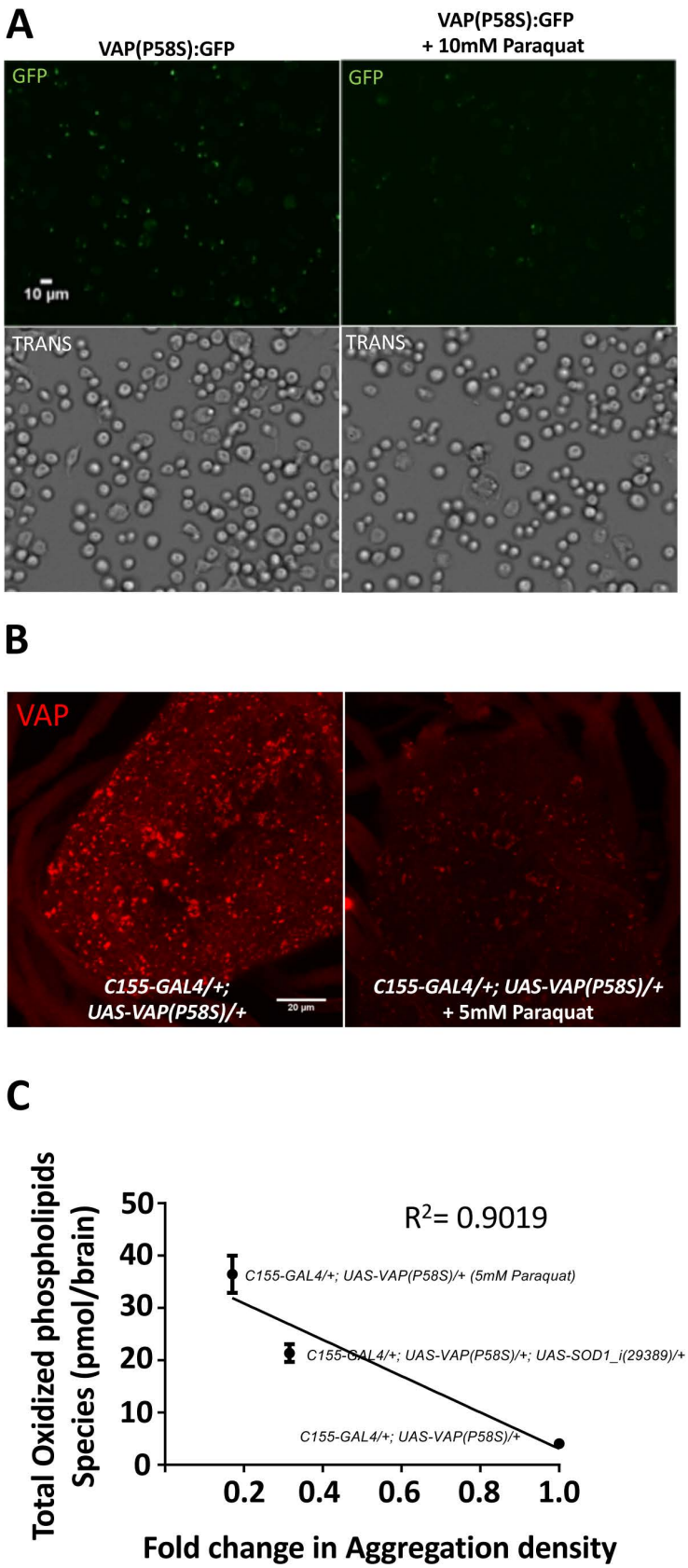

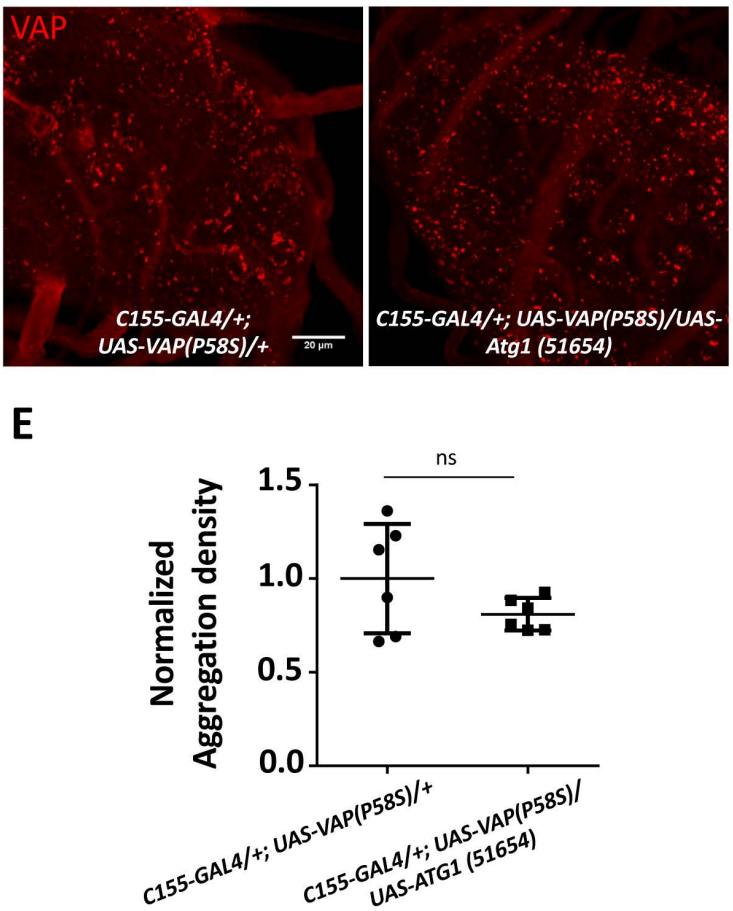

FIGURE S4: ROS induces clearance of VAP(P58S) aggregation, but not autophagy.

A: 10 mM Paraquat treatment for 4 hour, prior to inducing VAP(P58S):GFP in stable S2R+ cell line, reduces the fraction of cells showing aggregation observed 24 hours post-induction. Fraction of cell showing aggregation are plotted in Figure 4A.

B: Feeding 5 mM paraquat decreases aggregation density in the ventral nerve cord of third instar larval brains of *C155-GAL4/+; UAS-VAP(P58S)/+* flies. All images are taken at the same magnification. Aggregation density is plotted in Figure 4B.

C: Inverse correlation between total oxidized phospholipids and fold change in aggregation density.

D-E: Neuronal overexpression of Atg1 did not affect the aggregation density in the ventral nerve cord. Not Significant (ns), Students's t-test. All images were taken at the same magnification.

Disease Models & Mechanisms • Supplementary information

Table S1

A. List of 900 genes utilized for the screen. List is sorted alphabetically based on gene symbol.
B. 900 genes, utilized for the screen, classified and listed into 10 categories associated with ALS or VAP or proteostasis.
C. List of 150 modifiers of VAP(P58S) aggregation, based on average cell intensity, along with their human orthologs.
D. List of 85 modifiers of VAP(P58S) aggregation, based on total cell intensity, along with their human orthologs.
E. List of 57 common modifiers of VAP(P58S) aggregation, along with their human orthologs.

Click here to Download Table S1

Table S2

A. Details of the MRM transitions for the different phospholipids measured
B. LC-MS quantitation of the different phospholipids for different genotypes and paraquat treatment.
C. LC-MS quantitation of the different phospholipids for knockdown of *TOR*.

Click here to Download Table S2

Disease Models & Mechanisms • Supplementary information